water MDPI

Mechanistic Study of Pb^{2+} Removal from Aqueous Solutions Using Eggshells

Mohamed A. Hamouda [1,2,*], **Haliemeh Sweidan** [1], **Munjed A. Maraqa** [1,2] **and Hilal El-Hassan** [1]

[1] Department of Civil and Environmental Engineering, United Arab Emirates University, P.O. Box 15551, Al Ain, UAE; hsweidan@uaeu.ac.ae (H.S.); m.maraqa@uaeu.ac.ae (M.A.M.); helhassan@uaeu.ac.ae (H.E.-H.)

[2] National Water Center, United Arab Emirates University, P.O. Box 15551, Al Ain, UAE

* Correspondence: m.hamouda@uaeu.ac.ae; Tel.: +971-3-713-5155

Abstract: This study investigates the impact of eggshell particle size and solid-to-water (s/w) ratio on lead (Pb^{2+}) removal from aqueous solution. Collected raw eggshells were washed, crushed, and sieved into two particle sizes (<150 and 150–500 µm). Batch Pb^{2+} removal experiments were conducted at different s/w ratios with initial Pb^{2+} concentrations of up to 70 mg/L. The contribution of precipitation to Pb^{2+} removal was simulated by quantifying removal using eggshell water, whereas sorbed Pb^{2+} was quantified by acid digestion. Results indicated that eggshell particle sizes did not affect Pb^{2+} removal. High removal (up to 99%) of Pb^{2+} was achieved for low initial Pb^{2+} concentrations (<30 mg/L) across all s/w ratios studied. However, higher removal capacity was observed at lower s/w ratios. In addition, results confirmed that precipitation played a major role in the removal of Pb^{2+} by eggshells. Yet, this role decreased as the s/w ratio and initial concentration of Pb^{2+} increased. A predictive relationship that relates the normalized removal capacity of eggshells to the s/w ratio was developed to potentially facilitate the design of the reactor.

1. Introduction

The presence of lead (Pb^{2+}) in industrial wastewater has become a noteworthy source of water pollution and poses a significant health hazard to humans [1]. Physiological damage to human kidneys, liver, brain, and nervous system can happen as a result of ingesting levels of Pb^{2+} higher than the body's tolerance [2]. In addition, elevated levels of Pb^{2+} in the human body have been shown to have negative health effects including fatigue, a decreased reproductive ability, problems in the digestive tract, and anemia [1,3]. In fact, sterility, stillbirths, and neonatal deaths are associated with constant exposure to Pb^{2+} [1]. Pb^{2+} poisoning is especially dangerous for children, as high levels of Pb^{2+} in the blood stream are associated with depression of brain development and cognitive skills [4–6]. Pb^{2+} poisoning can be contracted by humans through polluted drinking water, ingestion from food, inhalation of contaminated dust, or occupational exposure [1,2,4,6–9]. It can infiltrate and contaminate the water sources, and from there, contaminate every level of the food chain [1,2,10]. It has been difficult to scientifically specify a level under which Pb^{2+} is no longer associated with negative health effects, therefore many jurisdictions focus on the ability of treatment technologies to completely remove Pb^{2+} from water. The maximum acceptable concentration of Pb^{2+} in drinking water is becoming more stringent, with some jurisdictions assigning a level as low as 5 µg/L [11], while the US EPA has set the maximum contaminant level goal for Pb^{2+} in drinking water at zero but an action level at 15 µg/L [12].

Sources of Pb^{2+} in water originate mainly from industrial activities such as mining, smelting, printing, and metal plating. In addition, manufacturing of batteries, paints, alloys, ceramic glass, and plastics contribute to increased Pb^{2+} pollution in water bodies [1]. Wastewater from battery manufacturing contains, on average, a Pb^{2+} content of 0.5–25 mg/L [13–16]. Regulations for industrial effluent discharge or reuse vary considerably between different jurisdictions. Certain jurisdictions specify a maximum Pb^{2+} level for discharge of effluent wastewater into the environment; this level can be as low as 0.1 mg/L (Saudi Arabia and Oman) or as high as 1 mg/L (Tunisia) [17].

Several methods were proposed and investigated for the removal of Pb^{2+} from industrial wastewater including ion exchange, filtration and membrane processes, electro-dialysis, chemical precipitation, solvent extraction, and chemical coagulation [1,2]. In addition, electrocoagulation, membrane electrodialysis, and biosorption were also employed for Pb^{2+} removal [14]. A widely used method for Pb^{2+} removal from industrial wastewater is to precipitate Pb^{2+} with caustic soda at a pH 8.5–9.2 in the presence of Fe (III) salts, followed by the addition of a polyelectrolyte, which facilitates the flocculation of the Pb^{2+} precipitate. The effluent is further treated with sedimentation and filtration, after which the Pb^{2+} concentration is reduced to the legal allowable limit [16]. Sorption by activated carbon is also a convenient and efficient treatment method. However, the use of commercial activated carbon for sorption can be costly [18]. Therefore, there is an increasing need to re-use biowaste in wastewater treatment [19]. Many studies have focused their efforts on deriving substitute sorbents from waste materials, particularly agricultural waste [20]. This not only helps to reduce the cost of sorbents, but it also helps recycle agricultural waste. Waste materials that have been used for Pb^{2+} removal include: *Chlorella vulgaris*, chicken feathers reinforced with chitosan, cow bone, leather, coconut shell, peach and apricot stones, *Alocacée* shell, *Mimosaceae* husk, and *Burseraceae* sawdust [1,21–25].

Eggshells are an example of an agricultural waste that could be used for Pb^{2+} removal. In fact, the per capita consumption of eggs in the United Arab Emirates (UAE) was 8.3 kg in 2013 [26]. Previous research reported that eggshells consist of (weight %) calcium carbonate (94%), magnesium carbonate (1%), calcium phosphate (1%), and organic matter (4%) [27]. Eggshells were studied for removal of various pollutants from water, including heavy metals such as copper, iron, cadmium, and Pb^{2+} [28–33]. Other work investigated the removal of dyes such as C.I. Reactive Yellow 205, methylene blue, and malachite green using eggshells [34–36]. However, few of these studies provided a detailed investigation of the mechanisms responsible for contaminant removal. It is plausible that, in addition to sorption, other removal mechanisms could be responsible for contaminant removal when using a naturally occurring material as a sorbent. Such mechanisms include ion exchange, as reported by Andersson et al. [37] for the removal of heavy metals from water onto the calcite surface, precipitation [38–40], or surface reactions [41]. However, only few studies investigated the impact of operation conditions (eggshell particle size and dose) on the mechanisms of Pb^{2+} removal. Nonetheless, existing literature on the use of eggshells for Pb^{2+} removal acknowledged that precipitation and sorption occurred [13,28,30,42]. However, the reviewed studies offer no quantification of the contribution of each mechanism, i.e., precipitation and sorption, which is an important aspect of process design.

Therefore, the objectives of this study were twofold: first, to identify the mechanisms responsible for the removal of Pb^{2+} from aqueous solutions using eggshells and to quantify the contribution of each of these mechanisms towards total removal. The authors were specifically interested in isolating the role of precipitation from surface attachment. While surface attachment may take different forms (i.e., sorption, ion exchange, complexation, etc.), for simplicity, it is referred to as sorption from here on. The second objective was to investigate the impact of the applied eggshells mass-to-solution volume ratio on Pb^{2+} removal. Results of this study provide novel and beneficial information for the design of eggshell reactors for optimal removal of Pb^{2+}, while also contributing to sustainable waste management by recycling eggshell material to treat wastewater.

2. Materials and Methods

A general framework for investigating and characterizing the use of biowaste materials for treatment and contaminant removal was previously published [19]. In this study, the framework is applied to carry out a mechanistic study of the removal of Pb^{2+} from aqueous solutions using eggshells (Figure 1).
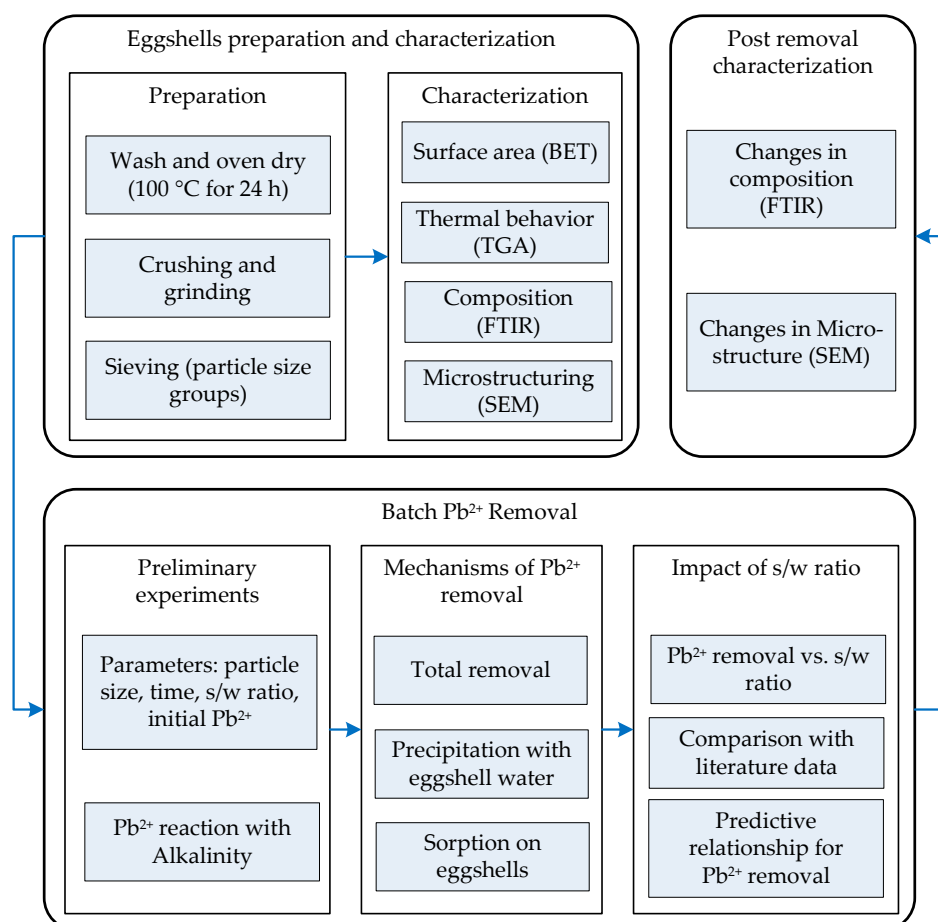

Figure 1. Summary of applied methodology.

2.1. Materials

Hanna Instruments 0.1M standard Pb^{2+} solution (HI4012-01) was used to prepare all Pb^{2+} solutions throughout this study. The required amount of standard Pb^{2+} solution was diluted in ultrapure water (Milli-Q® IQ 7000 Ultrapure, Merck, Darmstadt, Germany) as required to prepare the needed Pb^{2+} concentrations. In addition, H_2SO_4 (95–97% assay), ethanol (95% purity), phenolphthalein (Riedel-de Haën™, indicator grade, Honeywell International Inc., Charlotte, NC, US), and methyl orange powder (Fluka™, indicator grade, Honeywell International Inc., Charlotte, NC, US) were used for alkalinity measurements.

2.2. Preparation of Eggshells

Eggshells were collected from a local restaurant in the city of Al Ain, UAE. Two batches were collected from the restaurant across a period of two weeks; each batch contained the eggshells collected by the restaurant for the week. All batches of collected eggshells were then mixed and rinsed several times with deionized water to wash away any impurities. They were then dried at 100 °C for 24 h in a conventional drying oven (ULE 400, Memmert, Schwabach, Germany). The eggshells were then ground with a pulverizer (LC-53, Gilson Company Inc., Lewis Center, OH, USA). The distance between

the blades was set at about 0.7 mm to obtain particles in the range of 0.8–1.0 mm. This particle size was required to help physically remove the inner membranes. The eggshell inner membranes were then removed by soaking the eggshells in deionized water and mixing them, after which the inner membranes floated to the top and were physically removed. The eggshells were then rinsed several times to remove any residual membranes, dried again in the oven for 24 h at 100 °C, and further ground in the pulverizer. Subsequently, the obtained particles were sieved using stainless steel ASTM test sieves (Gilson Company Inc., Lewis Center, OH, USA). The resulting eggshells were classified into 4 groups depending on size, namely <150 μm, 150–500 μm, 500–800 μm, and >800 μm. The ground eggshells were stored in plastic sealable bags at room temperature until use.

2.3. Eggshells Characterization

The powdered eggshells were characterized to evaluate their potential performance for Pb^{2+} removal. Eggshell particles underwent nitrogen gas adsorption for characterization of their surface area and porosity. This was carried out with a Quantachrome Autosorb-1-C volumetric gas sorption instrument at 77K. Before measurements, samples were degassed at 150 °C for one hour. Further, Brunauer–Emmett–Teller (BET) theory was used to calculate surface area, and pore size distributions were determined by the Barett–Joyner–Halenda (BJH) model based on the desorption branch of the N_2 isotherms. Fourier-transform infrared (FTIR) spectroscopy and scanning electron microscopy (SEM) analyses were used to investigate the changes to the microstructure of eggshells as a result of Pb^{2+} removal, as will be discussed in detail in Section 2.8. Based on the results of eggshell particles characterization, it was decided to use only two particle sizes (<150 μm of d_{50} = 75 μm and 150–500 μm of d_{50} = 300 μm) in the Pb^{2+} removal experiments, as they had the highest surface area. In addition, the study focused on particle size 150–500 μm, which was thought to be more practical and feasible to scale to column studies.

2.4. Pb^{2+} Removal Experiments

For all Pb^{2+} removal batch experiments, Pb^{2+} solutions at the desired concentrations were prepared as stock solutions from which sample volumes of 50 or 100 mL were obtained. Specific amounts of crushed eggshell powder were added to the samples to achieve the desired solid-to-water (s/w) ratio. Samples were then subject to shaking in a water bath shaker (MaXturdy 18, Daihan Scientific Co., GANG-WON -DO, South Korea) at a temperature of 25 °C and rotational speed of 150 rpm. If required, they were filtered using syringe filters (Thermo Scientific[TM], PTFE, 0.45 μm, 25 mm). Measurements of Pb^{2+}, Mg^{2+}, and Ca^{2+} concentration in solution were taken by Varian ICP-OES 720 ES with standards by Chem-Lab[TM], Belgium. A Thermo Scientific[TM] Orion[TM] 3-star pH meter was used to carry out pH measurements. Alkalinity was measured by titration, according to method 2320 [43].

For all the experiments explained in the sections below, samples were analyzed in triplicate, and the coefficient of variation for Pb^{2+} concentration ranged from 0.3% to 8.4%. Average readings for the initial and final Pb^{2+} concentrations were used to calculate the capacity of removal (*m* in mg/g), regardless of the mechanism of removal, as shown in Equation (1): where *V* is the volume of solution used (L), *M* is the mass of eggshells used (g), C_0 is the initial Pb^{2+} concentration (mg/L), and C_e is the final (equilibrium) Pb^{2+} concentration (mg/L). The removal percentage of Pb^{2+} was also calculated using Equation (2).

$$m = \frac{(C_0 - C_e)V}{M} \tag{1}$$

$$Pb2+ \ removal \ (\%) \ = \frac{(C_0 - C_e)}{C_0} \times 100 \tag{2}$$

2.5. Preliminary Investigation of Pb^{2+} Removal

A screening experiment was conducted to determine the adequate contact time (until equilibrium) and to demonstrate the potential of eggshells for Pb^{2+} removal. At an s/w ratio of 1:200, eggshells were

added to Pb^{2+} solutions of concentrations 0 to 70 mg/L for a contact time of 2 h. To help theorize the removal mechanisms involved, other parameters besides Pb^{2+} were monitored including pH, alkalinity, Ca^{2+}, and Mg^{2+}.

To investigate the potential precipitation of Pb^{2+} due to the presence of dissolved carbonates and bicarbonates, stock solutions of 1000 mg/L of Na_2CO_3 and $NaHCO_3$ were prepared and then left to react with Pb^{2+} in solution. One milliliter of the 1000 mg/L Na_2CO_3 stock solution was added to the 20 mg/L (0.19 meq/L) of Pb^{2+} solution and filled to the 100 mL mark in a volumetric flask. The resulting solution had a concentration of 10.07 mg/L (0.19 meq/L) Na_2CO_3. Furthermore, 1.62 mL of the 1000 mg/L Na_2CO_3 solution was added to the 20 mg/L Pb^{2+} solution and filled to the 100 mL mark in a volumetric flask, leading to a solution of 16.2 mg/L (0.19 meq/L) $NaHCO_3$. These solutions were then left for 2 h to observe any precipitation of Pb^{2+} by CO_3^{2-} or HCO_3^-. Resulting solutions were then filtered and the Pb^{2+} concentration, pH, and total alkalinity were measured before and after the addition of Na_2CO_3 and $NaHCO_3$.

2.6. Effect of Particle Size and s/w Ratio on Removal of Pb^{2+}

In order to investigate the effect of eggshell particle size and s/w ratio on the removal of Pb^{2+}, 500 mL of Pb^{2+} solutions of 0 to 70 mg/L were prepared and their initial pH, Ca^{2+}, Mg^{2+}, and Pb^{2+} concentrations were measured. Then, 100 mL of each solution was added to 0.5 g of eggshells of particle size 150–500 μm, giving an s/w ratio of 1:200. The samples were shaken for 2 h then filtered. The filtrate was then analyzed for pH, alkalinity, Pb^{2+}, Ca^{2+}, and Mg^{2+} concentration. This process was also repeated for an s/w ratio of 1:100, 1:1000, and 1:2000 for eggshells of particle sizes 150–500 μm and <150 μm. This process is detailed in Figure 2.
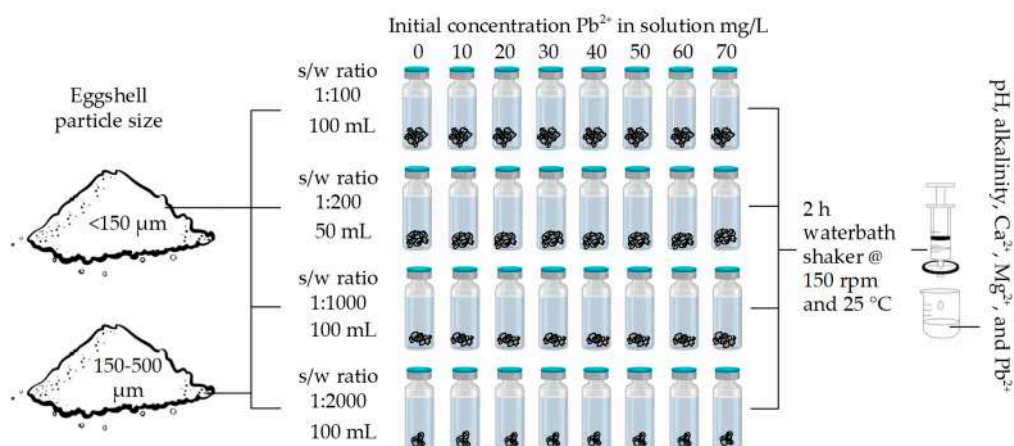

Figure 2. Experimental design for investigating the impact of solid-to-water (s/w) ratio and particle size on Pb^{2+} removal.

2.7. Differentiation between Removal of Pb^{2+} by Sorption and Precipitation

To elucidate the role of sorption versus precipitation in Pb^{2+} removal by eggshells, these mechanisms have to be isolated. To do so, eggshells used in the previous experiment (Figure 2) with an s/w ratio of 1:2000 and Pb^{2+} concentrations 0 to 60 mg/L were collected and separated from the solution with a sieve (number 120 mesh size 125 μm). The solution passing through the sieve was filtered through a 0.45 μm membrane, and a portion of the filtrate was used to rinse the eggshell particles to remove any Pb^{2+} precipitate on the surface. The eggshells were then dried in an oven at 60 °C for 16 h, and then subjected to ICP analysis after undergoing acid digestion according to method 3050B [44]. This was carried out to directly measure the amount of Pb^{2+} sorbed on the surface of the eggshells. The exact amount of Pb^{2+} sorbed was calculated using mass balance after accounting for the amount present in the water film originally surrounding the wet eggshells.

Another experiment was conducted to quantify the removal of Pb^{2+} by precipitation using eggshell extracts at different s/w ratios. A volume of 600 mL of eggshell water (ESW) with an s/w ratio of 1:200 was prepared using 150–500 μm eggshells. The mixture was mixed for 2 h in a water bath shaker at 150 rpm and 25 °C. The mixture was then decanted and filtered. The filtrate gave an ESW sample, which was used in the preparation of Pb^{2+} solutions. The pH, alkalinity, Ca^{2+}, and Mg^{2+} concentration of the ESW were measured. The ESW was then used to prepare 50 mL solutions of concentrations 0 to 70 mg/L Pb^{2+}. The solutions were mixed again for 2 h. Subsequently, they were filtered and analyzed for alkalinity, pH, Ca^{2+}, Mg^{2+}, and Pb^{2+} concentration. This process was repeated for the same eggshell size using an s/w ratio of 1:2000. This process is detailed in Figure 3.
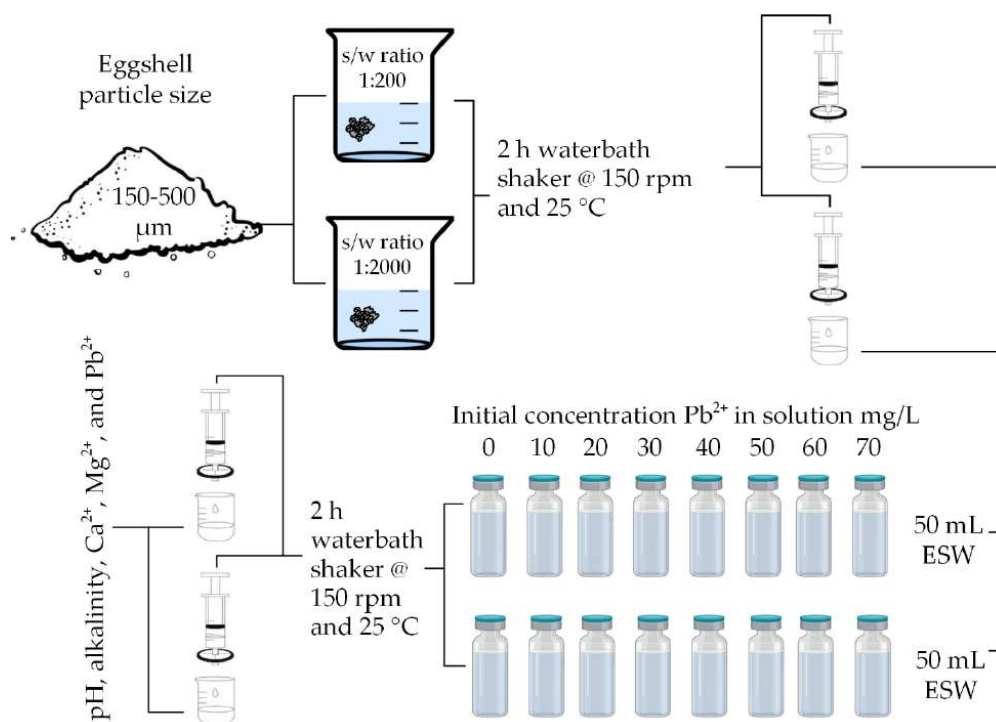

Figure 3. Experimental design for investigation of removal of Pb^{2+} in eggshell water (ESW).

2.8. Microstructure Characterization of Pb^{2+} Removal

FTIR and SEM analyses were used to investigate the changes in functional groups and morphology of selected eggshells post-exposure to Pb^{2+} and examine the removal mechanisms. FTIR spectroscopy was carried out on raw eggshells using a Shimadzu, IR-Prestige-21 spectrometer in transmittance mode at a resolution of 4 cm^{-1} from 500 to 4000 cm^{-1}. Similarly, it was performed on typical used eggshells after Pb^{2+} removal in a solution of 40 mg/L Pb^{2+} and an s/w ratio of 1:200. Samples were formulated by pulverizing eggshells into a powder, which was then sieved through an 80-micron sieve to remove coarse particles. Obtained powder samples were mixed with potassium bromide at a 3:1 ratio, by mass, and made into pellets for FTIR testing.

A JEOL-JSM 6390A scanning electron microscope was used to examine the morphology of eggshells with a particle size of 150–500 μm before and after Pb^{2+} removal. Pb^{2+} solutions of 20 mg/L at s/w ratios of 1:200 and 1:2000 were utilized. To separate the eggshells from the solution, the mixture was passed through a 125-micron sieve, rinsed with deionized water to remove any precipitated solids on the eggshell surface, and dried in the oven at 100 °C for 24 h. Samples were sputter-coated with a thin gold layer and examined in high-vacuum mode at 15 kV and magnification ranging from 100–1000.

3. Results and Discussion

3.1. Raw Eggshells Characterization

Removal of contaminants from solution by a biomass material depends on the material's surface area and accessibility to active sites [45]. Nitrogen adsorption curves were used to evaluate the surface area according to BET theory, while N_2 desorption curves were used to evaluate the pore size distributions based on the BJH model. The results are presented in Table 1 and Figure 4. As expected, the surface area was found to decrease with increasing eggshell particle size. It is worth noting that the BET surface area for eggshells was found to be comparable to the surface areas of other types of biomass used for sorption, as olive stones, tomato husks, and Bacillus badius (Table 1). In addition, the surface area of eggshells found in this study for particle size <150 μm, 0.977 m^2/g, was similar to that reported by Tsai et al. [35] for eggshells of particle size 77 μm, 1.023 m^2/g. Figure 4 shows a representative curve for the nitrogen adsorption of eggshells of particle size <150 μm; the eggshells follow a type II isotherm with negligible hysteresis. This indicates a lack of affinity between eggshells and N_2 molecules [35]. The N_2 adsorption isotherm signifies poor pore properties, owing possibly to a non-porous surface. Tsai et al. [35] also reached a similar conclusion when analyzing eggshells.

Table 1. BET and Langmuir surface area calculations of biowaste material at various particle size ranges.

Material	Size (μm)	Surface Area (m^2/g)	Pore Volume (10^3 cm^3/g)	Pore Size (nm)	Reference
Eggshells	<150	0.977	3.544	14.8	This work
	150–500	0.056	-	-	This work
Eggshells	77.9	1.023	6.5	-	[35]
Olive stones	<1000	0.163	1.84	45.302	[46]
Tomato husks	75–150	0.68	0.0015	-	[47]

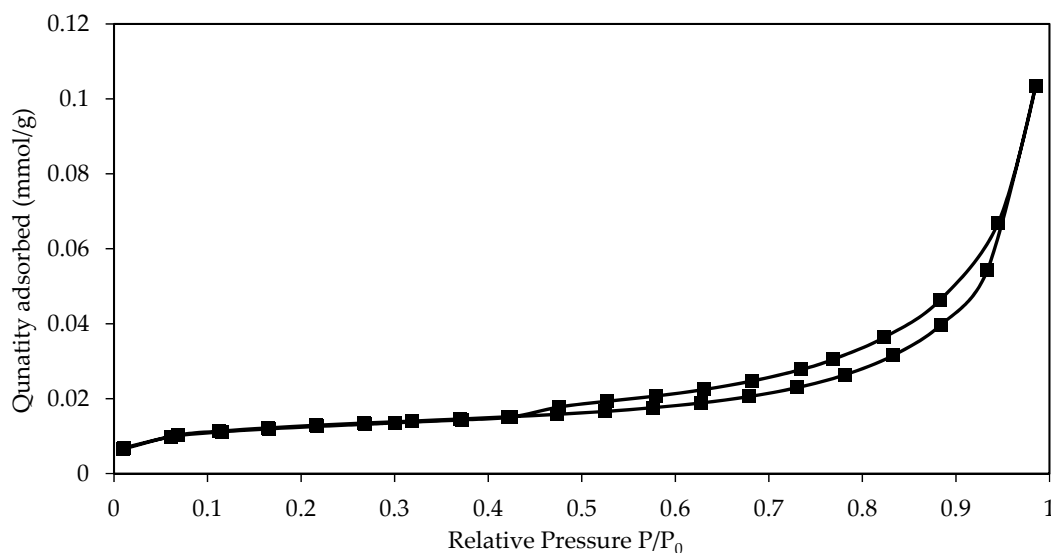**Figure 4.** Nitrogen adsorption isotherm curves for eggshell powder of particle size <150 μm.

The thermogravimetric analysis of raw eggshells has been examined in previous studies [48–50]. Such analysis highlights the change in eggshell powder mass with temperature and gives an indication of its composition. There is general agreement that the decomposition of raw eggshells with temperature has two regions of mass loss. In the first region, a minor mass loss (around 3%) indicates the decomposition of organic matter and occurs from 100 to 550 °C. Meanwhile, in the second region, a major mass loss (around 40%) takes place at higher temperatures up to 850 °C, signifying the decomposition of calcium carbonate [48–50].

3.2. Preliminary Pb^{2+} Removal Experiments

A screening experiment of removal with time indicated that Pb^{2+} removal happened over a short time period. The experiment was done using an initial Pb^{2+} concentration of 100 mg/L and s/w ratio of 1:100; measurements of Pb^{2+} concentration were taken at 30 min and every hour for 6 h. Little differences in removal were observed after 30 min of contact time. Therefore, to ensure equilibrium status is achieved, 2 h was chosen as the contact time for all further experiments. Another screening experiment was conducted to investigate the capacity of eggshells for Pb^{2+} removal at an s/w ratio of 1:200. The results indicated that eggshells showed a good potential for Pb^{2+} removal compared to previously investigated biowaste materials [1,23,46]. A removal capacity (*m*) of 8.18 mg/g (pH = 5.9) was found for an initial Pb^{2+} concentration of 70 mg/L, at which an equilibrium aqueous concentration of 29.5 mg/L was reached. During the analysis of Pb^{2+} solution after contact with eggshells, it was noticed that Ca^{2+} and Mg^{2+} were released into the solution by eggshells. Therefore, it was hypothesized that there could be other removal mechanisms, in addition to sorption, which could be responsible for the removal of Pb^{2+}. Previous studies have noted that Pb^{2+} precipitation due to reaction with carbonates could play a role in Pb^{2+} removal [51,52].

To confirm the potential precipitation of Pb^{2+} due to reaction with carbonates, an investigation was conducted to determine the extent of Pb^{2+} precipitation by reaction with CO$_3^{2-}$ and HCO$_3^{-}$. NaHCO$_3$ and Na$_2$CO$_3$ were added to 20 mg/L Pb^{2+} solution. As expected, the pH and alkalinity of Na$_2$CO$_3$ and NaHCO$_3$ solutions decreased when added to a Pb^{2+} solution. Indeed, immediately after the addition of Na$_2$CO$_3$, the pH was 8.29 and then decreased to 6.09, and alkalinity dropped from 14 to 11 mg/L as CaCO$_3$. Similarly, after the addition of NaHCO$_3$, the pH decreased from 7.31 to 5.94 and the alkalinity dropped from 16 to 5.6 mg/L as CaCO$_3$. The drop in alkalinity was accompanied by a drop in Pb^{2+} concentration from 23.66 to 0.75 and 2.53 mg/L for Na$_2$CO$_3$ and NaHCO$_3$ solutions, respectively. This indicates that alkalinity was consumed and Pb^{2+} was precipitated upon contact with CO$_3^{2-}$ and HCO$_3^{-}$. These findings provide evidence that Pb^{2+} is precipitated by carbonates that are released by eggshells in solution.

3.3. Effect of Particle Size and s/w Ratio on Removal of Pb^{2+}

The method outlined in Section 2.6 was used to investigate the effect of s/w ratio and particle size on the eggshell capacity for Pb^{2+} removal. The results, presented in Figure 5, show that eggshell particle size generally did not have a measurable effect on the removal capacity, but a higher removal capacity was achieved with the smaller particle size (<150 μm) at high initial Pb^{2+} concentrations (>50 mg/L). This effect at a higher initial concentration of Pb^{2+} was observed in previous studies where *m* decreased with the increase in eggshell particle size [42], or with the increase in the particle size of calcite and aragonite [51]. Despite the large difference in the surface area of the two eggshell sizes used in this study (Table 1), a rather insignificant difference in the eggshell capacity for Pb^{2+} removal was noticed between the two sizes for initial Pb^{2+} concentrations below 50 mg/L (Figure 5). However, eggshell particle size could result in a significantly lower removal capacity for larger particles and higher initial Pb^{2+} concentration.

Furthermore, the removal capacity of eggshells decreases as the s/w ratio increases; at s/w ratios 1:1000 and 1:2000, the removal capacity is higher than that for ratios 1:100 and 1:200 (Figure 6). If the removal of Pb^{2+} is due to sorption, then a decrease in the eggshell removal capacity with the increase in the s/w ratio may be due to less effective mixing at a higher density of eggshells in the solution causing reduced accessibility to sorption sites. On the other hand, if the removal of Pb^{2+} is due to precipitation, then a decrease in the eggshell capacity with the increase in the s/w ratio could be due to a decreased dissolution of CaCO$_3$ per unit mass of eggshells at higher s/w ratios. In addition, if precipitation occurs on the eggshell surface (microprecipitation) then less sites become available for sorption. In this batch experiment mode, the highest removal capacity was found to be about 70 mg/g which occurred for particle size <150 μm at an s/w ratio of 1:2000 and an initial Pb^{2+} concentration

of about 60 mg/L. Furthermore, high percentage removals (up to 99%) were achieved for low Pb^{2+} concentrations (<30 mg/L) across all s/w ratios studied (not shown here). The low concentration of solute ensured high removal.
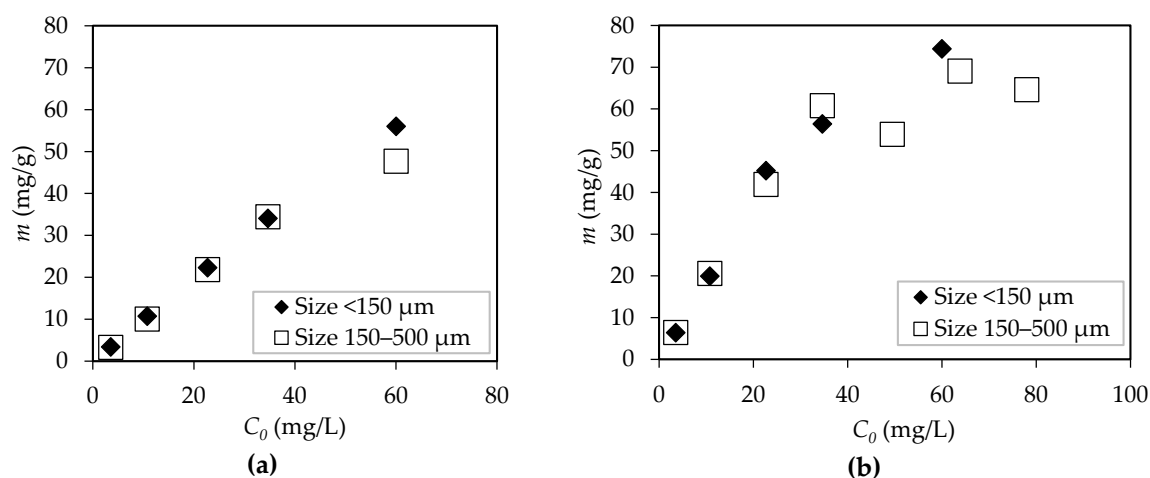

(a)

(b)

Figure 5. Removal of Pb^{2+} versus initial Pb^{2+} concentration for particle size 150–500 μm and <150 μm at (**a**) s/w ratio 1:1000 (pH increased from 5.49 (SD 0.25) to 8.64 (SD 0.64) for particle size <150 μm and from 5.49 (SD 0.25) to 6.92 (SD 0.67) for particle size 150–500 μm) and (**b**) s/w ratio 1:2000 (pH increased from 5.49 (SD 0.25) to 6.89 (SD 0.72) for particle size <150 μm and from 5.49 (SD 0.25) to 6.86 (SD 0.72) for particle size 150–500 μm).
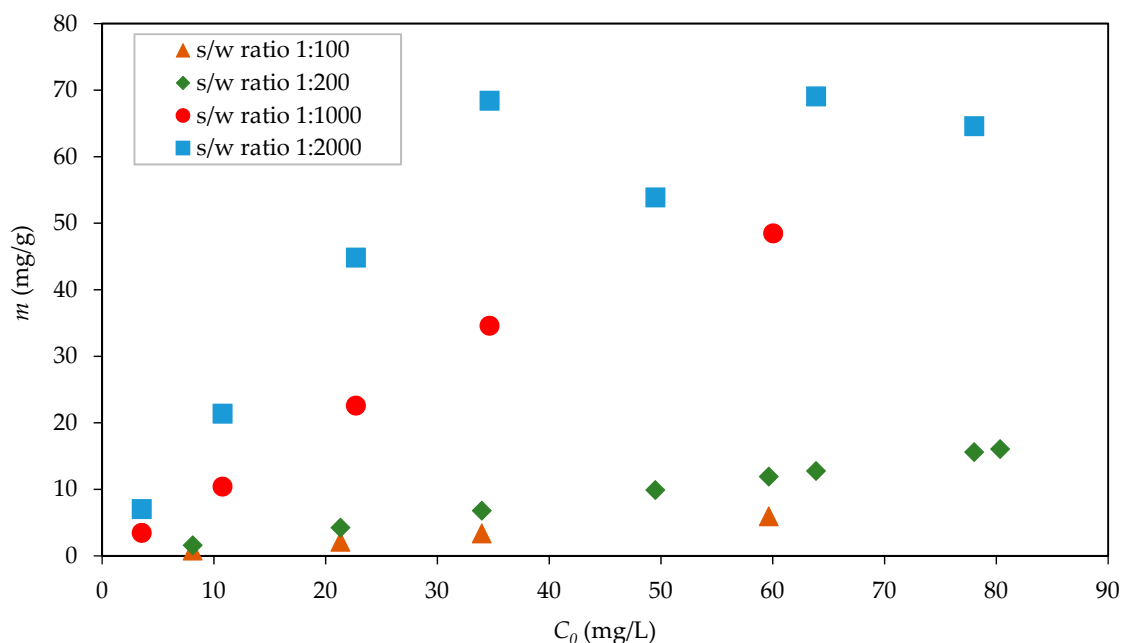

Figure 6. Removal capacity of eggshells for Pb^{2+} removal as a function of initial Pb^{2+} concentration and s/w ratio for particle size 150–500 μm (pH increased from 5.76 (SD 0.48) to 8.35 (SD 0.27) for s/w ratio 1:100; from 5.71 (SD 0.37) to 7.94 (SD 1.06) for s/w ratio 1:200; from 5.49 (SD 0.25) to 6.92 (SD 0.67) for s/w ratio 1:1000; and from 5.49 (SD 0.25) to 6.86 (SD 0.72) for s/w ratio 1:2000).

Previous studies (Table 2) showed variations in the capacity of eggshells employed for Pb^{2+} removal, with values as low as 0.12 mg/g [29] to as high as 156 mg/g [42]. Such variations could be due to differences in the experimental conditions employed, including differences in the initial concentration, particle size, and s/w ratio. However, these studies only included one s/w ratio in their investigation. As demonstrated in this study, the s/w ratio has a significant impact on the removal

capacity (m). To gain insight into the effect of s/w ratio, normalized removal capacity (m/C_0) is plotted versus s/w ratio as shown in Figure 7. Normalized capacity values for each s/w ratio used in this study were obtained from the slope of the best fit line with zero intercept of the corresponding data set presented in Figure 6. Data from previous studies [28–30,42] were superimposed for comparison purposes. Since these previous studies only included one s/w ratio in their investigation, an average value of the slope (m/C_0) was taken for each study. One study by Soares et al. [30] showed a decreasing trend of (m/C_0) with the increase in C_0 and therefore the selected data points (Figure 7) represent those before a plateau for removal capacity (m) was reached. The data of Figure 8 show a linear trend on a log–log scale.

Table 2. Eggshell capacity for removal of Pb^{2+} as reported by other studies.

Study	Eggshell Size (μm)	s/w Ratio	pH	C_0 (mg/L)	m (mg/g)
[42] [a]	750	1:500	5.0	523, 1045	156
[28]	<1000	1:40	5.5	10–150	2.24
[30] [b]	<500	1:100	5.0	100–1435	12.9
[29]	210–400	1:40	NA	3	0.12

[a] Only the results for the 750 μm particle size are considered here. [b] Considered values represent those before a plateau for removal capacity was reached.

From Figure 7, it is clear that the impact of the s/w ratio is significant. The best fit relationship for the data in Figure 7 is given in Equation (3). The relation shows that the slope (m/C_0) is almost inversely proportional to the s/w ratio. Equation (3) is valid only in the range of the s/w ratio presented in Figure 8 and before the removal capacity of eggshells (m) reaches a plateau, and for particle size <1 mm.

$$\log\left(\frac{m}{C_0}\right) = -0.933 \log(\text{s/w ratio}) - 2.9 \quad R^2 = 0.99 \tag{3}$$
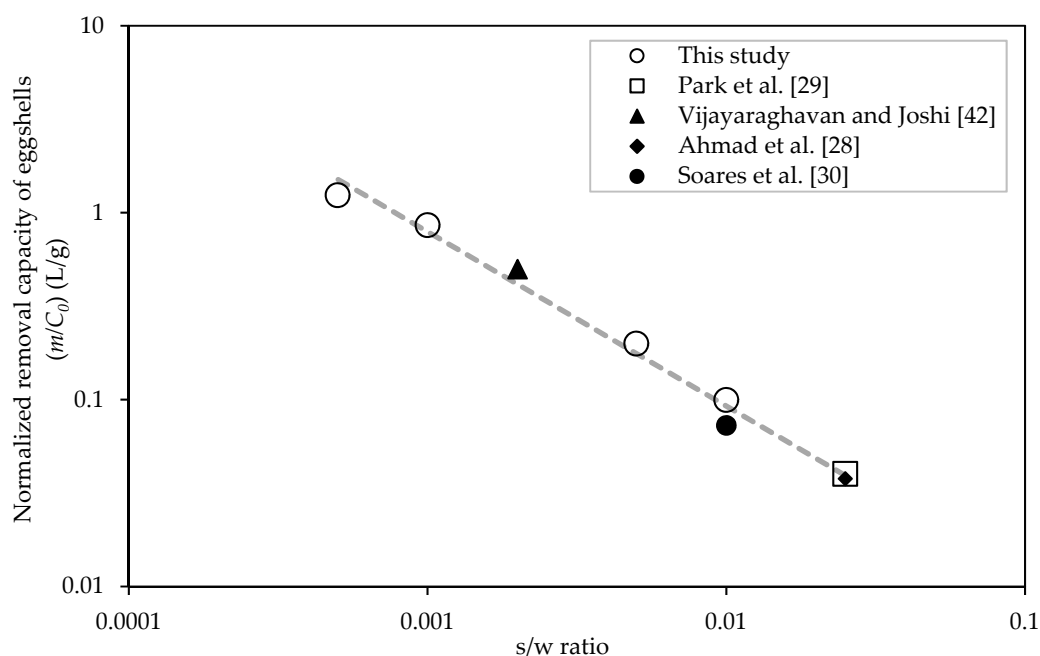

Figure 7. Comparison between normalized capacity of eggshells for Pb^{2+} removal (m/C_0) versus s/w ratio used in this study and previous studies.

The predictive relationship (Equation (3)) could be used in designing batch reactors utilizing eggshells for Pb^{2+} removal from wastewater. Specifically, this relationship could be used to optimize the design conditions and configuration of the batch reactors (single versus sequential batch reactors).

For example, based on Equation (3), 250 kg of eggshells would be required to reduce Pb^{2+} concentration from 55 to 1 mg/L with a reaction time of 2 h for 10 m^3 of contaminated water if one batch reactor is used. However, if two or three batch reactors in series were to be used, the mass of eggshells would be reduced to 80 and 12 kg, respectively, with a reaction time of 2 h for each reactor. Thus, using multiple reactors in series reduces the required mass of eggshells and consequently reduces the mass of generated waste. However, the use of multiple reactors as compared to a single reactor would entail higher construction and operation costs. As such, Equation (3) could serve as a guide to reach an optimal system design subject to economic and environmental constraints.
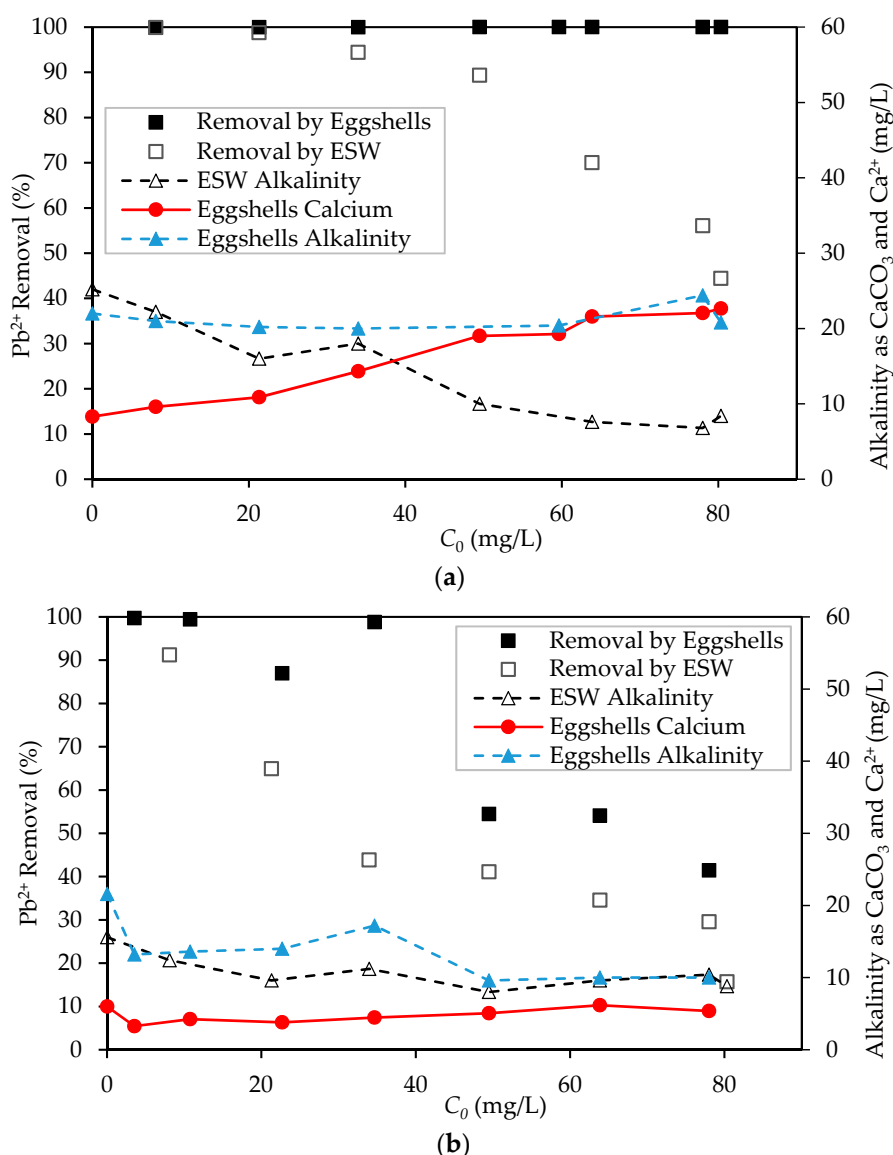

Figure 8. Comparison of percentage Pb^{2+} removal using eggshells of size 150–500 μm and ESW at (**a**) s/w ratio 1:200 (pH increased from 5.71 (SD 0.37) to 7.94 (SD 1.06) with eggshells, whereas with ESW the pH instantly drops from 9.36 (ESW only) to 6.18 (SD 0.75) right after mixing with lead solution) and (**b**) s/w ratio 1:2000 (pH increased from 5.49 (SD 0.25) to 6.86 (SD 0.72) with eggshells, whereas with ESW the pH instantly drops from 9.36 (ESW only) to 6.06 (SD 0.51) right after mixing with lead solution).

3.4. Differentiation between Removal of Pb^{2+} by Sorption and Precipitation

To study the removal of Pb^{2+} by precipitation, the method outlined in Section 2.7 was followed. The percentage of Pb^{2+} removal as a function of the initial Pb^{2+} in solution (C_0) is presented in Figure 8.

The figure compares the total Pb^{2+} removal obtained when eggshells were physically in solution and Pb^{2+} removal due to precipitation with eggshell water (ESW). Clearly, precipitation plays a major role in the removal of Pb^{2+} by eggshells. At a low initial concentration, Pb^{2+} removal could entirely be attributed to precipitation due to the presence of carbonates in the solution. However, the role of precipitation is reduced as the s/w ratio and initial concentration of Pb^{2+} become higher (Figure 8a). The difference between the removal in the two cases (eggshells and ESW) could be attributed to sorption. However, it was observed that aqueous Ca^{2+} in equilibrium with eggshells increased with the increase in initial Pb^{2+} concentration, while alkalinity remained almost constant (Figure 8a). The level of Ca^{2+}, in the case of ESW, remained the same at 8.3 and 7.5 mg/L for s/w ratios 1:200 and 1:2000, respectively, at all initial Pb^{2+} concentrations. Thus, comparison between Pb^{2+} removal with ESW versus that of eggshells may provide an underestimation of the extent of precipitation. Further, the increase in Ca^{2+} in the presence of eggshells was more pronounced at the high s/w ratio (Figure 8a) compared to that for the low s/w ratio (Figure 8b). Such a finding was accompanied by an almost constant alkalinity due to the continuous release of carbonates by eggshells. This could explain the higher difference between the removal of Pb^{2+} by eggshells and ESW at the high s/w ratio (Figure 8a).

To provide a better elucidation of the roles of different removal mechanisms. The authors resorted to direct quantification of the amount of sorbed Pb^{2+} by acid digestion. Precipitation was then calculated as the difference between total removal and percentage of Pb^{2+} sorbed on the eggshells. This quantification is presented in Figure 9, which distinguishes Pb^{2+} removed by sorption from that removed by precipitation at an s/w ratio of 1:2000. Though the percentage of Pb^{2+} removal declined with increasing initial Pb^{2+} concentration, precipitation continued to be more prominent than sorption up to an initial Pb^{2+} concentration of 60 mg/L, after which removal by precipitation significantly dropped (Figure 9a) and became almost similar to removal by sorption. On the other hand, the contribution of sorption to the percent removal was the same at different initial concentrations but slightly decreased after 60 mg/L. These findings are consistent with those of Ahmad et al. [28], who concluded that precipitation may become important for the removal of Pb^{2+} and Cu^{2+} by waste eggshells. It should be noted that some studies suggest that microprecipitation of Pb^{2+} by carbonates present in eggshells was followed by adsorption of the metal carbonates on the eggshell surface [30,42]. Thus, it is difficult to confirm that all the sorbed Pb was in the form of Pb^{2+}, as there could be some $PbCO_3$ remaining on the surface, which could result in an underestimation of the role of precipitation in Pb removal.
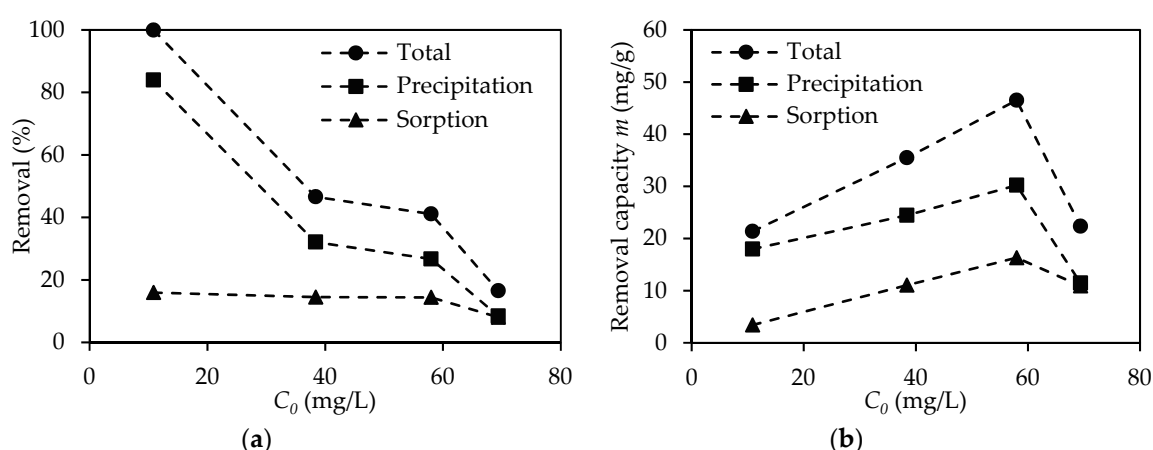

Figure 9. Removal of Pb^{2+} by sorption and precipitation versus initial Pb^{2+} concentration (size 150–500 μm and s/w ratio of 1:2000) expressed in (**a**) percent removal and (**b**) removal capacity.

Figure 9b shows the changes in removal capacity of eggshells as a function of initial Pb^{2+} concentration. The contribution of both sorption and precipitation to the removal capacity increased with the increase in the initial Pb^{2+}, but then both dropped after 60 mg/L. This behavior was also

observed for the total removal capacity at this s/w ratio (1:2000) and particle size (150–500 μm) as shown in Figures 5b and 6. The expectation is for the removal capacity (*m*) to reach a plateau value after a certain initial concentration, as shown for Pb^{2+} removal by eggshells in the work of Soares et al. (2016) and Cu^{2+} removal by eggshells in the work of Ahmad et al. (2012), in which the solution pH was maintained at a fixed value (at 5 and 5.5, respectively). However, in this study, the observed decline, rather than a plateau, in the removal capacity (*m*) could be attributed to a decrease in the available carbonates needed for the precipitation reaction, coupled with a decrease in the solution pH. The latter could be the reason why the observed removal capacity by sorption dropped as well.

3.5. Thermodynamic and Stiochiometric Analysis

Several Pb^{2+} solid phases could occur in the Pb-$CaCO_3$-H_2O system including PbO, $Pb(OH)_2$, $PbCO_3$ (cerussite), $Pb_3(CO_3)_2(OH)_2$ (hydrocerussite), and $Pb_{10}(OH)_6(CO_3)_6$ (plumbonacrite). PbO and plumbonacrite are thermodynamically stable at very high pH values (pH > 12) [53]. Pure $Pb(OH)_2(s)$ is believed not to exist, but the basic salt, used to prepare the Pb solution, combined with aqueous $Pb(OH)_2$ could exist as a solid form at high pH [54]. In this study, the solution pH started at around pH 5.5 (only Pb^{2+} in the water) and increased to less than 9.0 after two hours from the addition of eggshells, making lead carbonate, in the form of cerussite or/and hydrocerussite, the more probable solid that could be formed. The chemical reactions describing the formation of cerussite and hydrocerussite along with their solubility product (K_{sp}) values [52] are

$$Pb^{2+}(aq) + CO_3^{2-}(aq) = PbCO_3(s) \qquad\qquad K_{sp} = 7.9 \times 10^{-14} \qquad (4)$$

$$3Pb^{2+}(aq) + 2CO_3^{2-}(aq) + 2OH^-(aq) = Pb_3(CO_3)_2(OH)_2(s) \qquad K_{sp} = 3.16 \times 10^{-46} \qquad (5)$$

Thermodynamic analysis was conducted to investigate the possible formation of cerussite or hydrocerussite using the range of values of Pb^{2+}, CO_3^{2-}, and pH encountered in this study. Pb^{2+} ranged from 10 to 70 mg/L (4.8×10^{-5} to 3.3×10^{-4} mol/L) and alkalinity ranged from 10 to 40 mg/L as $CaCO_3$. If all alkalinity is due to the release of CO_3^{2-} from the eggshells, then the molar concentration of CO_3^{2-} would range from 1×10^{-4} to 4.2×10^{-4} mol/L. The activity coefficients of Pb^{2+} and CO_3^{2-} were determined using the Debye–Huckel law as described by Snoeyink and Jenkins [55] and fell in the range of 0.77 to 0.89 (an average value of 0.83 was considered here for Pb^{2+} and CO_3^{2-}). Based on that, the values of the ion activity product for cerussite ({Pb}{CO_3}, where { } refers to ion activity = activity coefficient × molar concentration) range from 3.3×10^{-9} to 9.7×10^{-8}. These values are higher than the K_{sp} of cerussite (7.9×10^{-14}), indicating favorable conditions for the formation of this solid. Analogous calculations of the ion activity product for hydrocerussite ({Pb}^3{CO_3}^2{OH}^2) resulted in values that range from 4.4×10^{-39} to 2.6×10^{-28}, which are higher than its K_{sp} (3.16×10^{-46}), and hence the conditions also favor the formation of hydrocerussite.

The above analysis indicates that the precipitate formed in the Pb-eggshell system of this study could be cerussite or/and hydrocerussite. There is no agreement in the literature about the relative stability of cerussite and hydrocerussite. For aqueous Pb^{2+} in contact with $CaCO_3$ in open systems, Bilinski and Schindler [56] concluded that hydrocerussite is the most stable solid phase, whereas Taylor and Lopata [53] indicated that cerussite is thermodynamically more stable than hydrocerussite at all pH values. On the other hand, for a closed aqueous system (i.e., with no exchange of atmospheric CO_2), hydrocerussite becomes more stable at pH > 7 [51].

Stoichiometric analysis was carried out to investigate the extent to which the experimental data of Pb^{2+} precipitation with eggshells are aligned with the formation of cerussite and hydrocerussite. Figure 10 plots the concentration of reacted Pb^{2+} (expressed as the difference between the initial and final Pb^{2+} concentration in solution) versus the drop in the carbonate level estimated from the alkalinity measurement of the control solution (with eggshells but without Pb^{2+}) and of the Pb^{2+} solution for two s/w ratios. The dotted line in Figure 10 represents the stoichiometry of the cerussite formation. This line has a slope of 1.0 since 1 mol of Pb^{2+} reacts with 1 mol carbonate to form cerussite. The solid

line represents the stoichiometry for hydrocerussite formation and has a slope of 1.5 (3 mol of Pb^{2+} reacts with 2 mol of carbonate to form hydrocerussite). Most of the experimental data lie within the two lines, which is consistent with the notion that the removal of Pb^{2+} from the eggshell solution is due to the formation of lead carbonate. As shown in Figure 10, some of the experimental data are above the lines of cerussite and hydrocerussite formation. This is expected and could be attributed to two reasons: (1) not all Pb^{2+} precipitated but some was sorbed on the eggshells which resulted in a higher reacted Pb^{2+} than what could be predicted by stoichiometry, and (2) the eggshells could release additional carbonate during the reaction to reach a new equilibrium state and this could result in an apparent lower CO_3^{2-} change than that estimated based on the reaction stoichiometry. Nonetheless, the observed drop in Pb^{2+} versus the drop in alkalinity is justified based on the stoichiometry for the formation of lead carbonate.
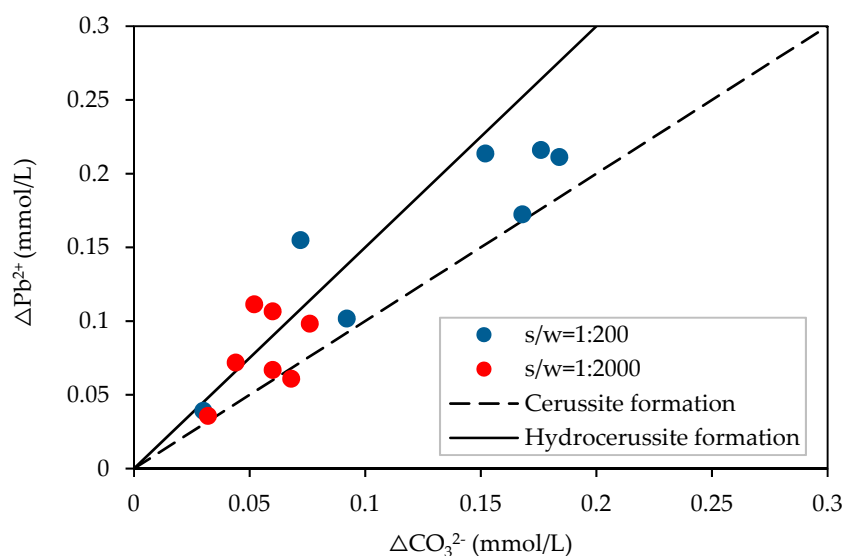

Figure 10. Alignment of experimental results of eggshells (size 150–500 μm) with the stoichiometry for the formation of cerussite and hydrocerussite. ΔPb^{2+} refers to the difference in the initial and final Pb^{2+} concentration in solution, while ΔCO_3^{2-} refers to the drop in the carbonate level estimated as the difference in the alkalinity of the control solution and of the Pb^{2+} solution for each bottle.

3.6. FTIR Analysis

The change in functional groups of eggshells before and after Pb^{2+} removal was examined using FTIR spectroscopy. Figure 11 shows the typical FTIR spectrum of raw and used eggshells with 40 mg/L Pb^{2+} solution. The infrared bands at 712 and 872 cm^{-1} are associated with the respective in-plane and out-of-plane bending vibrations of calcium carbonate ($CaCO_3$) in its polymorph form of calcite [35,57]. A broad band in the range of 1300–1500 cm^{-1}, centered at 1422 cm^{-1}, is recognized as a C–O stretching mode vibration of $CaCO_3$ [57]. Such bands have also been identified as v_4, v_2, and v_3 vibration modes of carbonate ion, respectively [58]. These bands are observed in both samples, providing evidence to the stability and inertness of calcite when exposed to the Pb^{2+} solution. Furthermore, raw eggshells were characterized by a major absorption peak at 2350 cm^{-1}, corresponding to a C=O stretching vibration [59]. However, such a peak was not detected in the used eggshells sample, indicating that this carbonate polymorph was less stable and was released into the Pb^{2+} solution to cause removal by precipitation.
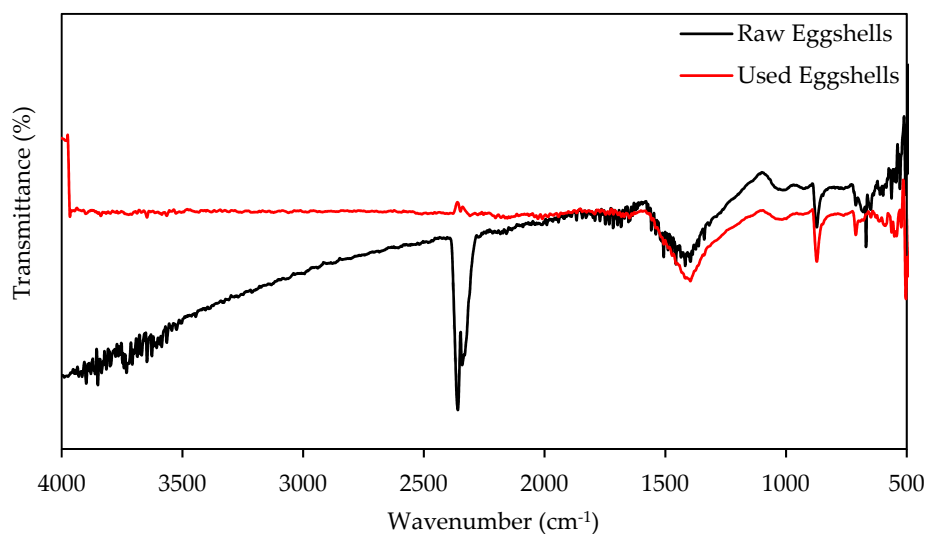
Figure 11. FTIR analysis of eggshells before and after Pb^{2+} removal (40 mg/L Pb^{2+}, s/w ratio 1:200, and particle size 150–500 μm).

3.7. SEM Analysis

SEM micrographs of Figures 12–14 illustrate the eggshells with a particle size of 150–500 μm before and after Pb^{2+} removal. Figure 12 of raw eggshells (processed based on the procedure in Section 2.2) shows the agglomeration of small particles, with the absence of connecting channels. This supports the BET results, suggesting eggshells to be a non-porous material. This conclusion is further supported by the N_2 isotherm type II curve (Figure 4), corresponding to non-porous materials. Similar findings have been reported for raw eggshells in other work [29,35]. In addition, the micrographs show that the surface texture of raw eggshells is rough and uneven.
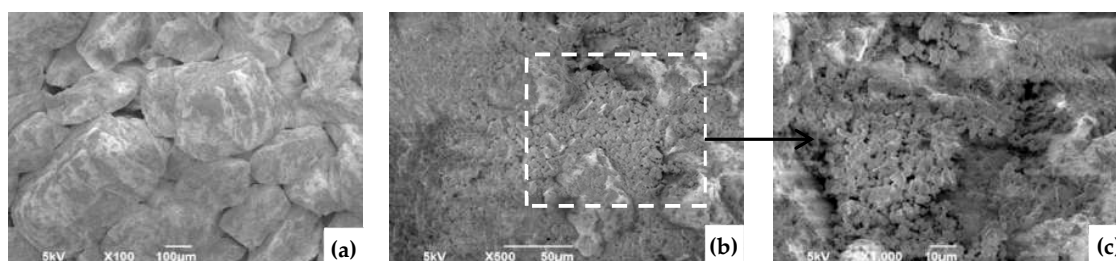

Figure 12. Raw eggshells, particle size 150–500 μm at magnification (**a**) × 100, (**b**) × 500, and (**c**) × 1000.
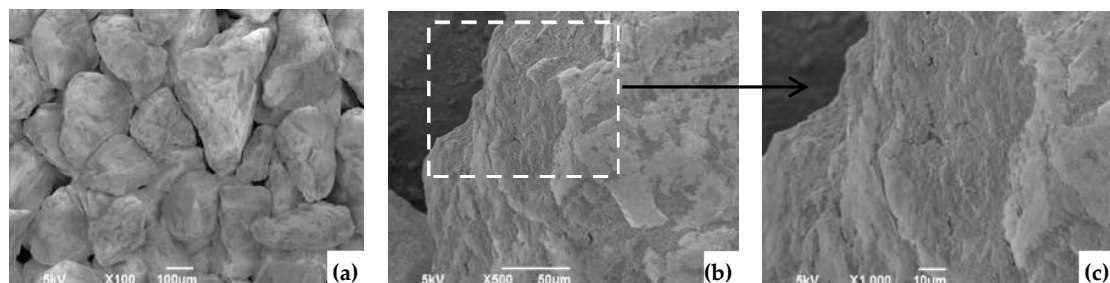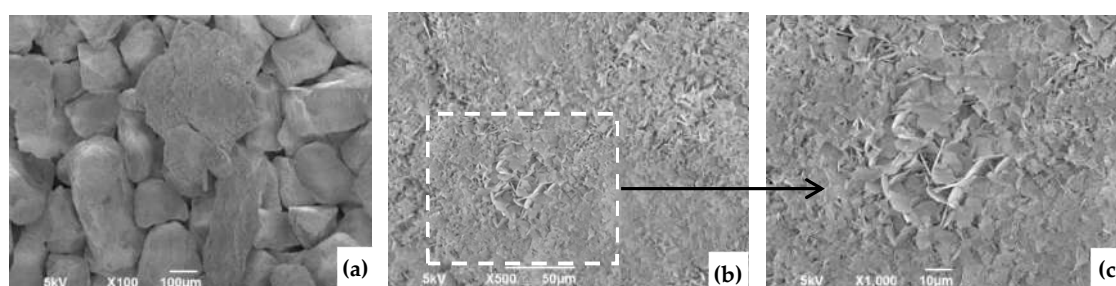

Figure 13. Eggshells, particle size 150–500 μm, after Pb^{2+} removal process with s/w ratio of 1:200 and 20 mg/L Pb^{2+} solution at magnification (**a**) ×100, (**b**) ×500, and (**c**) ×1000.

Figure 14. Eggshells, particle size 150–500 μm, after Pb^{2+} removal process with s/w ratio of 1:2000 and 20 mg/L Pb^{2+} solution at magnification (**a**) ×100, (**b**) ×500, and (**c**) ×1000.

The removal process induced changes to the morphology of the eggshells. Figure 13 presents the microstructure of eggshells post-exposure to Pb^{2+} with an s/w ratio of 1:200. It is clear that the surface of the eggshells is different from that of the raw eggshells. In fact, the surface is denser and less porous, owing to the deposition of Pb^{2+} and formation of lead carbonate ($PbCO_3$). At a lower s/w ratio of 1:2000 (Figure 14), more Pb^{2+} has been deposited on the eggshells surface, leading to the growth of needle-like $PbCO_3$ crystals. The morphology of $PbCO_3$ illustrated herein is consistent with that reported in previous studies [60,61]. This is also consistent with the trend of a higher removal capacity of eggshells (*m*) at lower s/w ratios (Figure 6). Nevertheless, SEM micrographs presented herein cannot be used to differentiate the mechanism of Pb^{2+} deposition onto the eggshells, i.e., microprecipitation or sorption.

4. Conclusions

Eggshells are a common biowaste that could be recycled for the removal of Pb^{2+} from wastewater, thus promoting the use of nature-based sustainable solutions for both waste management and wastewater treatment. In this study, the influence of the particle size of ground eggshells and s/w ratio on removal of Pb^{2+} from aqueous solutions was investigated. Results show that the percent Pb^{2+} removal was not significantly different for particle sizes 150–500 μm and <150 μm despite the large difference in the surface area of the two eggshell sizes. A high percentage removal (up to 99%) of Pb^{2+} by eggshells was achieved for low initial Pb^{2+} concentrations (<30 mg/L) across all s/w ratios studied. SEM images confirmed that the surface of eggshells used for Pb^{2+} removal became denser and less porous due to Pb^{2+} deposition and lead carbonate formation. Needle-like $PbCO_3$ crystals were observed in samples with a lower s/w ratio, which coincides with the trend where eggshells exhibited higher removal capacity at lower s/w ratios. A developed predictive relationship suggests that the removal capacity of eggshells normalized to the initial Pb^{2+} concentration is almost inversely proportional to the s/w ratio. The relationship explains differences in the Pb^{2+} removal capacities of eggshells reported by others. The developed relationship could be utilized to design batch reactors for Pb^{2+} removal by eggshells subject to economic and environmental constraints.

The study also attempted to quantify the role of different removal mechanisms in the total removal of Pb^{2+}. Results confirmed that precipitation played a major role in the removal of Pb^{2+} by eggshells. However, this role was reduced as the s/w ratio and initial concentration of Pb^{2+} became higher. The difference between the extent of Pb^{2+} removal by eggshells and eggshell water suggested that sorption also played a role in Pb^{2+} removal. This was confirmed by the direct quantification of the concentration of Pb^{2+} sorbed on the eggshells and by the results from FTIR spectroscopy. Indeed, FTIR spectroscopy of eggshells highlighted the presence of high- and low-stability calcium carbonate polymorphs that existed in raw eggshells. While the former polymorph was detected in the used eggshells sample, the latter was not, signifying its release into the Pb^{2+} solution to cause removal by precipitation. It was also observed that the contribution of both sorption and precipitation dropped at the high concentration. It was speculated that such decline was due to a decrease in the available carbonates needed for precipitation coupled with a decrease in the solution pH.

References

1. Anantha, R.K.; Kota, S. Removal of lead by adsorption with the renewable biopolymer composite of feather (*Dromaius novaehollandiae*) and chitosan (*Agaricus bisporus*). *Environ. Technol. Innov.* **2016**, *6*, 11–26. [CrossRef]

2. Gupta, V.K.; Agarwal, S.; Saleh, T.A. Synthesis and characterization of alumina-coated carbon nanotubes and their application for lead removal. *J. Hazard. Mater.* **2011**, *185*, 17–23. [CrossRef] [PubMed]

3. Ritchey, A.K.; O'Brien, S.H.; Keller, F.G. Chapter 152—Hematologic manifestations of childhood illness. In *Hematology*, 7th ed.; Hoffman, R., Benz, E.J., Silberstein, L.E., Heslop, H.E., Weitz, J.I., Anastasi, J., Salama, M.E., Abutalib, S.A., Eds.; Elsevier: Amsterdam, The Netherlands, 2018; pp. 2215–2237.e9, ISBN 978-0-323-35762-3.

4. Burke, D.M.; Morris, M.A.; Holmes, J.D. Chemical oxidation of mesoporous carbon foams for lead ion adsorption. *Sep. Purif. Technol.* **2013**, *104*, 150–159. [CrossRef]

5. Canfield, R.L.; Henderson, C.R.; Cory-Slechta, D.A.; Cox, C.; Jusko, T.A.; Lanphear, B.P. Intellectual impairment in children with blood lead concentrations below 10 µg per deciliter. *N. Engl. J. Med.* **2003**, *348*, 1517–1526. [CrossRef] [PubMed]

6. Lanphear, B.P.; Matte, T.D.; Rogers, J.; Clickner, R.P.; Dietz, B.; Bornschein, R.L.; Succop, P.; Mahaffey, K.R.; Dixon, S.; Galke, W.; et al. The contribution of lead-contaminated house dust and residential soil to children's blood lead levels: A pooled analysis of 12 epidemiologic studies. *Environ. Res.* **1998**, *79*, 51–68. [CrossRef]

7. Cooper, W.C.; Wong, O.; Kheifets, L. Mortality among employees of lead battery plants and lead-producing plants, 1947–1980. *Scand. J. Work Environ. Health* **1985**, *11*, 331–345. [CrossRef]

8. Lancranjan, I.; Popescu, H.I.; GAvănescu, O.; Klepsch, I.; Serbănescu, M. Reproductive ability of workmen occupationally exposed to lead. *Arch. Environ. Health* **1975**, *30*, 396–401. [CrossRef]

9. Lanphear, B.P.; Roghmann, K.J. Pathways of lead exposure in urban children. *Environ. Res.* **1997**, *74*, 67–73. [CrossRef]

10. Mahmoud, M.T.; Hamouda, M.A.; Al Kendi, R.R.; Mohamed, M.M. Health risk assessment of household drinking water in a district in the UAE. *Water* **2018**, *10*, 1726. [CrossRef]

11. Health Canada. *Guidelines for Canadian Drinking Water Quality—Summary Table*; Water and Air Quality Bureau; Healthy Environments and Consumer Safety Branch, Health Canada: Ottawa, ON, Canada, 2019.

12. US EPA. *National Primary Drinking Water Regulations*; EPA 816-F-09-004; Office of Water United States Environmental Protection Agency: Washington, DC, USA, 2009.

13. Arunlertaree, C.; Kaewsomboon, W.; Kumsopa, A.; Pokethitiyook, P.; Panyawathanakit, P. Removal of lead from battery manufacturing wastewater by egg shell. *Songklanakarin J. Sci. Technol.* **2007**, *29*, 13.

14. Dermentzis, K.; Valsamidou, E.; Marmanis, D. Simultaneous removal of acidity and lead from acid lead battery wastewater by aluminum and iron electrocoagulation. *J. Eng. Sci. Technol. Rev.* **2012**, *5*, 1–5. [CrossRef]

15. Khaoya, S.; Pancharoen, U. Removal of lead (II) from battery industry wastewater by HFSLM. *Int. J. Chem. Eng. Appl.* **2012**, 98–103. [CrossRef]

16. Macchi, G.; Pagano, M.; Santori, M.; Tiravanti, G. Battery industry wastewater: Pb removal and produced sludge. *Water Res.* **1993**, *27*, 1511–1518. [CrossRef]

17. WHO. *A Compendium of Standards for Wastewater Reuse in the Eastern Mediterranean Region*; World Health Organization, Regional Office for the Eastern Mediterranean: Cairo, Egypt, 2006.

18. Babel, S.; Kurniawan, T.A. Low-cost adsorbents for heavy metals uptake from contaminated water: A review. *J. Hazard. Mater.* **2003**, *97*, 219–243. [CrossRef]

19. Sweidan, H.; Hamouda, M.; El-Hassan, H.; Maraqa, M. A framework for the investigation of biowaste materials as potential adsorbents for water treatment. In Proceedings of the 4th World Congress on Civil, Structural, and Environmental Engineering, Rome, Italy, 7–9 April 2019.

20. Podstawczyk, D.; Witek-Krowiak, A.; Chojnacka, K.; Sadowski, Z. Biosorption of malachite green by eggshells: Mechanism identification and process optimization. *Bioresour. Technol.* **2014**, *160*, 161–165. [CrossRef]

21. Eba, F.; Biboutou, R.K.; Nlo, J.N.; Bibalou, Y.G.; Oyo, M. Lead removal in aqueous solution by activated carbons prepared from *Cola edulis* shell (Alocacée), *Pentaclethra macrophylla* husk (Mimosaceae) and *Aucoumea klaineana* sawdust (Burseraceae). *Afr. J. Environ. Sci. Technol.* **2011**, *5*, 197–204. [CrossRef]

22. El-Naas, M.H.; Al-Rub, F.A.; Ashour, I.; Al Marzouqi, M. Effect of competitive interference on the biosorption of lead(II) by *Chlorella vulgaris*. *Chem. Eng. Process. Process Intensif.* **2007**, *46*, 1391–1399. [CrossRef]

23. Rashed, M.N. Fruit stones from industrial waste for the removal of lead ions from polluted water. *Environ. Monit. Assess.* **2006**, *119*, 31–41. [CrossRef]

24. Sekar, M.; Sakthi, V.; Rengaraj, S. Kinetics and equilibrium adsorption study of lead(II) onto activated carbon prepared from coconut shell. *J. Colloid Interface Sci.* **2004**, *279*, 307–313. [CrossRef]

25. Yan, T.; Luo, X.; Lin, X.; Yang, J. Preparation, characterization and adsorption properties for lead (II) of alkali-activated porous leather particles. *Colloids Surf. A Physicochem. Eng. Asp.* **2017**, *512*, 7–16. [CrossRef]

26. Ritchie, H.; Roser, M. Meat and Dairy Production. Available online: https://ourworldindata.org/meat-production (accessed on 7 September 2020).

27. Stadelman, W.J. EGGS|Structure and Composition. In *Encyclopedia of Food Sciences and Nutrition*, 2nd ed.; Caballero, B., Ed.; Academic Press: Oxford, UK, 2003; pp. 2005–2009. ISBN 978-0-12-227055-0.

28. Ahmad, M.; Usman, A.R.A.; Lee, S.S.; Kim, S.-C.; Joo, J.-H.; Yang, J.E.; Ok, Y.S. Eggshell and coral wastes as low cost sorbents for the removal of Pb^{2+}, Cd^{2+} and Cu^{2+} from aqueous solutions. *J. Ind. Eng. Chem.* **2012**, *18*, 198–204. [CrossRef]

29. Park, H.J.; Jeong, S.W.; Yang, J.K.; Kim, B.G.; Lee, S.M. Removal of heavy metals using waste eggshell. *J. Environ. Sci.* **2007**, *19*, 1436–1441. [CrossRef]

30. Soares, M.; Marto, S.; Quina, M.; Gando-Ferreira, L.; Quinta-Ferreira, R. Evaluation of eggshell-rich compost as biosorbent for removal of Pb(II) from aqueous solutions. *Water Air Soil Pollut.* **2016**, *227*, 1–16. [CrossRef]

31. Vijayaraghavan, K.; Jegan, J.; Palanivelu, K.; Velan, M. Removal and recovery of copper from aqueous solution by eggshell in a packed column. *Miner. Eng.* **2005**, *18*, 545–547. [CrossRef]

32. Yeddou, N.; Bensmaili, A. Equilibrium and kinetic modelling of iron adsorption by eggshells in a batch system: Effect of temperature. *Desalination* **2007**, *206*, 127–134. [CrossRef]

33. Zhang, T.; Tu, Z.; Lu, G.; Duan, X.; Yi, X.; Guo, C.; Dang, Z. Removal of heavy metals from acid mine drainage using chicken eggshells in column mode. *J. Environ. Manag.* **2017**, *188*, 1–8. [CrossRef]

34. Pramanpol, N.; Nitayapat, N. Adsorption of reactive dye by eggshell and its membrane. *Agric. Nat. Resour.* **2006**, *40*, 192–197.

35. Tsai, W.T.; Yang, J.M.; Lai, C.W.; Cheng, Y.H.; Lin, C.C.; Yeh, C.W. Characterization and adsorption properties of eggshells and eggshell membrane. *Bioresour. Technol.* **2006**, *97*, 488–493. [CrossRef]

36. Witek-Krowiak, A.; Chojnacka, K.; Podstawczyk, D.; Dawiec, A.; Pokomeda, K. Application of response surface methodology and artificial neural network methods in modelling and optimization of biosorption process. *Bioresour. Technol.* **2014**, *160*, 150–160. [CrossRef]

37. Andersson, M.P.; Sakuma, H.; Stipp, S.L.S. Strontium, nickel, cadmium, and lead substitution into calcite, studied by density functional theory. *Langmuir* **2014**, *30*, 6129–6133. [CrossRef]

38. Davis, A.D.; Webb, C.J.; Sorensen, J.L.; Dixon, D.J.; Hudson, R. Geochemical thermodynamics of cadmium removal from water with limestone. *Environ. Earth Sci.* **2018**, *77*, 37. [CrossRef]

39. Lee, Y.-C.; Kim, E.J.; Yang, J.-W.; Shin, H.-J. Removal of malachite green by adsorption and precipitation using aminopropyl functionalized magnesium phyllosilicate. *J. Hazard. Mater.* **2011**, *192*, 62–70. [CrossRef] [PubMed]

40. Xie, Y.; Giammar, D.E. Effects of flow and water chemistry on lead release rates from pipe scales. *Water Res.* **2011**, *45*, 6525–6534. [CrossRef] [PubMed]

41. Xie, L.; Giammar, D.E. Chapter 13 Influence of phosphate on adsorption and surface precipitation of lead on iron oxide surfaces. In *Developments in Earth and Environmental Sciences*; Barnett, M.O., Kent, D.B., Eds.; Adsorption of Metals by Geomedia II: Variables, Mechanisms, and Model Applications; Elsevier: Amsterdam, The Netherlands, 2007; Volume 7, pp. 349–373.

42. Vijayaraghavan, K.; Joshi, U.M. Chicken eggshells remove Pb(II) ions from synthetic wastewater. *Environ. Eng. Sci.* **2013**, *30*, 67–73. [CrossRef]

43. APHA; AWWA; WEF. *Standard Methods for the Examination of Water and Wastewater*, 23rd ed.; Rice, E.W., Baird, R.B., Eaton, A.D., Eds.; American Public Health Association: Washington, DC, USA, 2017.

44. U.S. EPA. *Method 3050B: Acid Digestion of Sediments, Sludges, and Soils, Revision 2*; U.S. EPA: Washington, DC, USA, 1996.

45. Spagnoli, A.A.; Giannakoudakis, D.A.; Bashkova, S. Adsorption of methylene blue on cashew nut shell based carbons activated with zinc chloride: The role of surface and structural parameters. *J. Mol. Liq.* **2017**, *229*, 465–471. [CrossRef]

46. Martín-Lara, M.A.; Blázquez, G.; Ronda, A.; Pérez, A.; Calero, M. Development and characterization of biosorbents to remove heavy metals from aqueous solutions by chemical treatment of olive stone. *Ind. Eng. Chem. Res.* **2013**, *52*, 10809–10819. [CrossRef]

47. García-Mendieta, A.; Olguín, M.T.; Solache-Ríos, M. Biosorption properties of green tomato husk (Physalis philadelphica Lam) for iron, manganese and iron–manganese from aqueous systems. *Desalination* **2012**, *284*, 167–174. [CrossRef]

48. Queirós, M.V.A.; Bezerra, M.N.; Feitosa, J.P.A. Composite superabsorbent hydrogel of acrylic copolymer and eggshell: Effect of biofiller addition. *J. Braz. Chem. Soc.* **2017**, *28*, 2004–2012. [CrossRef]

49. da Silva Castro, L.; Barañano, A.G.; Pinheiro, C.J.G.; Menini, L.; Pinheiro, P.F. Biodiesel production from cotton oil using heterogeneous CaO catalysts from eggshells prepared at different calcination temperatures. *Green Process. Synth.* **2019**, *8*, 235–244. [CrossRef]

50. Habte, L.; Shiferaw, N.; Mulatu, D.; Thenepalli, T.; Chilakala, R.; Ahn, J.W. Synthesis of nano-calcium oxide from waste eggshell by sol-gel method. *Sustainability* **2019**, *11*, 3196. [CrossRef]

51. Godelitsas, A.; Astilleros, J.M.; Hallam, K.; Harissopoulos, S.; Putnis, A. Interaction of calcium carbonates with lead in aqueous solutions. *Environ. Sci. Technol.* **2003**, *37*, 3351–3360. [CrossRef] [PubMed]

52. Macchi, G.; Marani, D.; Pagano, M.; Bagnuolo, G. A bench study on lead removal from battery manufacturing wastewater by carbonate precipitation. *Water Res.* **1996**, *30*, 3032–3036. [CrossRef]

53. Taylor, P.; Lopata, V.J. Stability and solubility relationships between some solids in the system PbO–CO$_2$–H$_2$O. *Can. J. Chem.* **1984**, *62*, 395–402. [CrossRef]

54. Powell, K.J.; Brown, P.L.; Byrne, R.H.; Gajda, T.; Hefter, G.; Leuz, A.-K.; Sjöberg, S.; Wanner, H. Chemical speciation of environmentally significant metals with inorganic ligands. Part 3: The Pb^{2+} + OH$^-$, Cl$^-$, CO$_3$$^{2-}$, SO$_4$$^{2-}$, and PO$_4$$^{3-}$ systems (IUPAC Technical Report). *Pure Appl. Chem.* **2009**, *81*, 2425–2476. [CrossRef]

55. Snoeyink, V.L.; Jenkins, D. *Water Chemistry*; Wiley: New York, NY, USA, 1980; ISBN 978-0-471-05196-1.

56. Bilinski, H.; Schindler, P. Solubility and equilibrium constants of lead in carbonate solutions (25 °C, I = 0.3 mol dm^{-3}). *Geochim. Cosmochim. Acta* **1982**, *46*, 921–928. [CrossRef]

57. Li, Z.; Yang, D.-P.; Chen, Y.; Du, Z.; Guo, Y.; Huang, J.; Li, Q. Waste eggshells to valuable Co$_3$O$_4$/CaCO$_3$ materials as efficient catalysts for VOCs oxidation. *Mol. Catal.* **2020**, *483*, 110766. [CrossRef]

58. Abeywardena, M.R.; Elkaduwe, R.K.W.H.M.K.; Karunarathne, D.G.G.P.; Pitawala, H.M.T.G.A.; Rajapakse, R.M.G.; Manipura, A.; Mantilaka, M.M.M.G.P.G. Surfactant assisted synthesis of precipitated calcium carbonate nanoparticles using dolomite: Effect of pH on morphology and particle size. *Adv. Powder Technol.* **2020**, *31*, 269–278. [CrossRef]

59. Ismail, S.; Ahmed, A.S.; Anr, R.; Hamdan, S. Biodiesel production from castor oil by using calcium oxide derived from mud clam shell. *J. Renew. Energy* **2016**, *2016*, 8. [CrossRef]

60. Seignez, N.; Gauthier, A.; Bulteel, D.; Buatier, M.; Recourt, P.; Damidot, D.; Potdevin, J.L. Effect of Pb-rich and Fe-rich entities during alteration of a partially vitrified metallurgical waste. *J. Hazard. Mater.* **2007**, *149*, 418–431. [CrossRef]

61. Ng, D.-Q.; Lin, Y.-P. Effects of pH value, chloride and sulfate concentrations on galvanic corrosion between lead and copper in drinking water. *Environ. Chem.* **2015**, *13*, 602–610. [CrossRef]

Article

Adsorption Mechanisms and Characteristics of Hg^{2+} Removal by Different Fractions of Biochar

Xiaoli Guo, Menghong Li *, Aijv Liu, Man Jiang, Xiaoyin Niu and Xinpeng Liu

Department of Resource and Environmental Engineering, Shandong University of Technology, Zibo 255000, China; gwmy1027@163.com (X.G.); liuajsdut@gmail.com (A.L.); jiangman@sdut.edu.cn (M.J.); zbnxy@sdut.edu.cn (X.N.); wangbaohua1996@163.com (X.L.)

* Correspondence: zblmh76180@sdut.edu.cn; Tel.: +86-139-5336-9334

Abstract: The adsorption mechanisms of mercury ion (Hg^{2+}) by different fractions of biochar were studied, providing a theoretical basis and practical value for the use of biochar to remediate mercury contamination in water. Biochar (RC) was prepared using corn straw as the raw material. It was then fractionated, resulting in inorganic carbon (IC), organic carbon (OC), hydroxyl-blocked carbon (BHC), and carboxyl-blocked carbon (BCC). Before and after Hg^{2+} adsorption, the biochar fractions were characterized by several techniques, such as energy-dispersive X-ray spectroscopy (EDS), Fourier-transform infrared spectroscopy (FTIR), and X-ray photoelectron spectroscopy (XPS). Obtained results indicate that the reaction mechanisms of RC for Hg^{2+} removal mainly include electrostatic adsorption, ion exchange, reduction, precipitation, and complexation. The equilibrium adsorption capacity of RC for Hg^{2+} is 75.56 mg/g, and the adsorption contribution rates of IC and OC are approximately 22.4% and 77.6%, respectively. Despite the lower rate, IC shows the largest adsorption capacity, of 92.63 mg/g. This is attributed to all the mechanisms involved in Hg^{2+} adsorption by IC, with ion exchange being the main reaction mechanism (accounting for 39.8%). The main adsorption mechanism of OC is the complexation of carboxyl and hydroxyl groups with Hg^{2+}, accounting for 71.6% of the total OC contribution. BHC and BCC adsorb mercury mainly via the reduction–adsorption mechanism, accounting for 54.6% and 54.5%, respectively. Among all the adsorption mechanisms, the complexation reaction of carboxyl and hydroxyl groups with Hg^{2+} is the dominant effect.

Keywords: biochar; different fractions; Hg^{2+}; characterization; adsorption mechanism

---

1. Introduction

Mercury is a highly toxic, non-essential heavy metal. Even at low concentrations, it poses potential threat to human health [1]. Inorganic mercury is the most common form of mercury found in aquatic ecology. It stably accumulates in aqueous solutions and does not degrade easily. Under natural conditions, it easily reacts with chemicals and microorganisms via a methylation reaction, producing mercury forms with increased toxicity, such as methylmercury or dimethylmercury [2]. According to United States Environmental Protection Agency (EPA) regulations, mercury concentrations in treated wastewater and drinking water must be less than 10 and 2 µg/L, respectively [3]. Therefore, it is of great significance to study mercury removal from water. Treatment methods for mercury removal mainly include chemical precipitation, ion exchange, reduction, coagulation, solvent extraction, and adsorption methods. Among them, adsorption is widely applied due to its advantages of fast action, superior removal efficiency, inexpensive nature of adsorbents, and easy access to raw materials that can be used as adsorbents [4–6]. Biochar is the most commonly used adsorbent material, showing high adsorption efficiency [7]. In previous studies, commonly used raw materials for biochar preparation

included walnut shells [8], flax shive [9], guava skin [10], fruit shell of Terminalia catappa [11], rice husk [12], sugarcane bagasse [13], coconut husk [14], and peanut husk [15], all showing good adsorption results. In general, biochar adsorbs heavy metals mainly via combining metal ions with aromatic alcohols or acids, and carbonates [16]. The main adsorption pathways are through electrostatic effect, reduction, complexation, and cation exchange. Kong et al. [17] showed that the phenolic hydroxyl groups contained in soybean stalk-based biochar had a strong reduction effect, reducing Hg^{2+} to Hg^0 during Hg^{2+} adsorption. Das et al. [18] studied Hg^{2+} adsorption by Aspergillus versicolor biomass and suggested complexation as the main mechanism between oxygen-containing functional groups and Hg^{2+}. Kílíç et al. [19] observed the release of a large concentration of basic metal ions (Ca^{2+}, Na^+, and K^+) during Hg^{2+} adsorption by activated sludge biomass, indicating that an ion exchange mechanism was involved in the adsorption process. Dong et al. [20] used XPS to analyze the adsorption mechanisms of Hg^{2+} by Brazilian pepper biochars at different pyrolysis temperatures. It was shown that biochar prepared at relatively low temperatures (300 and 450 °C) adsorbs Hg^{2+} mainly through complexation with hydroxyl and carboxyl functional groups, while biomass carbon prepared at 600 °C has a graphite-like structure and Hg–Cπ is formed between Hg^{2+} and the C=C structure. As a heterogeneous material, biochar is mainly composed of inorganic mineral components (ash) and organic carbonaceous components. Current studies on adsorption of pollutants by biochar mainly focus on the overall removal effect of biochar, with research on the adsorption mechanisms of pollutants by different fractions of biochar being very limited. The contribution rate of each fraction of the adsorbent during the adsorption mechanism for a certain pollutant needs to be further studied.

Herein, biochar was prepared using corn stover as the raw material, which was then fractionated to prepare inorganic, organic, hydroxyl-blocked, and carboxyl-blocked carbonaceous fragments. Through physicochemical analysis (element composition, pH value, and isoelectric point pH_{pzc}), Boehm titration and surface analysis (FTIR, XPS, and EDS) measurements before and after Hg^{2+} adsorption, the mercury adsorption mechanisms, and structure–property relationships of biochar and its fractions were studied. This research has important practical significance for mercury removal from water by biochar.

2. Materials and Methods

2.1. Preparation of Biochar Fractions

Raw carbon was synthesized from cornstalk (sourced from Da Xu Village, Zibo, Shandong, China) and air-dried outdoors. It was ground when the moisture content dropped below 10% and was put in a ceramic crucible for pyrolysis and carbonization at 500 °C with a rate of 20 °C/min for 6 h under N_2 atmosphere. The biochar removed from the furnace was cooled in a desiccator, weighed, and stored in airtight plastic bags. Raw carbon was referred to as RC. RC was placed in a tube furnace, the temperature of which was raised to 600 °C at a rate of 20 °C/min and kept for 4 h to obtain inorganic carbon (IC). RC was thoroughly mixed for 24 h with an acid mixture (0.3 M HF + 0.1 M HCl), at a solid/liquid ratio of 1:250 (g/mL). The mixture was then washed and dried to obtain organic carbon (OC). Meanwhile, a quantity of 9.0 g of RC was thoroughly mixed with 633 mL of anhydrous methanol and 5.4 mL of 0.1 M HCl to block carboxylic acid groups (–COOH) by methyl esterification of carboxyl groups. After being stirred for 6 h, the mixture was washed and dried to obtained carboxyl-blocked carbon (BCC). Similarly, hydroxyl-blocked carbon (BHC) was prepared by blocking hydroxyl groups (–OH) via thoroughly mixing and stirring 5.0 g of biochar and 100 mL of HCHO for 6 h [21–23]. The yield of each fraction of biochar was calculated.

2.2. Physicochemical Properties of Biochar Fractions

Typically, 1.0 g of biochar was weighed and placed in a 100 mL covered conical flask. Meanwhile, 20 mL of deionized water was boiled and let to cool before being added into the flask. Subsequently, the mixture was shaken at 120 r/min and 25 °C for 24 h. It was then taken out and let to sit still for

5 min. The pH of the solution was determined using a Mettler Delta 320 pH Meter (Mettler Toledo, Guangzhou, China) [24].

For a typical test, 50 mL of 0.01 M KNO_3 solution was pipetted into a 100 mL covered conical flask. The initial pH value was adjusted to a value within the range of 2–10, using 0.10 M HCl or NaOH solution, and denoted as pH_i. Then, 0.1 g biochar was added and the mixture was shaken at 120 r/min and 25 °C, for 48 h. Subsequently, the mixture was filtered and the pH of the filtrate was marked as pH_f. In the case where ΔpH ($\Delta pH = pH_f - pH_i$) is 0, the value of pH_i (or pH_f) is the pH_{pzc} of the biochar [25].

A Vario EL cube elemental analyzer (Elementar, Karlsruhe, Germany) was used to determine the C, H, and N content of biochar and its fractions, and the H/C value was calculated.

2.3. Determination of Oxygen-Containing Functional Groups on Biochar Surface

Boehm titration [26] was applied to quantitatively determine the oxygen-containing functional groups on the surface of biochar. Specifically, 1.0 g of biochar was placed in a 100 mL covered conical flask, and 25 mL of 0.05 M alkaline solution ($NaHCO_3$, Na_2CO_3, and NaOH) and 25 mL of 0.05 M acidic solution (HCl) were added, respectively. The mixture was shaken at 120 r/min and 25 °C for 24 h before being subjected to filtration. Subsequently, back titration was carried out with 0.05 M NaOH and HCl [27] to determine the content of acidic and basic groups on the surface of biochar.

2.4. Adsorption Experiment and Characterization before and after Hg^{2+} Adsorption

A $HgCl_2$ 3 mM solution was prepared. Then, 1.0 g of biochar (passed through a 200-mesh sieve) and 200 mL $HgCl_2$ solution were placed into a 250 mL covered conical flask. The mixture was shaken at 120 r/min and 25 °C for 24 h and filtrated upon reaching adsorption equilibrium. The pH of the filtrate was measured, and the concentration of Hg^{2+} was determined via an inductively coupled plasma mass spectrometer (ICP-MS, Santa Clara, CA, USA). On this basis, the Hg^{2+} amount adsorbed was calculated. Meanwhile, the leaching experiments of all biochars were conducted under the same conditions, with samples withdrawn at certain time intervals (3, 5, 10, 20, 30, 60, 90, 120, 150, 180, 240, 300, 420, 540, and 720 min). After filtration, the changes in the concentrations of K^+, Na^+, and Hg^{2+} in the leaching solution were measured.

The surface functional groups of the samples before and after mercury adsorption were identified by Fourier-transform infrared spectroscopy (FTIR), using a Nicolet 5700 machine (Thermo Nicolet, Waltham, MA, USA). The change in the valence state of Hg^{2+} before and after mercury adsorption was determined by X-ray photoelectron spectroscopy (XPS), using an Axis Ultr DLD machine (Thermo Fisher Scientific, Waltham, MA, USA) and analyzing the experimental data using the software Peak 4.1. (Hampton, MA, USA) The main elemental composition of biochar was detected by an energy-dispersive spectrometer (EDS), using a Quanta 250 (FEI, Hillsboro, OR, USA).

3. Results and Discussion

3.1. Physicochemical Properties of Biochar and Analysis of Surface Functional Groups

The different biochar fractions examined displayed varied physicochemical properties, as well as difference in the concentration of surface functional groups. According to Lehmann [28] and Shaaban et al. [29], when the pH value of the biochar is greater than pH_{pzc}, the biochar surface is negatively charged, which combined with positively charged ions present in the solution, leads to weakened competitiveness of H^+. As shown in Table 1, the pH of the biochar was greater than pH_{pzc}, so the surfaces of the five biochar fractions are all negatively charged, posing an electrostatic adsorption effect on Hg^{2+}. OC has the lowest pH with the highest contents of acidic functional groups such as –OH and –COOH groups. This may be caused due to OC not being cleaned thoroughly after acid washing or due to a replacement of the cations in the functional groups, such as –COOM (M is a metal cation) by H^+ during the acid washing process, resulting in the acidity of OC [30,31]. The pH value

of OC did not change significantly after Hg^{2+} adsorption, which may be due to the release of H^+ by the complexation reaction between carboxyl/hydroxyl functional groups and Hg^{2+} [32]. Hg^{2+} mainly exists in the anion forms of $HgCl^-$ and $HgClO^-$ in acidic solutions [33]. The carboxyl and hydroxyl functional groups present on OC surface consume H^+ by protonation, forming positively charged $-OH^{2+}$ and $-COOH^{2+}$, which combine with $HgCl^-$ and $HgClO^-$ through electrostatic effect to remove Hg^{2+}. IC has the highest concentration of strongly basic functional groups, possibly attributed to it being the product of RC pyrolysis and carbonization at 600 °C. Thy et al. [34] showed that after high-temperature pyrolysis, graphitization of biochar occurs via polycondensation of low-temperature aromatization, which removes organic components, resulting in increased alkali metal ions. The pH of IC dropped significantly after Hg^{2+} adsorption, attributed to the fact that Hg^{2+} easily reacts with OH^- to form $Hg_2(OH)_2$ precipitation under alkaline conditions, resulting in decreased concentration of OH^- [35]. Although the concentration of carboxyl and hydroxyl oxygen-containing functional groups in BHC and BCC decreased significantly, the H/C value of BHC and BCC decreased, and the number of lactone groups increased significantly. Dougherty et al. [36] showed that a smaller H/C value represents a lower degree of carbonation and a higher degree of aromatization. They showed that the strength of the cation $-\pi$ effect is mainly determined by the aromaticity degree of biochar surface, i.e., the more abundant the $-\pi$ conjugated aromatic structure, the stronger the electron donating ability of the biochar, and thereby, the more significant the reduction effect. Therefore, BHC and BCC show a strong reduction effect.

Table 1. Physicochemical properties and the number of surface functional groups of biochar (mmol/g).

Biochar	pH_{pzc}	pH	pH after Adsorption	H/C	Carboxyl	Lactone Group	Phenolic Hydroxyl	Acid Functional Groups	Basic Functional Groups
RC	9.3	9.5	7.6	0.036	0.370	0.050	0.125	0.545	0.970
IC	10.4	10.9	8.6	0.314	0.105	0.210	0.080	0.395	1.390
OC	3.3	3.6	3.3	0.043	0.495	0.090	0.355	0.940	0.285
BHC	8.2	8.4	6.4	0.017	0.400	0.190	0.015	0.605	0.905
BCC	8.1	8.3	6.5	0.018	0.180	0.195	0.175	0.550	0.895

RC: raw carbon; IC: inorganic carbon; OC: organic carbon; BHC: hydroxyl-blocked carbon; BCC: carboxyl-blocked carbon.

3.2. FTIR Analysis of Biochar Fractions before and after Hg^{2+} Adsorption

The FTIR spectra of different biochar fractions before and after Hg^{2+} adsorption are shown in Figure 1. A significant characteristic peak at 3431 cm^{-1} was observed for all the five biochar fractions. This was assigned to $-OH$ stretching vibration of alcohol hydroxyl groups and phenolic hydroxyl groups formed via intermolecular hydrogen bonding, indicating the large concentration of $-OH$ contained in the biochar fractions [37]. The broad peak around 1578 cm^{-1} was assigned to the stretching vibration of $C=O$ in the lactone group and $C=C$ in mononuclear aromatic hydrocarbons [38], while the stretching vibration of $-COOH$ resulted in the broad peak observed around 1425 cm^{-1} [39]. Therefore, it can be concluded that biochar contains oxygen-containing functional groups, such as $-COOH$, $-OH$, and lactone groups, observations consistent with the results in Table 1.

The absorption peaks weakened after Hg^{2+} adsorption for all the five biochar fractions, with the most significant changes observed for absorption bands at 3431 and 1425 cm^{-1}, indicating that the concentration of $-OH$ and $-COOH$ groups were significantly affected by Hg^{2+} adsorption. The absorbance of OC, RC, and BCC at 3431 cm^{-1} decreased by 0.474, 0.327, and 0.185, respectively, after Hg^{2+} adsorption, indicating that the $-OH$ groups possibly reacted with Hg^{2+}. This is consistent with the perspective proposed by Herrero et al. [40] that the phenolic hydroxyl groups on the adsorbent surface undergo a complexation reaction with Hg^{2+}. At 1425 cm^{-1}, the absorbance of OC, RC, and BHC decreased by 0.178, 0.103, and 0.083, respectively, after Hg^{2+} adsorption. Zhang [41] and Goyal [42] et al. also found that the oxygen-containing functional groups (e.g., $-COOH$) on the biochar surface reacted with Hg^{2+}, which weakened the vibration signal of $-COOH$ in FTIR.

Before Hg^{2+} adsorption, the concentration of lactone functional groups in BHC and BCC was big (Table 1). After Hg^{2+} adsorption, the absorbance of BHC and BCC at 1578 cm^{-1} decreased by 0.166 and 0.182, respectively, indicating that the C=O in the lactone group and C=C in aromatic hydrocarbons engaged in a reaction with Hg^{2+}. A smaller H/C value represents a more significant reduction effect of cation $-\pi$, as the $-\pi$ electron of the benzene ring can reduce Hg^{2+} to Hg^+ [36,43]. This also proves that BHC and BCC have a strong reduction effect, in accordance with Table 1.
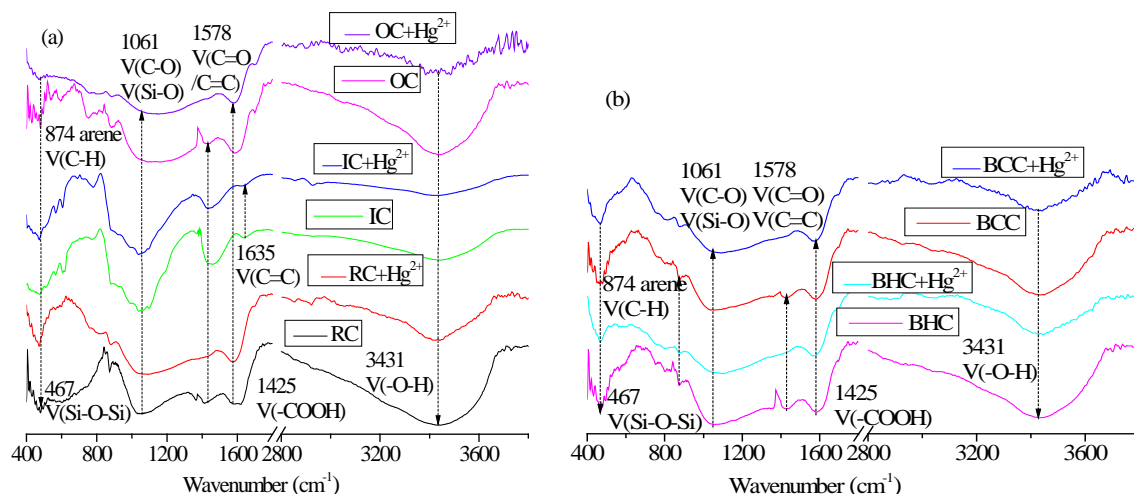
Figure 1. FTIR spectra before and after Hg^{2+} adsorption by biochar (**a**): RC, IC, and OC; (**b**): BHC and BCC.

### 3.3. XPS Analysis of Biochar Fractions before and after Hg^{2+} Adsorption

XPS characterization was carried out for biochar fractions before and after mercury adsorption, to analyze the valence changes of C, O, and Hg and to further clarify the adsorption mechanisms of mercury by biochar. Table 2 shows the peak area changes of different forms of C and O in the five biochar fractions before and after mercury adsorption. After mercury adsorption by RC and OC, the contents of carboxyl C (288 eV) decreased by 6.4% and 9.5%, and the contents of carboxyl O (534.6 eV) decreased by 9.6% and 13.0%, respectively. Meanwhile, the contents of hydroxyl O (532.4 eV) decreased by 4.7% and 5.6% in RC and OC, respectively. These results are consistent with the FTIR analysis, indicating that the –COOH and –OH functional groups on the biochar surface complexed with Hg^{2+}. The variation of carboxyl and hydroxyl groups on the OC surface is more significant than that on RC surface, attributed to OC being weakly acidic whereas RC is alkaline. Hg^{2+} is more likely to form $Hg(OH)_2$ under alkaline conditions [44], but OC contains more –COOH and –OH functional groups and, therefore, engages more Hg^{2+}. The content of hydroxyl O on BCC surface decreased by 7.1%, while the contents of carboxyl C and O on BHC surface dropped by 5.3% and 6.8%, respectively. This indicates that the –COOH groups of BHC and –OH groups of BCC also contribute greatly to mercury removal. After Hg^{2+} adsorption by IC, BHC, and BCC, the areas of C peaks at 284.7 (C=C) and 531.7 eV (C=O) decreased significantly, and the O peak at 531.7 eV decreased by 3.1%, 13.0%, and 15.9%, respectively. These changes indicate that C=C and C=O are also involved in Hg^{2+} removal, by combining with mercury to form Hg–Cπ and remove Hg^{2+} [45].

Table 2. Elemental binding energy and mass content of different biochar components before and after Hg^{2+} adsorption.

Element	BE(eV) [a]	PA(%) [b] of RC		PA(%) [b] of IC		PA(%) [b] of OC		PA(%) [b] of BHC		PA(%) [b] of BCC	
		BS [c]	AS [d]	BS	AS	BS	AS	BS	AS	BS	AS
C$_{1s}$(C=C)	284.7	54.0%	49.7%	55.8%	51.2%	50.6%	52.1%	61.4%	55.5%	60.7%	52.8%
C$_{1s}$(C–O)	285.6	25.7%	36.7%	14.0%	27.1%	12.9%	24.1%	5.7%	25.4%	7.5%	23.6%
C$_{1s}$(C=O)	287.1	8.0%	7.7%	22.2%	18.6%	16.4%	15.1%	22.1%	13.6%	27.4%	19.7%
C$_{1s}$(–COO)	288.8	12.3%	5.9%	8.0%	3.1%	18.1%	8.6%	10.8%	5.5%	4.5%	4.0%
O$_{1s}$(C=O)	531.7	25.5%	33.2%	41.2%	38.1%	27.4%	37.7%	51.5%	38.5%	53.4%	37.5%
O$_{1s}$(hydroxyl)	532.4	23.5%	18.8%	15.5%	11.7%	25.5%	16.9%	7.4%	7.2%	21.7%	14.6%
O$_{1s}$(C–O)	533.6	25.2%	31.7%	21.3%	36.9%	17.0%	28.3%	15.1%	35.1%	19.8%	40.9%
O$_{1s}$(COO)	534.6	25.8%	16.3%	21.0%	13.3%	30.2%	17.2%	26.1%	19.3%	5.1%	5.0%

[a] BE: binding energy, [b] PA: peak area, [c] BS: before sorption of Hg^{2+}, [d] AS: after sorption of Hg^{2+}.

The XPS pattern analysis of Hg$_{4f}$ (Figure 2) confirms that a certain amount of Hg^{2+} was adsorbed on biochar. Obvious Hg$_{4f\,7/2}$ and Hg$_{4f\,5/2}$ peaks were observed for RC, IC, and OC, at the binding energies of 101.50 and 101.80 eV, which are two states of spin orbits with a split value of 4.1 eV (distance between two Hg$_{4f}$ peaks), representing the complexes of (–COO)$_2$Hg and (–O)$_2$Hg [46,47]. According to the areas of fitted peaks assigned to (–COO)$_2$Hg and (–O)$_2$Hg, the complexations by IC, RC, and OC account for 39.8%, 68.9%, and 71.6%, respectively, with the corresponding (–COO)$_2$Hg taking up 18.0%, 51.0%, and 64.6%, respectively. Therefore, it can be concluded that the main adsorption mechanism of RC and OC is a complexation, dominated by –COOH functional groups. Manivannan [48], Wang [49], and Hyland [50] et al. have discovered that the peaks at the binding energies of 102.5 (Hg$_{4f\,7/2}$) and 106.4 eV (Hg$_{4f\,5/2}$) correspond to Hg^{2+}; the fitted peak at 103.6 eV is attributed to Hg$_2$Cl$_2$; and the peak at 99.8 eV is assigned to Hg^0. The fitted peak of Hg$^+$ at 103.6 eV is present in the XPS spectra of all the five biochar factions, with the fitted peak of Hg^0 at 99.8 eV being observed only for IC (Figure 2). According to FTIR analysis and the significant decrease of the concentration of phenolic hydroxyl groups on biochar (except BHC) after Hg^{2+} adsorption (Figure 1, Table 2), there may be a reduction effect of phenolic hydroxyl groups and –π electrons during mercury adsorption, causing the reduction of Hg^{2+} to Hg$^+$ and Hg^0. Such reduction reactions account for 25.2%, 36.4%, and 13.0% in the Hg^{2+} adsorption by RC, OC, and IC, respectively.
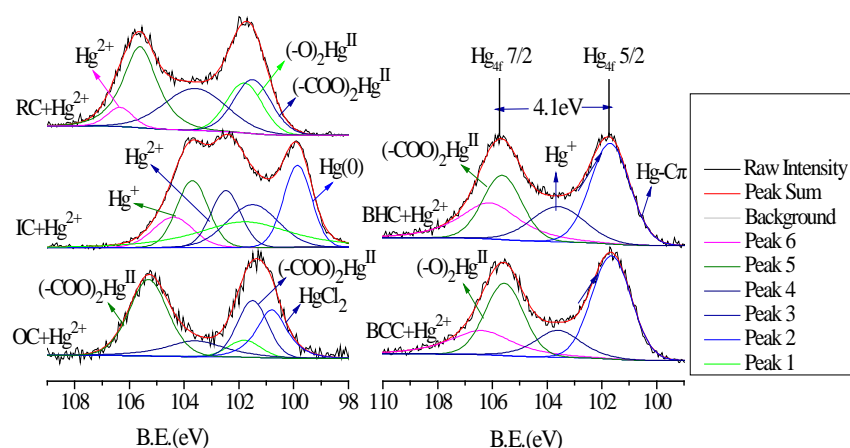
Figure 2. XPS spectra of Hg$_{4f}$ after adsorption of Hg^{2+} by biochars.

According to the above analysis, the fitted peaks at 105.6 and 105.9 eV represent (–COO)$_2$Hg and (–O)$_2$Hg, respectively, indicating that the complexation reaction accounts for 23.3% and 28.3% in the adsorptions by BHC and BCC, respectively. Xu et al. [51] assigned the fitted peak around 101.7 eV to Hg–Cπ, formed from the reduction of Hg^{2+} to Hg$^+$ by the –π bond and the further combination of Hg$^+$ with C=C and C=O. Its peak area accounts for 37.1% and 41.4% in the XPS spectra of BHC and BCC, respectively. According to the areas of fitted peaks at 103.6 eV (Hg$_2$Cl$_2$) in the XPS spectra of BHC and

BCC, reduction accounts for 17.5% and 13.1%, respectively. Thus, the overall reduction effect of BHC and BCC contribute 54.6% and 54.5%, respectively. Therefore, the main adsorption mechanism of BHC and BCC is by reduction.

3.4. EDS Analysis of Biochar Fractions before and after Hg^{2+} Adsorption and Leaching Experiments

According to the EDS spectra of the five biochar fractions before and after Hg^{2+} adsorption and leaching experiments of all biochar, IC contains the most basic cations. Therefore, only IC analysis results were displayed. As shown in Figure 3a, after Hg^{2+} adsorption by IC, the concentration of metal cations, such as K^+, Na^+, Mg^{2+}, and Al^{2+}, on the biochar decreased, accompanied by the appearance of a relatively obvious mercury peak, indicating that there may be an ion exchange mechanism during the adsorption process. Among the various cations, the most significant reduction was observed for K^+, followed by Na^+, implying that Hg^{2+} is more prone to ion exchange with K^+ and Na^+. As suggested by Figure 3b, the K^+ and Na^+ concentrations gradually increased with time, and the Hg^{2+} concentration simultaneously decreased, until the adsorption equilibrium. The adsorption contribution rates of K^+ and Na^+ (30.6% and 10.3%, respectively) were calculated, and based on the concentration of K^+, Na^+, and Hg^{2+} at the adsorption equilibrium, the adsorption contribution rate of ion exchange was 40.9%. According to studies carried out by Kílíç [19] and Carro et al. [52], K^+ and Na^+ are more prone to ion exchange with Hg^+. The contents of Hg^+ and Hg^{2+} determined by XPS analysis are 17.3% and 23.9%, respectively. Hence, in the total ion exchange of 40.9%, Hg^+ and Hg^{2+} take up 17.3% and 23.6%, respectively. Associating with XPS analysis, the complexation and reduction reactions during Hg^{2+} adsorption by IC account for 39.8% and 36.4%, respectively. Therefore, the main mechanism for Hg^{2+} adsorption by IC is ion exchange. In addition, the adsorption contribution rates of ion exchange in the removal of Hg^{2+} (40.9%) by IC is higher in comparison with other adsorbents such as 31.7% by activated sludge biomass [19] and 35.0% by algal biomass [52].
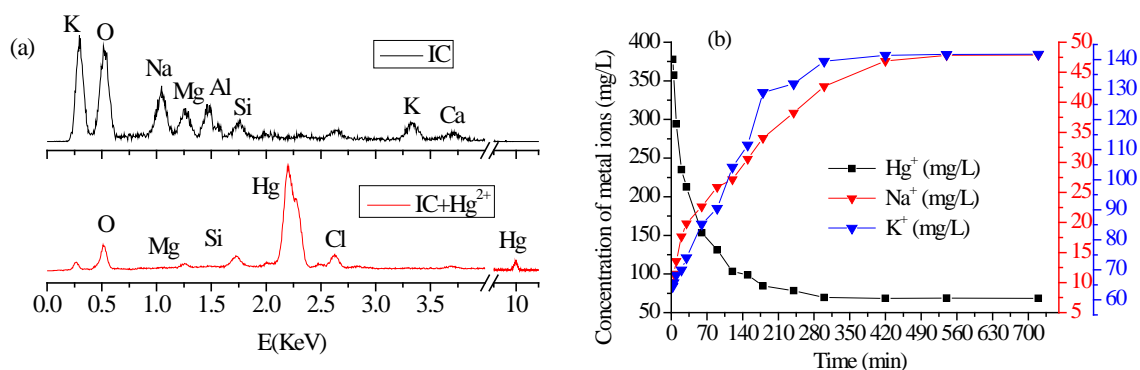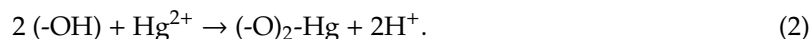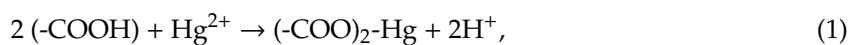

Figure 3. (**a**) EDS analysis before and after adsorption of Hg^{2+} by IC; (**b**) The concentration change of K^+, Na^+, and Hg^{2+} with oscillation time after adsorption of Hg^{2+} by IC.

3.5. Adsorption Mechanisms

All five biochar fractions have negatively charged surfaces and can adsorb positively charged Hg^{2+} via, for example, electrostatic effects (Table 1). According to the above analysis, the main adsorption mechanisms and contribution rates of Hg^{2+} adsorption by RC and its fractions were determined. Based on Table 3, the equilibrium adsorption amount of Hg^{2+} by RC is 75.56 mg/g. As calculated based on the mass fractions of IC and OC, the theoretical adsorption capacity of RC is 75.52 mg/g, which is very close to the measured value of 75.56 mg/g, indicating that the adsorption contribution rates of inorganic and organic components in RC account for approximately 22.4% and 77.6%, respectively. The main adsorption mechanism of RC and OC in the Hg^{2+} adsorption process is based on a complexation reaction, where oxygen-containing functional groups, such as –COOH and –OH groups, react with Hg^{2+} to form $(–COO)_2Hg$ and $(–O)_2Hg$ complexes. The complexation effects of RC and OC contribute

68.9% and 71.6%, respectively. In the complexation reaction of RC, the contribution rates of the adsorption by –COOH and –OH groups are 51.0% and 17.9%, respectively. The reaction formulae are as follows [17]:

$$2 \text{ (-COOH)} + Hg^{2+} \rightarrow \text{(-COO)}_2\text{-Hg} + 2H^+, \tag{1}$$

$$2 \text{ (-OH)} + Hg^{2+} \rightarrow \text{(-O)}_2\text{-Hg} + 2H^+. \tag{2}$$

IC has the maximum equilibrium capacity for Hg^{2+} adsorption of 92.63 mg/g. This may be due to the reduction of Hg^{2+} to Hg^+ and Hg^0 by $-\pi$ electrons and phenolic hydroxyl groups (36.4%), the complexation reaction between carboxyl/hydroxyl functional groups and Hg^{2+} (39.8%), and the ion exchange of Hg^{2+} and Hg^+ with K^+ and Na^+ (40.9%) occurring simultaneously. The main adsorption mechanism of IC is ion exchange, during which the ion exchange of Hg^+ and Hg^{2+} contributes 17.3% and 23.6%, respectively.

As shown in Table 3, the equilibrium capacities for Hg^{2+} adsorption by BHC and BCC are significantly lower compared to IC, being 66.30 and 61.13 mg/g, respectively. In addition, the calculated theoretical adsorption capacities of BHC and BCC, based on their mass fractions, are 65.96 and 61.43 mg/g, respectively, which are close to the measured values. The $-\pi$ electrons and phenolic hydroxyl groups on the surfaces of BHC and BCC reduce Hg^{2+} to Hg^+, and total reduction ratios take up 54.6% and 54.5%, respectively. According to the adsorption capacities of BHC and BCC, the adsorption contribution rates of the –COOH groups on BHC surface and the –OH functional groups on BCC surface are 20.4% and 12.3%, respectively. As for RC, –COOH and –OH groups contribute 51.0% and 17.9% respectively, to the total adsorption. The reason for this difference may be attributed to the presence of some –COOH and –OH functional groups remaining after the blocking of the biochar functional groups (Table 1).

Table 3. Contribution rate (%) and adsorption quantity of Hg^{2+} (mg/g) at equilibrium by biochars.

Biochars	Mass Percentage (%)	Adsorption Quantity of Hg^{2+} (mg/g)	Adsorption Mechanism	Adsorption Contribution Rate (%)
RC	100.0	75.56	Complexation with –COOH and –OH	68.9
			Reduction reaction	25.2
IC	22.4	92.63	Complexation with –COOH and –OH	39.8
			Reduction reaction	36.4
			Cation exchange	41.2
OC	77.6	70.57	Complexation with –COOH and –OH	71.6
			Reduction reaction	13.0
BHC	87.3	66.30	Complexation with –COOH	23.3
			Reduction reaction	54.6
BCC	81.3	61.13	Complexation with –OH	28.3
			Reduction reaction	54.5

The adsorption mechanisms of Hg^{2+} removal by RC include electrostatic adsorption, ion exchange, reduction, precipitation, and complexation. Among all adsorption mechanisms, the complexation reaction of –COOH/–OH groups with Hg^{2+} plays the dominating roles, and the adsorption contribution rate of –COOH functional groups is greater than that of –OH functional groups.

The adsorption capacity of Hg^{2+} by corn-straw-based biochar (75.56 mg/g) was found to be higher than some values reported in literature, such as 35.71 mg/g by sugarcane bagasse [13], 22.82 mg/g by peanut husk biochar [15], 19.30 mg/g by activated sludge biomass [19], and 24.20 mg/g by Brazilian pepper biochars [20]. It is, however, similar to the value determined for *Aspergillus versicolor* biomass (75.60 mg/g) [18], and slightly lower than the adsorption capacities reported for flax shive sorbent (89.50 mg/g) [9] and fruit shell of *Terminalia catappa* (82.93 mg/g) [11]. Moreover, the irreversible complexation reaction of –COOH/–OH groups with Hg^{2+} is the main adsorption

mechanism, which reduces the secondary pollution to aqueous solution even depositing it to the water bottom. Therefore, it is helpful to provide theoretical basis and data support for the special adsorption of functional adsorbents and has practical significance for the treatment of mercury pollution in water. In addition, by studying the adsorption mechanisms of biochar different fractions for Hg^{2+}, the contribution rate of each fraction of the adsorbent to Hg^{2+} was calculated, providing a certain theoretical basis for the research on the removal of Hg from biochar.

4. Conclusions

Except for OC, which is weakly acidic, the other four biochar fractions are basic (IC has the strongest basicity), and their pH values are significantly lower after Hg^{2+} adsorption. In addition, the pH values of all five biochar fractions are greater than their corresponding pH_{pzc} values. The surfaces of the biochar fractions are negatively charged and adsorb positively charged Hg^{2+}.

The equilibrium adsorption capacity of RC for Hg^{2+} is 75.56 mg/g, with IC and OC contributing 22.4% and 77.6%, respectively. IC has the largest equilibrium adsorption capacity of 92.63 mg/g, which may be due to all the adsorption mechanisms involved in the adsorption process. Moreover, the equilibrium adsorption capacities of BHC and BCC are significantly lower, being 66.30 and 61.13 mg/g, respectively.

There are five reaction mechanisms identified for Hg^{2+} removal by biochar: electrostatic adsorption, cation exchange, precipitation, reduction effect of $-\pi$ and phenolic hydroxyl groups, and complexation by $-OH$ and $-COOH$ groups. The main adsorption mechanism of RC and OC is the complexation of oxygen-containing functional groups with Hg^{2+}, accounting for 68.9% and 71.6%, respectively. The contribution rates of $-COOH$ and $-OH$ groups in RC complexation reaction are 51.0% and 17.9%, respectively, while those in OC complexation reaction are 64.6% and 7.0%, respectively. Among the five examined fractions, IC plays a major role in mercury adsorption by RC. All adsorption mechanisms identified are involved in the adsorption process by IC, with ion exchange being the main one, accounting for 39.8%. The reduction effect of phenolic hydroxyl groups and $-\pi$ electrons is the main mechanism for Hg^{2+} removal by BHC and BCC, taking up 54.6% and 54.5% of the total adsorption for each fragment, respectively. In addition, the adsorption contribution rates of $-COOH$ groups on BHC surface and $-OH$ functional groups on BCC surface are 20.4% and 12.3%, respectively. Among all the adsorption mechanisms, the complexation reaction of $-COOH/-OH$ groups with Hg^{2+} plays the dominating roles, and the adsorption contribution rate of $-COOH$ functional groups is greater than that of $-OH$ functional groups. These conclusions play a guiding role in the remediation mechanism of heavy metals by biochar in water. The prepared RC could be a promising low-cost adsorbent for the treatment of Hg^{2+}-contaminated water.

References

1. Lyu, H.H.; Xia, S.Y.; Tang, J.C.; Zhang, Y.R.; Cao, B.; Shen, B.X. Thiol-Modified biochar synthesized by a facile ball-milling method for enhanced sorption of inorganic Hg^{2+} and organic CH_3Hg^+. *J. Haz. Mater.* **2019**, *384*, 121357. [CrossRef] [PubMed]
2. Inbaraj, B.S.; Wang, J.; Lu, J.; Siao, F.; Chen, B. Adsorption of toxic mercury(II) by an extracellular biopolymer poly(γ-glutamic acid). *Bioresour. Technol.* **2009**, *100*, 200–207. [CrossRef]

3. Zhu, Y.C.; Peng, S.C.; Lu, P.P.; Chen, T.H.; Yang, Y. Mercury Removal from Aqueous Solutions Using Modified Pyrite: A Column Experiment. *Minerals* **2019**, *10*, 43. [CrossRef]

4. Mahmudov, R.; Huang, C.P. Selective adsorption of oxyanions on activated carbon exemplified by Filtrasorb 400 (F400). *Sep. Purif. Technol.* **2011**, *77*, 294–300. [CrossRef]

5. Wang, T.; Wu, J.W.; Zhang, Y.S.; Liu, J.; Sui, Z.F.; Zhang, H.C.; Chen, W.Y.; Norris, P.; Pan, W.P. Increasing the chlorine active sites in the micropores of biochar for improved mercury adsorption. *Fuel* **2018**, *229*, 60–67. [CrossRef]

6. Liu, Z.Y.; Yang, W.; Xu, W.; Liu, Y.X. Removal of elemental mercury by bio-chars derived from seaweed impregnated with potassium iodine. *Environ. Sci. Health* **2018**, *339*, 468–478. [CrossRef]

7. Xu, Y.L. *Thermodynamic Properties of Biochar Preparation and Sorption Characteristics and Mechanisms of Cadmium onto Biochars*; Zhejiang University: Hangzhou, China, 2013.

8. Zabihi, M.; Ahmadpour, A.; Haghighi, A.A. Removal of mercury from water by carbonaceous sorbents derived from walnut shell. *J. Hazard. Mater.* **2008**, *167*, 230–236. [CrossRef]

9. Cox, M.; El-Shafey, E.I.; Pichugin, A.A.; Appleton, Q. Removal of mercury (II) from aqueous solution on a carbonaceous sorbent prepared from flax shive. *J. Chem. Technol. Biotechnol.* **2000**, *75*, 427–435. [CrossRef]

10. Minaxi, B.; Lohani Amarika, S.; Rupainwar, D.C.; Dhar, D.N. Studies on efficiency of guava (Psidium guajava) bark as bioadsorbent for removal of Hg(II) from aqueous solutions. *J. Hazard. Mater.* **2008**, *159*, 626–629. [CrossRef]

11. Stephen Inbaraj, B.; Sulochana, N. Mercury adsorption on a carbon sorbent derived from fruit shell of Terminalia catappa. *J. Hazard. Mater.* **2005**, *133*, 283–290. [CrossRef]

12. El-Shafey, E.I. Removal of Zn(II) and Hg(II) from aqueous solution on a carbonaceous sorbent chemically prepared from rice husk. *J. Hazard. Mater.* **2009**, *175*, 319–327. [CrossRef] [PubMed]

13. Khoramzadeh, E.; Nasernejad, B.; Halladj, R. Mercury biosorption from aqueous solutions by Sugarcane Bagasse. *J. Taiwan Inst. Chem. Eng.* **2013**, *44*, 266–269. [CrossRef]

14. Johari, K.; Saman, N.; Song, S.T.; Chin, C.S.; Kong, H.; Mat, H. Adsorption enhancement of elemental mercury by various surface modified coconut husk as eco-friendly low-cost adsorbents. *Int. Biodeter. Biodegr.* **2016**, *109*, 45–52. [CrossRef]

15. Xue, Y.W.; Gao, B.; Yao, Y.; Inyang, M.D.; Zhang, M.; Zimmerman, A.R.; Ro, K.S. Hydrogen peroxide modification enhances the ability of biochar (hydrochar) produced from hydrothermal carbonization of peanut hull to remove aqueous heavy metals: Batch and column tests. *Chem. Eng. J.* **2012**, *200*, 673–680. [CrossRef]

16. Li, H.B.; Dong, X.L.; da Silva, E.B.; de Oliveira, L.M.; Chen, Y.; Ma, L.Q. Mechanisms of metal sorption by biochars: Biochar characteristics and modifications. *Chemosphere* **2017**, *178*, 466–478. [CrossRef]

17. Kong, H.; He, J.; Gao, Y.; Wu, H.; Zhu, X. Cosorption of phenanthrene and mercury(II) from aqueous solution by soybean stalk-based biochar. *J. Agric. Food. Chem.* **2011**, *59*, 12116–12123. [CrossRef]

18. Das, S.K.; Das, A.R.; Guha, A.K. A study on the adsorption mechanism of mercury on Aspergillus versicolor biomass. *Environ. Sci. Technol.* **2007**, *41*, 8281–8287. [CrossRef]

19. Kílíç, M.; Keskin, M.E.; Mazlum, S.; Mazlum, N. Hg(II) and Pb(II) adsorption on activated sludge biomass: Effective biosorption mechanism. *Int. J. Miner. Process.* **2008**, *87*, 1–8. [CrossRef]

20. Dong, X.L.; Ma, L.Q.; Zhu, Y.J.; Li, Y.C.; Gu, B. Mechanistic investigation of mercury sorption by Brazilian pepper biochars of different pyrolytic temperatures based on X-ray photoelectron spectroscopy and flow calorimetry. *Environ. Sci. Technol.* **2013**, *47*, 12156–12164. [CrossRef]

21. Gardea-Torresdey, J.L.; Becker-Hapak, M.K.; Hosea, J.M.; Darnall, D.W. Effect of chemical modification of algal carboxyl groups on metal ion binding. *Environ. Sci. Technol.* **1990**, *24*, 1372–1378. [CrossRef]

22. Chen, J.P.; Yang, L. Study of a heavy metal biosorption onto raw and chemically modified Sargassum sp. via spectroscopic and modeling analysis. *Langmuir* **2006**, *22*, 8906–8914. [CrossRef] [PubMed]

23. Lu, H.L.; Zhang, W.H.; Yang, Y.X.; Huang, X.; Wang, S.; Qiu, R. Relative distribution of Pb^{2+} sorption mechanisms by sludge-derived biochar. *Water Res.* **2012**, *46*, 854–862. [CrossRef] [PubMed]

24. Wang, Z.Y.; Liu, G.C.; Zheng, H.; Li, F.M.; Ngo, H.H.; Guo, W.S.; Liu, C.; Chen, L.; Xing, B.S. Investigating the mechanisms of biochar's removal of lead from solution. *Bioresour. Technol.* **2015**, *177*, 308–317. [CrossRef] [PubMed]

25. Ofomaja, A.E.; Naidoo, E.B.; Modise, S.J. Removal of copper(II) from aqueous solution by pine and base modified pine cone powder as biosorbent. *J. Hazard. Mater.* **2009**, *168*, 909–917. [CrossRef]

26. Boehm, H.P. Some aspects of the surface chemistry of carbon blacks and other carbons. *Carbon* **1994**, *32*, 759–769. [CrossRef]

27. Goertzen, S.L.; Thériault, K.D.; Oickle, A.M.; Tarasuk, A.C.; Andreas, H.A. Standardization of the Boehm titration. Part, I. CO_2 expulsion and endpoint determination. *Carbon* **2010**, *48*, 1252–1261. [CrossRef]

28. Lehmann, J. A handful of carbon. *Nature* **2007**, *447*, 143–144. [CrossRef] [PubMed]

29. Shaaban, A.; Se, S.M.; Dimin, M.F.; Juoi, J.M.; Mohd Husin, M.H.; Mitan, N.M.M. Influence of heating temperature and holding time on biochars derived from rubber wood sawdust via slow pyrolysis. *J. Anal. Appl. Pyrol.* **2014**, *107*, 31–39. [CrossRef]

30. Sari, A.; Tuzen, M. Removal of mercury (II) from aqueous solution using moss (Drepanocladus revolvens) biomass: Equilibrium, thermodynamic and kinetic studies. *J. Hazard. Mater.* **2009**, *171*, 500–507. [CrossRef]

31. Jia, M.Y.; Wang, F.; Bian, Y.R.; Jin, X.; Song, Y.; Kengara, F.O.; Xu, R.K.; Jiang, X. Effects of pH and metal ions on oxytetracycline sorption to maize-straw-derived biochar. *Bioresour. Technol.* **2013**, *136*, 87–93. [CrossRef]

32. Tüzün, İ.; Bayramoğlu, G.; Yalçın, E.; Başaran, G.; Celik, G.; Arica, M.Y. Equilibrium and kinetic studies on biosorption of Hg(II), Cd(II) and Pb(II) ions onto microalgae Chlamydomonas reinhardtii. *J. Environ. Manag.* **2005**, *77*, 85–92. [CrossRef]

33. Walcarius, A.; Delacôte, C. Mercury(II) binding to thiol-functionalized mesoporoussilicas: Critical effect of pH and sorbent properties on capacity and selectivity. *Anal. Chim. Acta* **2005**, *547*, 3–13. [CrossRef]

34. Thy, P.; Jenkins, B.M.; Grundvig, S.; Shiraki, R.; Lesher, C. High temperature elemental losses and mineralogical changes in common biomass ashes. *Fuel* **2006**, *85*, 783–795. [CrossRef]

35. Yardim, M.F.; Budinova, T.; Ekinci, E.; Petrov, N.; Razvigorova, M.; Minkova, V. Removal of mercury(II) from aqueous solution by activated carbon obtained from furfural. *Chemosphere* **2003**, *52*, 835–841. [CrossRef]

36. Dougherty, D.A. The cation -π interaction. *Acc. Chem. Res.* **2012**, *46*, 885–893. [CrossRef] [PubMed]

37. Tang, L.; Yang, G.D.; Zeng, G.M.; Cai, Y.; Li, S.S.; Zhou, Y.Y.; Pang, Y.; Liu, Y.Y.; Zhang, Y.; Luna, B. Synergistic effect of iron doped ordered mesoporous carbon on adsorption-coupled reduction of hexavalent chromium and the relative mechanism study. *Chem. Eng. J.* **2014**, *239*, 114–122. [CrossRef]

38. Chen, T.; Zhang, Y.; Wang, H.; Lu, W.; Zhou, Z.; Zhang, Y.; Ren, L. Influence of pyrolysis temperature on characteristics and heavy metal adsorptive performance of biochar derived from municipal sewage sludge. *Bioresour. Technol.* **2014**, *164*, 47–54. [CrossRef] [PubMed]

39. Lammers, K.; Arbuckle-Keil, G.; Dighton, J. FT-IR study of the changes in carbohydrate chemistry of three New Jersey pine barrens leaf litters during simulated control burning. *Soil Biol. Biochem.* **2009**, *41*, 340–347. [CrossRef]

40. Herrero, R.; Lodeiro, P.; Rey-Castro, C.; Vilariño, T.; Sastre de Vicente, M.E. Removal of inorganic mercury from aqueous solutions by biomass of the marine macroalga Cystoseira baccata. *Water Res.* **2005**, *39*, 3199–3210. [CrossRef]

41. Zhang, S.; Yang, X.; Ju, M.T.; Liu, L.; Zheng, K. Mercury adsorption to aged biochar and its management in China. *Environ. Sci. Pollut. Res.* **2019**, *26*, 4867–4877. [CrossRef]

42. Goyal, M.; Bhagat, M.; Dhawan, R. Removal of mercury from water by fixed bed activated carbon columns. *J. Hazard. Mater.* **2009**, *171*, 1009–1015. [CrossRef] [PubMed]

43. Carro, L.; Anagnostopoulos, V.; Lodeiro, P.; Barriada, J.L.; Herrero, R.; Sastre de Vicente, M.E. A dynamic proof of mercury elimination from solution through a combined sorption-reduction process. *Bioresour. Technol.* **2010**, *101*, 8969–8974. [CrossRef] [PubMed]

44. Pulido-Novicio, L.; Kurimoto, Y.; Aoyama, M.; Seki, K.; Doi, S.; Hata, T.; Ishihara, S.; Imamura, Y. Adsorption of mercury by sugi wood carbonized at 1000 °C. *J. Wood Sci.* **2001**, *47*, 159–162. [CrossRef]

45. Park, J.H.; Wang, J.J.; Zhou, B.; Mikhael, J.E.R.; DeLaune, R.D. Removing mercury from aqueous solution using sulfurized biochar and associated mechanisms. *Environ. Pollut.* **2018**, *244*, 627–635. [CrossRef]

46. Bond, A.M.; Miao, W.; Raston, C.L. Mercury(II) immobilized on carbon nanotubes: Synthesis, characterization, and redox properties. *Langmuir* **2000**, *16*, 6004–6012. [CrossRef]

47. Behra, P.; Bonnissel-Gissinger, P.; Alnot, M.; Revel, R.; Ehrhardt, J.J. XPS and XAS study of the sorption of Hg(II) onto pyrite. *Langmuir* **2001**, *17*, 3970–3979. [CrossRef]

48. Manivannan, S.; Park, S.; Jeong, J.; Kim, K. Aggregation-Free optical and colorimetric detection of Hg(II) with M13 bacteriophage-templated Au nanowires. *Biosens. Bioelectron.* **2020**, *161*, 112237. [CrossRef] [PubMed]

49. Wang, J.; Deng, B.L.; Chen, H.; Wang, X.R.; Zheng, J.Z. Removal of aqueous Hg(II) by polyaniline: Sorption characteristics and mechanisms. *Environ. Sci. Technol.* **2009**, *43*, 5223–5228. [CrossRef]

50. Hyland, M.M.; Jean, G.E.; Bancroft, G.M. XPS and AES studies of Hg(II) sorption and desorption reactions on sulphide minerals. *Pergamon* **1990**, *54*, 1957–1967. [CrossRef]

51. Xu, X.Y.; Ariette, S.; Xu, N.; Cao, X.D. Comparison of the characteristics and mechanisms of Hg(II) sorption by biochars and activated carbon. *J. Colloid Interf. Sci.* **2016**, *463*, 55–60. [CrossRef]

52. Carro, L.; Barriada, J.L.; Herrero, R.; Sastre de Vicente, M.E. Adsorptive behavior of mercury on algal biomass: Competition with divalent cations and organic compounds. *J. Hazard. Mater.* **2011**, *192*, 284–291. [CrossRef] [PubMed]

Removal Efficiencies of Manganese and Iron Using Pristine and Phosphoric Acid Pre-Treated Biochars Made from Banana Peels

Hyunjoon Kim [1,†], Ryun-Ah Ko [1,†], Sungyun Lee [2,*] and Kangmin Chon [1,*]

[1] Department of Environmental Engineering, College of Engineering, Kangwon National University, Kangwondaehak-gil, 1, Chuncheon-si, Gangwon-do 24341, Korea; guswns863@naver.com (H.K.); rh6468@naver.com (R.-A.K.)

[2] Department of Civil Environmental Engineering, School of Disaster Prevention and Environmental Engineering, Kyungpook National University, 2559, Gyeongsang-daero, Sangju-si, Gyeongsangbuk-do 37224, Korea

* Correspondence: sungyunlee@knu.ac.kr (S.L.); kmchon@kangwon.ac.kr (K.C.);
  Tel.: +82-54-530-1446 (S.L.); +82-33-250-6352 (K.C.)

† These authors contributed equally to this work and should be considered as co-first authors.

Abstract: The purpose of this study was to compare the removal efficiencies of manganese (Mn) and iron (Fe) using pristine banana peel biochar (BPB) and phosphoric acid pre-treated biochars (PBPB) derived from banana peels. The removal efficiencies of Mn and Fe were investigated under different adsorbent dosages (0.4–2 g L^{-1}), temperatures (15–45 °C), and ionic strengths (0–0.1 M), and were directly correlated to the differences in physicochemical properties of BPB and PBPB, to identify the removal mechanisms of heavy metals by adsorption processes. The removal of Mn by PBPB obeyed the Freundlich isotherm model while the removal of Mn and Fe by BPB followed the Langmuir isotherm model. However, the removal of Fe by PBPB followed both Freundlich and Langmuir isotherm models. The removal efficiencies of Mn and Fe by BPB and PBPB increased with increasing temperatures and decreased with increasing ionic strengths. PBPB more effectively removed Mn and Fe compared to BPB due to its higher content of oxygen-containing functional groups (O/C ratio of PBPB = 0.45; O/C ratio of BPB = 0.01), higher surface area (PBPB = 27.41 m^2 g^{-1}; BPB = 11.32 m^2 g^{-1}), and slightly greater pore volume (PBPB = 0.03 cm^3 g^{-1}; BPB = 0.027 cm^3 g^{-1}). These observations clearly show that phosphoric acid pre-treatment can improve the physicochemical properties of biochar prepared from banana peels, which is closely related to the removal of heavy metals by adsorption processes.

1. Introduction

Water pollution by heavy metals released from various industrial activities such as metal plating and cleaning, mining, refineries, coatings, batteries, and automobile radiators, is an emerging environmental issue in water treatment engineering since heavy metals may pose adverse effects on human health and aquatic ecosystems due to their high toxicity, carcinogenicity, and non-biodegradability [1,2]. Among various heavy metals used in industrial activities, manganese (Mn) and iron (Fe) are known to be major inorganic pollutants affecting water quality [3]. Although Mn is essential to activate enzymes in the human system, high Mn concentrations can generate respiratory diseases, and continuous administration can cause neurotoxicity risk in humans [3,4]. In the case of Fe, it can cause undesirable aesthetic concerns (i.e., metallic tastes) and lead to the growth of ferrobacteria

related to odor problems [3]. The World Health Organization (WHO) have set a safe drinking water concentration of 0.05 and 0.3 mg L^{-1} for Mn and Fe, respectively [5]. Based on these reasons, there is great need to develop an economic and efficient method for removing heavy metals from wastewater.

Several treatment techniques, including membrane filtration (e.g., reverse osmosis and nanofiltration), chemical precipitation, and oxidation/reduction, are available for the removal of heavy metals, including Mn and Fe, from industrial wastewater [6–10]. A commonly practiced Mn and Fe treatment approach is to chemically oxidize dissolved Mn(II) to particulate Mn(IV) or dissolved Fe(II) to particulate Fe(III), followed by physical separation of the insoluble precipitates from water using clarification and filtration processes [9,11]. However, most of those are not applicable for wastewater treatment due to their low removal efficiencies when the heavy metal concentrations are lower than 100 mg L^{-1} [12]. In contrast, activated carbon may effectively remove heavy metals from wastewater even at low concentrations [13]. Despite this advantage, the use of the activated carbon adsorption process for the removal of heavy metals has been limited as it requires high maintenance and operational costs [14]. In recent years, biochars, which can be produced at low cost, have attracted great attention as an alternative to activated carbon [15–18]. Biochar is an ecofriendly adsorbent produced using by-products of the agricultural industries and wastes from various crops, and is effective for removing heavy metals from wastewater [18–21].

Over the wide range of crops, bananas cultivated in more than 130 countries are regarded to be one of the most widely grown tropical fruits in the world [22]. The world production of bananas was approximately 117.9 million tons in 2015 [23], and about 7 million tons of banana peel wastes are produced annually (the proportion of banana peels in total dry weight = 25–30%) [24]. Currently, most banana peel wastes are used as natural fertilizers on soils in agricultural fields, and some of them are fed to animals [25]. Banana peels contain a large amount of pectins which are complex polysaccharides consisting of galacturonic acids, arabinoses, galactoses, and rhamnoses. Among them, galacturonic acids have a strong binding capacity to the metal cations in the aqueous phases due to the presence of carboxyl groups [22,26]. Therefore, biochar derived from banana peels is considered to be a promising option for removing heavy metals effectively from wastewater.

Raw biochars have showed feasibility for adsorbent material to remove contaminants including heavy metals and organic pollutants [17,18,21,27,28]. However, the sorption capacities can be enhanced by treatment with acids, nanocomposites, and activation agents [17,29,30]. For example, Chu et al. showed that phosphoric acid treatment improved the porosity of biochars from pine sawdust, cellulose, and lignin [31]. The modified biochars provided better sorption of carbamazepine and bisphenol A. The sorption for 15 different pesticides by biochars from rice straw and corn stover was also increased by phosphoric acid treatment due to increased functional groups and aromatization of the biochars [32]. Considering the effects of phosphoric acid treatment on porosity and the modification of functional groups of biochars, the treatment method can be applied to improve removal efficiencies of heavy metals by biochars from other sources. In addition, phosphoric acid has advantages in low pyrolysis temperature, low cost, and low corrosivity to the equipment [31]. Nevertheless, to the best of our knowledge, phosphoric acid pre-treatment has not been used to enhance the physicochemical properties of biochars from banana peels in association with the adsorption of heavy metals.

The main purpose of this study was to evaluate the effects of phosphate pre-treatment on the adsorption of heavy metals (i.e., Mn and Fe) using biochars prepared from banana peels. First, the physicochemical characteristics of pristine and phosphoric acid pre-treated biochars derived from banana peels were rigorously characterized. Then, various adsorption experiments were conducted to investigate optimum adsorbent dosages, adsorption kinetics, adsorption isotherms, and effects of temperature and ionic strengths on adsorption. The improved adsorption efficiencies by phosphoric acid treatment were analyzed based on the physicochemical characteristics of the biochar, and the adsorption mechanisms of Mn and Fe were discussed. This study improves our understanding of the effect of phosphoric acid treatment on modification of the surface structure and functional groups of biochars for heavy metal removal.

2. Materials and Methods

2.1. Materials

Banana peel wastes were collected in Chuncheon-si (Gangwon-do, Korea). Mn (KMnO$_4$, oxidation state = +7, concentration = 1000 mg L^{-1}) and Fe (Fe(NH$_4$)$_2$·(SO$_4$)$_2$, oxidation state = +2, concentration = 1000 mg L^{-1}) AA standard solutions and phosphoric acid (H$_3$PO$_4$), were purchased from Daejung Chemicals & Metals (Siheung-Si, Gyeonggi-Do, Korea). Mn(VII) and Fe(II) solutions for adsorption experiments were prepared by diluting the concentrated standard solutions in deionized water.

2.2. Production of Biochar

The banana peel wastes were dried in an oven at 105 °C for 24 h, ground using a mortar, washed several times with deionized (DI) water to remove impurities on their surfaces, and then dried in the oven at 105 °C for 12 h. From the resulting banana peel powder, 50 g was immersed in a 500 mL phosphoric acid solution (20 wt. %) for 2 h to activate adsorption sites, and dried at 105 °C for 12 h. Pristine and phosphoric acid pre-treated banana peel wastes (weight of each banana peel waste = 20 g) were pyrolyzed in the tubular furnace (PyroTech, Namyangju, Gyeonggi-do, Korea) at 600 °C (heating rates = 0.2 °C min^{-1}) under N$_2$ conditions (N$_2$ flow rate = 0.25 L min^{-1}) for 2 h and then cooled to room temperature. Biochars prepared from banana peel wastes were washed several times with DI water, filtered with a 0.7 μm GF/F filter (Whatman, Maidstone, UK), and then dried in the oven at 105 °C for 12 h. Biochars produced from pristine and phosphoric acid pre-treated banana peel wastes are defined as BPB (banana peel biochar without pre-treatment) and PBPB (pre-treated banana peel biochar), respectively.

2.3. Characterization of Biochar

Element composition of BPB and PBPB was analyzed using an elemental analyzer (EuroEA3000 CHNS-O, Euro Vector S.p.A, Via Tortona, Milan, Italy). The ash content was calculated by subtracting the quantities of carbon (C), hydrogen (H), nitrogen (N), and oxygen (O) from the total mass fraction of the adsorbents. The specific surface area of biochar was determined with a Bronauer–Emmett–Teller (BET) analyzer (BELSORP-mini II, MicrotracBEL, Japan). The functional group composition of the adsorbents was identified using attenuated total reflectance-Fourier transform infrared spectroscopy (ATR-FTIR) (Frontier Optica, Perkin Elmer, Waltham, MA, USA).

2.4. Adsorption Experiments

2.4.1. Optimal Adsorbent Dosages

Prior to the adsorption kinetics experiments, the optimum dosage of BPB and PBPB for each heavy metal was determined. The adsorbents (dosage = 0.02–4 g L^{-1}) were added to 25 mL of heavy metal solution (each metal concentration = 10 mg L^{-1}, pH = 7.0) and then mixed at 150 rpm and 25 °C using a shaking incubator (VS-8480, Vision Scientific, Daejeon-Si, Korea) for 3 h. All the adsorption tests were repeated three times to minimize experimental errors.

2.4.2. Adsorption Kinetics Analysis

For adsorption kinetics experiments, the optimum dosage of each adsorbent was added to 25 mL of sample solutions (each heavy metal concentration = 10 mg L^{-1}) and mixed at 150 rpm using the shaking incubator for 0–24 h (temperature = 25 °C, pH = 7.0). The concentrations of Mn and Fe at the initial and equilibrium states were measured using colorimetric methods with a UV-Vis spectrophotometer (UV-1280, Shimadzu, Kyoto, Japan) at UV absorbances of 525 and 510 nm, respectively. All the

adsorption tests were repeated three times to minimize experimental errors. The amount of adsorbed heavy metals at time t (q_t (mg g^{-1})) was calculated as follows [14]:

$$q_t = \frac{(C_0 - C)V}{m} \tag{1}$$

where C_0 and C are the initial and final concentrations (mg L^{-1}) of heavy metals in the solutions, V is the volume (L) of the solution, and m is the mass (g) of the used adsorbents.

The removal efficiencies of heavy metals were calculated using Equation (2) [14]:

$$\text{Removal efficiency of heavy metal (\%)} = \frac{(C_0 - C_e)}{C_0} \times 100 \tag{2}$$

where C_e represents the concentrations of each heavy metal (mg L^{-1}) at equilibrium of the solutions.

The adsorption kinetics of Mn and Fe were investigated using Equations (3) and (4):

$$\text{Pseudo-first-order model}: \quad \log(q_e - q_t) = \log(q_e) - \frac{k_1 t}{2.303} \tag{3}$$

$$\text{Pseudo-second-order model}: \quad \frac{t}{q_t} = \frac{1}{k_2 q_e^2} + \frac{t}{q_e} \tag{4}$$

where k_1 (min^{-1}) is the constant of the pseudo-first-order equation, and k_2 (g mg^{-1} min^{-1}) is the constant of the pseudo-second-order equation. q_e (mg g^{-1}) is the adsorption capacity at equilibrium.

2.4.3. Adsorption Isotherm Analysis

The adsorption isotherms of Mn and Fe by BPB and PBPB were identified with 6 different initial concentrations (each heavy metal concentration = 1–10 mg L^{-1}) under controlled conditions (agitation time = 24 h, mixing speed = 150 rpm, temperature = 25 °C, pH = 7.0). The adsorption results were analyzed using the Langmuir and Freundlich isotherm models.

$$\text{Langmuir isotherm}: \quad q_e = \frac{q_{max} K_L c_e}{1 + K_L c_e} \tag{5}$$

where q_e (mg g^{-1}) is the maximum monolayer adsorption capacity of heavy metals, and K_L (L mg^{-1}) is the equilibrium constant of the Langmuir equation.

$$\text{Freundlich isotherm}: \quad q_e = K_F c_e^{1/n} \tag{6}$$

where K_F (mg$^{1-(1/n)}$ L$^{1/n}$ g^{-1}) is the Freundlich adsorption constant, and n is the dimensionless empirical coefficient related to adsorption strength, which depends on the surface heterogeneity.

2.4.4. Effects of Temperatures and Ionic Strengths

The effects of temperature and ionic strength on the adsorption of heavy metals by BPB and PBPB were investigated at various temperatures (15–45 °C) and ionic strength conditions (0.005–0.1 M) (each heavy metal concentration = 10 mg L^{-1}, agitation time = 6 h, mixing speed = 150 rpm, temperature = 25 °C, pH = 7.0). The removal efficiencies of Mn and Fe using BPB and PBPB were calculated using Equations (2) and (3) as described in the previous section.

3. Results and Discussion

3.1. Physical Properties of Biochar

Figure 1 illustrates the functional group composition of BPB and PBPB, measured using ATR-FTIR. The functional group composition of BPB and PBPB was similar, but the intensities of the IR peaks of

the functional group composition affecting the adsorption of heavy metals were different. The IR peaks related to O-H stretching and C-O stretching of alcohols appeared at 3500–3000 cm^{-1} (BPB = 3443 cm^{-1}, PBPB = 3431 cm^{-1}) and 1210–1100 cm^{-1} (BPB = 1103 cm^{-1}, PBPB = 1180 cm^{-1}) due to the presence of alcohol functional groups (-CH$_2$OH-) derived from the cellulose component of the banana peels [33]. The IR peaks related to N-H stretching of amides were found in the range of 1650–1550 cm^{-1} (BPB = 1565 cm^{-1}, PBPB = 1575 cm^{-1}). Furthermore, C-H stretching of alkanes and C-H stretching of aromatics exhibited relatively strong IR peaks in the range of 1500–1300 cm^{-1} and 900–670 cm^{-1}, respectively [34]. The IR peak derived from C-O stretching of alcohols exhibited a relatively high IR intensity in PBPB compared to BPB in the range of 1210–1100 cm^{-1} because the phosphoric acid pre-treatment promoted the formation of oxygen-containing functional groups closely associated with the adsorption of heavy metals [34,35].
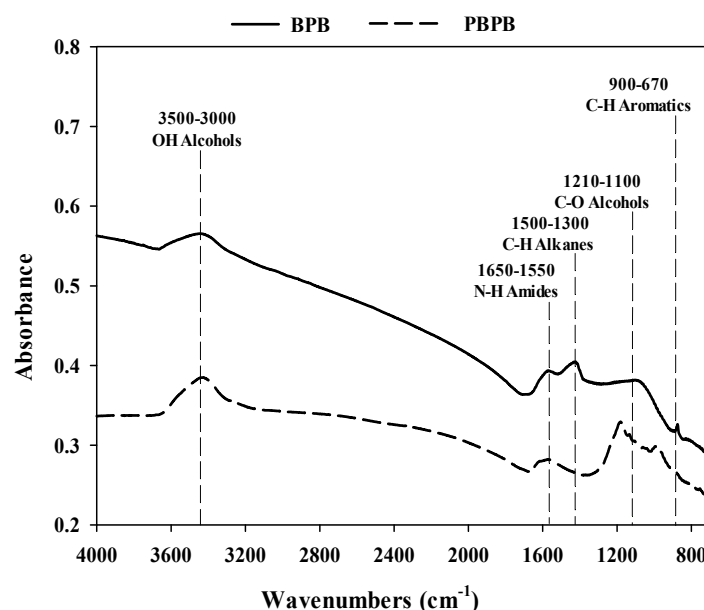
Figure 1. Attenuated total reflectance (ATR)-FTIR spectra of banana peel biochar without pre-treatment (BPB) and pre-treated banana peel biochar (PBPB).

Table 1 shows the elemental composition and surface properties of BPB and PBPB. Although the hydrogen, nitrogen, and ash content of BPB and PBPB were similar (H content of BPB = 1.6%, H content of PBPB = 1.9%; N content of BPB = 2.9%, N content of PBPB = 2.2%; ash content of BPB = 19.0%, ash content of PBPB = 16.4%), PBPB had lower carbon content (54.7%) and higher oxygen content (24.8%) compared to BPB (C content = 75.4%, O content = 1.1%). Therefore, the H/C, O/C, and N/C ratios of PBPB were much higher than those of BPB. These observations indicate that increases in hydroxyl and carboxyl functional groups in PBPB after phosphoric acid pre-treatment may enhance electrostatic attractions between heavy metals and the adsorbent surfaces intimately related to the adsorption of heavy metals [36]. Furthermore, the specific surface area and total pore volume of PBPP (specific surface area = 27.41 m^2 g^{-1}; total pore volume = 0.032 cm^3 g^{-1}) were considerably greater compared to BPB (BPB = 11.32 m^2 g^{-1}; total pore volume = 0.027 cm^3 g^{-1}). These results suggest that heavy metals can be adsorbed more readily by PBPB than BPB due to its abundance of adsorption sites [12].

Table 1. Physicochemical properties of BPB and PBPB.

	Elements Composition (%)					Atomic Ratio			S_{BET} (m^2 g^{-1})	Pore Volume (cm^3 g^{-1})
	C	H	O	N	Ash	H/C	O/C	N/C		
BPB	75.4	1.6	1.1	2.9	19.0	0.022	0.014	0.038	11.32	0.027
PBPB	54.7	1.9	24.8	2.2	16.4	0.035	0.453	0.039	27.41	0.032

3.2. Effects of Adsorbent Dosages

Figure 2 presents the change in the removal efficiencies of Mn and Fe as a function of adsorbent dosages. The removal efficiencies of Mn and Fe using BPB and PBPB were increased with increasing adsorbent dosages because of the increased availability of adsorption sites on the adsorbent surfaces [14]. The lower removal efficiencies of Mn by BPB and PBPB compared to those of Fe might be attributed to differences in the electronegativity and ion radius of Mn and Fe. Since Fe has a higher electronegativity than Mn (Fe = 1.8, Mn = 1.5) and a small ion radius, it can more easily diffused into the pores of PBPB and BPB [37,38]. In the equilibrium state, PBPB exhibited higher removal efficiencies of Mn and Fe than BPB (removal efficiency of Mn by BPB = 32%, removal efficiency of Mn by PBPB = 46%, removal efficiency of Fe by PBPB = 96%, removal efficiency of Fe by BPB = 85%). These results mean that phosphate pre-treatment promoted the formation of functional groups on the biochar surfaces capable of adsorbing heavy metals [27,39]. The removal efficiencies of Mn by BPB and PBPB reached the steady state at an adsorbent dosage of 3 g L^{-1} while the steady states of Fe adsorption occurred at 0.1 g L^{-1} for BPB and 0.3 g L^{-1} for PBPB, respectively. Hence, the PBPB and BPB dosages obtained at their steady states for Mn and Fe were applied for further adsorption experiments.
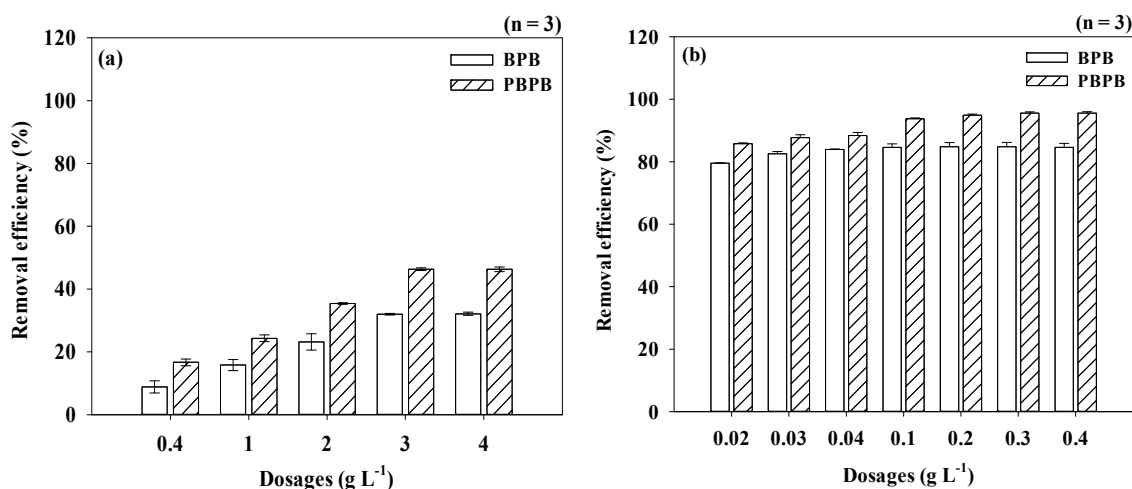

Figure 2. Effects of biochar dosages on the adsorption of heavy metals using BPB and PBPB: (**a**) Mn and (**b**) Fe (agitation time = 3 h, agitation speed = 150 rpm, initial concentration of Mn and Fe = 10 mg L^{-1}, pH = 7, and temperature = 25 °C).

3.3. Adsorption Kinetics of Mn and Fe

Figure 3 depicts the adsorption kinetics of Mn and Fe by BPB and PBPB. The adsorption proceeded rapidly in the beginning for both heavy metals (Mn ≤360 min; Fe ≤180 min) and almost reached equilibrium at 10 h. A possible explanation for these results is that the availability of adsorption sites plays key roles in the adsorption of Fe and Mn by BPB and PBPB [19]. Table 2 presents the kinetic model parameters for the adsorption of Mn and Fe by BPB and PBPB. Based on the correlation coefficient values (R^2), the pseudo-second-order model better described the adsorption of Mn and Fe by BPB and PBPB than the pseudo-first-order model. These observations indicate that the adsorption of Mn and Fe by BPB and PBPB is predominantly governed by chemical adsorption (i.e., covalent

bonding or ion/electron exchange) [27]. As shown in Figure 3, the adsorption capacities at equilibrium (q_e) of Mn and Fe by BPB were 1.14 and 31.61 mg g^{-1}, respectively. Meanwhile, the q_e of Mn and Fe by PBPB were 2.03 and 32.99 mg g^{-1}, respectively. The higher q_e values by PBPB support the assumption that PBPB is more effective for the adsorption of heavy metals than BPB due to its higher content of oxygen-containing functional groups [34,35].
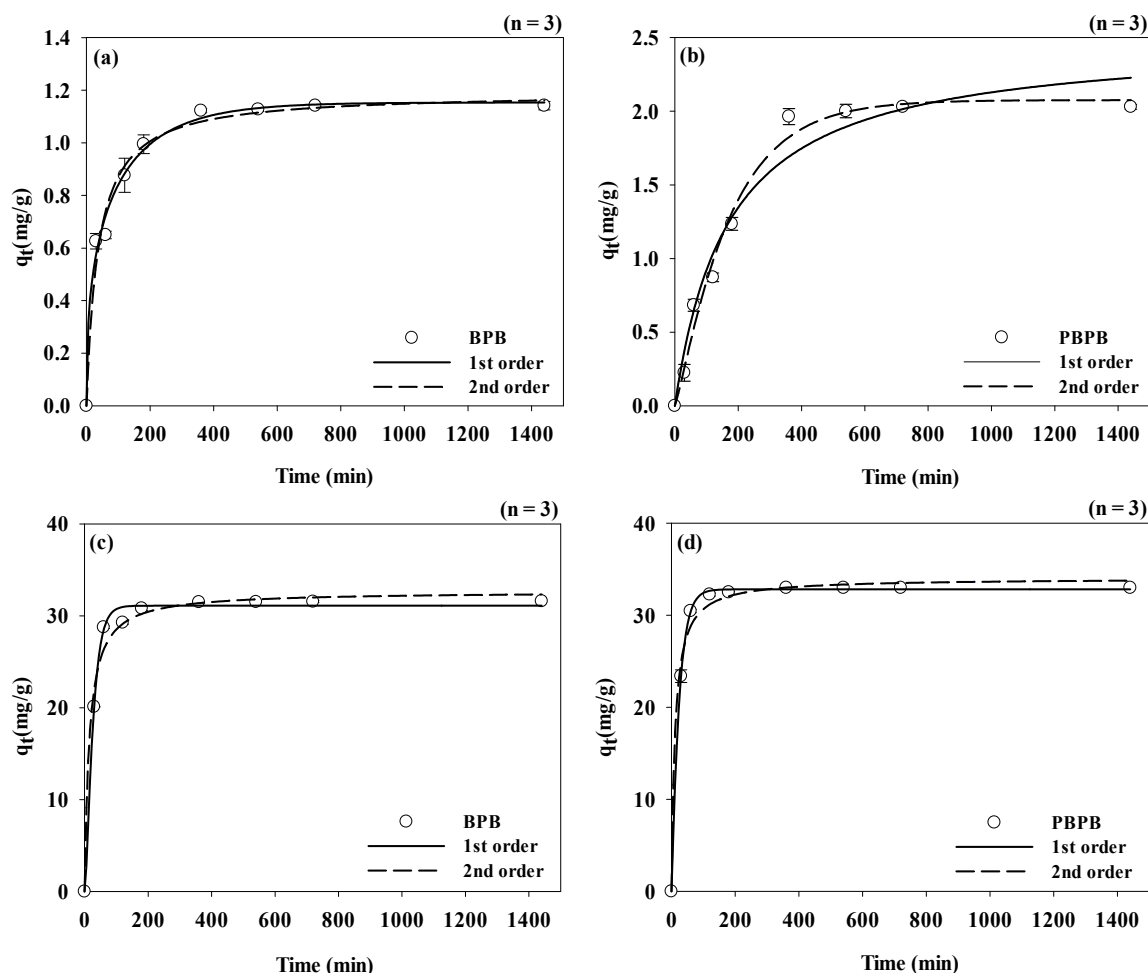

Figure 3. Adsorption kinetics of heavy metals onto BPB and PBPB: (**a**,**b**) Mn and (**c**,**d**) Fe (agitation time = 24 h, agitation speed = 150 rpm, adsorbent dosage of BPB and PBPB for Mn = 3 g L^{-1}, adsorbent dosage of BPB for Fe = 0.1 g L^{-1}, adsorbent dosage of PBPB for Fe = 0.3 g L^{-1}, initial concentration of Mn and Fe = 10 mg L^{-1}, pH = 7, and temperature = 25 °C).

Table 2. Kinetic model parameters for the adsorption of Mn and Fe by BPB and PBPB (n = 3).

			k	R^2
BPB	Mn	First-order (min^{-1})	0.008	0.944
		Second-order (g mg^{-1} min^{-1})	0.029	0.999
	Fe	First-order (min^{-1})	0.007	0.867
		Second-order (g mg^{-1} min^{-1})	0.004	0.999
PBPB	Mn	First-order (min^{-1})	0.009	0.965
		Second-order (g mg^{-1} min^{-1})	0.003	0.977
	Fe	First-order (min^{-1})	0.019	0.892
		Second-order (g mg^{-1} min^{-1})	0.006	0.999

3.4. Adsorption Isotherms of Mn and Fe

The adsorption mechanisms of Mn and Fe by BPB and PBPB were analyzed using the Langmuir and Freundlich adsorption isotherm models (Figure 4 and Table 3). The Langmuir isotherm model was well-fitted to the adsorption of Mn and Fe by BPB (R^2 of Mn = 0.972, R^2 of Fe = 0.869). These results imply that monolayer adsorption is responsible for the adsorption of Mn and Fe by BPB [7]. The adsorption of Mn by PBPB followed the Freundlich isotherm model (R^2 = 0.993) more closely than the Langmuir isotherm model (R^2 = 0.898). It is evident that multilayer adsorption strongly contributes to the adsorption of Mn by PBPB [13]. However, the adsorption of Fe by PBPB followed both Freundlich (R^2 = 0.933) and Langmuir isotherms (R^2 = 0.949). The n value of the Freundlich isotherm model was used to examine the adsorption affinity of Mn and Fe onto BPB and PBPB (Table 3): (i) n > 1 (favorable), (ii) n = 1 (linear), and (iii) n < 1 (unfavorable) [30]. The adsorption of Mn and Fe by BPB (n value of Mn = 7.267, n value of Fe = 1.069) and the adsorption of Mn by PBPB (n value = 2.471) were favorable whereas the adsorption of Fe by PBPB (n value = 0.977) was not favorable. The separation parameter R_L value, based on $R_L = 1/(1 + K_L C_0)$ of the Langmuir isotherm model, was also calculated to assess the adsorption preference of Mn and Fe toward BPB and PBPB: (i) $R_L > 1$ (unfavorable), (ii) $R_L = 1$ (linear), (iii) $1 > R_L > 0$ (favorable), and (iv) $R_L = 0$ (irreversible) [40]. Since the R_L values of Mn and Fe by BPB and PBPB were in the range of 0–1 (R_L of Mn by BPB = 0.003; R_L of Fe by BPB = 0.146; R_L of Mn by PBPB = 0.012; R_L of Fe by PBPB = 0.156), the adsorption of Mn and Fe by BPB and PBPB seemed to be favorable.
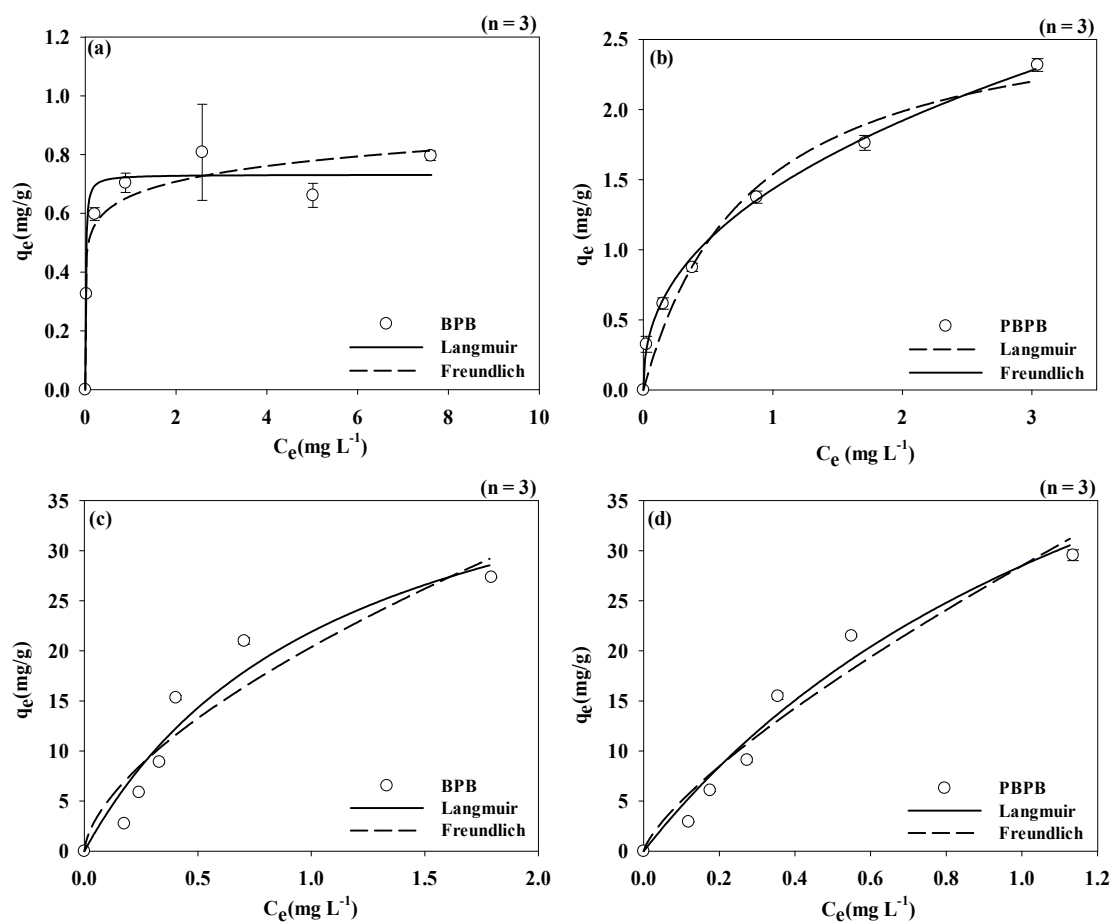

Figure 4. Adsorption isotherms of heavy metals onto BPB and PBPB: (**a**,**b**) Mn and (**c**,**d**) Fe (agitation time = 24 h, agitation speed = 150 rpm, adsorbent dosage of BPB and PBPB for Mn = 3 g L^{-1}, adsorbent dosage of BPB for Fe = 0.1 g L^{-1}, adsorbent dosage of PBPB for Fe = 0.3 g L^{-1}, initial concentration of Mn and Fe = 10 mg L^{-1}, pH = 7, and temperature = 25 °C).

Table 3. Isotherm model parameters for adsorption of Mn and Fe by BPB and PBPB (n = 3).

			Mn	Fe
BPB	Langmuir	K_L (L mg^{-1})	32.204	0.583
		q_e (mg g^{-1})	0.796	27.355
		R_L	0.003	0.146
		R^2	0.972	0.869
	Freundlich	K_F (mg$^{1-(1/n)}$ L$^{1/n}$ g^{-1})	0.821	3.864
		n	7.267	1.069
		R^2	0.81	0.826
PBPB	Langmuir	K_L (dm^3 mg^{-1})	7.943	0.540
		q_e (mg g^{-1})	2.319	29.55
		R_L	0.012	0.156
		R^2	0.898	0.949
	Freundlich	K_F (mg$^{1-(1/n)}$ L$^{1/n}$ g^{-1})	1.161	4.611
		n	2.471	0.977
		R^2	0.993	0.933

3.5. Effects of Temperature on Adsorption of Mn and Fe

The effects of temperature on the adsorption of Mn and Fe by BPB and PBPB are compared in Figure 5. The removal efficiencies of Mn and Fe by both BPB and PBPB were increased with increasing temperatures from 15 (removal efficiency of Mn by BPB = 17%, removal efficiency of Mn by PBPB = 46%, removal efficiency of Fe by BPB = 88%, removal efficiency of Fe by PBPB = 97%) to 45 °C (removal efficiency of Mn by BPB = 32%, removal efficiency of Mn by PBPB = 65%, removal efficiency of Fe by BPB = 97%, removal efficiency of Fe by PBPB = 99%). These results suggest that high temperatures may provide sufficient energy for the adsorption of heavy metals on the surficial and interior layers of biochars [41]. From the higher removal efficiencies of Mn and Fe by PBPB than BPB, it can be concluded that the abundance of oxygen-containing functional groups facilitates the adsorption of heavy metals by carbonaceous adsorbents [36].
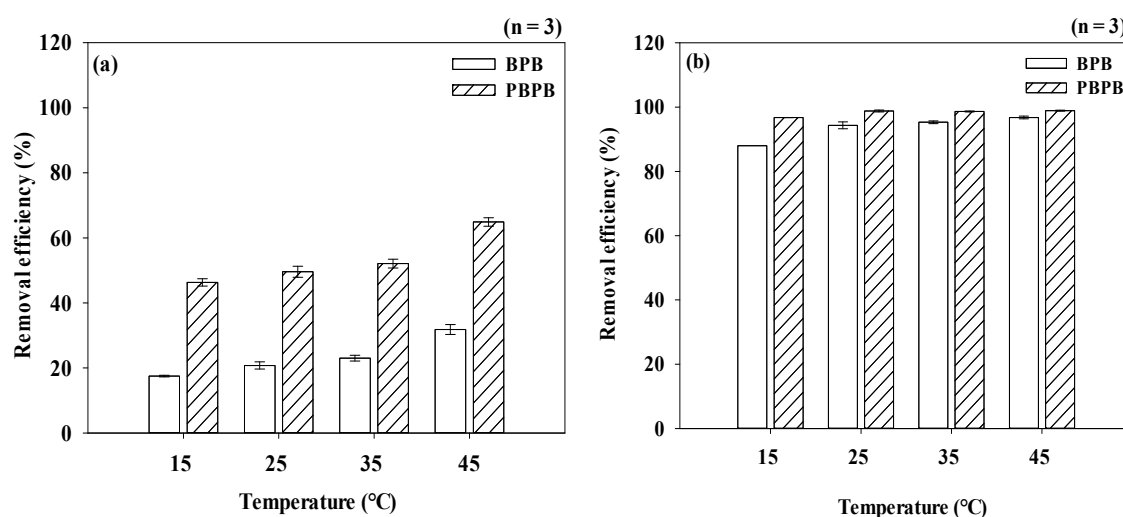

Figure 5. Effects of temperature on the adsorption of heavy metals using BPB and PBPB: (**a**) Mn and (**b**) Fe (agitation time = 6 h, agitation speed = 150 rpm, adsorbent dosage of BPB and PBPB for Mn = 3 g L^{-1}, adsorbent dosage of BPB for Fe = 0.1 g L^{-1}, adsorbent dosage of PBPB for Fe = 0.3 g L^{-1}, initial concentration of Mn and Fe = 10 mg L^{-1}, pH = 7, and temperature = 15–45 °C).

3.6. Effects of Ionic Strength on Adsorption of Mn and Fe

Figure 6 illustrates the effects of ionic strength on the removal of heavy metals by BPB and PBPB. The removal efficiencies of Mn and Fe by BPB and PBPB were gradually decreased with increasing ionic strengths. For example, when ionic strength was increased from 0 to 0.1 M, the removal efficiencies of Mn by BPB and PBPB were decreased from 35% and 54% to 21% and 32%, respectively. Meanwhile, the removal efficiencies of Fe by BPB and PBPB were decreased from 95% and 99% to 84% and 96%, respectively. These observations imply that increases of ionic strength may reinforce the electrostatic repulsion between heavy metals and the biochar surfaces and reduce the availability of adsorption sites on the biochar surfaces through the aggregation of biochars [42]. The removal efficiencies of Fe by BPB and PBPB were less affected by the changes in ionic strength compared to the removal efficiencies of Mn by BPB and PBPB because Fe has a smaller ion radius and higher electronegativity than Mn [37,38]. These inherent natures allowed Fe to exhibit higher attractive charges in the nucleus on the electron orbital [37,38]. Therefore, Fe more easily penetrated into the pores of biochars compared to Mn [37,38]. In addition, the higher removal efficiencies of Mn and Fe by PBPB (removal efficiency of Mn = 32–54%; removal efficiency of Fe = 96–99%) than BPB (removal efficiency of Mn = 21–35%; removal efficiency of Fe = 84–95%) at all the tested ionic strengths provide evidence that the surface structural features and oxygen-containing functional group abundance govern the adsorption of heavy metals by carbonaceous adsorbents [12,21,22].
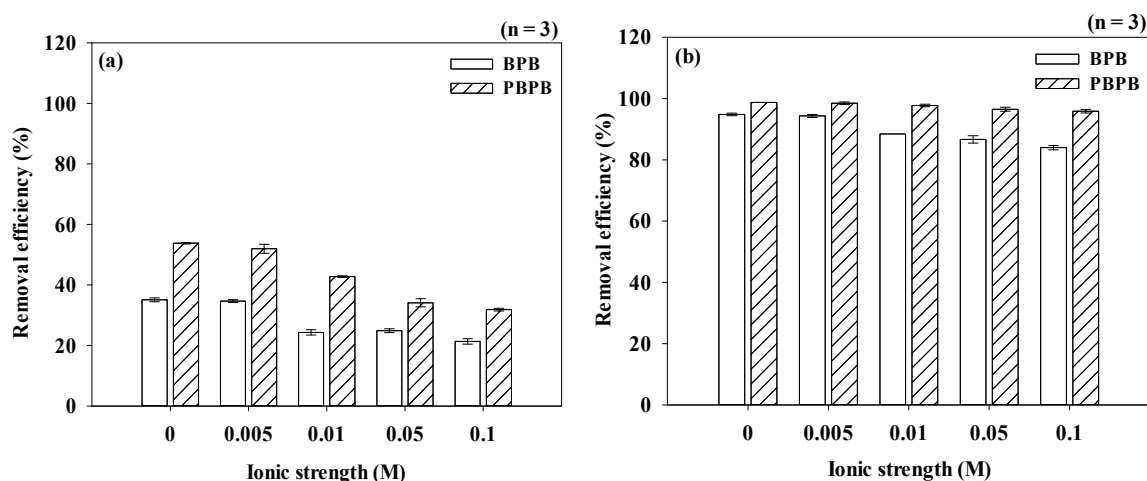

Figure 6. Effects of ionic strength on the adsorption of heavy metals using BPB and PBPB: (**a**) Mn and (**b**) Fe (agitation time = 6 h, agitation speed = 150 rpm, adsorbent dosage of BPB and PBPB for Mn = 3 g L^{-1}, adsorbent dosage of BPB for Fe = 0.1 g L^{-1}, adsorbent dosage of PBPB for Fe = 0.3 g L^{-1}, initial concentration = 10 mg L^{-1}, pH = 7, and temperature = 25 °C).

4. Conclusions

In this study, phosphoric acid pre-treatment on banana peel biochar was investigated for enhancement of Mn and Fe removal efficiencies. The physicochemical characteristics of pristine and phosphoric acid pre-treated biochars were characterized using the elemental analyzer, BET, and ATR-FTIR. These characterizations revealed that phosphoric acid pre-treatment facilitated the formation of oxygen-containing functional groups (i.e., hydroxyl and carboxyl functional groups), which could enhance the adsorption of heavy metals on the biochar surfaces. In addition, phosphoric acid pre-treatment improved specific surface area and pore volume for more adsorption sites for heavy metals. The adsorption experiments showed that phosphoric acid pre-treatment can improve the removal of Mn and Fe significantly. The results of the adsorption kinetics of Mn and Fe by BPB and PBPB were well-matched to the pseudo-second-order, indicating that adsorption was predominantly governed by chemical adsorption. The adsorption of Mn and Fe by BPB obeyed the Langmuir

isotherm model, whereas the Freundlich isotherm model described the adsorption of Mn by PBPB well. The adsorption of Fe by PBPB followed both Freundlich and Langmuir isotherm models. Furthermore, the adsorption of Mn and Fe by both BPB and PBPB increased with increasing temperature. However, the removal efficiencies were decreased with increasing ionic strength. From the excellent adsorption performance of Mn and Fe by PBPB compared to BPB, it can be concluded that phosphoric acid pre-treatment is a promising method to enhance Mn and Fe removal by banana peel biochar.

Author Contributions: H.K.: methodology and conceptualization, R.-A.K.: formal analysis and data curation, S.L.: writing—original draft preparation, K.C.: writing—review, editing, and funding acquisition. All authors have read and agree to the published version of the manuscript.

Conflicts of Interest: The authors declare no conflict of interest.

References

1. Ihsanullah; Abbas, A.; Al-Amer, A.M.; Laoui, T.; Al-Marri, M.J.; Nasser, M.S.; Khraisheh, M.; Atieh, M.A. Heavy metal removal from aqueous solution by advanced carbon nanotubes: Critical review of adsorption applications. *Sep. Purif. Technol.* **2016**, *157*, 141–161. [CrossRef]

2. Wang, F.; Yuanfeng, P.; Cai, P.; Guo, T.; Xiao, H. Single and binary adsorption of heavy metal ions from aqueous solutions using sugarcane cellulose-based adsorbent. *Bioresour. Technol.* **2017**, *241*, 482–490. [CrossRef]

3. Elsehly, E.M.; Chechenin, N.G.; Bukunov, K.; Makunin, A.V.; Priselkova, A.B.; Vorobyeva, E.A.; Motaweh, H.A. Removal of iron and manganese from aqueous solutions using carbon nanotube filters. *Water Supply* **2015**, *16*, 347–353. [CrossRef]

4. Idrees, M.; Batool, S.; Ullah, H.; Hussain, Q.; Al-Wabel, M.I.; Ahmad, M.; Hussain, A.; Riaz, M.; Ok, Y.S.; Kong, J. Adsorption and thermodynamic mechanisms of manganese removal from aqueous media by biowaste-derived biochars. *J. Mol. Liq.* **2018**, *266*, 373–380. [CrossRef]

5. Kwakye-Awuah, B.; Sefa-Ntiri, B.; Von-Kiti, E.; Nkrumah, I.; Williams, C. Adsorptive Removal of Iron and Manganese from Groundwater Samples in Ghana by Zeolite Y Synthesized from Bauxite and Kaolin. *Water* **2019**, *11*, 1912. [CrossRef]

6. Al-Rashdi, B.; Johnson, D.; Hilal, N. Removal of heavy metal ions by nanofiltration. *Desalination* **2013**, *315*, 2–17. [CrossRef]

7. Chen, Q.; Yao, Y.; Li, X.; Lu, J.; Zhou, J.; Huang, Z. Comparison of heavy metal removals from aqueous solutions by chemical precipitation and characteristics of precipitates. *J. Water Process. Eng.* **2018**, *26*, 289–300. [CrossRef]

8. Bazrafshan, E.; Mohamadi, L.; Ansari-Moghaddam, A.; Mahvi, A.H. Heavy metals removal from aqueous environments by electrocoagulation process- a systematic review. *J. Environ. Health Sci. Eng.* **2015**, *13*, 74. [CrossRef]

9. Khatri, N.; Tyagi, S.; Rawtani, D. Recent strategies for the removal of iron from water: A review. *J. Water Process. Eng.* **2017**, *19*, 291–304. [CrossRef]

10. Patil, D.S.; Chavan, S.M.; Oubagaranadin, J.U.K. A review of technologies for manganese removal from wastewaters. *J. Environ. Chem. Eng.* **2016**, *4*, 468–487. [CrossRef]

11. Tobiason, J.E.; Bazilio, A.; Goodwill, J.; Mai, X.; Nguyen, C. Manganese Removal from Drinking Water Sources. *Curr. Pollut. Rep.* **2016**, *2*, 168–177. [CrossRef]

12. Pérez-Marín, A.B.; Zapata, V.M.; Ortuño, J.F.; Aguilar, M.I.; Saez, J.; Lloréns, M. Removal of cadmium from aqueous solutions by adsorption onto orange waste. *J. Hazard. Mater.* **2007**, *139*, 122–131. [CrossRef]

13. Demirbas, A. Heavy metal adsorption onto agro-based waste materials: A review. *J. Hazard. Mater.* **2008**, *157*, 220–229. [CrossRef]

14. Pellera, F.-M.; Giannis, A.; Kalderis, D.; Anastasiadou, K.; Stegmann, R.; Wang, J.-Y.; Gidarakos, E. Adsorption of Cu(II) ions from aqueous solutions on biochars prepared from agricultural by-products. *J. Environ. Manag.* **2012**, *96*, 35–42. [CrossRef]

15. Liu, Z.; Zhang, F.-S. Removal of lead from water using biochars prepared from hydrothermal liquefaction of biomass. *J. Hazard. Mater.* **2009**, *167*, 933–939. [CrossRef]

16. Liu, Z.; Zhang, F.-S.; Wu, J. Characterization and application of chars produced from pinewood pyrolysis and hydrothermal treatment. *Fuel* **2010**, *89*, 510–514. [CrossRef]

17. Jun, B.-M.; Kim, Y.; Han, J.; Yoona, Y.; Kim, J.; Park, C.M. Preparation of Activated Biochar-Supported Magnetite Composite for Adsorption of Polychlorinated Phenols from Aqueous Solutions. *Water* **2019**, *11*, 1899. [CrossRef]

18. Lucaci, A.R.; Bulgariu, D.; Ahmad, I.; Lisa, G.; Mocanu, A.M.; Bulgariu, L. Potential Use of Biochar from Various Waste Biomass as Biosorbent in Co(II) Removal Processes. *Water* **2019**, *11*, 1565. [CrossRef]

19. Gupta, P.; Ann, T.-W.; Lee, S.-M. Use of biochar to enhance constructed wetland performance in wastewater reclamation. *Environ. Eng. Res.* **2016**, *21*, 36–44. [CrossRef]

20. Zhao, J.; Shen, X.-J.; Domene, X.; Alcañiz, J.-M.; Liao, X.; Palet, C. Comparison of biochars derived from different types of feedstock and their potential for heavy metal removal in multiple-metal solutions. *Sci. Rep.* **2019**, *9*, 9869. [CrossRef]

21. Wang, X.; Li, X.; Liu, G.; He, Y.; Chen, C.; Liu, X.; Li, G.; Gu, Y.; Zhao, Y.; He, Y. Mixed heavy metal removal from wastewater by using discarded mushroom-stick biochar: Adsorption properties and mechanisms. *Environ. Sci. Process. Impacts* **2019**, *21*, 584–592. [CrossRef] [PubMed]

22. Vilardi, G.; Di Palma, L.; Ochando-Pulido, J.M. Heavy metals adsorption by banana peels micro-powder: Equilibrium modeling by non-linear models. *Chin. J. Chem. Eng.* **2018**, *26*, 455–464. [CrossRef]

23. Martínez-Ruano, J.A.; Caballero-Galván, A.S.; Restrepo-Serna, D.L.; Alzate, C.A.C. Techno-economic and environmental assessment of biogas production from banana peel (Musa paradisiaca) in a biorefinery concept. *Environ. Sci. Pollut. Res.* **2018**, *25*, 35971–35980. [CrossRef] [PubMed]

24. Sagar, N.A.; Pareek, S.; Sharma, S.; Yahia, E.M.; Lobo, M.G. Fruit and Vegetable Waste: Bioactive Compounds, Their Extraction, and Possible Utilization. *Compr. Rev. Food Sci. Food Saf.* **2018**, *17*, 512–531. [CrossRef]

25. Omulo, G.; Banadda, N.; Kabenge, I.; Seay, J.R. Optimizing slow pyrolysis of banana peels wastes using response surface methodology. *Environ. Eng. Res.* **2018**, *24*, 354–361. [CrossRef]

26. Ibarra-Rodríguez, D.; Lizardi-Mendoza, J.; López-Maldonado, E.A.; Oropeza-Guzman, M.T.; Diana, I.-R.; Jaime, L.-M. Capacity of 'nopal' pectin as a dual coagulant-flocculant agent for heavy metals removal. *Chem. Eng. J.* **2017**, *323*, 19–28. [CrossRef]

27. Zhou, N.; Chen, H.; Xi, J.; Yao, D.; Zhou, Z.; Tian, Y.; Lu, X. Biochars with excellent Pb(II) adsorption property produced from fresh and dehydrated banana peels via hydrothermal carbonization. *Bioresour. Technol.* **2017**, *232*, 204–210. [CrossRef]

28. Amin, M.T.; Alazba, A.A.; Shafiq, M. Removal of Copper and Lead using Banana Biochar in Batch Adsorption Systems: Isotherms and Kinetic Studies. *Arab. J. Sci. Eng.* **2017**, *43*, 5711–5722. [CrossRef]

29. Tan, X.; Liu, S.; Liu, Y.; Gu, Y.-L.; Zeng, G.-M.; Hu, X.; Wang, X.; Liu, S.-H.; Jiang, L. Biochar as potential sustainable precursors for activated carbon production: Multiple applications in environmental protection and energy storage. *Bioresour. Technol.* **2017**, *227*, 359–372. [CrossRef]

30. Wang, Z.; Wu, J.; He, T.; Wu, J. Corn stalks char from fast pyrolysis as precursor material for preparation of activated carbon in fluidized bed reactor. *Bioresour. Technol.* **2014**, *167*, 551–554. [CrossRef]

31. Chu, G.; Zhao, J.; Huang, Y.; Zhou, D.; Liu, Y.; Wu, M.; Peng, H.; Zhao, Q.; Pan, B.; Steinberg, C.E. Phosphoric acid pretreatment enhances the specific surface areas of biochars by generation of micropores. *Environ. Pollut.* **2018**, *240*, 1–9. [CrossRef]

32. Taha, S.M.; Amer, M.E.; Elmarsafy, A.E.; Elkady, M.Y. Adsorption of 15 different pesticides on untreated and phosphoric acid treated biochar and charcoal from water. *J. Environ. Chem. Eng.* **2014**, *2*, 2013–2025. [CrossRef]

33. Wu, C.; Wang, Z.; Huang, J.; Williams, P.T. Pyrolysis/gasification of cellulose, hemicellulose and lignin for hydrogen production in the presence of various nickel-based catalysts. *Fuel* **2013**, *106*, 697–706. [CrossRef]

34. Coates, J. Interpretation of infrared spectra, a practical approach. In *Encyclopedia of Analytical Chemistry: Applications, Theory and Instrumentation*; John Wiey & Sons, Inc.: Hoboken, NJ, USA, 2006; pp. 10815–10837.

35. O'Connell, D.W.; Birkinshaw, C.; O'Dwyer, T.F. Heavy metal adsorbents prepared from the modification of cellulose: A review. *Bioresour. Technol.* **2008**, *99*, 6709–6724. [CrossRef] [PubMed]

36. Wang, Z.; Liu, G.; Zheng, H.; Li, F.; Ngo, H.-H.; Guo, W.; Liu, C.; Chen, L.; Xing, B. Investigating the mechanisms of biochar's removal of lead from solution. *Bioresour. Technol.* **2015**, *177*, 308–317. [CrossRef] [PubMed]

37. Dastgheib, S.A.; Rockstraw, D.A. A model for the adsorption of single metal ion solutes in aqueous solution onto activated carbon produced from pecan shells. *Carbon* **2002**, *40*, 1843–1851. [CrossRef]

38. Bin Jusoh, A.; Cheng, W.; Low, W.; Nora'Aini, A.; Noor, M.M.M. Study on the removal of iron and manganese in groundwater by granular activated carbon. *Desalination* **2005**, *182*, 347–353. [CrossRef]

39. Moreno-Castilla, C.; Álvarez-Merino, M.A.; López-Ramón, M.; Rivera-Utrilla, J. Cadmium Ion Adsorption on Different Carbon Adsorbents from Aqueous Solutions. Effect of Surface Chemistry, Pore Texture, Ionic Strength, and Dissolved Natural Organic Matter. *Langmuir* **2004**, *20*, 8142–8148. [CrossRef]

40. Gorgievski, M.; Božić, D.; Stanković, V.; Strbac, N.; Šerbula, S. Kinetics, equilibrium and mechanism of Cu2+, Ni2+ and Zn2+ ions biosorption using wheat straw. *Ecol. Eng.* **2013**, *58*, 113–122. [CrossRef]

41. Abdelhafez, A.A.; Li, J. Removal of Pb(II) from aqueous solution by using biochars derived from sugar cane bagasse and orange peel. *J. Taiwan Inst. Chem. Eng.* **2016**, *61*, 367–375. [CrossRef]

42. Park, C.M.; Han, J.; Chu, K.H.; Al-Hamadani, Y.; Her, N.; Heo, J.; Yoona, Y. Influence of solution pH, ionic strength, and humic acid on cadmium adsorption onto activated biochar: Experiment and modeling. *J. Ind. Eng. Chem.* **2017**, *48*, 186–193. [CrossRef]

A Biosorption-Pyrolysis Process for Removal of Pb from Aqueous Solution and Subsequent Immobilization of Pb in the Char

Yue Wang, Jinhong Lü *, Dongqing Feng, Sen Guo and Jianfa Li

College of Chemistry and Chemical Engineering, Shaoxing University, Zhejiang 312000, China;
wangyue835@163.com (Y.W.); fengdongqing@yeah.net (D.F.); gsen1041@gmail.com (S.G.); ljf@usx.edu.cn (J.L.)
* Correspondence: lvjinhong@usx.edu.cn; Tel.: +86-575-8834-1524

Abstract: The application of biosorption in the removal of heavy metals from water faces a challenge of safe disposal of contaminated biomass. In this study, a potential solution for this problem was proposed by using a biosorption-pyrolysis process featured by pretreatment of biomass with phosphoric acid (PA). The PA pretreatment of biomass increased the removal efficiency of heavy metal Pb from water by sorption, and subsequent pyrolysis helped immobilize Pb in the residual char. The results indicate that most (>95%) of the Pb adsorbed by the PA-pretreated biomass was retained in the char, and that the lower pyrolysis temperature (350 °C) is more favorable for Pb immobilization. In this way, the bioavailable Pb in the char was hardly detected, while the Pb leachable in acidic solution decreased to <3% of total Pb in the char. However, higher pyrolysis temperature (450 °C) is unfavorable for Pb immobilization, as both the leachable and bioavailable Pb increased to >28%. The reason should be related to the formation of elemental Pb and unstable Pb compounds during pyrolysis at 450 °C, according to the X-ray diffraction study.

1. Introduction

Water pollution by heavy metals, such as Pb, is one of the most serious environmental issues in the world. In comparison with other technologies for removing heavy metals from water, biosorption has the advantages of low operation cost, abundant biomass availability, and easy acceptance by the public [1–5]. Many kinds of plant-derived biomass wastes have been used for sorption of heavy metals, such as Pb, Cd, and Cu [6–8]. However, the practical applications of biosorption in the removal of heavy metals face two challenges. The first is that the sorption capacity of many indigenous biosorbents needs to be enhanced. Except for some biosorbents derived from algae and wheat bran, the maximum sorption of Pb by many lignocellulosic materials (seed husks, hulls and leaves, etc.) has shown to be <50 mg/g [6,9]. For seeking the solution of this problem, chemical modifications of biomass have been used for enhancing the sorption capacity [10–12]. The chemical modifying agents, including inorganic bases (e.g., NaOH), mineral acids (e.g., HNO_3), and organic compounds (e.g., urea) can enhance the ion exchange, and increase the functional groups and metal holding capacity of biosorbents. Among these modifying agents, phosphoric acid (PA) has shown to be a good candidate. PA has been used to modify olive pomace [13], corncob [14], rice husk [15], bagasse [16], wheat straw biochar [17] and so forth, so that their sorption to heavy metals was greatly enhanced. The second and more significant challenge is related to the safe disposal of the contaminated biomass after sorption of heavy metals. As the biomass is readily decomposed, the adsorbed heavy metals would be released or leached from the contaminated biomass if it was not properly disposed.

The proposed methods for disposal of heavy metal-contaminated biomass include incineration [18], composting [19], and pyrolysis [20], among others. Both incineration and composting have the problem of secondary pollution because the heavy metals will be dispersed into surroundings. In comparison, pyrolysis is operated in a closed system, and dispersion of heavy metals is controllable. Thus, pyrolysis has been used more frequently for post-treatment of heavy metal-contaminated biomass [21–26]. Pyrolysis is useful for valorization of contaminated biomass by transforming it into bio-fuel [27,28], and has also been used for preparing biochars that are good adsorbents to many pollutants [29–31]. The distribution of heavy metals in various fractions of pyrolysis product (e.g., oil or char) depends on the specific pyrolysis technique and heavy metal species [32–34]. For example, higher pyrolysis temperatures resulted in more emission of heavy metals into volatile fractions (e.g., oil) [27,35]. In contrast, slow pyrolysis at relatively low temperatures is more efficient for retention of heavy metals in the char [36,37]. Furthermore, at the same pyrolysis conditions, the heavy metals Cu, Zn, and Pb are more readily retained in the char than Cd [38]. As the char is more resistant to degradation than the biomass, pyrolysis is a feasible solution for disposal of heavy metal-contaminated biomass if most of the heavy metals are retained in the char and their stability in the char is guaranteed. In our previous studies, we investigated the stability of Pb and Cd in the char, and found that addition of phosphates in the contaminated biomass before pyrolysis enhanced the retention and stability of heavy metals [39–41].

In this work, a novel biosorption-pyrolysis process using PA-pretreated biomass was used to attempt to remove Pb from aqueous solution and subsequently immobilize Pb in the char. The specific objectives were to test two hypotheses: the first is that the PA pretreatment of biomass will enhance its sorption to Pb, and the second and more significant is that the subsequent pyrolysis of the contaminated biomass will increase the stability of Pb in the char. Different from our previous studies using phosphates as the additive for pyrolysis of the contaminated biomass [39], the biomass derived from an aquatic plant was firstly treated with PA, and then used for sorption of Pb in aqueous solution. The Pb-contaminated biomass was pyrolyzed, and the retention and stability of Pb in the char was evaluated. The comparison with the biosorption-pyrolysis process using un-pretreated biomass was also performed, and the immobilization mechanism of Pb in the char was investigated by using X-ray diffraction (XRD) and infrared spectra (IR).

2. Materials and Methods

2.1. Biomass and PA Pretreatment

The plant biomass was derived from the *Hydrocotyle verticillata* species, an aquatic plant that is widely distributed in tropical and subtropical zones. Its great adaptability and vitality makes it a good choice for phytoremediation of polluted or eutrophic water. The floating part (leaves and stems) of the *Hydrocotyle* plant was collected from a local river at Shaoxing, Zhejiang Province of China. The biomass was dried in an oven at 100 °C to a constant weight, and pulverized to a size of <0.15 mm. Elemental analysis using the EA3000 elemental analyser (Euro Vector, Italy) indicates that the pristine biomass (Mass) is composed of C 40.7%, O 29.7%, H 5.9%, N 1.5%, and S 0.6% by weight. The ash content of the biomass measured at 750 °C is 15.7% by weight. Phosphoric acid (H_3PO_4, PA) of analytical grade (Sinopharm Chemical Reagent Co. Ltd., China) was used for pre-treating the biomass. The biomass powder was soaked in 30 wt% PA solution for 24 h, then washed by water until the pH of the effluent reached 6.0. Two PA dosages with the mass ratio of PA/biomass = 0.5 or 1.0 were chosen according to the preliminary experiments. The dry solid residue obtained by PA pretreatment is labeled hereafter as $PA_{0.5}Mass$ or $PA_{1.0}Mass$, respectively, according to the PA dosage (0.5 or 1.0) used for pretreatment.

2.2. Pb Removal and Sorption Experiments

$Pb(NO_3)_2$ of analytical grade (Sinopharm Chemical Reagent Co. Ltd., Shanghai, China) was used to prepare Pb solutions for removal and sorption experiments. Of the biosorbent (un-pretreated biomass (Mass) or PA-pretreated biomass ($PA_{0.5}Mass$ or $PA_{1.0}Mass$)), 50 mg was added to 20 mL of

aqueous Pb solution with initial concentrations (C_0, mg/L) ranging from 5 to 50 mg/L. The slurry was adjusted to an initial pH of 5.0 with diluted HNO$_3$ solution, and placed in a thermostatic shaker bath at 25.0 ± 0.2 °C and shaken for 6 h when the sorption reached equilibrium according to our preliminary experiments. The supernatant solution was sampled and the Pb concentration (C_e) in solution was analyzed by the flame atomic absorption spectrometry (AAS) (AA-7000, Shimadzu, Japan). The removal efficiency (%) was calculated by Equation (1).

$$\text{Removal efficiency}(\%) = \frac{C_0 - C_e}{C_0} \times 100\% \tag{1}$$

The isothermal sorption experiments were conducted in a way similar to the removal experiments, except that a higher C_0 range (50–300 mg/L) was used, so as to leave a certain equilibrium Pb concentration (C_e) in the solution. The quantity adsorbed (Q_e, mg/g) was calculated by Equation (2):

$$Q_e = (C_0 - C_e) \times \frac{V}{m} \tag{2}$$

where V is the volume of aqueous Pb solution (0.02 L) and m is the mass of biomass used for sorption experiments (0.05 g). The isothermal sorption data were further analyzed with the Langmuir and Freundlich sorption isotherm models. The Langmuir model has been expressed in Equation (3):

$$Q_e = \frac{Q_m b C_e}{1 + b C_e} \tag{3}$$

where Q_m gives the maximum sorption capacity (mg/g) based on the monolayer adsorption model, and b (L/mg) is the Langmuir constant. The empirical Freundlich model has been expressed in Equation (4):

$$Q_e = k_F C_e^{1/n} \tag{4}$$

where k_F is the Freundlich sorption constant, and n gives the sorption intensity of biosorbents.

2.3. Pyrolysis of Pb-Contaminated Biomass

To obtain an adequate amount of contaminated biomass for subsequent pyrolysis, the biomass sample (1.5 g) was mixed with 500 mL of Pb solution with $C_0 = 100$ mg/L at initial pH = 5.0, and the mixture was stirred magnetically at room temperature for 6 h. Then the solid residue was filtered out and dried at 100 °C. The Pb-contaminated biomass powder was marked as Pb@Mass, Pb@PA$_{0.5}$Mass, or Pb@PA$_{1.0}$Mass according to the biomass sample used for biosorption. Pyrolysis of the Pb-contaminated biomass was carried out at 350 or 450 °C in a quartz tube furnace filled with N$_2$ gas. The relatively lower pyrolysis temperature was used because a higher temperature will lead to less retention of Pb in the char, according to a previous report [39]. The resulting Pb-concentrated chars are referred to hereafter as Pb@Char350, Pb@PA$_{0.5}$Char350, Pb@PA$_{1.0}$Char350, Pb@Char450, Pb@PA$_{0.5}$Char450, and Pb@PA$_{1.0}$Char450, respectively, depending on the temperature and feedstock biomass used for pyrolysis. The amount of Pb loaded in the biomass (Q_{mass}, mg/g) and then concentrated in the chars (Q_{char}, mg/g) was determined using a microwave digestion method [40], and the Pb concentration in the dilute digestion solution was determined using AAS. Retention efficiency of Pb (%) in the char after pyrolysis was calculated by Equation (5).

$$\text{Retention efficiency in the char}(\%) = \frac{Q_{char}}{Q_{mass}} \times \text{Yield of char}(\%) \tag{5}$$

2.4. Evaluation of the Stability of Pb in the Solid Samples

The bioavailable Pb, namely that available for utilization by living organisms, was evaluated with the DTPA extraction method using a buffer DTPA (diethylene triamine pentacetate acid) solution

according to the ISO standard (ISO 14870-2001). The leachable Pb in the samples was evaluated based on the amount of extractable Pb with the acid solution used in the Toxicity Characteristic Leaching Procedure (TCLP, EPA Test Method 1311). The details for the DTPA extraction and the TCLP test follow the procedures reported previously [40,42].

2.5. Sample Analysis

Surface composition of the biomass samples was determined with a JSM-6360LV scanning electron microscope (SEM) (JEOL, Tokyo, Japan) equipped with an X-act energy dispersive X-ray spectrometer (EDS) (Oxford, UK). Infrared spectra (IR) were recorded in the 4000–400 cm^{-1} region on a Nexus FT-IR spectrophotometer (Nicolet, Glendale, WI, USA) using a KBr pellet. The crystalline species in the biomass and chars were identified by X-ray diffraction (XRD) using D/MAX3A (Rigaku, Tokyo, Japan) equipment with CuKα radiation and a goniometer rate of 4°/min.

3. Results and Discussion

3.1. Influence of PA Pretreatment on the Removal of Pb by Biomass

The results in Figure 1a indicate that the removal efficiency of Pb by the *Hydrocotyle* biomass (Mass) is enhanced after PA treatment, despite that the sample (PA$_{1.0}$Mass) pretreated with more PA performed worse than the counterpart using less PA (PA$_{0.5}$Mass). At the dosage of biomass used in this study (2.5 g/L), Pb is almost completely removed by PA$_{0.5}$Mass when the initial concentration (C_0) of Pb (II) ranged from 5~50 mg/L. In contrast, the removal efficiency of Pb by the un-pretreated biomass dropped to <85% with the C_0 increase to 50 mg/L. The enhanced removal efficiency corresponds well to the improved sorption of Pb by biomass after PA pretreatment (Figure 1b). The maximum sorption (Q_m) calculated with the Langmuir model (Equation (3)) increased to 78.7 mg/g for PA$_{0.5}$Mass from 69.6 mg/g for the indigenous biomass (Mass) (Table 1). The Q_m values of the biosorbents in this study are close to those lignocellulosic materials with high sorption capacity to Pb reported in literature [6,7]. In addition, the *n* values calculated with the Freundlich model are much larger than 1 (Table 1), indicating that all the biosorbents favored the sorption of Pb [17]. The kinetic analysis indicates that the sorption of Pb by all three biosorbents (Mass, PA$_{0.5}$Mass, and PA$_{1.0}$Mass) fitted well to the pseudo-second-order model (R^2 > 0.99), and the sorption rate by the biomass was increased by PA-pretreatment according to the calculated rate constants (Table S1 in the Supplementary Materials). The quantity of Pb adsorbed by all three biosorbents (Mass, PA$_{0.5}$Mass and PA$_{1.0}$Mass) increased with the initial pH and the initial Pb concentrations in solution (Figures S2 and S3 in the Supplementary Materials). Therefore, the *Hydrocotyle* biomass and its PA-pretreated derivatives are potential sorbents for removal of heavy metals from water.

The relatively high sorption of Pb by the *Hydrocotyle* biomass and its PA-pretreated derivatives is related to their surface properties. Figure 2 shows the SEM images of the un-pretreated biomass (Figure 2a) and the PA-pretreated biomass (Figure 2b). The rough surface of PA$_{0.5}$Mass favors the sorption by providing more reactive sites. The specific surface area measured by the BET method is 7.24 m^2/g for PA$_{0.5}$Mass, which is higher than that of the un-pretreated biomass (1.42 m^2/g). Thus, PA-pretreatment increases the surface area of biomass and makes more reactive sites available for the sorption of Pb. The EDS analysis indicates that there are some inorganic minerals composed of Ca and K on the biomass surface, which are useful for sorption of Pb through cation exchange. For example, Pb can replace K in carbonate and sulfate to form precipitates, and this is a major pathway for sorption of Pb by those biomasses and biochars rich in inorganic minerals [43–45]. The sorption of Pb by biomass is also related to the surface functional groups. As can be seen in Figure 3, the bands at 1735, 1440, 1160–1060 cm^{-1} indicate oxygen-containing functional groups (C=O, C–OH, and C–O) on the biomass surface, which facilitate the sorption of Pb through surface complexation that has also been reported to contribute much to biosorption of heavy metals [46,47]. Some previous studies have shown that PA treatment can strengthen the acid functional groups of biomass [13,16,48], due to the

dissociation of these groups. In addition, PA pretreatment of the biomass introduces a new PO_4^{3-} group (at 1023 cm^{-1}) that can bind Pb through formation of phosphates, according to the IR spectra (Figure 3). However, pretreatment with a higher dosage of PA (1.0 g/g dry biomass) may result in over-acidification of biomass, which may inhibit the precipitation of Pb, so that the decreased removal efficiency and sorption capacity was observed on PA$_{1.0}$Mass in comparison with PA$_{0.5}$Mass (Figure 1). The over-acidification of biomass is confirmed by the change of pH before and after sorption of Pb. For example, at the same initial Pb concentration (e.g., $C_0 = 250$ mg/L) and same initial pH = 5.0, pH in the solution after sorption of Pb dropped to 4.8, 4.7, and 4.4, respectively for the sorption systems using Mass, PA$_{0.5}$Mass, and PA$_{1.0}$Mass. Namely, the pH in the PA$_{1.0}$Mass system is much lower than the other two systems, and lower pH favors dissolution of Pb and impacts its removal by biomass.
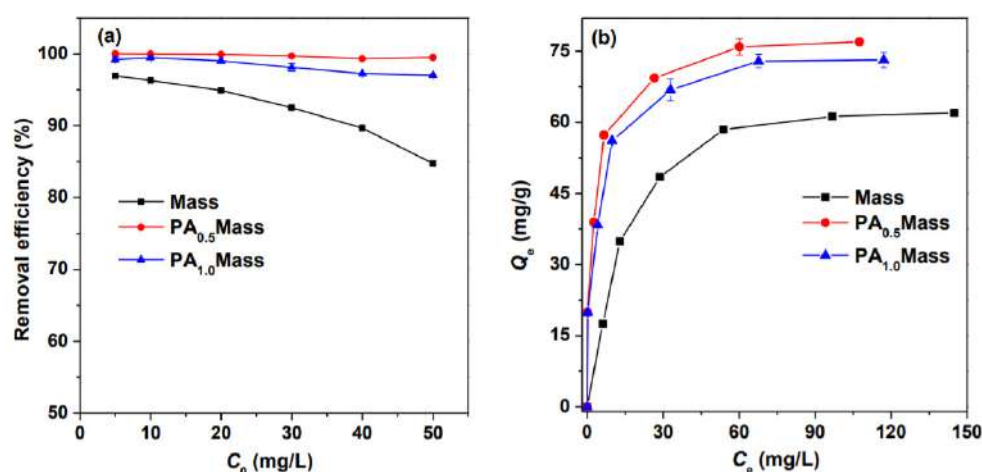
Figure 1. (**a**) Removal of Pb and (**b**) sorption isotherms (at 25 °C) of Pb by the *Hydrocotyle* biomass (Mass) and the biomass samples after PA pretreatment (PA$_{0.5}$Mass and PA$_{1.0}$Mass).
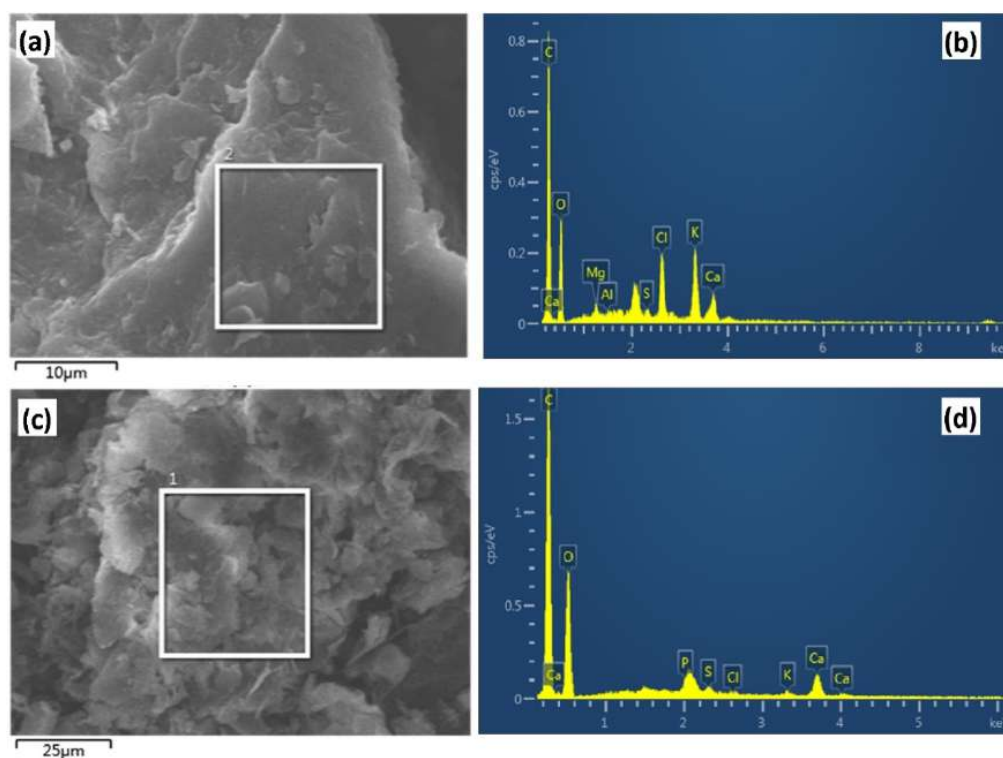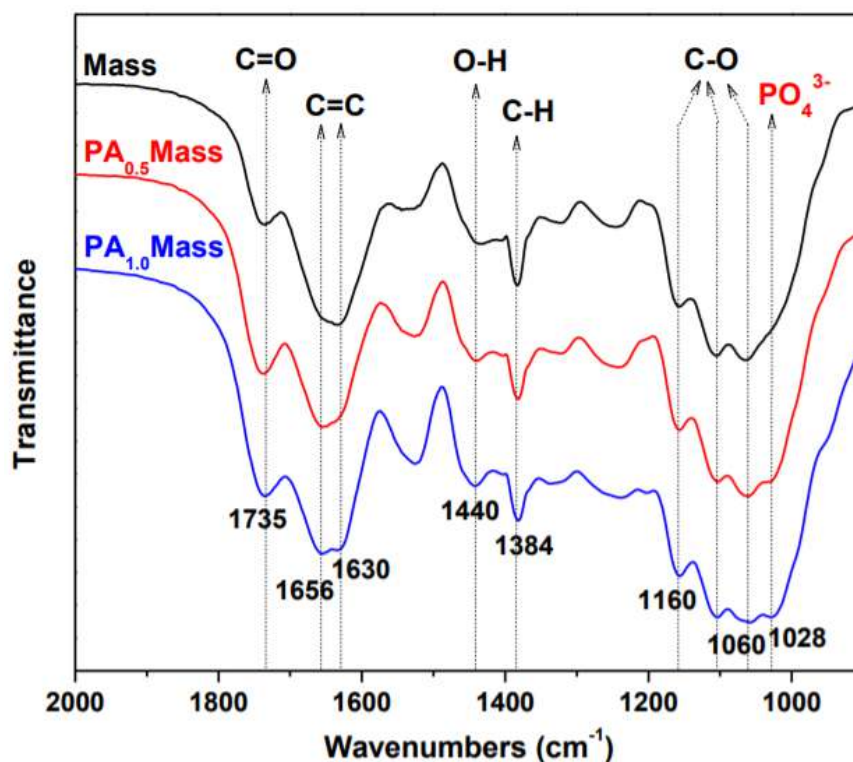

Figure 2. SEM image and EDS mapping results of (**a**,**b**) the *Hydrocotyle* biomass, and (**c**,**d**) PA-pretreated biomass (PA$_{0.5}$Mass).

Table 1. Fitting results of the sorption data with the Langmuir and the Freundlich models.

Models	Langmuir			Freundlich		
	Q_m (mg/g)	b (L/mg)	R^2	k_F	n	R^2
Mass	69.6	0.0788	0.992	20.6	4.21	0.855
$PA_{0.5}Mass$	78.7	0.373	0.996	36.7	5.72	0.853
$PA_{1.0}Mass$	76.9	0.242	0.993	32.8	5.39	0.839

Figure 3. IR spectra of the *Hydrocotyle* biomass and its PA-pretreated derivatives.

3.2. Influence of Pyrolysis on Pb Retention in the Char

Pyrolysis of the contaminated biomass at high temperatures will increase the risk of emission of Pb with volatile matters, and decrease the retention of Pb in the char, according to the previous studies [40–42]. Thus, two relatively low temperatures (350 and 450 °C) were used for pyrolysis of the Pb-contaminated biomass in this work, and the retention efficiency of Pb in various chars is shown in Figure 4. As can be seen, the Pb retentions in the two chars derived from the un-pretreated biomass were both less than 85%, and higher pyrolysis temperature (450 °C) led to lower retention efficiency due to the emission of Pb with volatile matters [27,35]. In comparison, the Pb retentions in the four chars ($PA_{0.5}char350$, $PA_{1.0}char350$, $PA_{0.5}char450$, and $PA_{1.0}char450$) derived from the PA-pretreated biomass were all >95%, and a higher dosage of PA used for pretreatment favors retention of more Pb in the char, indicating that PA pretreatment helped inhibit the emission of Pb during pyrolysis. PA is often used for activation of carbonization of biomass [49,50], and has shown to be effective for increasing the yield of char according to the previous reports [51,52], which is in consistency with that observed in this study (Figure 4a). The higher yield of char means less production of volatile matters, and introduction of PO_4^{3-} may also strengthen the binding of Pb to the solid char, which will be investigated in-depth in the following Section 3.4. Therefore, PA pretreatment of the biomass and subsequent pyrolysis enhanced the retention of Pb in the char, which is beneficial for reducing the hazard of secondary pollution due to pyrolysis of heavy metal-contaminated biomass.
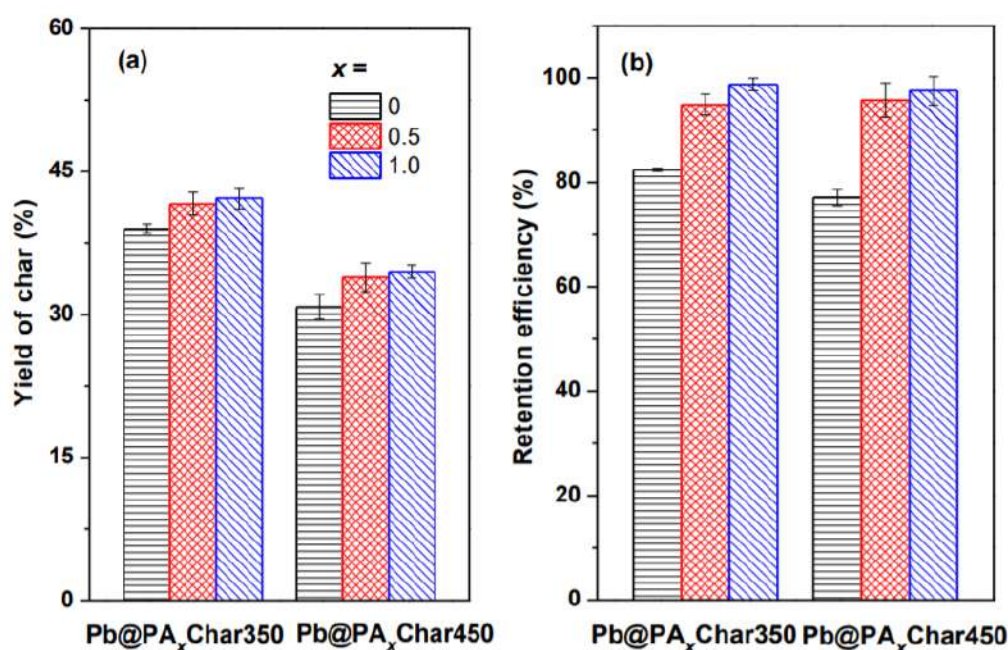
Figure 4. (**a**) Yield of chars, and (**b**) retention efficiency of Pb in the chars obtained by pyrolysis of Pb-contaminated biomass pretreated with various dosages of PA (0, 0.5 and 1.0 g/g mass).

3.3. Influence of Pyrolysis on Stability of Pb in the Char

The stability of Pb retained in the chars was first evaluated with the DTPA extraction method. Figure 5a shows the bioavailability of Pb in six chars, and the three Pb-contaminated biomass samples were also included for comparison. As can be seen, Pb adsorbed by biomass is readily bioavailable, whether the un-pretreated biomass or the PA-pretreated biomass was used as the sorbent. The DTPA- extractable Pb from the three biomass are all over 85%, so the sole PA pretreatment could not ensure the stability of Pb, although its sorption was enhanced as that shown in Figure 1b. Pyrolysis of the contaminated biomass sharply reduced the bioavailability of Pb in the char; in particular, the DTPA-extractable Pb is lower than 5% for the three chars obtained by pyrolysis at a lower temperature (Pb@Char350, Pb@PA$_{0.5}$Char350, and Pb@PA$_{1.0}$Char350). The DTPA-extractable Pb in the last two chars derived from the PA-pretreated biomass is close to zero. The results show that pyrolysis significantly enhanced the stability of Pb, and PA pretreatment can further reduce the bioavailability of Pb in the char. However, the DTPA-extractable Pb from the chars was lifted to >28% as the pyrolysis temperature increased to 450 °C, indicating that a higher pyrolysis temperature is unfavorable for immobilization of Pb. The similar results about the influence of pyrolysis temperature on stability of heavy metals in the char have been reported by Shi et al. [40]. The reason may be related to the different binding states between Pb and the chars obtained at different pyrolysis temperatures, which will be further discussed in the following Section 3.4.

The Pb immobilization by pyrolysis was further assessed with the TCLP test, and the results of leachable Pb in the biomass and chars are shown in Figure 5b. Interestingly, Pb adsorbed in the biomass was not readily leachable, with the highest leachable ratio of 5.34% observed on the biomass without PA pretreatment, although most of the Pb adsorbed in the biomass was bioavailable (Figure 5a). Such a difference should be related to the interactions between Pb and biomass, which are dominated by surface complexation and cation exchange, because there are plentiful oxygen-containing functional groups and exchangeable cations (e.g., K$^+$) on the biomass surface according to the IR and EDS analysis (Figures 2 and 3). These interactions are readily broken down by a chelating agent, such as DTPA, but insensitive to acetic acid used in the TCLP test. Furthermore, pyrolysis increased the amount of leachable Pb in the Pb@Char350 and Pb@Char450 chars, and higher pyrolysis temperatures resulted in more leachable Pb (Figure 5b). The reasons should be mainly related to the change of solid's properties

during the pyrolysis. Pyrolysis makes biomass lose functional groups such as –OH and C–O that are essential for sorption of Pb through surface complexation. At the meantime, inorganic minerals in biomass will be transformed into alkaline matter, such as carbonates or (hydr)oxides [53]. Thus, the interactions between Pb and solid will be changed by formation of Pb oxide or carbonates that are readily dissolved in acid. Therefore, direct pyrolysis, especially at higher temperatures (450 °C), is not favorable for immobilization of Pb in an acidic environment, because nearly half of Pb in the Pb@Char450 sample is leachable (Figure 5b). Despite this result, the encouraging fact is that the two chars (Pb@PA$_{0.5}$Char350 and Pb@PA$_{1.0}$Char350) obtained at 350 °C and derived from the PA-pretreated biomass show good immobilization of Pb, with the ratio of leachable Pb accounting for less than 3%. In combination with the results shown in Figure 5a, we conclude that pyrolysis at 350 °C can immobilize Pb adsorbed by the PA-pretreated biomass. The similar immobilization of heavy metals in the char using phosphates as the additive for pyrolysis has been observed in our previous studies [39–41]. What makes this work differently is that the biomass was firstly pretreated with PA, which enhanced its efficiency for removal of Pb before it was immobilized by pyrolysis. In general, such a combined biosorption-pyrolysis will be a promising strategy for removal of heavy metals from aqueous solution and subsequent safe disposal of the contaminated biosorbents.
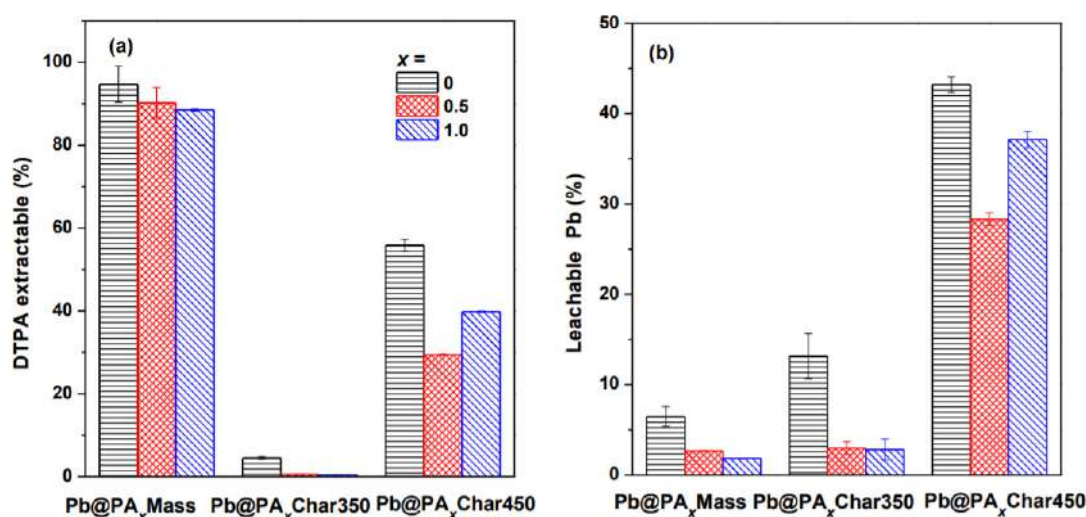

Figure 5. (**a**) DTPA-extractable Pb from, and (**b**) TCLP-leachable Pb from the biomass samples pretreated with various dosages of PA (0, 0.5, and 1.0 g/g mass) and the corresponding chars obtained at different pyrolysis temperatures (350 or 450 °C).

3.4. Investigations about the Immobilization Mechanisms

The X-ray diffraction (XRD) technique and IR spectra were used to examine the biomass and chars obtained by different treatments, so as to understand the mechanisms of Pb immobilization. The XRD patterns (Figure 6) indicate that there is no crystalline constituent other than cellulose in the Pb-contaminated biomass. However, the stable PbS crystal was found in all the chars, which should be one reason for immobilization of Pb. Furthermore, several strong peaks attributed to the lead phosphates (e.g., Ca$_8$Pb$_2$(PO$_4$)$_6$(OH)$_2$ at 2θ = 51.6°, and Pb$_9$(PO$_4$)$_6$ at 2θ = 26.8° and 33.2°) were observed in the Pb@PA$_{1.0}$Char350 sample. These lead phosphates contribute to the enhanced stability of Pb in this char, so the bioavailability and leachability of Pb were suppressed. However, as the pyrolysis temperature increased to 450 °C, the elemental Pb and unstable Pb compounds (PbO and Pb$_3$(CO$_3$)(OH)$_2$) were formed according to the XRD patterns (Figure 6), which can explain the results obtained in the TCLP test, in which more leachable Pb was observed in the chars obtained at a high pyrolysis temperature (450 °C) (Figure 5). Further, a new peak at 1156 cm^{-1} was found in the IR spectra (Figure 7) of two chars derived from the PA-pretreated biomass (Pb@PA$_{1.0}$Char350 and Pb@PA$_{1.0}$Char450), which could be assigned to C–O stretching vibrations in P–O–C (aromatic)

linkage [49]. Thus, Pb phosphates would be bound to the carbon matrix through this linkage, which made Pb be stably anchored on the char [52].
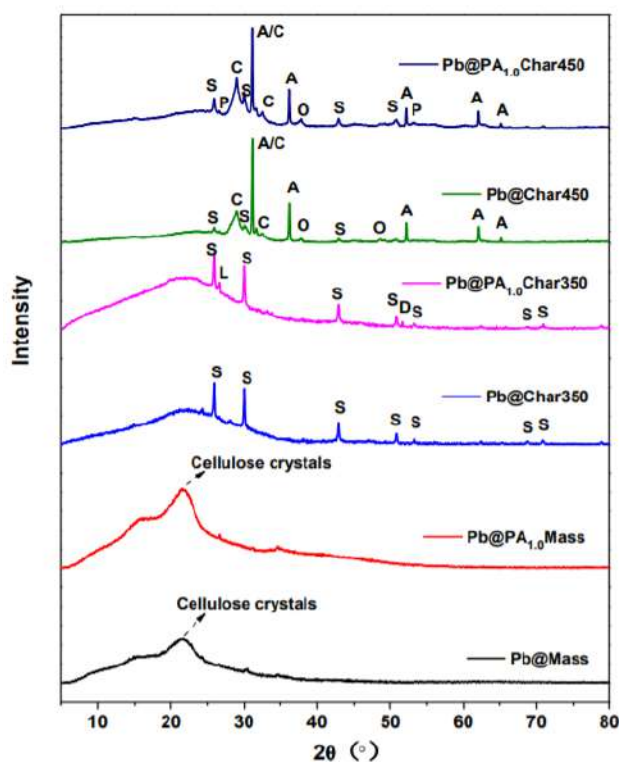

Figure 6. XRD patterns of two biomass and four char samples (A: Pb, C: $Pb_3(CO_3)(OH)_2$, D: $Ca_8Pb_2(PO_4)_6(OH)_2$, L: $Pb_9(PO_4)_6$, O: PbO, P: $Pb_5(PO_4)_3(OH)$, and S: PbS).
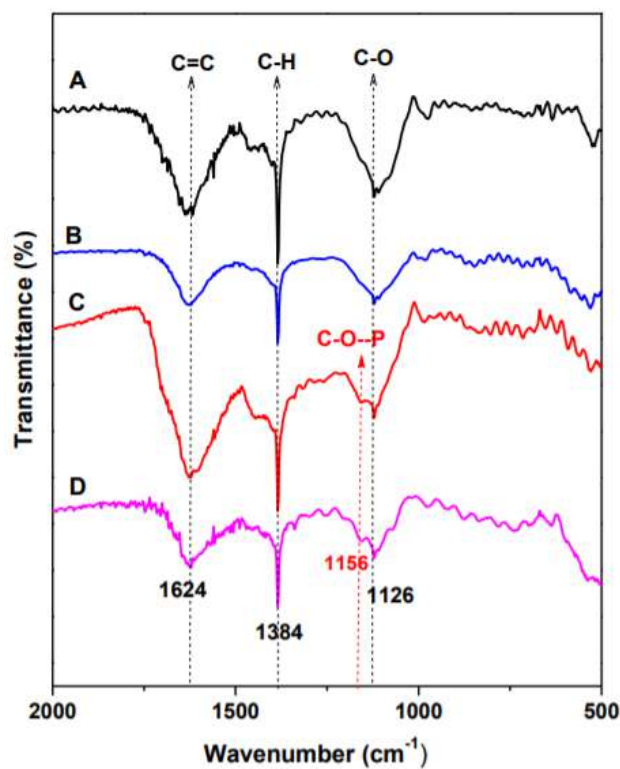

Figure 7. IR spectra of four char samples (A: Pb@Char350, B: Pb@Char450, C: Pb@PA$_{1.0}$Char350, and D: Pb@PA$_{1.0}$Char450).

4. Conclusions

The combined biosorption-pyrolysis process can be used for efficient removal of Pb from aqueous solution and then immobilization of Pb in the char, when the *Hydrocotyle* biomass is pretreated with PA. The PA-pretreatment increased the surface area and introduced more functional groups in the biomass, and enhanced the removal efficiency of Pb by biosorption. The subsequent pyrolysis of the Pb-contaminated biomass at relatively low temperatures (350 and 450 °C) retained most of the Pb in the char, and use of the PA-pretreatment further increased the retention efficiency to >95%. Furthermore, both the bioavailability and leaching potential of Pb in the char were significantly reduced by pyrolysis with the aid of PA-pretreatment, and pyrolysis at 350 °C is more favorable for the immobilization of Pb than that at 450 °C. The immobilization mechanisms are related to the formation of Pb phosphates and their linkage to the carbon matrix, according to the investigations with XRD and IR spectra. Despite the promising results obtained in this study, the long-time stability of Pb in the char deserves further investigation by considering more environmental factors, such as pH, temperature, humidity, and microbial effect, before the safe disposal of the char.

References

1. Ungureanu, G.; Santos, S.; Boaventura, R.; Botelho, C. Arsenic and antimony in water and wastewater: Overview of removal techniques with special reference to latest advances in adsorption. *J. Environ. Manag.* **2015**, *151*, 326–342. [CrossRef] [PubMed]
2. Ayangbenro, A.S.; Babalola, O.O. A new strategy for heavy metal polluted environments: A review of microbial biosorbents. *Int. J. Environ. Res. Public Health* **2017**, *14*, 94. [CrossRef] [PubMed]
3. Czikkely, M.; Neubauer, E.; Fekete, I.; Ymeri, P.; Fogarassy, C. Review of heavy metal adsorption processes by several organic matters from wastewaters. *Water* **2018**, *10*, 1377. [CrossRef]
4. Fernández-González, R.; Martín-Lara, M.Á.; Blázquez, G.; Pérez, A.; Calero, M. Recovering metals from aqueous solutions by biosorption onto hydrolyzed olive cake. *Water* **2019**, *11*, 2519. [CrossRef]
5. Filote, C.; Volf, I.; Santos, S.C.; Botelho, C.M. Bioadsorptive removal of Pb(II) from aqueous solution by the biorefinery waste of Fucusspiralis. *Sci. Total Environ.* **2019**, *648*, 1201–1209. [CrossRef]
6. Farooq, U.; Kozinski, J.A.; Khan, M.A.; Athar, M. Biosorption of heavy metal ions using wheat based biosorbents—A review of the recent literature. *Bioresour. Technol.* **2010**, *101*, 5043–5053. [CrossRef]
7. Abdolali, A.; Guo, W.S.; Ngo, H.H.; Chen, S.S.; Nguyen, N.C.; Tung, K.L. Typical lignocellulosic wastes and by-products for biosorption process in water and wastewater treatment: A critical review. *Bioresour. Technol.* **2014**, *160*, 57–66. [CrossRef]
8. Shaikh, R.B.; Saifullah, B.; Rehman, F.U. Greener method for the removal of toxic metal ions from the wastewater by application of agricultural waste as an adsorbent. *Water* **2018**, *10*, 1316. [CrossRef]
9. Salman, M.; Athar, M.; Farooq, U. Biosorption of heavy metals from aqueous solutions using indigenous and modified lignocellulosic materials. *Rev. Environ. Sci. BioTechnol.* **2015**, *14*, 211–228. [CrossRef]
10. Feng, N.; Guo, X.; Liang, S.; Zhu, Y.; Liu, J. Biosorption of heavy metals from aqueous solutions by chemically modified orange peel. *J. Hazard. Mater.* **2011**, *185*, 49–54. [CrossRef]

11. Abdolali, A.; Ngo, H.H.; Guo, W.; Zhou, J.L.; Du, B.; Wei, Q.; Wang, X.C.; Nguyen, P.D. Characterization of a multi-metal binding biosorbent: Chemical modification and desorption studies. *Bioresour. Technol.* **2015**, *193*, 477–487. [CrossRef]

12. Pintor, A.M.; Vieira, B.R.; Boaventura, R.A.; Botelho, C.M. Removal of antimony from water by iron-coated cork granulates. *Sep. Purif. Technol.* **2020**, *233*, 116020. [CrossRef]

13. Martín-Lara, M.A.; Pagnanelli, F.; Mainelli, S.; Calero, M.; Toro, L. Chemical treatment of olive pomace: Effect on acid-basic properties and metal biosorption capacity. *J. Hazard. Mater.* **2008**, *156*, 448–457. [CrossRef] [PubMed]

14. Buasri, A.; Chaiyut, N.; Tapang, K.; Jaroensin, S.; Panphrom, S. Equilibrium and kinetic studies of biosorption of Zn(II) ions from wastewater using modified corn cob. *APCBEE Procedia* **2012**, *3*, 60–64. [CrossRef]

15. Dada, A.O.; Olalekan, A.P.; Olatunya, A.M.; Dada, O.J.I.J.C. Langmuir, Freundlich, Temkin and Dubinin–Radushkevich isotherms studies of equilibrium sorption of Zn^{2+} unto phosphoric acid modified rice husk. *IOSR J. Appl. Chem.* **2012**, *3*, 38–45.

16. Xu, Y.L.; Song, S.Y.; Chen, J.D.; Chi, R.A.; Yu, J.X. Simultaneous recovery of Cu^{2+} and Pb^{2+} from metallurgical wastewater by two tandem columns fixed respectively with tetraethylenepentamine and phosphoric acid modified bagasse. *J. Taiwan Inst. Chem. Eng.* **2019**, *99*, 132–141. [CrossRef]

17. Naeem, M.A.; Imran, M.; Amjad, M.; Abbas, G.; Tahir, M.; Murtaza, B.; Zakir, A.; Shahid, M.; Bulgariu, L.; Ahmad, I. Batch and column scale removal of cadmium from water using raw and acid activated wheat straw biochar. *Water* **2019**, *11*, 1438. [CrossRef]

18. Nzihou, A.; Stanmore, B. The fate of heavy metals during combustion and gasification of contaminated biomass—A brief review. *J. Hazard. Mater.* **2013**, *256*, 56–66. [CrossRef]

19. Cao, X.; Ma, L.; Shiralipour, A.; Harris, W. Biomass reduction and arsenic transformation during composting of arsenic-rich hyperaccumulator *Pterisvittata* L. *Environ. Sci. Pollut. Res.* **2010**, *17*, 586–594. [CrossRef]

20. Bădescu, I.S.; Bulgariu, D.; Ahmad, I.; Bulgariu, L. Valorisation possibilities of exhausted biosorbents loaded with metal ions—A review. *J. Environ. Manag.* **2018**, *224*, 288–297. [CrossRef]

21. Liu, W.J.; Zeng, F.X.; Jiang, H.; Zhang, X.S.; Yu, H.Q. Techno-economic evaluation of the integrated biosorption–pyrolysis technology for lead (Pb) recovery from aqueous solution. *Bioresour. Technol.* **2011**, *102*, 6260–6265. [CrossRef] [PubMed]

22. Gonsalvesh, L.; Yperman, J.; Carleer, R.; Mench, M.; Herzig, R.; Vangronsveld, J. Valorisation of heavy metals enriched tobacco biomass through slow pyrolysis and steam activation. *J. Chem. Technol. Biotechnol.* **2016**, *91*, 1585–1595. [CrossRef]

23. Martín-Lara, M.Á.; Iáñez-Rodríguez, I.; Blázquez, G.; Quesada, L.; Pérez, A.; Calero, M. Kinetics of thermal decomposition of some biomasses in an inert environment: An investigation of the effect of lead loaded by biosorption. *Waste Manag.* **2017**, *70*, 101–113. [CrossRef]

24. Han, Z.; Guo, Z.; Zhang, Y.; Xiao, X.; Peng, C. Potential of pyrolysis for the recovery of heavy metals and bioenergy from contaminated *Broussonetia papyrifera* biomass. *BioResources* **2018**, *13*, 2932–2944. [CrossRef]

25. Gong, X.; Huang, D.; Liu, Y.; Zeng, G.; Wang, R.; Wei, J.; Huang, C.; Xu, P.; Wan, J.; Zhang, C. Pyrolysis and reutilization of plant residues after phytoremediation of heavy metals contaminated sediments: For heavy metals stabilization and dye adsorption. *Bioresour. Technol.* **2018**, *253*, 64–71. [CrossRef] [PubMed]

26. He, J.; Strezov, V.; Zhou, X.; Kumar, R.; Kan, T. Pyrolysis of heavy metal contaminated biomass pre-treated with ferric salts: Product characterisation and heavy metal deportment. *Bioresour. Technol.* **2020**, *313*, 123641. [CrossRef] [PubMed]

27. Stals, M.; Thijssen, E.; Vangronsveld, J.; Carleer, R.; Schreurs, S.; Yperman, J. Flash pyrolysis of heavy metal contaminated biomass from phytoremediation: Influence of temperature, entrained flow and wood/leaves blended pyrolysis on the behaviour of heavy metals. *J. Anal. Appl. Pyrol.* **2010**, *87*, 1–7. [CrossRef]

28. Dastyar, W.; Raheem, A.; He, J.; Zhao, M. Biofuel production using thermochemical conversion of heavy metal-contaminated biomass (HMCB) harvested from phytoextraction process. *Chem. Eng. J.* **2018**, *358*, 759–785. [CrossRef]

29. Chen, B.; Chen, Z.; Lv, S. A novel magnetic biochar efficiently sorbs organic pollutants and phosphate. *Bioresour. Technol.* **2011**, *102*, 716–723. [CrossRef]

30. Li, L.; Zou, D.; Xiao, Z.; Zeng, X.; Zhang, L.; Jiang, L.; Wang, A.; Ge, D.; Zhang, G.; Liu, F. Biochar as a sorbent for emerging contaminants enables improvements in waste management and sustainable resource use. *J. Clean. Prod.* **2019**, *210*, 1324–1342. [CrossRef]

31. Kim, H.; Ko, R.-A.; Lee, S.; Chon, K. Removal efficiencies of manganese and iron using pristine and phosphoric acid pre-treated biochars made from banana peels. *Water* **2020**, *12*, 1173. [CrossRef]

32. Stals, M.; Carleer, R.; Reggers, G.; Schreurs, S.; Yperman, J. Flash pyrolysis of heavy metal contaminated hardwoods from phytoremediation: Characterisation of biomass, pyrolysis oil and char/ash fraction. *J. Anal. Appl. Pyrol.* **2010**, *89*, 22–29. [CrossRef]

33. He, J.; Strezov, V.; Kan, T.; Weldekidan, H.; Asumadu-Sarkodie, S.; Kumar, R. Effect of temperature on heavy metal (loid) deportment during pyrolysis of Avicennia marina biomass obtained from phytoremediation. *Bioresour. Technol.* **2019**, *278*, 214–222. [CrossRef]

34. Li, S.; Zou, D.; Li, L.; Wu, L.; Liu, F.; Zeng, X.; Wang, H.; Zhu, Y.; Xiao, Z. Evolution of heavy metals during thermal treatment of manure: A critical review and outlooks. *Chemosphere* **2020**, *247*, 125962. [CrossRef] [PubMed]

35. Han, H.; Hu, S.; Syed-Hassan, S.S.A.; Xiao, Y.; Wang, Y.; Xu, J.; Xiang, J. Effects of reaction conditions on the emission behaviors of arsenic, cadmium and lead during sewage sludge pyrolysis. *Bioresour. Technol.* **2017**, *236*, 138–145. [CrossRef] [PubMed]

36. Al Chami, Z.; Amer, N.; Smets, K.; Yperman, J.; Carleer, R.; Dumontet, S.; Vangronsveld, J. Evaluation of flash and slow pyrolysis applied on heavy metal contaminated Sorghum bicolor shoots resulting from phytoremediation. *Biomass Bioenergy* **2014**, *63*, 268–279. [CrossRef]

37. He, J.; Strezov, V.; Kumar, R.; Weldekidan, H.; Jahan, S.; Dastjerdi, B.H.; Zhou, X.; Kan, T. Pyrolysis of heavy metal contaminated *Avicennia marina* biomass from phytoremediation: Characterisation of biomass and pyrolysis products. *J. Clean. Prod.* **2019**, *234*, 1235–1245. [CrossRef]

38. Lievens, C.; Yperman, J.; Vangronsveld, J.; Carleer, R. Study of the potentialvalorization of heavy metal contaminated biomass via phytoremediation by fast pyrolysis: Part I. Influence of temperature, biomass species and solid heat carrier on the behaviour of heavy metals. *Fuel* **2008**, *87*, 1894–1905. [CrossRef]

39. Li, S.; Zhang, T.; Li, J.; Shi, L.; Zhu, X.; Lü, J.; Li, Y. Stabilization of Pb(II) accumulated in biomass through phosphate-pretreated pyrolysis at low temperatures. *J. Hazard. Mater.* **2017**, *324*, 464–471. [CrossRef]

40. Shi, L.; Wang, L.; Zhang, T.; Li, J.; Huang, X.; Cai, J.; Wang, Y. Reducing the bioavailability and leaching potential of lead in contaminated water hyacinth biomass by phosphate-assisted pyrolysis. *Bioresour. Technol.* **2017**, *241*, 908–914. [CrossRef]

41. Zhang, T.; Wang, Y.; Liu, X.; Lü, J.; Li, J. Functions of phosphorus additives on immobilizing heavy metal cadmium in the char through pyrolysis of contaminated biomass. *J. Anal. Appl. Pyrol.* **2019**, *144*, 104721. [CrossRef]

42. Zeng, X.; Xiao, Z.; Zhang, G.; Wang, A.; Li, Z.; Liu, Y.; Wang, H.; Zeng, Q.; Liang, Y.; Zou, D. Speciation and bioavailability of heavy metals in pyrolytic biochar of swine and goat manures. *J. Anal. Appl. Pyrol.* **2018**, *132*, 82–93. [CrossRef]

43. Lu, H.; Zhang, W.; Yang, Y.; Huang, X.; Wang, S.; Qiu, R. Relative distribution of Pb^{2+} sorption mechanisms by sludge-derived biochar. *Water Res.* **2012**, *46*, 854–862. [CrossRef] [PubMed]

44. Xu, X.; Cao, X.; Zhao, L. Comparison of rice husk-and dairy manure-derived biochars for simultaneously removing heavy metals from aqueous solutions: Role of mineral components in biochars. *Chemosphere* **2013**, *92*, 955–961. [CrossRef]

45. Zhang, T.; Zhu, X.; Shi, L.; Li, J.; Li, S.; Lü, J.; Li, Y. Efficient removal of lead from solution by celery-derived biochars rich in alkaline minerals. *Bioresour. Technol.* **2017**, *235*, 185–192. [CrossRef]

46. Cantrell, K.B.; Hunt, P.G.; Uchimiya, M.; Novak, J.M.; Ro, K.S. Impact of pyrolysis temperature and manure source on physicochemical characteristics of biochar. *Bioresour. Technol.* **2012**, *107*, 419–428. [CrossRef]

47. Blázquez, G.; Ronda, A.; Martín-Lara, M.A.; Pérez, A.; Calero, M. Comparative study of isotherm parameters of lead biosorption by two wastes of olive-oil production. *Water Sci. Technol.* **2015**, *72*, 711–720. [CrossRef]

48. Patra, C.; Shahnaz, T.; Subbiah, S.; Narayanasamy, S. Comparative assessment of raw and acid-activated preparations of novel Pongamiapinnata shells for adsorption of hexavalent chromium from simulated wastewater. *Environ. Sci. Pollut. R.* **2020**, *27*, 14836–14851. [CrossRef]

49. Puziy, A.M.; Poddubnaya, O.I.; Martınez-Alonso, A.; Suárez-Garcıa, F.; Tascón, J.M.D. Synthetic carbons activated with phosphoric acid: I. Surface chemistry and ion binding properties. *Carbon* **2002**, *40*, 1493–1505. [CrossRef]

50. Shu, Y.; Tang, C.; Hu, X.; Jiang, L.; Hu, X.; Zhao, Y. H_3PO_4-activated cattail carbon production and application in chromium removal from aqueous solution: Process optimization and removal mechanism. *Water* **2018**, *10*, 754. [CrossRef]

51. Zhao, L.; Cao, X.; Zheng, W.; Kan, Y. Phosphorus-assisted biomass thermal conversion: Reducing carbon loss and improving biochar stability. *PLoS ONE* **2014**, *9*, e115373. [CrossRef] [PubMed]

52. Zhao, L.; Cao, X.; Zheng, W.; Scott, J.W.; Sharma, B.K.; Chen, X. Copyrolysis of biomass with phosphate fertilizers to improve biochar carbon retention, slow nutrient release, and stabilize heavy metals in soil. *ACS Sustain. Chem. Eng.* **2016**, *4*, 1630–1636. [CrossRef]

53. Yuan, J.H.; Xu, R.K.; Zhang, H. The forms of alkalis in the biochar produced from crop residues at different temperatures. *Bioresour. Technol.* **2011**, *102*, 3488–3497. [CrossRef] [PubMed]

Use of Chemically Treated Human Hair Wastes for the Removal of Heavy Metal Ions from Water

Helan Zhang [1], Fernando Carrillo-Navarrete [2,3] , Montserrat López-Mesas [1] and Cristina Palet [1,*]

[1] Centre Grup de Tècniques de Separació en Química, Unitat de Química Analítica, Departament de Química, Universitat Autònoma de Barcelona, 08193 Bellaterra, Spain; hlzhang1126@163.com (H.Z.); montserrat.lopez.mesas@uab.cat (M.L.-M.)

[2] Institut d'Investigació Tèxtil i Cooperació Industrial de Terrassa (INTEXTER), Universitat Politècnica de Catalunya (UPC), Colom 15, 08222 Terrassa, Spain; fernando.carrillo@upc.edu

[3] Departament d'Enginyeria Química, ESEIAAT—Universitat Politècnica de Catalunya (UPC), Colom 1, 08222 Terrassa, Spain

* Correspondence: cristina.palet@uab.cat; Tel.: +34-93-581-3475; Fax: +34-93-581-1985

Abstract: Human hair is considered a ubiquitous waste product and its accumulation can cause environmental problems. Hence, the search for alternatives that take advantage of this waste as a new raw material is of interest, and contributes to the idea of the circular economy. In this study, chemically modified human hair was used as a low cost biosorbent for the removal of heavy metal ions from aqueous solutions. The effect of the contact time, the pH, and the biosorbent concentration on the biosorption process were investigated. Kinetic modeling indicated that the pseudo-second order kinetic equation fitted well with $R^2 > 0.999$. Furthermore, the equilibrium data fitted the Langmuir adsorption isotherm at 295 K resulting in saturation concentrations of 9.47×10^{-5}, 5.57×10^{-5}, 3.77×10^{-5}, and 3.61×10^{-5} mol/g for the sorption of Cr(III), Cu(II), Cd(II), and Pb(II), respectively. The biosorption process did not change the chemical structure and morphology of the hair, which was shown by FTIR and SEM. In addition, desorption experiments prove that 0.1 mol/L EDTA solution is an efficient eluent for the recovery of Pb(II) from the treated human hair. To summarize, treated human hair showed satisfactory biosorption capacity and can be considered as an effective biosorbent for the treatment of water with a low concentration of heavy metal ions.

Keywords: human hair; heavy metal; kinetics; isotherms; biosorption

1. Introduction

Heavy metal ions are considered extremely harmful to humans, aquatic organisms, and other life forms because of their toxicity, accumulation, and non-biodegradable nature, causing various diseases and disorders [1]. Hence, the removal of heavy metal ions from wastewater has attracted attention for the protection of public health and the environment [2]. Conventional methods for removing heavy metal ions, including chemical precipitation, flotation, ion exchange, evaporation, and membrane processes are practical and cost-effective only with high strength wastewater (which contains high concentration levels of pollutants), and they are ineffective when applied to low strength aqueous effluents with heavy metal ion concentrations less than 100 ppm [3]. Adsorption techniques currently play an important role in the removal of heavy metal ions from wastewater, offering considerable advantages, such as low-cost, availability, profitability, ease of operation, and efficiency [4,5]. Various materials have been developed as adsorbents for the removal of heavy metal ions. In particular, activated carbon is frequently used as an adsorbent due to its high surface area, high adsorption capacity, and high degree of surface reactivity [6]. However, activated carbon is relatively expensive and

is difficult to recycle by eluting the heavy metal ions because of the strong interaction between activated carbon and heavy metal ions. Waste biogenic materials are considered ideal alternative biosorbents for the removal of heavy metal ions from low strength wastewater due to their relatively good cost-effective adsorption capacity [7]. Accordingly, various biogenic materials, including chitosan derivatives [8], agricultural waste materials [9], chicken feathers [10,11], cork waste [12,13], rubber leaf powder [14], chemically modified plant waste [15], and soybean stalks [16], among others, have been proposed and applied as biosorbents to effectively remove heavy metal ions. The good biosorption properties of these biogenic materials are attributed to the presence of abundant metal binding functional groups of these materials, such as carbonyl, carboxyl, hydroxyl, sulphate, sulfur, phosphate, and amido and amino groups [17].

Among natural resources, keratinous materials can be used as biosorbents, either directly or after activation, to remove heavy metal ions due to their intricate networks characterized by high stability, insolubility in water, and high surface area containing many carboxyl, amido, and sulfur functional groups [18]. In addition, keratin is an abundant nonfood protein; in fact, it is the major component of wool, hair, horns, nails, and feathers. Moreover, keratin wastes, such as feathers, horns, nails from butchery [19], human hair from hairdressers, poor quality raw wools from sheep breeding, and some by-products from the textile industry, amount globally to more than four millions tons per year [20]. Several examples of the use of keratinous materials have been already reported, especially using modified keratinous materials. Al-Asheh et al. compared adsorption capacities between inactivated and chemically activated chicken feathers as a biosorbent for removing heavy metal ions (i.e., Cu(II) and Zn(II)) from wastewater [21]. Park et al. prepared wool and silk blend nanofibrous membranes by electrospinning, which exhibited an excellent performance as an adsorbent of heavy metal ions [22]. The Aluigi research group successfully prepared keratin-rich nanofiber mats by electrospinning wool keratin/polyamide blends. This material shows good adsorption capacity for Cu(II) ions from water, with the adsorption capacity increasing with the increase of the specific surface area of the nanofiber mats [23].

Keratinous-composed human hair is considered a ubiquitous waste product and its accumulation can cause environmental problems. Hence, the search for alternatives that take advantage of this waste as a new raw material is of interest, and contributes to the idea of circular economy. In this sense, human hair can contribute significantly in many critical areas of public importance, such as agriculture, medicine, construction materials, and pollution control [24]. In particular, the presence of carboxyl, amido, and disulfide groups in human hair suggest this waste product could be a good biosorbent of several chemicals, including heavy metals, although it has been rarely studied for this application [11]. In this regard, one of the major drawbacks is that its hydrophobic nature in native form limits the diffusion of heavy metal ions from the solution to the external surface of the human hair [22]. To overcome this issue, disulfide bonds present in human hair can be readily oxidized to yield the corresponding cysteic acid residues, which increase the hydrophilic properties of the human hair and subsequently improve its capability to bind positively charged metal ions [25]. For this reason, oxidized human hair was chosen in the present work as a biosorbent for the removal of heavy metal ions from aqueous solutions. Environmental parameters affecting the biosorption process, such the pH value, biosorbent concentration, and contact time were studied. In addition, FT-IR and SEM analysis were conducted for the structural and morphological characterization of the biosorbent after the oxidation pretreatment and after the subsequent heavy metal biosorption process. The kinetic and isotherm data experimentally obtained were correlated with the established kinetic models (pseudo-first order, pseudo-second order, and Weber–Morris intraparticle diffusion model) and with well-known thermodynamic models (Freundlich and Langmuir). A comparison between these was performed. Finally, a desorption/regeneration test was performed in order to study the reusability of the biosorbent.

2. Experimental

2.1. Chemicals

All the chemicals used in this work were of analytical grade. Stock solutions of separate heavy metal ions, such as Cr(III), Mn(II), Ni(II), Co(II), Cu(II), Zn(II), Cd(II), and Pb(II) were prepared by dissolving their nitric salts (>99%, all from Panreac, Spain) in deionized water. A 1000 ppm stock solution of metal ions was first prepared, which was then diluted to the initial heavy metal concentration for each experiment. Sodium hydroxide (>98%, Panreac, Spain) and nitric acid (>70%, JT-Baker, Spain) were alternatively used for the pH adjustment of the initial aqueous solution prior to commencing the biosorption experiments. In all the experiments, the initial pH was measured, and usually the final pH was also checked, using an Omega 300 pH meter (Crison instruments, S.A., Spain).

2.2. Human Hair

Human hair waste (from different male individuals of approximately 13 years of age) was collected from local barbershops. The human hair samples were mixed together, washed with common laboratory detergent, rinsed several times with deionized water (purified with a milli-Q Gradient system from Millipore Corporation) and then left to dry at room temperature (22 ± 1 °C). The hair was cut to an approximate length of 1–2 mm using scissors.

2.3. Chemical Treatment of Human Hair

The treatment process of the human hair was carried out as follows: 20.0 g of the untreated human hair was weighed and soaked in 400 mL of the pretreatment reagent of known concentration (10% H_2O_2, originally at 35% in water, from Sigma-Aldrich, Germany) and at adjusted pH of 9 (pH 9.0 yields better biosorption results in comparison with others, when pH 5.0, pH 7.0 and pH 9.0 are assayed) [26]. After a given soaking time (5 h), the solution was filtered. The hair separated from the solution was washed many times with deionized water. To minimize any loss of the treated hair, at each washing step, the hair was separated by centrifugation, and the liquid was then decanted. Finally, the treated and cleaned hair was dried at room temperature.

2.4. Characterization of Human Hair

Structural characterization of the human hair was carried out to analyze any chemical change produced in the samples after the oxidative pretreatment and/or after the biosorption of heavy metals. The identification of the functional groups in the untreated and treated human hair was performed using a Fourier transform infrared (FT-IR) spectrometer (Tensor 27, Bruker, Germany). The spectra were recorded in the range of 600–4000 cm^{-1} with 16 scans and a resolution of 4 cm^{-1}. The surface morphology of the human hair samples (untreated and treated) was observed by scanning electron microscope (SEM; ZEISS EVO® MA 10, Oberkochen, Germany). The samples used the sputter-coating arrangement.

2.5. Heavy Metal Ions Biosorption Experiments

The uptake of heavy metal ions onto the hair systems was carried out by batch experiments at a constant temperature (22 ± 1 °C) on a rotary mixer (CE 2000 ABT-4, SBS Instruments SA, Barcelona, Spain) at 25 rpm. In all sets of experiments, 0.1 g of human hair (untreated or treated) was weighed in 50 mL plastic extraction tubes; the 10 mL of heavy metal ion aqueous solution was added and the final system was shaken for a certain period of time. Usually, the concentration of each heavy metal ion was 0.10 mmol/L (for multiple heavy metal system containing eight ions) and 0.18 mmol/L (in the multiple-metal system containing four ions, and also in the single-metal systems). The pH was adjusted to 4.0, unless otherwise specified. The initial pH of the multiple heavy metal aqueous solution was varied within the range 1.0 to 6.0 (higher pH values were not considered to avoid precipitation

of metal hydroxides). To study the effect of the biosorbent concentration on metal uptake, its mass was varied from 1 to 20 g/L. The effect of the initial metal ion concentration on biosorption isotherms was studied in single-metal systems with 0.1 g of treated human hair. A range of initial metal ion concentrations from 0.5×10^{-3} to 2.0 mmol/L was used. In all cases, after agitation, the two phases were separated by decantation and the liquid was filtered through 0.22 μm syringe Millipore filters (Millex-GS, Millipore, Ireland). Then, the heavy metal concentration in the remaining aqueous solution was determined by an inductively coupled plasma optical emission spectrophotometer with mass detector, ICP-MS (XSERIES 2 ICP-MS, Thermo Scientific, Bremen, Germany).

The uptake of the metal ions by human hair was calculated using Equation (1), which quantifies the biosorption efficacy:

$$\% \; biosorption = \frac{C_i - C_f}{C_i} \times 100 \tag{1}$$

where C_i and C_f are the initial and the final concentration of heavy metal in the aqueous phase solution, respectively (in mmol/L).

The amount of metal sorbed per unit of mass of biosorbent at time t (q_t in mmol/g) was calculated using Equation (2):

$$q_t (\text{mmol/g}) = \frac{(C_i - C_f) \times V}{W} \tag{2}$$

where V is the total volume of the solution (in L), W is the amount of biosorbent (in g), and C_i and C_f are the initial and the final concentrations of heavy metal in the aqueous solution (each given in units of mmol/L), respectively.

The amount of metal sorbed at the equilibrium per unit of mass of biosorbent (q_e in mmol/g) was obtained as follows:

$$q_e (\text{mmol/g}) = \frac{(C_i - C_e) \times V}{W} \tag{3}$$

where V is the total volume of the solution (in L), W is the amount of biosorbent (in g), and C_i and C_e are the initial and equilibrium concentrations of heavy metal in the aqueous solution (each given in units of mmol/L), respectively.

All batch biosorption experiments were carried out in duplicate and the results are reported as their average in the corresponding figures (experimental errors found were less than 2.5% and 0.0025 mmol/g in the biosorption percentage and the biosorption capacity, respectively).

2.6. Desorption, Regeneration and Reuse

Desorption experiments were performed only for the removal of Pb(II) from treated human hair samples as biosorbent. Each hair sample containing the adsorbed Pb(II) was contacted and stirred with 10 mL of 0.1 mol/L HNO_3 or 10 mL of 0.1 mol/L EDTA. After 24 h of mixing (with the rotary mixer) at room temperature (22 ± 1 °C), the aqueous and solid phases were separated by centrifugation and subsequent filtration, and the Pb(II) content of the final solution was analyzed by ICP-MS, as indicated in Section 2.5. Desorption percentage was calculated using Equation (4):

$$\% \; desorption = \frac{amount \;\; of \;\; Pb(II) \;\; desorbed}{amount \;\; of \;\; Pb(II) \;\; adsorbed} \times 100 \tag{4}$$

The reuse of the treated human hair in a second biosorption step, after elution of the adsorbed metal ions (with nitric acid or EDTA), requires the cleaning of the remaining eluting solution from the surface of the biomaterial. The treated human hair was washed with deionized water and dried in an oven at 40 °C overnight. These regenerated human hair samples were employed to adsorb heavy metals again.

All batch biosorption, desorption, and regeneration experiments were carried out in duplicate and the results are reported as their average in the corresponding figures (experimental errors found were

less than 2% and 0.002 mmol/g, in the biosorption and desorption percentages and the biosorption capacity, respectively).

3. Results and Discussion

3.1. Comparison of Biosorption Efficacy between Untreated and Treated Human Hair

The oxidation of human hair usually takes place with hydrogen peroxide in an acid or alkaline medium by attacking the disulfide bond of keratin. As a result of this reaction, sulfonic acid groups are formed, and hair samples are functionalized. In an alkaline medium, the oxidation process is much more effective [26]. Moreover, during oxidation, other proteins in the human hair are also oxidized, which leads to cell membrane damage causing the cortex and the cuticle to open and separate. The objective of this pretreatment is to increase the hydrophilicity of the human hair surface and also to increase its specific surface area. The biosorption capacities of untreated and treated human hair samples for recovering eight metal ions (Cr(III), Mn(II), Ni(II), Co(II), Cu(II), Zn(II), Cd(II), and Pb(II)) were determined. The obtained results are shown in Figure 1. As seen from the figure, the metal biosorption capacity of chemically treated human hair is significantly better than that of untreated human hair. Moreover, the affinity of both types of hair for Cr(III), Cu(II), and Pb(II) is greater than that for the other metal ions, which can be explained by the stronger interactions between the functional groups of the biosorbent and these three metal ions. The metal biosorption onto the treated human hair follows in the order of Cr(III) > Pb(II) > Cu(II) > Cd(II) > Ni(II) > Co(II) > Mn(II) > Zn(II). Finally, four metal ions, namely, Cr(III), Cu(II), Cd(II), and Pb(II), were selected from those metals to study the biosorption mechanism of treated human hair in subsequent experiments.
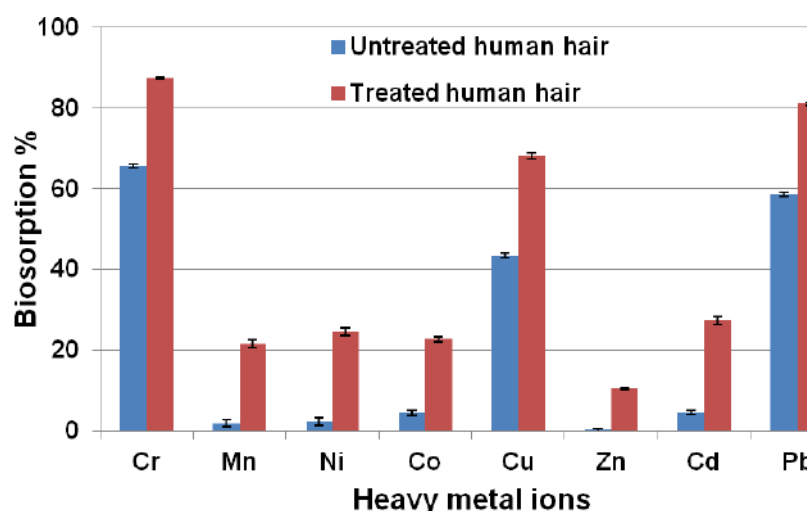

Figure 1. Comparison of biosorption between untreated and treated human hair in a multiple-metal system. The initial metal ion concentration was 0.1 mmol/L, the contact time was 24 h, the pH was 4.0, and the biosorbent was 0.1 g in 10 mL of the initial solution.

3.2. FT-IR and SEM Characterization

In order to understand how metal ions bind to the biosorbent, it is essential to identify the functional groups of its surface as these could be responsible for the metal binding. Thus, the untreated, treated, and metal loaded-treated human hairs were discriminated by FT-IR, as can be seen from the infrared spectra collected in Figure 2. The full-scan spectra of human hair (Figure 2a) display their corresponding infrared peaks. The broad and medium intensity band ranging from 3000 to 3600 cm^{-1} is indicative of the stretches of the bonds belonging to the carboxylic acid (-COOH), alcohol (-OH), and amino acid (-NH$_2$) groups. The peaks located at 1632 cm^{-1} (amide I), 1520 cm^{-1} (amide II), and 1241 cm^{-1} (amide III) are related to typical human hair amino acids. The peaks at 1041, 1075, 1180, and 1229 cm^{-1} all

correspond to different products of cystine oxidation in human hair, and their peak assignment belongs to sulfonate (S-O sym. stretch), cystine monoxide (R-SO-S-R), sulfonate (S-O asym. stretch), and cystine dioxide (R-SO2-S-R), respectively. Carefully comparing the spectra of the three different hair samples, some differences can be seen between them, as expected, due first to the oxidation process (treated human hair), and, later, to the metal biosorption (metal loaded-treated human hair), particularly in the region from 850 to 1750 cm^{-1} (see Figure 2b). The intensity of the peaks at 1041 and 1180 cm^{-1} increased after chemical pretreatment, which means that conversion of cystine to cysteic acid, cystine monoxide, and cystine dioxide, as well as to sulfonates, occurred during this treatment process. The weak broad shoulder between approximately 1000 and 1130 cm^{-1} in the untreated human hair infrared spectra is probably due to environmental factors, such as sunlight, chlorinated water, and frequent shampooing causing partial oxidation of the hair surface [27]. The FT-IR spectra from treated human hair before and after the metal biosorption are very similar, indicating that the main functional groups on treated human hair did not change during the metal biosorption process (which can be an indication of a possible reuse of such biomaterial). However, the slight differences found around 1400 cm^{-1}, and some red shift of the emission spectra (from 3277.2 cm^{-1} to 3274.8 cm^{-1}, from 1526.8 cm^{-1} to 1519.7 cm^{-1}, and from 1078.4 cm^{-1} to 1074.9 cm^{-1}), before and after the biosorption process, is probably related to the presence of the heavy metal ions on the hair surface. Based on the FT-IR spectra changes, as seen in Figure 2, some hair surface chemical functional groups (including hydroxyl, amino, carboxyl, and sulfonic acid) could act as important biosorption sites for heavy metal ions.
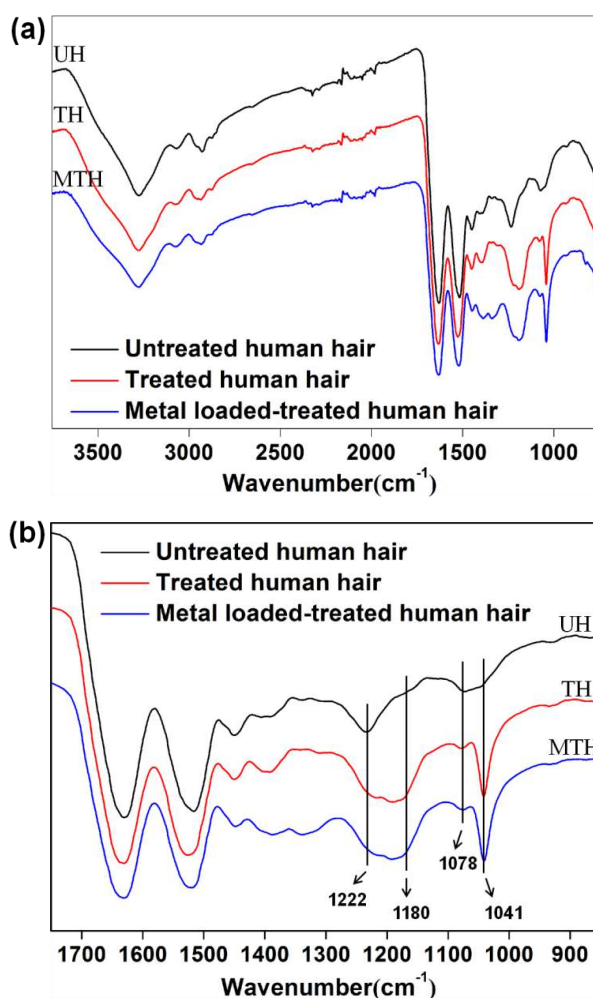

Figure 2. FT-IR spectra of human hair. UH: untreated human hair, TH: treated human hair, MTH: metal loaded-treated human hair. (**a**) Full-scan spectra, and (**b**) spectra in the range from 850 to 1750 cm^{-1}.

The scanning electron microscopy (SEM) technique was applied to address concern about the alteration of the human hair surface morphologies in the different cases of the study. Figure 3 shows the SEM micrographs of the untreated, treated, and metal-loaded treated human hair. It is observed that each cuticle scale of the human hair is uniquely shaped. Some have smooth rounded edges and others have jagged edges, overlapping each other as they ascend along the length of the fiber towards the tip (Figure 3). The surface topographies of the untreated and treated human hair are different (see Figure 3a,b for comparison): the majority of the cuticle scales of the treated human hair fibers represent a more jagged appearance, probably due to the oxidation treatment. After metal biosorption, the surface appears to be somewhat smoother compared with the hair prior to its use, suggesting that the cuticle scales are closed through biosorption, probably due to the acidic water media (see Figure 3b,c).
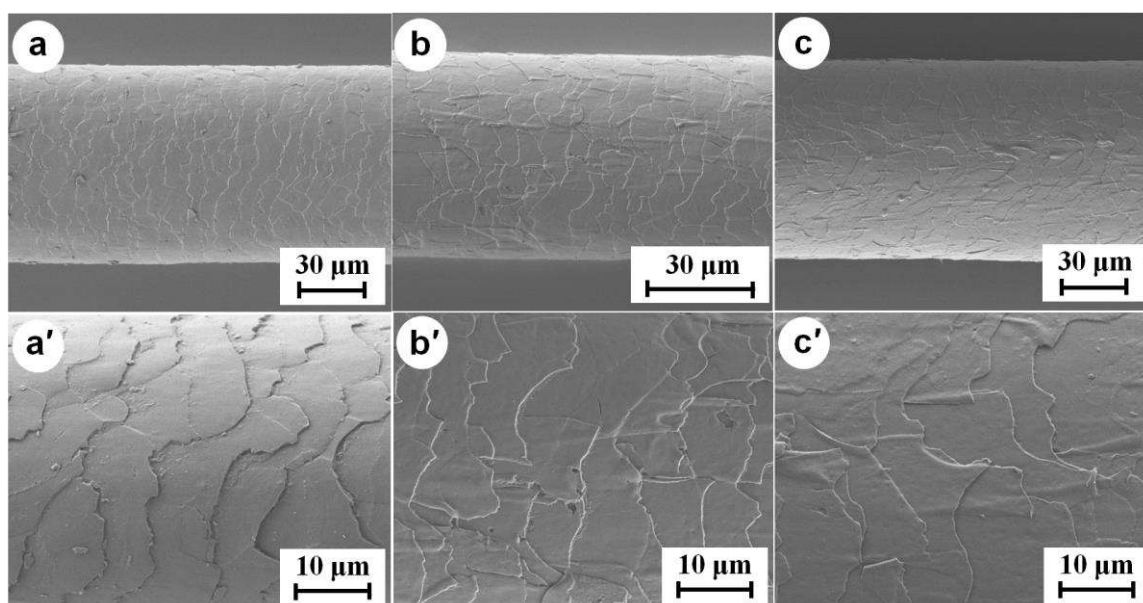

Figure 3. Scanning electron microscopy (SEM) micrographs of the human hair: (**a**) and (**a'**) correspond to the untreated human hair; (**b**) and (**b'**) correspond to the treated human hair; and (**c**) and (**c'**) correspond to the metal loaded-treated human hair.

3.3. Effect of the pH in Multiple Metal System

The pH level of the aqueous solution is an important variable for the biosorption of metal ions onto the biosorbents, due to the metal speciation and the speciation of the chemical functional groups present on the biosorbent's surface. The pH was controlled at the beginning and end of the experiments in order to evaluate any differences. The changes observed were lower than 0.3 units, and thus considered not significant.

The effect of the pH solution on the removal efficacy of the treated human hair for Cr(III), Cu(II), Cd(II), and Pb(II) was studied between pH 1.0 and 6.0 in the multiple-metal system (Figure 4). As observed from the results in Figure 4, the biosorption of metal ions increases significantly with increasing the pH. This behavior can be explained by the competition between the protons and the metal ions for the same binding site on the surface of the treated human hair. At low pH values, the surface of the biosorbent would also be surrounded by H^+ ions, which decrease the Cr(III), Cu(II), Cd(II), and Pb(II) ions interaction with binding sites of the treated human hair. As the pH increases, the basic forms of the chemical functional groups on the hair surface predominate, increasing negative charge, so metal cation biosorption increases. However, when the pH is around 5, the partial hydrolysis of metal ions (particularly for Cu; the remaining metals could occur at pH higher than 5) results in the formation of $M(OH)_n^{(m-n)}$ species affecting the biosorption hair capability. The biosorption percentage

found could be related to the precipitation of the metals. Therefore, pH 4.0 was selected as the optimal condition in the subsequent experiments.
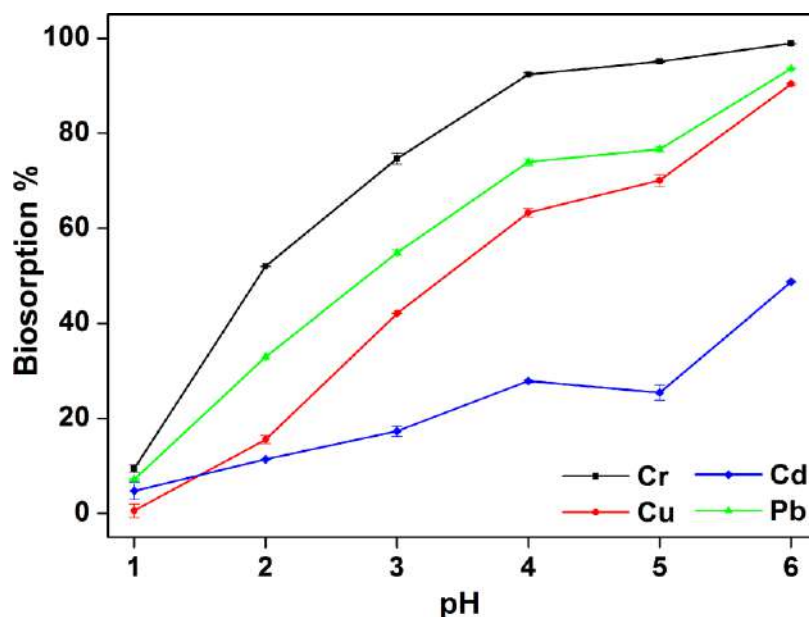

Figure 4. Effect of pH on the biosorption of the treated human hair for Cr(III), Cu(II), Cd(II), and Pb(II) in the multiple-metal system. The initial concentration was 0.18 mmol/L, the contact time was 24 h, and the biosorbent was 0.1 g in 10 mL initial solution.

3.4. Effect of Biosorbent Concentration

The effect of the biosorbent concentration on the removal efficacy of Cr(III), Cu(II), Cd(II), and Pb(II) ions was studied in the range of 1–20 g/L in a multiple-metal system (Figure 5). It was observed that the removal efficacy of the treated human hair for Cr(III), Cu(II), Cd(II), and Pb(II) ions increased with the increase of biosorbent concentration (Figure 5a). This can be explained by the increase in surface area of the biosorbent when increasing its amount, which in turn increases the binding sites. For Cr(III) and Pb(II), the sorbed metal ion (mmol) per unit weight of biosorbent significantly decreased by increasing the biosorbent concentration (Figure 5b). This can be explained due to the fact that at high biosorbent concentration, the available metal ions in the aqueous solution are insufficient to cover all the biosorbent sites due to the corroborated high affinity of these two metals (as can be seen from results collected in Figures 1 and 4). Furthermore, the metal uptakes (mmol/g) for Cu(II) and Cd(II) are basically stable with the increase of biosorbent concentration; this means the biosorption quantity of Cu(II) and Cd(II) increases through increasing the biosorbent concentration. Thus, functional groups induced on the biosorbent hair surface have stronger affinity for Cr(III) and Pb(II) than for Cu(II) and Cd(II).
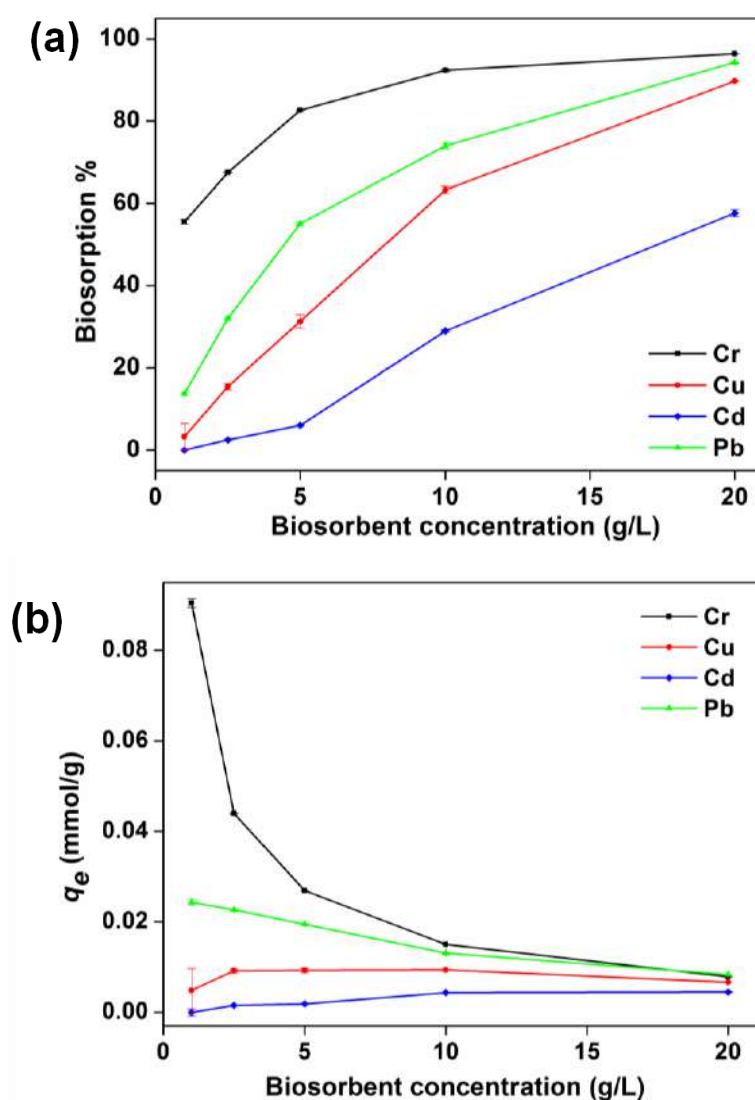
Figure 5. Effect of the biosorbent concentration on the percentage of biosorption (**a**) and on the amount of sorbed metal ion per unit weight of biosorbent (**b**) of the treated human hair for Cr(III), Cu(II), Cd(II), and Pb(II) in the multiple-metal system. The initial metal ions concentration was 0.18 mmol/L, the contact time was 24 h, and the pH of the 10 mL initial aqueous solution was 4.0.

3.5. Effect of Contact Time

Contact time with aqueous contaminated samples is an important parameter for successful usage of biosorbents in practice. Multiple- and single-metal aqueous systems (at pH = 4) of Cr(III), Cu(II), Cd(II), and Pb(II) were placed in contact with treated human hair (0.1 g) for periods of 5, 10, 20, 30, and 45 min, and 1, 2, 3, 4, 6, 12, 24, 48, and 72 h. Results plotted in Figure 6 show the biosorption capacity of treated human hair for removing Cr(III), Cu(II), Cd(II), and Pb(II) ions. Three steps can be differentiated during biosorption: the initial step with fast metal biosorption, the second step with gradual biosorption, and the third step, which can be related to the equilibrium uptake. The first step can be related to the diffusion of metal species from the solution to the external surface of the hair, which occurred instantaneously. The second step corresponds to a gradual biosorption uptake of heavy metal ions until reaching an equilibrium (the third stage). For each metal ion, the biosorption efficacy is higher for the single-metal system than for the multiple-metal system. Among these, the percentage of biosorption for Cd(II) is outstanding, with an increase from 29% to 86%. Furthermore, the single-metal system reached the biosorption equilibrium more rapidly than the multiple-metal system (around

only 30 min in the former case), which is attributed to the effect of the competition between the heavy metal ions. Therefore, the selectivity order is Cr(III) > Pb(II) > Cu(II) > Cd(II), which corresponds to biosorption efficacy in the single-metal system of 98%, 96%, 95%, and 86%, respectively.
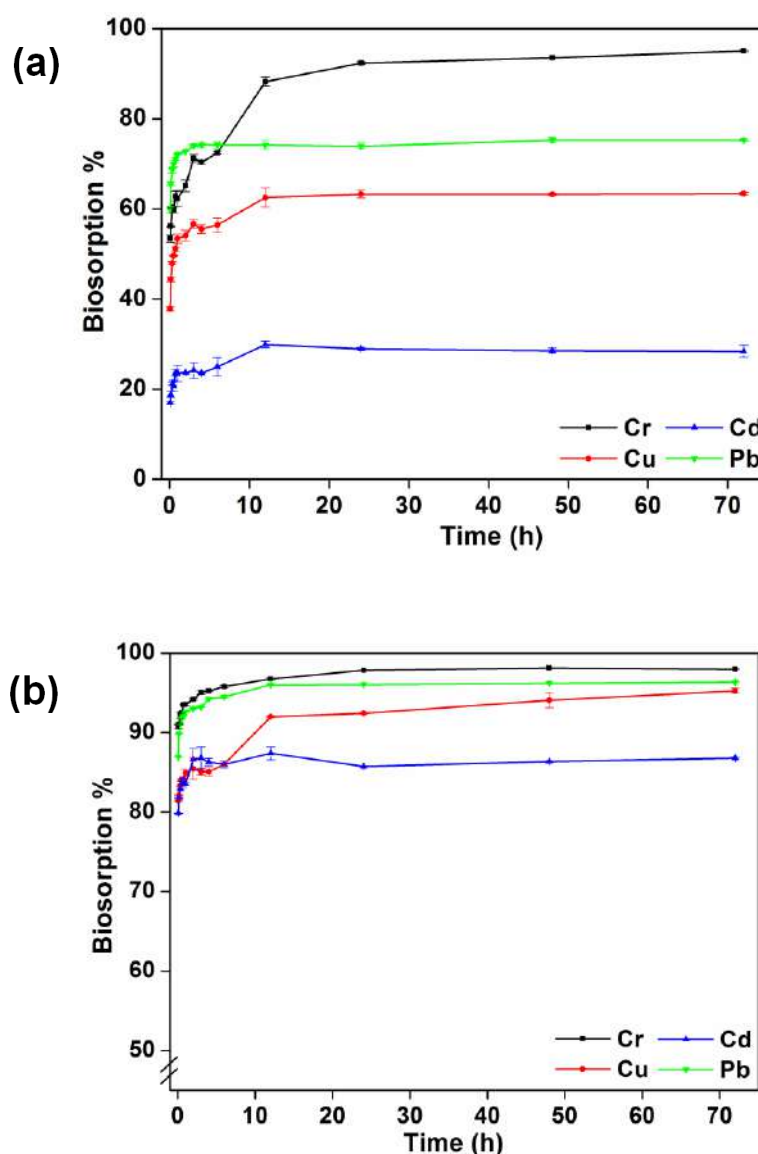

Figure 6. Percentage of biosorption of the treated human hair for Cr(III), Cu(II), Cd(II), and Pb(II) at different contact times. (**a**) Multiple-metal system, and (**b**) single-metal system. The initial metal ion concentration was 0.18mmol/L, the pH was 4.0, and the sorbent concentration was 10 g/L.

3.6. Kinetic Studies

Kinetic models have been used to model experimental data in order to investigate the mechanism of biosorption. Furthermore, it is important to determine the potential rate controlling steps, such as mass transport, chemical reaction, and intraparticle diffusion processes, in such systems. Many attempts have been made to formulate a general expression describing the kinetics of liquid–solid phase sorption systems [28]. In the present case, the kinetic models applied to the treated human hair as a biosorbent of heavy metals in solution were the pseudo-first order equation [29], the pseudo-second order equation, and the Weber–Morris intraparticle diffusion model. These are given by Equations (5)–(7), respectively:

$$\log(q_e - q_t) = \log q_e - \frac{k_1}{2.303}t \tag{5}$$

$$\frac{t}{q_t} = \frac{1}{k_2 q_e^2} + \frac{t}{q_e} \tag{6}$$

$$q_t = k_3 t^{1/2} + k_d \tag{7}$$

where, q_e and q_t are the amount of biosorbed metal ions per unit of mass biosorbent (in mmol/g) at the equilibrium and at time t (min), respectively; k_1 (in min^{-1}) is the rate constant of the pseudo-first order equation; k_2 (in g/(mmol·min)) is the rate constant of the pseudo-second order equation; k_3 is the intraparticle diffusion rate constant (in mmol/(g·min$^{1/2}$)); and k_d is the intercept that relates to the thickness of the boundary layer.

Experimental data were fitted to pseudo-first and pseudo-second order kinetic models and the rate corresponding constants (k), correlation coefficients (R^2), and q_e were estimated (values shown in Table 1). It is noteworthy that the pseudo-first order equation does not fit well for the whole range of time, which is generally applicable only over the initial time of the sorption processes, i.e., 30 and 60 min for the multiple- and single- metal biosorption systems, respectively [30]. Moreover, for the four metal ions in single and multiple systems, the calculated q_e did not match well with experimental data, which suggests the insufficiency of the pseudo-first order model to fit the experimental data.

The pseudo-second order model is more likely to predict kinetic behavior for the whole range of time studied, which indicates that chemical sorption is the rate-controlling step [31]. Correlation coefficients were always greater than 0.999, and the values of the predicted equilibrium biosorption capacities showed a good correlation with the experimental q_e values for all four metal ions in both systems. This shows that the biosorption process perfectly complies with the pseudo-second order model. In other words, the chemical sorption due to the formation of chemical bonds between the metal and sorbent in a monolayer onto the surface is the rate-controlling step [32]. The equilibrium biosorption capacities for Cr(III), Cu(II), Cd(II), and Pb(II) were 0.0166, 0.0174, 0.0165, and 0.0174 mmol/g, respectively, in the single-metal system, and 0.0155, 0.00945, 0.00429, and 0.0133 mmol/g, respectively, in the multiple-metal system.

Table 1. Sorption kinetic constants in the multiple- and single-metal systems for Cr(III), Cu(II), Cd(II), and Pb(II) for both pseudo-first and pseudo-second order models.

Metal		Cr		Cu		Cd		Pb	
System		Single	Multiple	Single	Multiple	Single	Multiple	Single	Multiple
Pseudo first order	$k_1 \times 10^3$ (min^{-1})	9.21 [a]	4.19 [b]	6.91 [a]	15.0 [b]	26.3 [a]	12.9 [b]	26.8 [a]	27.3 [b]
	q_e (mmol/g)	0.00132	0.00655	0.00263	0.00346	0.00151	0.00190	0.00173	0.00233
	R^2	0.9327	0.7343	0.9905	0.8794	0.9136	0.8592	0.8381	0.9030
Pseudo second order	k_2 (g/mmol min)	15.4	1.51	3.83	6.75	38.2	16.2	17.8	16.6
	q_e (mmol/g)	0.0166	0.0155	0.0174	0.00945	0.0165	0.00429	0.0174	0.0133
	R^2	1.000	0.9993	0.9999	0.9999	1.000	0.9997	1.000	1.000
	k_d (mmol/g)	0.0151	0.00831	0.0145	0.00517	0.0148	0.00223	0.0157	0.0103

[a]: 30 min, [b]: 1 h.

For the single-metal system, the kinetic constant values found for the pseudo-second order model (k_2) decreased in the following order: Cd (II) > Pb(II) > Cr(III) > Cu(III). This indicates that Cd (II) was more easily and rapidly adsorbed by treated human hair than Pb(II), Cr (III), and Cu (II). In this case, the sorption rate was lower for the heavy metal with the smallest ionic radius since Cu(II) has an ionic radius of 0.069 nm compared to 0.097 nm for Cd(II), 0.119 nm for Pb(II), and 0.070 nm for Cr(III).

The pseudo-first and pseudo-second order models cannot provide information about the diffusion mechanism controlling biosorption. Thus, the Weber–Morris intraparticle diffusion model was adjusted [33]. The plots of q_t versus $t^{1/2}$ are shown in the Figure 7. Unlike some simple cases, mathematical formulations representing the diffusion and biosorption are generally solvable analytically. In this case, these plots can be divided into multi-linear correlations, which indicates that the biosorption process take place in three steps and is not controlled solely by the intraparticle diffusion mechanism. The first stage corresponds to the sharper stage, where the metal ions move from the solution to the external surface of the biosorbent, through film diffusion, or the boundary layer diffusion of the metal species [34]. The second step describes the gradual biosorption onto the surface of the treated hair, where the intraparticle diffusion is the rate-limiting [35]. The third stage corresponds to the final biosorption equilibrium where the intraparticle diffusion starts to slow down due to extremely low metal ion concentration left in the solution. The presence of these three stages in the plots (Figure 7) suggests that the film diffusion and intraparticle diffusion were simultaneously controlling the biosorption process and both are enhanced with the increase of the initial metal concentration.
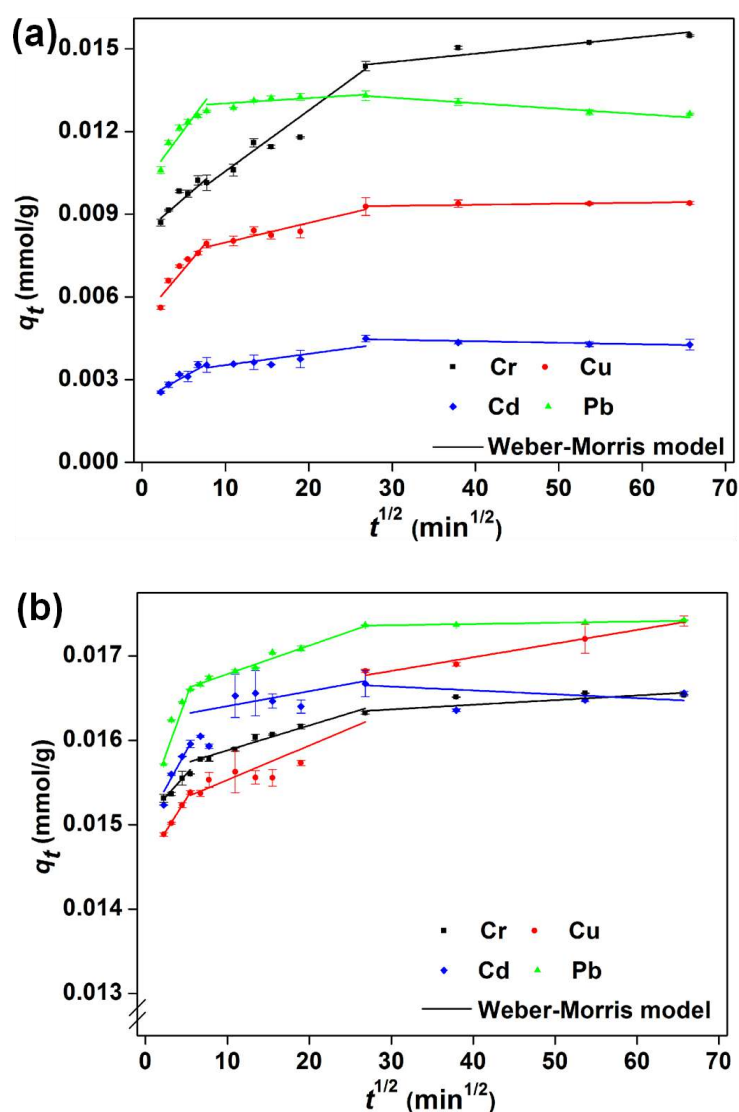

Figure 7. Weber–Morris intraparticle diffusion kinetic model applied for the metal ion biosorption onto the treated human hair, with time: (**a**) in the multiple-metal system, and (**b**) in the single-metal system.

3.7. Thermodynamic Isotherm Characterization

Sorption isotherms at equilibrium are very important data to understand the mechanism of each sorption system from a physicochemical perspective. The sorption capacity of a sorbent can be also described by the equilibrium sorption isotherm, which is characterized by some specific constants whose values provide information about the affinity between the liquid–solid sorption systems.

In the present study, two isotherm models were selected to fit the experimental data, namely, the Freundlich and Langmuir isotherm models [36]. The linear forms of the Freundlich and Langmuir isotherms are presented by Equations (8) and (9), respectively:

$$\log q_e = \log k_F + \frac{1}{n} \log C_e \tag{8}$$

$$\frac{C_e}{q_e} = \frac{b}{K_L} C_e + \frac{1}{K_L} \tag{9}$$

where C_e is the equilibrium concentration of the metal ion in the residual solution (in mol/L); q_e is the amount of the sorbed metal at the equilibrium per unit of mass of sorbent (in mol/g); k_F and n are Freundlich constants; and $K_L = Q_0 b$, where Q_0 and b are the Langmuir constants, corresponding to the saturation concentration of the sorbed metal ion per unit of mass of sorbent (in mol/g) and the ratio of sorption/desorption rates (in L/mol), respectively.

For both models and following Equations (8) and (9), $\log q_e$ versus $\log C_e$ and C_e/q_e versus C_e are calculated and compared with the experimental data, respectively. In addition, all the constants and correlation coefficients obtained for each model are summarized in Table 2.

Table 2. Freundlich and Langmuir isotherm constants for the biosorption of Cr(III), Cu(II), Cd(II), and Pb(II) by the treated human hair.

	Constant	Cr	Cu	Cd	Pb
Freundlich	$K_F \times 10^3$	1.56	2.87	0.546	0.247
	n	2.30	1.90	2.86	3.63
	R^2	0.8646	0.8402	0.9291	0.8607
Langmuir	$Q_0 \times 10^5$ (mol/g)	9.47	5.57	3.77	3.61
	$B \times 10^{-4}$ (L/mol)	1.07	2.06	8.64	8.04
	K_L (L/g)	1.01	1.15	3.26	2.90
	R^2	0.9912	0.9905	0.9952	1.000
	$-\Delta G^0$ (kJ/mol)	22.8	24.4	27.9	27.7

From the correlation coefficient values of both isotherm equations, it was observed that the Langmuir isotherm fitted the data better than the Freundlich isotherm, showing that the biosorption process relies on a specific site's sorption mechanism where adsorbate molecules occupy specific sites on the biosorbent. In Figure 8, experimental and calculated data for the Langmuir isotherm model are represented showing good correlation between the data. Taking on board the Langmuir equation, the saturated biosorption capacities of the treated human hair at 295 K for Cr(III), Cu(II), Cd(II), and Pb(II) were 9.47×10^{-5}, 5.57×10^{-5}, 3.77×10^{-5}, and 3.61×10^{-5} mol/g, respectively.

It is worth noting that the theoretical maximum values of adsorption capacity given by the Langmuir equation (Q_o) for the treated human hair were found to decrease in the order Cr (III) > Cu(II) > Cd(II) ~Pb(II). The metals with highest absorption capacities are those with lowest ionic radius, i.e., Cu(II) and Cr(III), while Pb(II), which has the largest ionic radius (0.119 nm), shows the smallest sorption capacity. This observed trend, based on the ionic radius, may be caused by the quick saturation of adsorption sites induced by the largest ions. This behavior is in agreement with that observed for the absorption of Pb(II), Cd (II), Ni(II), and Zn(II) using natural zeolite as a sorbent, where the adsorbed amount decreased as the ionic radius increased [37].
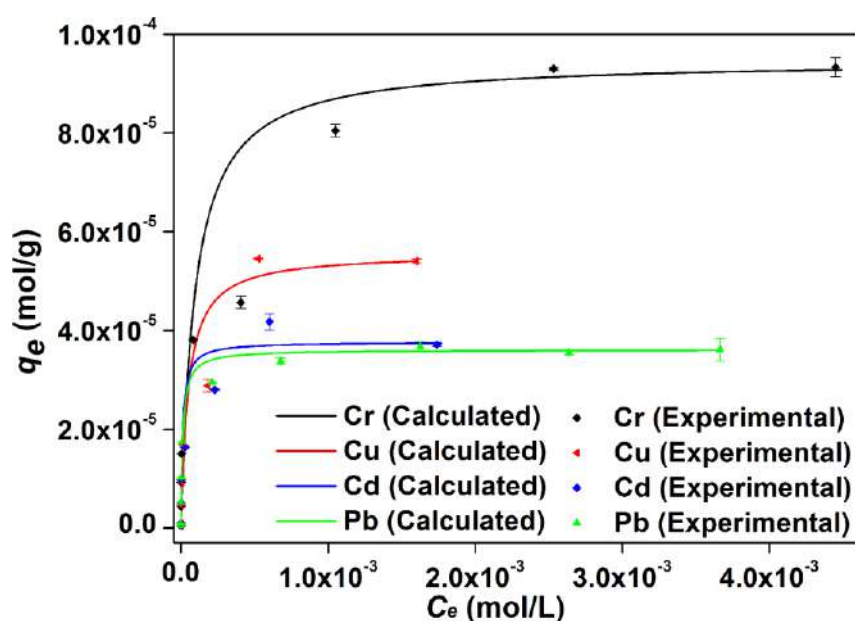
Figure 8. Experimental (.) and calculated (-) values adjusting using the Langmuir isotherm model for the sorption of Cr(III), Cu(II), Cd(II), and Pb(II) using the treated human hair.

In addition, from the estimated Langmuir sorption/desorption constant, the standard Gibb's free energy (ΔG^0) of the biosorption process can be evaluated by using Equation (10):

$$\Delta G^0 = -RT \ln b \tag{10}$$

where b is the Langmuir equilibrium constant shown in Equation (8), R is the universal gas constant (8.314 J/mol K), and T is the absolute temperature (K). The standard Gibb's free energy (ΔG^0) values are shown in Table 2. The negative ΔG^0 values indicate that the biosorption of metals into human hair is thermodynamically feasible and of spontaneous nature.

3.8. Desorption, Regeneration, and Reuse Studies

Recovery of the adsorbed heavy metals and reuse of the biosorbent are of significance from the viewpoint of practical application. As indicated previously, two eluent solutions, EDTA and HNO_3, were screened for their potential to desorb Pb(II) ions from metal-adsorbed treated human hair (98% of biosorption). Both eluents can effectively desorb the heavy metal ions from the metal loaded-treated human hair, with the elution efficiency of EDTA solution being slightly better than that of the HNO_3 solution, 89% ± 1% and 85% ± 1%, respectively. EDTA may combine both acidic and complexing effects, while nitric acid only has the acidic effect to liberate the adsorbed metals, which explains the higher ability of EDTA for removing the metal. In addition, the ability of EDTA to complex heavy metals, such as lead, due to the high complex constant, is well known.

The reuse of regenerated human hair for the possible continuous removal of heavy metals was investigated. After the desorption process, the hair samples were washed several times (following two different methods of cleaning), dried in an oven at 40 °C overnight, and their performance in a second biosorption step of fresh Pb(II) aqueous sample was then checked. The results show that the metal removal percentages (in the second biosorption step) of the regenerated hair samples are dependent on the elution methods. When using EDTA as eluent and deionized water for rinsing the used biomaterials, the Pb(II) removal percentage was 87 ± 2 %, while for samples eluted with HNO_3 the metal removal was 38 ± 4 %. Consequently, although HNO_3 is a very powerful metal eluent, it shows negative effects for the reuse of hair samples and results in a decrease of metal uptake capacity during the second application. This is probably because the acidic environment after the desorption

step with nitric acid leads to the ionization state of functional groups on the biomaterial's surface, thus becoming a competitive medium for the next metal biosorption step. To confirm this concept, another set of samples were first eluted using EDTA, then rinsed with HNO_3 solution, and later washed with deionized water and dried. The biosorption capacities of the regenerated human hair samples by this method also decreased the second time (75 ± 1 %). It is clear that the desorption of metal adsorbed onto the biomaterials using HNO_3 negatively affects their reuse.

4. Conclusions

Chemically treated human hair behaved better than untreated hair in the process of removing metals from aqueous effluent. In particular, treated human hair was demonstrated to be an effective biosorbent for the removal of Cr(III), Cu(II), Cd(II), and Pb(II), and showed less effectiveness for metals such as Ni(II), Co(II), Mn(II), and Zn(II). It was observed that the operating parameters controlling the biosorption process, such as the pH of the aqueous heavy metal solution, the biosorbent concentration, and the contact time, had a significant influence on the metal uptake. In addition, treated human hair showed higher biosorption capacity when metals were applied in the single-system compared with the multiple-system solution, due to the induced competition between metal ions for the biosorbent sites. In the single system, removal efficacy of the treated human hair was found to be 86% for Cd(II), 92% for Cu(II), 96% for Pb(II), and 98% for Cr(III) when working with 10 g/L of biosorbent concentration at pH = 4.0.

According to the kinetic study, the biosorption of metal ions onto the treated human hair followed well the pseudo-second order kinetic model. Hence, physico-chemical interaction between induced functional groups (i.e., sulfonic acid groups as demonstrated by FTIR) in treated hair and metal ions is the fundamental mechanism controlling biosorption, with the film diffusion being the rate limiting step. Biosorption at equilibrium was better correlated with the Langmuir isotherm model compared to the Freundlich model, corroborating the finding that the mechanism of sorption is based on site-specific molecular sorption. The calculated standard Gibb's free energy (ΔG^0) indicated the thermodynamically feasible and spontaneous nature of the biosorption process.

Preliminary desorption experiments proved that EDTA and HNO_3 solutions were efficient eluents for the recovery of Pb(II) from the treated human hair. In particular, the treated human hair regenerated with EDTA showed the best biosorption efficiency when reused.

Taking into consideration the present findings, it can be stated that treated human hair could potentially be used as an effective and low-cost biosorbent for the removal of heavy metal ions from aqueous solution.

References

1. Jaishankar, M.; Tseten, T.; Anbalagan, N.; Mathew, B.B.; Beer, K.N. Toxicity, mechanism and health effects of some heavy metals. *Interdiscip. Toxicol.* **2014**, *7*, 60–72. [CrossRef]
2. Vilela, D.; Parmar, J.; Zeng, Y.; Zhao, Y.; Sánchez, S. Graphene-Based Microbots for Toxic Heavy Metal Removal and Recovery from Water. *Nano Lett.* **2016**, *16*, 2860–2866. [CrossRef]

3. Saeed, A.; Iqbal, M.; Akhtar, M.W. Removal and recovery of lead(II) from single and multimetal (Cd, Cu, Ni, Zn) solutions by crop milling waste (black gram husk). *J. Hazard. Mater.* **2005**, *117*, 65–73. [CrossRef]

4. Ostovaritalab, M.; Hayati-Ashtiani, M. Investigation of Cs(I) and Sr(II) removal using nanoporous bentonite. *Part. Sci. Technol.* **2019**, *37*, 877–885. [CrossRef]

5. Shiferaw, Y.; Yassin, J.M.; Tedla, A. Removal of organic dye and toxic hexavalent chromium ions by natural clay adsorption. *Desalin. Water Treat.* **2019**, *165*, 222–231. [CrossRef]

6. Koohzad, E.; Jafari, D.; Esmaeili, H. Adsorption of lead and arsenic ions from aqueous solution by activated carbon prepared from tamarix leaves. *ChemistrySelect* **2019**, *4*, 12356–12367. [CrossRef]

7. De Freitas, G.R.; da Silva, M.G.C.; Vieira, M.G.A. Biosorption technology for removal of toxic metals: A review of commercial biosorbents and patents. *Environ. Sci. Pollut. Res.* **2019**, *26*, 19097–19118. [CrossRef]

8. Ngah, W.S.W.; Fatinathan, S. Pb(II) biosorption using chitosan and chitosan derivatives beads: Equilibrium, ion exchange and mechanism studies. *J. Environ. Sci.* **2010**, *22*, 338–346. [CrossRef]

9. Sud, D.; Mahajan, G.; Kaur, M.P. Agricultural waste material as potential adsorbent for sequestering heavy metal ions from aqueous solutions—A review. *Bioresour. Technol.* **2008**, *99*, 6017–6027. [CrossRef]

10. Kar, P.; Misra, M. Use of keratin fiber for separation of heavy metals from water. *J. Chem. Technol. Biotechnol.* **2004**, *79*, 1313–1319. [CrossRef]

11. Zhang, H.; Carrillo, F.; López-Mesas, M.; Palet, C. Valorization of keratin biofibers for removing heavy metals from aqueous solutions. *Text. Res. J.* **2019**, *89*, 1153–1165. [CrossRef]

12. López-Mesas, M.; Navarrete, E.R.; Carrillo, F.; Palet, C. Bioseparation of Pb(II) and Cd(II) from aqueous solution using cork waste biomass. Modeling and optimization of the parameters of the biosorption step. *Chem. Eng. J.* **2011**, *174*, 9–17. [CrossRef]

13. Sfaksi, Z.; Azzouz, N.; Abdelwahab, A. Removalof cr(VI) from water by cork waste. *Arab. J. Chem.* **2014**, *7*, 37–42. [CrossRef]

14. Kamal, M.H.M.A.; Azira, W.M.K.W.K.; Kasmawati, M.; Haslizaidi, Z.; Saime, W.N.W. Sequestration of toxic Pb(II) ions by chemically treated rubber (Hevea brasiliensis) leaf powder. *J. Environ. Sci.* **2010**, *22*, 248–256. [CrossRef]

15. Ngah, W.S.W.; Hanafiah, M.A.K.M. Removal of heavy metal ions from wastewater by chemically modified plant wastes as adsorbents: A review. *Bioresour. Technol.* **2008**, *99*, 3935–3948. [CrossRef] [PubMed]

16. Kong, H.; He, J.; Gao, Y.; Wu, H.; Zhu, X. Cosorption of Phenanthrene and Mercury(II) from Aqueous Solution by Soybean Stalk-Based Biochar. *J. Agric. Food Chem.* **2011**, *59*, 12116–12123. [CrossRef]

17. Lindholm-Lehto, P.C. Biosorption of heavy metals by lignocellulosic biomass and chemical analysis. *BioResources* **2019**, *14*, 4952–4995.

18. Saha, S.; Zubair, M.; Khosa, M.A.; Song, S.; Ullah, A. Keratin and chitosan biosorbents for wastewater treatment: A review. *J. Polym. Environ.* **2019**, *27*, 1389–1403. [CrossRef]

19. Salminen, E.; Rintala, J. Anaerobic digestion of organic solid poultry slaughterhouse waste—A review. *Bioresour. Technol.* **2002**, *83*, 13–26. [CrossRef]

20. Yin, J.; Rastogi, S.; Terry, A.E.; Popescu, C. Self-organization of Oligopeptides Obtained on Dissolution of Feather Keratins in Superheated Water. *Biomacromolecules* **2007**, *8*, 800–806. [CrossRef]

21. Al-Asheh, S.; Banat, F.; Al-Rousan, D. Beneficial reuse of chicken feathers in removal of heavy metals from wastewater. *J. Clean. Prod.* **2003**, *11*, 321–326. [CrossRef]

22. Ki, C.S.; Gang, E.H.; Um, I.C.; Park, Y.H. Nanofibrous membrane of wool keratose/silk fibroin blend for heavy metal ion adsorption. *J. Membr. Sci.* **2007**, *302*, 20–26. [CrossRef]

23. Aluigi, A.; Tonetti, C.; Vineis, C.; Tonin, C.; Mazzuchetti, G. Adsorption of copper(II) ions by keratin/PA6 blend nanofibres. *Eur. Polym. J.* **2011**, *47*, 1756–1764. [CrossRef]

24. Gupta, A. Human hair "waste" and its utilization: Gaps and possibilities. *J. Waste Manag.* **2014**, *2014*, 498018. [CrossRef]

25. Freddi, G.; Arai, T.; Colonna, G.M.; Boschi, A.; Tsukada, M. Binding of metal cations to chemically modified wool and antimicrobial properties of the wool–metal complexes. *J. Appl. Polym. Sci.* **2001**, *82*, 3513–3519. [CrossRef]

26. Brenner, L.; Squires, P.L.; Garry, M.; Tumosa, C.S. A measurement of human hair oxidation by Fourier transform infrared spectroscopy. *J. Forensic Sci.* **1985**, *30*, 420. [CrossRef]

27. Akhtar, W.; Edwards, H.G.M.; Farwell, D.W.; Nutbrown, M. Fourier-transform Raman spectroscopic study of human hair. *Spectrochim. Acta Part A Mol. Biomol. Spectrosc.* **1997**, *53*, 1021–1031. [CrossRef]

28. Febrianto, J.; Kosasih, A.N.; Sunarso, J.; Ju, Y.-H.; Indraswati, N.; Ismadji, S. Equilibrium and kinetic studies in adsorption of heavy metals using biosorbent: A summary of recent studies. *J. Hazard. Mater.* **2009**, *162*, 616–645. [CrossRef]

29. Lagergren, S. About the theory of so-called adsorption of soluble substances, Kungliga Svenska Vetenskapsakademiens. *Handlingar* **1898**, *24*, 1–39.

30. Ho, Y.S.; McKay, G. A comparison of chemisorption kinetic models applied to pollutant removal on various sorbents. *Process Saf. Environ. Prot.* **1998**, *76*, 332–340. [CrossRef]

31. Ho, Y.S.; McKay, G. Pseudo-second order model for sorption processes. *Process Biochem.* **1999**, *34*, 451–465. [CrossRef]

32. Ho, Y.S.; McKay, G. The kinetics of sorption of divalent metal ions onto sphagnum moss peat. *Water Res.* **2000**, *34*, 735–742. [CrossRef]

33. Weber, W.J.; Morris, J.C. Kinetics of adsorption of carbon from solution, Journal of the Sanitary Engineering Division. *Am. Soc. Civ. Eng.* **1963**, *89*, 31–60.

34. Onal, Y.; Akmil-Başar, C.; Sarici-Ozdemir, C. Investigation kinetics mechanisms of adsorption malachite green onto activated carbon. *J. Hazard. Mater.* **2007**, *146*, 194–203. [CrossRef] [PubMed]

35. Wu, F.-C.; Tseng, R.-L.; Juang, R.-S. Initial behavior of intraparticle diffusion model used in the description of adsorption kinetics. *Chem. Eng. J.* **2009**, *153*, 1–8. [CrossRef]

36. Guechi, E.; Benabdesselam, S. Removal of cadmium and copper from aqueous media by biosorption on cattail (typha angustifolia) leaves: Kinetic and isotherm studies. *Desalin. Water Treat.* **2020**, *173*, 367–382. [CrossRef]

37. Virgen, M.D.R.M.; Vázquez, O.F.G.; Montoya, V.H.; Gómez, R.T. Removal of heavy metals using adsorption processes subject to an external magnetic field. In *Heavy Metals*; Intechopen: London, UK, 2018; pp. 253–280. Available online: https://www.intechopen.com/books/heavy-metals/removal-of-heavy-metals-using-adsorption-processes-subject-to-an-external-magnetic-field (accessed on 28 April 2020).

Removal of Aquatic Cadmium Ions Using Thiourea Modified Poplar Biochar

Yanfeng Zhu [1], Huageng Liang [2], Ruilian Yu [1], Gongren Hu [1],* and Fu Chen [2],*

[1] College of Chemical Engineering, Huaqiao University, Xiamen 361021, China; 18014087032@stu.hqu.edu.cn (Y.Z.); ruiliany@hqu.edu.cn (R.Y.)

[2] Low Carbon Energy Institute, China University of Mining and Technology, Xuzhou 221008, China; lianghg@cumt.edu.cn

* Correspondence: grhu@hqu.edu.cn (G.H.); chenfu@cumt.edu.cn (F.C.); Tel.: +86-516-8388-3501 (F.C.)

Abstract: Removal of aquatic cadmium ions using biochar is a low-cost method, but the results are usually not satisfactory. Modified biochar, which can be a low-cost and efficient material, is urgently required for Cd-polluted water and soil remediation. Herein, poplar bark (SB) and poplar sawdust (MB) were used as raw materials to prepare modified biochar, which is rich in N- and S- containing groups, i.e., TSBC-600 and TMBC-600, using a co-pyrolysis method with thiourea. The adsorption characteristics of Cd^{2+} in simulated wastewater were explored. The results indicated that the modification optimized the surface structure of biochar, Cd^{2+} adsorption process by both TSBC-600 and TMBC-600 was mainly influenced by the initial pH, biochar dosage, and contact time, sthe TSBC-600 showed a higher adsorption capacity compared to TMBC-600 under different conditions. The Langmuir adsorption isotherm model and pseudo-second-order kinetic model were more consistent with the adsorption behavior of TSBC-600 and TMBC-600 to Cd^{2+}, the maximum adsorption capacity of TSBC-600 and TMBC-600 calculated by the Langmuir adsorption isotherm model was 19.998 mg/g and 9.631 mg/g, respectively. The modification method for introducing N and S into biochar by the co-pyrolysis of biomass and thiourea enhanced the removal rate of aquatic cadmium ions by biochar.

Keywords: biochar; thiourea; cadmium pollution; adsorption characteristics; water treatment

1. Introduction

Cadmium (Cd) has extreme biological toxicity, long half-life, and low elimination efficiency [1]. It is one of the "ten chemicals of major public health concern" listed by the World Health Organization [2]. Cd can readily cause damage to the internal organs and systems of the human body, and is the most toxic transition metal element that poses global human health risks [3]. In 2014, the fraction of points that exceeded the standard quantity of Cd in cultivated land in China was 7% [4], and the area of farmland polluted by Cd reached 20 million hectares, which was mainly caused by irrigation due to industrial wastewater [5]. With the improvement in food safety standards and environmental awareness of the public, the prevention of Cd contamination of the food chain has become a common concern [6].

Irrigation using wastewater is the main source of Cd pollution in farmland soil [7]. Therefore, eliminating Cd from wastewater is the most effective remediation method [8]. Currently, the methods for the removal of Cd^{2+} in wastewater are mainly chemical precipitation, ion exchange, membrane separation, coagulation, and adsorption [9]. Among them, the adsorption method is widely used due to the low energy consumption, high removal rate, and simple operation. Biochar is a type of carbon-rich porous material [10], which is accessible by high-temperature conversion of biomass

in anoxic or anaerobic environments. It has been widely used in sewage treatment. Li et al. used vinegar-residue biochar to adsorb Cd^{2+} in water, while the maximum adsorption capacity for Cd^{2+} was only 2.91 mg/g [11]. Yakkala et al. prepared Buffal weed biochar to adsorb Cd^{2+} and Pb^{2+} in water, and the adsorption capacity was 11.63 mg/g and 333.33 mg/g, respectively [12]. Jing et al. prepared biochar to adsorb Cd^{2+} in soil, and the adsorption capacity was 5.00 mg/g [13]. Although biochar can adsorb cadmium ion to some extent, it is limited by the surface pore structure and functional groups, and the single biochar adsorption capacity is very limited [14]. To maximize the adsorption of biochar, modification by doping becomes an important method to optimize the pore structure of biochar and increase the functional groups and specific adsorption sites. Currently, the main methods include chemical modification of the surface, co-pyrolysis, and catalytic esterification [15–17]. Previous studies have shown that the type of modifier, as well as the modification method can affect the quality of the modified biochar [18–20]. Ma et al. synthesized modified biochar rich in -NH_2 by cross-linking using polyethyleneimine as the modifier, and the maximum adsorption capacity of the modified biochar to Cr^{6+} was 435 mg/g, much higher than the 23.09 mg/g before modification [21]. Park et al. prepared sulfur-modified biochar by the co-pyrolysis of sulfur and wood chips at 600 °C; after impregnation, the maximum adsorption capacity of the modified biochar for mercury was 107.5 mg/g, which was higher than that of the raw materials by 86%. This modification method enables sulfur to be doped into the biochar structure in the form of groups and enhanced the specific adsorption capacity of biochar [22]. At present, sulfur and nitrogen-modified biochar are the most common technologies, which have several disadvantages such as low practicability, low utilization of modifiers, and one modifier that can only be completed via modification [23].

Therefore, the specific objectives of this study are: (1) to prepare biochar with stable performance, rich functions, strong adsorption capacity, and multiple modifications as one step pyrolysis; (2) to compare the microstructure and physical characteristics of raw biochar and modified biochar by multiple techniques; (3) to evaluate the adsorption characteristics of thiourea-modified biochar on cadmium ions under different conditions, and experimental data were investigated with isotherm model and kinetic sorption model. The main aims of this study include understanding the role of the modified biochar produced from co-pyrolysed thiourea in the removal of Cd^{2+}, and providing technical support for its application in environmental remediation.

2. Materials and Methods

2.1. Preparation of Thiourea Modified Biochar

The collected sawdust and bark (from Wenchang Campus of China University of Mining and Technology, Xuzhou, Jiangsu, China) were thoroughly washed with deionized water and dried in an oven at 60 °C for 24 h. The biomass raw material and thiourea were weighed at a mass ratio of 1:1, respectively, and placed in a tubular furnace under an argon atmosphere after even mixing. The furnace was heated up to 300 to 700 °C at a heating rate of 5 °C/min and kept at the same temperature for 2 h to prepare thiourea-modified biochar (denoted as TSBC-600 and TMBC-600, where T stands for the pyrolysis temperature). The samples were crushed, passed through a 60-mesh sieve, and stored for future use (preparation is shown in Figure S1).

For comparison, unmodified biochar materials (MBC-600, SBC-600) were prepared by heating to 600 °C at 5 °C/min in an argon atmosphere without adding thiourea.

2.2. Physicochemical Properties and Structural Characterization of Biochar

Deionized water and biochar were mixed at a mass ratio of 20:1, and the pH value of the aqueous solution was measured with a pH meter to determine the acidity and basicity of the biochar. The ash content was measured by the combustion method [24]. The specific surface area and pore size distribution of biochar were investigated using N_2-isothermal adsorption and desorption experiments. The specific surface area of the material was calculated using the Brauner-Emmett-Teller (BET) equation,

and the pore size distribution of the materials was determined by using the Density functional theory (DFT) model.

Field emission scanning electron microscope/energy-dispersive X-ray spectroscopy (SEM-EDX) (FEI QuantaTM 250, FEI, Boston, MA, USA) was used to observe the surface morphology; Fourier transform infrared spectroscopy (FTIR) (VERTEX 80V, Bruker, Karlsruhe, Germany) was used to characterize the surface properties of biochar. Typically, approximately 0.02 g of the dry sample was thoroughly mixed with KBr and pressed into semi-transparent pellets using a manual hydraulic press, and all spectra were acquired with a resolution of 2 cm^{-1} for 28 scans, over a wavenumber range between 400 and 4000 cm^{-1}. X-ray photoelectron spectroscopy (XPS) (ESCALAB 250Xi, Thermo Fisher, Boston, MA, USA) was used to characterize the chemical state of the biomass carbon material, and the binding energy values were all calibrated based on the hydrocarbon contamination using the C 1s peak at 284.8 eV.

2.3. Batch Adsorption Experiment

2.3.1. Determining the Relationship between Pyrolysis Temperature and Biochar Adsorption Performance

An amount of 0.02 g of the modified biochar prepared at five different temperatures was placed into a centrifuge tube, 20 mL of 10 mg/L Cd^{2+} solution was added and then shaken well. The mixture was oscillated at 25 °C for 24 h. Finally, the optimal pyrolysis temperature of biochar was determined.

2.3.2. Determining the Relationship between pH and the Amount of Cd^{2+} Adsorbed by Biochar

Amounts of 0.01 mol/L HCl and 0.01 mol/L NaOH were used to modulate the pH of 20 mL of 10 mg/L Cd^{2+} solution to 2, 3, 4, 5, 6, and 7 for minimizing the effect of Cd-chloride hydrolysis, then weremplaced one hour and there was no observed precipitation by the transillumination test, and then 0.02 g modified biochar were added. The mixture was mixed well and oscillated at 25 °C for 24 h.

2.3.3. Determination of the Relationship between the Dosage and the Capacity of Cd^{2+} Adsorbed by Biochar

The concentration of modified biochar was controlled to be 1, 2, 3, 4, 5, 6, 7, 8, 9, 10 g/L, respectively. The pH of the TMBC solution and TSBC solution was modulated to be 7, respectively. The initial concentration of Cd^{2+} in each solution was 10 mg/L. Finally, the optimal dose of biochar was determined.

2.3.4. Adsorption Kinetics

0.10 g of TMBC-600 was added into a 50 mL centrifuge tube, and subsequently, 20 mL of 100 mg/L Cd^{2+} solution was added. The pH was adjusted to be 7, and the samples were taken after oscillation for 5, 10, 30, 60, 120, 240, 360, 720, and 1440 min, respectively. For TSBC-600, the mass was 0.08 g, and the other procedures were the same as those of TMBC-600.

The adsorption kinetic equation can reflect the change in the adsorption capacity of the adsorbent to the solute as a function of time, i.e., the speed of the adsorption rate [25]. In this study, the more commonly used pseudo-first-order and pseudo-second-order kinetic model equations were used to fit the adsorption data.

Adsorption capacity:

$$q_e = \frac{(C_0 - C_e) \times V}{m} \tag{1}$$

$$q_t = \frac{(C_0 - C_t) \times V}{m} \tag{2}$$

pseudo-first-order kinetic model equation:

$$\ln(1 - \frac{q_t}{q_e}) = -k_1 t \tag{3}$$

pseudo-second-order kinetic model equation:

$$\frac{t}{q_t} = \frac{1}{k_2 q_e^2} + \frac{t}{q_e} \tag{4}$$

where t is the adsorption time (min); C_0 is the initial concentration of Cd^{2+} in the solution (mg/L); C_e is concentration of Cd^{2+} in the solution when the adsorption reaches equilibrium (mg/L); C_t is the concentration of Cd^{2+} in the solution at t (mg/L); V is the volume of the solution participation in the adsorption reaction (L); m is the mass of the added biochar (g); q_e is the equilibrium adsorption capacity for biochar when the adsorption reaches equilibrium(mg/g); q_t is the adsorption capacity for biochar at t (mg/g); k_1 is the rate constant of the pseudo-first-order kinetic equation (min^{-1}); k_2 is the rate constant of the pseudo-first-order kinetic equation (g/mg/min).

2.3.5. Isothermal Adsorption

An amount of 0.10 g of TMBC-600 was added into a 50 mL centrifuge tube, and then 20 mL of 5, 10, 30, 100, 250, and 500 mg/L Cd^{2+} solution was added, respectively. The pH was adjusted to be 7 and subsequently oscillated for 24 h at room temperature. For TSBC, the mass was 0.08 g, and the other procedures were the same as those of TMBC-600.

In this study, Langmuir and Freundlich isothermal adsorption models were used to analyze the adsorption of the two modified biochars. For the Langmuir model, it is assumed that the surface of the adsorbent has the same adsorption active sites and that the adsorption occurs in the monolayer [26].

Langmuir equation:

$$Q_e = \frac{Q_m \times K_L \times C_e}{1 + K_L C_e} \tag{5}$$

Freundlich equation:

$$Q_e = K_f C_e^{1/n} \tag{6}$$

where Q_m is the maximum adsorption capacity (mg/g); K_L (L/g) is the affinity constant of the interaction between the adsorbate and the adsorbent; C_e is the concentration of the adsorbate when the adsorption reaches equilibrium (mg/L); K_f is the Freundlich adsorption capacity parameter; n is the empirical parameter of the adsorption strength (determined by the heterogeneity of the material).

3. Results

3.1. Effects of Modification on the Physicochemical Properties of Biochar

The physicochemical properties of biochar before and after modification are shown in Table 1. It can be seen from Table 1 that the biochar is alkaline due to the release of alkaline salts during the pyrolysis, and the pH of the biochar is increased after modification. This indicates that the change in pH and the ash content are positively correlated, as the ash of biochar contains K, Ca, Na, Mg, S, and other elements. These elements are attached to the surface of the biochar in the form of oxides and carbonates, and are alkaline in solution [27]. In addition, these inorganic components can co-precipitate with cadmium ions to remove [28]. The N_2 adsorption was carried out for the TMBC-600 and TSBC-600 (Figure S2). TMBC-600 and TSBC-600 exhibit reversible type I isotherm, a microporous filling at low P/P_0 and a H4 typed hysteresis loop within intermediate and high P/P_0, indicating the coexistence of both micropores and meso-/macropores in TMBC-600 and TSBC-600 [29]. From the DFT pore width distribution, TMBC-600 demonstrates low micropores and abundant mesopores, and TSBC-600 shows more micropores. Compared with the samples before modification, the BET specific surface area of

TMBC-600 and TSBC-600 increased by 3.08 m^2/g and 2.93 m^2/g, respectively, and the internal pore diameter increased by 0.17% and 1.48%, indicating that the surface and pore structure of the modified biochar has changed significantly. This is because, during the slow pyrolysis process, the steam generated by the modifier at high temperature penetrates the internal structure of the raw biochar, dredging the pores in it. This is consistent with the research results reported by O'Connor et al. [16].

Table 1. Physicochemical properties of MBC-600, SBC-600, TMBC-600, and TSBC-600. BET, Brauner-Emmett-Teller.

Samples	Yield (%)	Ash (%)	pH	BET Surface Area (m^2/g)	Average Pore Diameter (nm)
MBC-600	24.26	46.75	7.07	2.46	4.66
SBC-600	31.42	41.68	9.92	2.77	1.94
TMBC-600	—	57.46	8.94	5.54	4.83
TSBC-600	—	47.71	10.85	5.70	3.42

Notes: MBC-600, poplar sawdust biochar; SBC-600, poplar bark biochar; TMBC-600, thiourea modified poplar sawdust biochar; TSBC-600, thiourea modified Poplar bark biochar.

3.2. Effect of Modification on Morphology and Structure of Biochar

Figure 1 shows the SEM-EDS images of two materials before and after modification. From Figure 1, it is observed that before the modification, both SBC-600 and MBC-600 have a lamellar structure, which is more regularly arranged. The internal and external structures are well-formed and the surface is rough. The lamellar stack structure is obvious with an obvious pore structure. As proposed by Wu et al. [30] also, after modification, the granular and block structure of TSBC-600 and TMBC-600 increased, presumably due to the introduction of sulfur-containing groups that increased the number of biochar particles and the surface became smooth. Part of the pore structure was blocked, the impurities on the biochar surface reduced, and the outline of the structure was clear. EDS analysis indicated that the nitrogen content of the TSBC-600 increased from 3.57% to 15.43%, and the sulfur content increased from 0.30% to 3.68%; the nitrogen content of the TMBC-600 increased from 3.30% to 13.61%, and the sulfur content increased from 0.17% to 2.89%, which fully confirmed that N and S were successfully doped into the biochar during the modification process.
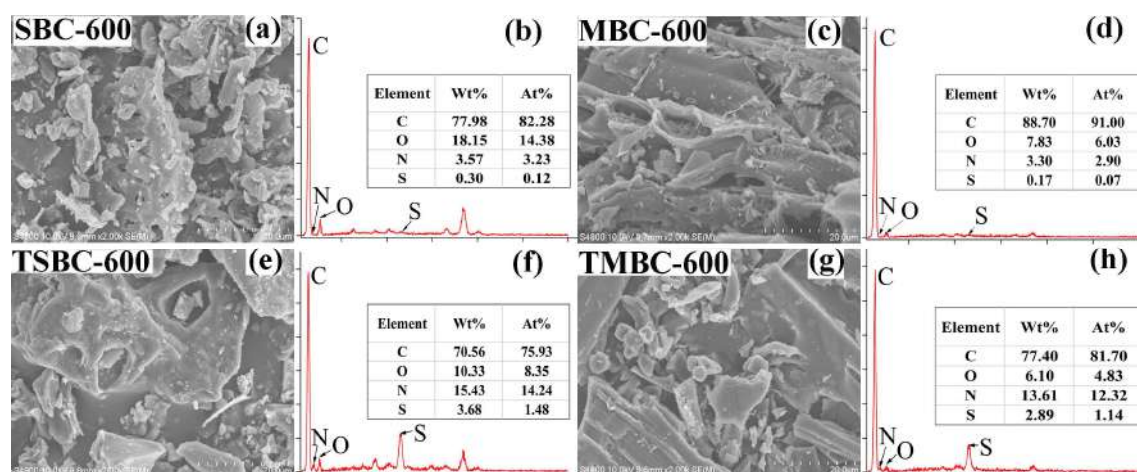

Figure 1. SEM image (**a,c,e,g**) and EDS spectrum (**b,d,f,h**) of MBC-600, SBC-600, TMBC-600 and TSBC-600.

3.3. Effects of Modification on Functional Groups on the Biochar Surface

The FTIR spectra of the two biochars (TMBC-600 and TSBC-600) before and after modification and before and after adsorption are shown in Figure 2. From Figure 2, the absorption peak at approximately

3300 cm^{-1} is assigned to the stretching vibration of -OH [31], and the strong absorption peaks appearing near 2988 cm^{-1} at TMBC-600 and TSBC-600 are the stretching vibration of -NH$_2$ [32], indicating that the nitrogen in thiourea participated in the amination of the surface of the biochar during the modification process. The absorption peak at 2901 cm^{-1} was assigned to the stretching vibration of -CH$_2$ or -CH [33]. The characteristic peak appearing at 2358 cm^{-1} after modification may be caused by the stretching vibration of the -C$\equiv$N triple bond, and the two strong absorption peaks, i.e., 1066 cm^{-1} and 1244 cm^{-1} appearing in the frequency band of 1050–1250 cm^{-1} are the stretching vibration absorption peaks of C-S and C=S [30], respectively, indicating the presence of sulfurization during the modification of biochar. The characteristic absorption peak at 1439 cm^{-1} is attributed to the stretching vibration of C-N [34], and the absorption peak at 1585 cm^{-1} may be the absorption characteristic peak of C=N or C=O [14]. Generally, C-H stretching vibrational absorption peaks of methyl and methylene appear in the vicinity of 2960 cm^{-1}, and the adsorption frequency of methylene will shift to the low-frequency region and the absorption intensity will become weaker after the introduction of the S atoms [35]. The peak at 2901 cm^{-1} evidences this and confirms that the S-containing groups were involved in the modification. The absorption peak in the 1400–1600 cm^{-1} band shifted after the reaction and the peak intensity weakened, indicating that Cd^{2+} and the functional group on the surface of the biochar were bound to the adsorption site by complexation [36]. The characteristic peaks of -NH$_2$ and sulfur-containing groups weakened after the adsorption reaction, indicating that the newly introduced functional groups participated in the adsorption of Cd^{2+}.
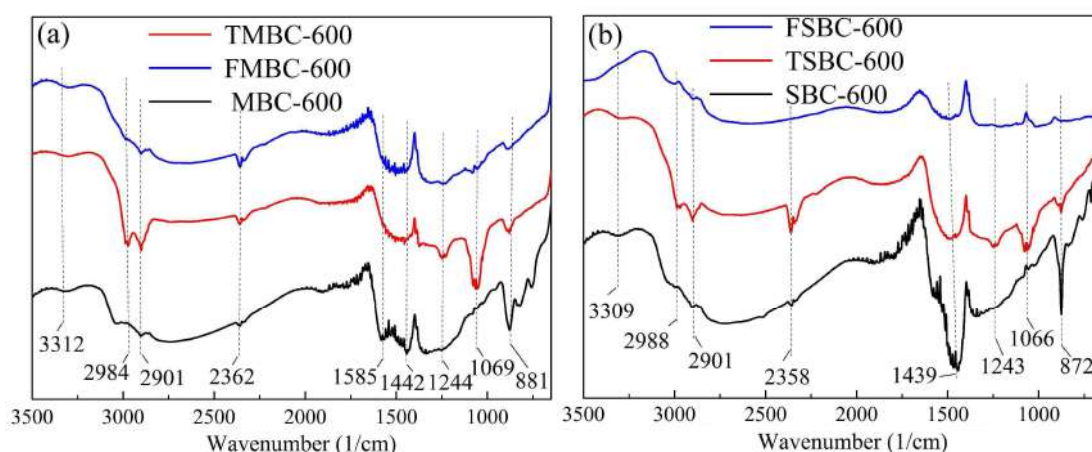

Figure 2. FTIR spectra of MBC-600, TMBC-600 and FMBC-600 (after Cd^{2+} adsorption) (**a**), and SBC-600, TSBC-600 and FSBC-600 (after Cd^{2+} adsorption) (**b**), (F stands for adsorption reaction).

3.4. XPS Analysis of Biochar before and after Modification

To further verify whether this modification method successfully doped N and S into the biochar carbon lattice, X-ray photoelectron spectroscopy analysis was used to analyze the change in the binding energy of C, N, and S in the biochar before and after modification. Figure 3a shows the XPS survey spectrum of MBC-600 and TMBC-600, in which the nitrogen content increased by 1.43% and the sulfur content increased by 2.03%. Figure 3b shows the XPS survey spectrum of SBC-600 and TSBC-600, in which the nitrogen content increased by 6.53% and the sulfur content increased by 3.39%. After modification, the extent of doping with N and S has improved significantly. The change in the mass fraction of the surface element is closely related to the functional group type and quantity of biochar before and after modification, which indicates that the modified material has better electrochemical performance [37]. Figure S3 (A1) and (A2) show the C 1s spectra of the two materials before and after modi3fication, in which the carbon was present in three forms, i.e., C-C (284.7 eV), C-O/C-N/C-S (286.2 eV), and C=O (288.6 eV) [38]. It can be seen from (A1) that, after the modification, the content of the three types of carbon in TMBC-600 changed significantly, while TSBC-600 in (A2) has not changed much. The changes in C-N and C-S indicate that N and S substitute C and become part of the carbon

skeleton in the form of structural nitrogen and structural sulfur [39]. Figure S3 (B1) and (B2) show the N 1s spectra of the materials before and after modification. The nitrogen is mainly present in four forms, i.e., N-6 (pyridine nitrogen, 398.5 eV), N-5 (pyrrole nitrogen, 399.5 eV), and N-Q (graphite nitrogen, 400.7 eV) and NOx (nitrogen oxide, 402.2 eV) [40,41]. The N 1s spectra of MBC-600 and SBC-600 in (A1) and (A2) show that the nitrogen content of unmodified biochar is very small. Compared with MBC-600 and SBC-600, the number of different forms of nitrogen in TMBC-600 and TSBC-600 increased significantly and mainly existed in the form of pyridine nitrogen and graphite nitrogen, indicating that the nitrogen atom was successfully introduced into the carbon lattice and formed a bond with the carbon atom. The number of pyridine nitrogen was higher than that of graphite nitrogen, which has been confirmed in studies with thiourea as an additional doped nitrogen source [15]. Pyridine nitrogen can promote the coordination of metal ions, and thus, is more favorable for the removal of metal ions [42]. Figure S3 (C1) is the S 2p spectrum of MBC-600 and TMBC-600. It can be seen from the figure that the sulfur content of MBC-600 is small, while that in TMBC-600 is significantly increased, existing mainly in three forms, i.e., C=S (163.9 eV), C-S (165.1 eV), and S(=O)2 (168.3 eV). Figure S3 (C2) is the S 2p spectrum of SBC-600 and TSBC-600. Compared with SBC-600, the sulfur content of TSBC-600 is significantly increased, and the sulfur exists in five main forms, i.e., C=S (163.9 eV), C-S (165.1 eV), S(=O)2 (168.3 eV), Sul S (sulfide sulfur, 161.8 eV), and S(-II) (160.6 eV) [35,43]. This confirms that the sulfur was successfully doped into the biochar carbon skeleton structure after modification. The doping of N and S elements has given biochar materials some specific properties, such as easier electrochemical reaction and adsorption.
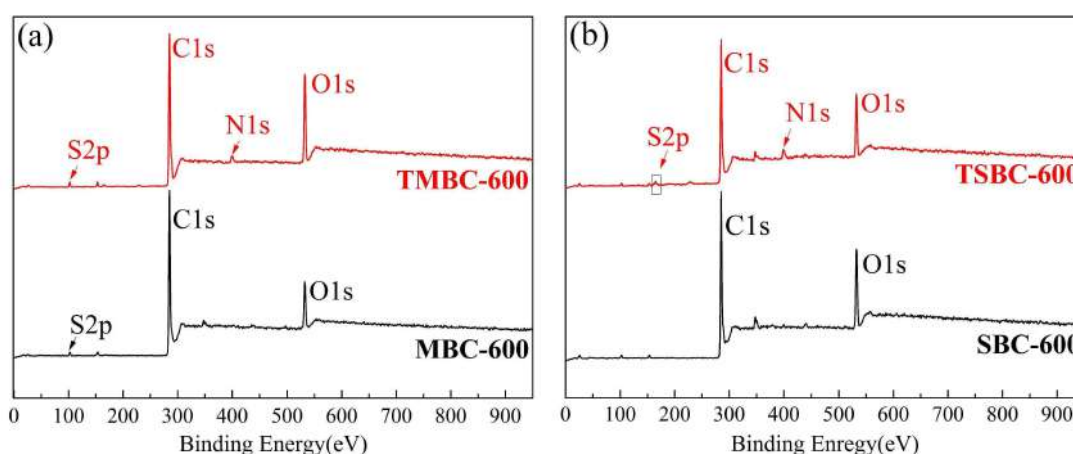

Figure 3. XPS spectra of MBC-600, SBC-600, TMBC-600 and TSBC-600 (**a,b**).

3.5. Adsorption Experiment Results

3.5.1. Effect of Pyrolysis Temperature on Cd^{2+} Adsorption by Modified Biochar

Cd^{2+} was removed by modified biochar at different pyrolysis temperatures and the results are shown in Figure 4. It can be seen from Figure 4 that when the dosage of biochar is 1 g/L and the initial pH of the solution is 7, the removal rate of Cd^{2+} by TSBC increases as the pyrolysis temperature increases. The removal rate of Cd^{2+} by TMBC in the range of 300–600 °C showed an upward trend, and the removal rate decreased above 600 °C. The removal rate of Cd^{2+} by TSBC was higher than that of TMBC. The removal rate of TMBC-600 and TSBC-600 were the highest at 43.83% and 87.29%, respectively. The removal rate associated with TMBC-600 increased by 36.53% compared with TMBC-300, and that of TSBC-600 increased by 81.07% compared with TSBC-300. Considering the energy consumption and raw material utilization in the process of preparing biochar, biochar was prepared at a pyrolysis temperature of 600 °C in this study.
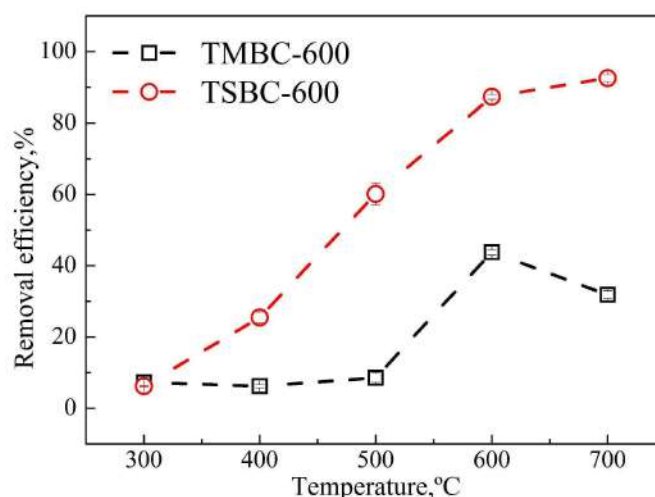
Figure 4. Effect of different pyrolysis temperatures on Cd^{2+} adsorption by TMBC-600 and TSBC-600.

3.5.2. Effect of Initial pH on Cd^{2+} Adsorption by Biochar

As shown in Figure 5, when the dosage of modified biochar was 1 g/L and the initial concentration of Cd^{2+} is 10 mg/L, as the pH increases, the removal rate of Cd^{2+} by both the biochars increase. Under strongly acidic conditions, the removal rate of Cd^{2+} by TSBC-600 is higher and that of TMBC-600 is lower. When the pH is in the range of 4–7 and 6–7, respectively, the adsorption of TSBC-600 and TMBC-600 is better, and the adsorption efficiency of TSBC-600 was higher than that of TMBC-600. When the pH was 4–7, the removal rate of Cd^{2+} in the solution can reach 93%; when pH = 7, the removal rate of Cd^{2+} by TSBC-600 became the highest, which was 96.05%. For TMBC-600, when the pH was at 2–6, the removal rate of Cd^{2+} increased slowly. When pH = 7, TMBC-600 had the highest removal rate of Cd^{2+}, which was 58.41%. Due to the difference in biomass materials, the alkalinity of the two modified biochars differed significantly. From Figure 6, it can be seen that the equilibrium pH of the biochar solution has increased to varying degrees after Cd^{2+} adsorption. The equilibrium pH of TSBC-600 was higher than TMBC-600, indicating that the basicity of TSBC-600 is greater, which is consistent with the pH measurement results in 2.1.
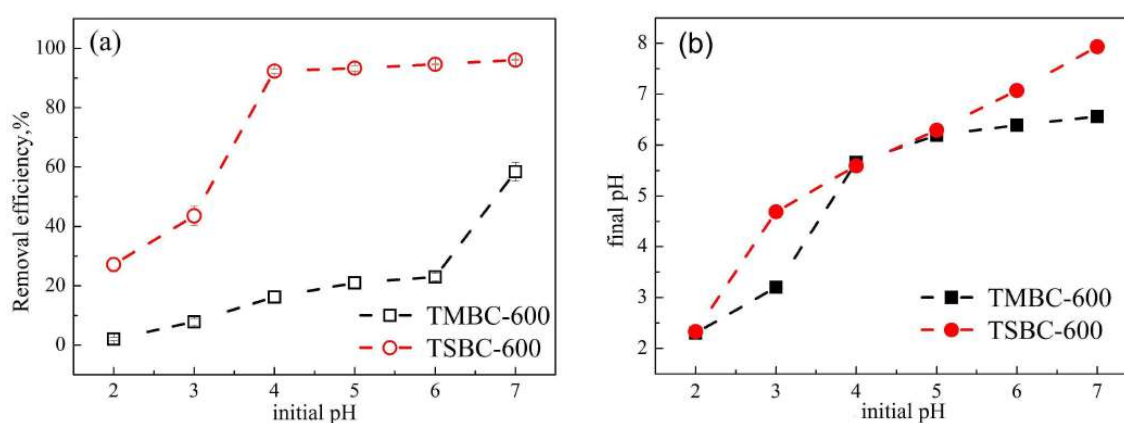

Figure 5. Effect of different pH on Cd^{2+} removal efficiency by TMBC-600 and TSBC-600 (**a**), comparison between the initial and final pH after the reaction (**b**).
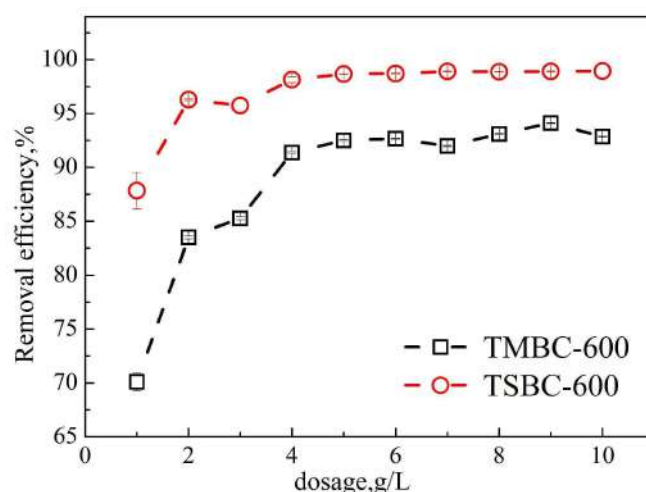
Figure 6. Effect of different dosage on adsorption of Cd^{2+} by TMBC-600 and TSBC-600.

Experiments have shown that TSBC-600 has good acid resistance. In the set pH range, TSBC-600 showed a strong removal rate of Cd^{2+}, which might be related to the role of the nitrogen-sulfur functional groups and cadmium ions. This has important implications for the research on the removal of cadmium in typical acidic wastewater such as mining wastewater.

3.5.3. Effect of Dosage of Biochar on Cd^{2+} Adsorption

It can be seen from Figure 6 that as the initial pH of the solution was 7, and the initial c (Cd^{2+}) of the solution was 10 mg/L, the removal rate of Cd^{2+} increased with the increase in the two kinds of biochar. When the dosage of TMBC-600 and TSBC-600 was 5 g/L and 4 g/L, the adsorption of Cd^{2+} by biochar reached saturation, and the removal rate reached 92.50% and 98.15%, respectively. As the dosage was increased continuously, the removal rate of Cd^{2+} did not vary much. This is possibly because the binding of cadmium ions to the limited adsorption sites on the surface of biochar reaches saturation when the dosage is small. With the increase in the dosage, the remaining cadmium ions in the solution bind to the new adsorption sites. Finally, the adsorption reached equilibrium, and further increase in dosage had little effect on the removal rate.

3.5.4. Analysis of Adsorption Kinetics

The adsorption capacity of Cd^{2+} by biochar as a function of time is shown in Figure 7. As shown in Figure 7, the adsorption capacity of TSBC-600, SBC-600, TMBC-600, and MBC-600 all increase with the increase of the adsorption time, and eventually reach equilibrium. TSBC-600, SBC-600, TMBC-600, and MBC-600 reached adsorption equilibrium at 240, 960, 360, and 960 min, respectively. In the initial stage of adsorption, the adsorption efficiency of each biochar is high and it gradually decreases with the increase in adsorption time. This is because there are more sites on the biochar surface that can bind to Cd^{2+} at the beginning of adsorption, and Cd^{2+} can be quickly adsorbed by the biochar. At this time, there is no competitive adsorption. As the adsorption time increases, the effective adsorption sites on the surface of the biochar gradually decrease, and Cd^{2+} needs to diffuse into the inside of porous medium. At this time, the mass transfer rate becomes slower, and the competitive adsorption becomes more and more obvious [44]. TSBC-600 showed a higher adsorption rate in the initial stages of adsorption, indicating that the surface of TSBC-600 has more binding sites.
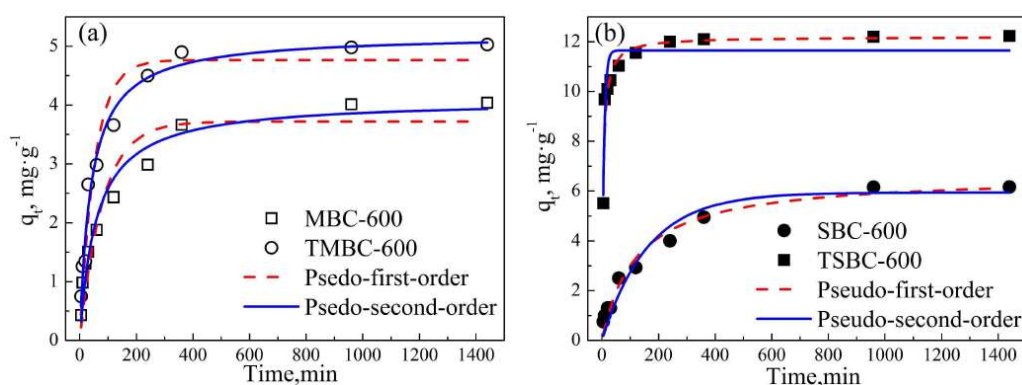
Figure 7. Fitting curves of the kinetics of TMBC-600 and MBC-600 (**a**) and TSBC-600 and SBC-600 (**b**) (C_0 = 100 mg/L, pH = 7, doage$_{TMBC-600}$ = 5 g/L and doage$_{TSBC-600}$ = 4 g/L, 25 °C).

3.5.5. Analysis of Isothermal Adsorption

The adsorption isotherm can reflect the affinity of the adsorbate for the adsorbent and can be used to describe the interaction between the adsorbate and the adsorbent [45]. The adsorption isotherms of Cd^{2+} solutions after adding biochar with different initial concentrations are shown in Figure 8. The adsorption capacity of TSBC-600, SBC-600, TMBC-600, and MBC-600 all increased with the initial concentration of Cd^{2+} and eventually reached equilibrium. At low concentrations of Cd^{2+}, biochar showed a higher adsorption rate, and then gradually flattened as the concentration increased. It can be seen from Figure 8 that the adsorption capacity of the four types of biochar is TSBC-600 > SBC-600 > TMBC-600 > MBC-600, among which TSBC-600 has the strongest adsorption capacity.
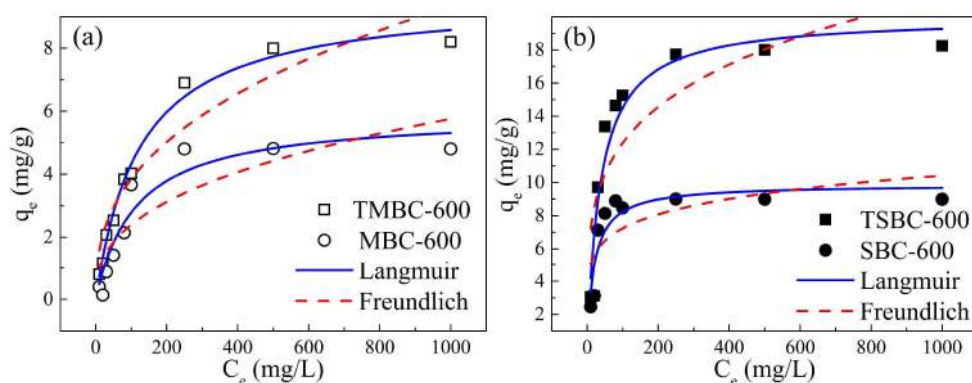

Figure 8. Fitting curves of isothermal adsorption of TMBC-600 and MBC-600 (**a**) and TSBC-600 and SBC-600 (**b**) (pH = 7, doage$_{TMBC-600}$ = 5 g/L and doage$_{TSBC-600}$ = 4 g/L, 25 °C).

4. Discussion

4.1. Effects of Pyrolysis Temperature, Dosage, and Initial pH on Cd^{2+} Removal

Biomass pyrolysis is a fairly complex thermochemical reaction process, in which temperature is a key factor that determines the performance of biochar [46]. The effect of modified biochar prepared at different pyrolysis temperatures on the removal rate of Cd^{2+} in aqueous solution is shown in Figure 4. When the initial concentration of Cd^{2+} in the solution was 10 mg/L, TMBC and TSBC had a high removal rate of Cd^{2+} at 600 °C. This is because, as the temperature increases, the moisture and volatile matter of the biomass is gradually released, and a large number of pore structures are formed on the biochar surface, the specific surface area increases, and the number of adsorption sites on the surface increases [47]. The reason for the lower growth may be that the introduction of sulfur and nitrogen enhances the ability of primary biochar to adsorb Cd^{2+}. At the same pyrolysis temperature,

the difference in adsorption capacity between TMBC-600 and TSBC is remarkable. This may be because MB has volatile components up to 81.1% volatile components and its structure is loose. When the temperature is relatively low, organic solids in MB did not fully decompose and generate abundant biomass oil [48]. When the temperature was relatively high, the high temperature destroyed the pore structure of the biochar, which caused the TMBC pore structure to collapse, and the adsorption sites on the biochar surface decreased [49].

The dosage of adsorbent added is one of the important parameters that determine the adsorption capacity of the adsorbent for Cd^{2+}. The removal rate of TMBC-600 and TSBC-600 for Cd^{2+} in aqueous solution is shown in Figure 6. When the initial Cd^{2+} concentration of the solution was 10 mg/L, the dosage of TMBC-600 and TSBC-600 increased from 1 g/L to 10 g/L, and the removal rates of Cd^{2+} by TMBC and TSBC increased from 70.1% to 94.1% and from 87.8% to 99.0%, respectively. When the dosage increased to 4 g/L, the increase in removal rate did not vary much, similar results also appeared during the adsorption of transition metal element by sugarcane biochar and sulfurized biochar [22,50,51].

The initial pH of the solution is an important factor that affects the adsorption process. Cd-chloride hydrolysis have resulted in sacrificial dissolution of adsorbent and cannot be ignored, therefore, the neutralization method was used to minimize the effect of Cd-chloride hydrolysis on adsorption, so as to ensure that the adsorption of Cd^{2+} only affected by the initial pH of solution. Changes in pH can affect the surface charge of the adsorbent and the degree of ionization of the adsorbed cadmium ions [52]. The effect of initial pH on the adsorption of Cd^{2+} by modified biochar is shown in Figure 5. When the initial Cd^{2+} concentration is 20 mg/L and the amount of modified biochar is 1 g/L, TSBC-600 can still remove 93% of the Cd^{2+} in the solution at low pH, and TMBC-600 can obtain a removal rate of approximately 60%. In the same situation, Tang et al. found that the removal rate of Cd^{2+} by single amino-modified biochar was only 28%, and the removal rate of Cd^{2+} by single thiol-modified biochar was 48% [34]. Li et al. reported that when the dosage of nitrogen-added biochar was 8 g/L, the removal rate of Cd^{2+} could reach 98% at pH 4.0 [53]. Compared with single sulfur modification and nitrogen modification, the thiourea-modified biochar materials examined in this study have a higher tolerance to pH. The modified biochar mainly achieves the removal of Cd^{2+} through the specific binding of nitrogen and sulfur groups with Cd^{2+} and the non-specific complexation or ion exchange of oxygen-containing functional groups such as hydroxyl and carboxyl groups on the surface of biochar with Cd^{2+}. When the content of H^+ in the solution increases, a large amount of H^+ will dissociate the functional groups that are beneficial to the adsorption of Cd^{2+} [54,55], thereby reducing the removal rate of Cd^{2+}. Meanwhile, H^+ preferentially occupies the adsorption sites when competing with Cd^{2+}, causing a decrease in the number of sites bound to Cd^{2+}. In addition, the lower the pH of the solution, the higher the density of positive charges on the surface of biochar, and the stronger the mutual electrostatic repulsion between the positively charged metal cations and the surface of biochar [56–58], which will reduce the removal rate of Cd^{2+}.

4.2. Adsorption Kinetics of Cd^{2+} Adsorbed by Biochar before and after Modification

The pseudo-first-order kinetic equation and pseudo-second-order kinetic equation were used to fit the biochar adsorption kinetic data, and the fitting parameters are shown in Table 2. It can be seen from Table 2 that the R^2 values fitted by the pseudo-second-order kinetic equation are greater than those fitted by the pseudo-first-order kinetic equation, indicating that the adsorption rate of biochar are mainly controlled by the chemisorption mechanism, and Cd^{2+} adsorbed on the surface of biochar via the interaction with biochar, such as that shared by the electron-electron pairs, ion exchange, and surface complexation [59]. The adsorption process mainly includes external liquid film diffusion, surface adsorption, and intra-particle diffusion. The relationship between the equilibrium adsorption capacity of biochar for Cd^{2+} is TSBC-600 > SBC-600 > TMBC-600 > MBC-600. The adsorption of modified biochar was enhanced, indicating the important role of N- and S- containing groups on the adsorption of Cd^{2+}. Comparing the adsorption rate constant k^2 of the four biochars, 0.0184 (TSBC-600)

> 0.0049 (TMBC-600) > 0.0042 (MBC-600) > 0.0013 (SBC-600), indicating that the adsorption rate of TSBC-600 is faster, which is consistent with the analysis of k_1 in the pseudo-first order kinetic equation. This demonstrates that the affinity of SB to thiourea is greater than that of MB. In summary, thiourea-modified biochar can effectively increase the adsorption rate of Cd^{2+} by biochar.

Table 2. Adsorption kinetic parameters of MBC-600, SBC-600, TMBC-600, and TSBC-600 ($C_0 = 100$ mg/L, pH = 7, doage$_{TMBC-600}$ = 5 g/L and doage$_{TSBC-600}$ = 4 g/L, 25 °C).

Samples	Pseudo First Order			Pseudo Second Order		
	Q_e (mg/g)	k_1 (1/min)	R^2	Q_e (mg/g)	k_2 (g/mg/min)	R^2
TSBC-600	11.65	0.1391	0.88	12.19	0.0184	0.92
SBC-600	5.93	0.0062	0.94	6.63	0.0013	0.97
TMBC-600	4.76	0.0189	0.94	5.20	0.0049	0.98
MBC-600	3.72	0.0124	0.90	4.09	0.0042	0.96

Note: Q_m is the maximum adsorption capacity; k_1 is the rate constant of the pseudo-first-order kinetic equation; k_2 is the rate constant of the pseudo-first-order kinetic equation.

4.3. Isothermal Adsorption Curves before and after Biochar Modification

According to the shape of the isotherms, the isotherms of the four types of biochar can be designated as type I isotherms as per the BDDT (Brunauer Deming Deming Teller) classification [60]. Therefore, the commonly used Langmuir and Freundlich equations are used for fitting. The detailed fitting parameters and correlation coefficients are listed in Table 3. By comparing the R^2 fit using the two models, it is found that the Langmuir equation is more suitable than the Freundlich equation. This indicates that the adsorption of Cd^{2+} by the four biochars is monolayer adsorption. The functional groups on the absorbent surface are the main adsorption sites during the adsorption process, and the process takes place under the electrostatic attraction and hydrogen bonding [61]. There was no interaction between the homogeneity of the adsorbent surface and adsorption sites. The maximum adsorption capacity Q_m calculated by the Langmuir equation is not significantly different from the actual adsorption amount q_e. The maximum adsorption capacity of each biochar is TSBC-600 (19.998 mg/g) > SBC-600 (9.880 mg/g) > TMBC-600 (9.631 mg/g) > MBC-600 (5.898 mg/g). The adsorption capacity of thiourea modified TSBC-600 and TMBC-600 increased by 2.02 and 1.63 times, respectively. The adsorption capacities reported by other different adsorbents varied greatly among previous studies (Table S1). The adsorption capacity of TSBC-600 and TMBC-600 is nearly five times than biochar through pyrolysis with thiourea impregnation [15], the reason for this differentiation may be different activation of raw biochar in one-step co-pyrolysis. Moreover, the different feedstock and modifier made the variation of different surface characteristics, minerals, and functional groups of biochar.

Table 3. The fitting parameters for isothermal adsorption of MBC-600, SBC-600, TMBC-600, and TSBC-600 (pH = 7, doage$_{TMBC-600}$ = 5 g/L and doage$_{TSBC-600}$ = 4 g/L, 25 °C).

Samples	Langmuir Model			Freundlich Model		
	Q_m (mg/g)	K_L (L/mg)	R^2	K_F (L/g)	1/n	R^2
TSBC-600	19.998	0.026	0.91	4.230	0.233	0.70
SBC-600	9.880	0.050	0.83	3.506	0.158	0.55
TMBC-600	9.631	0.008	0.99	0.652	0.385	0.90
MBC-600	5.898	0.009	0.91	0.417	0.380	0.78

Notes: Q_m is the maximum adsorption capacity; K_L is the affinity constant of the interaction between the adsorbate and the adsorbent; K_f is the Freundlich adsorption capacity parameter; n is the empirical parameter of the adsorption strength.

For the separation factor R_L ($R_L = 1/(1 + R_L C_0)$), when $R_L > 1$, the adsorption is unfavorable; when $0 < R_L < 1$, the adsorption is favorable; when $R_L = 1$, the adsorption is linear [62]. In the Langmuir model, the R_L of biochar for Cd^{2+} is between zero and one, indicating that the adsorption behavior of biochar to Cd^{2+} is favorable. Similarly, the value of n in the Freundlich model can also confirm this viewpoint. The value of n is related to the properties of the adsorption material and the adsorption system. The larger the value of n, the better the adsorption performance of the material. When $0.1 < 1/n < 0.5$, it means that the adsorption is easier to perform; when $1/n > 2$, it means that the adsorption is difficult to carry out [53]. The 1/n values of the four biochars are all in the range of 0.1–0.5, which indicates that the N and S groups on the surface of the biochar have a higher modification efficiency. This demonstrates that the full adsorption process is preferential adsorption. The adsorption performance is relatively good, and the adsorption process is non-linear isothermal adsorption. The adsorption of Cd^{2+} by the four biochars is completed by a variety of mechanisms [14,50,63].

5. Conclusions

In this study, an N, S modified biochar was prepared by the co-pyrolysis of thiourea and poplar bark (SB) or poplar sawdust (MB), and used for the removal of aquatic cadmium ions. The results showed that the performance of thiourea-modified biochar was stable. The introduction of S and N optimized the surface structure of biochar, which was beneficial for enhancing the adsorption efficiency of biochar for Cd^{2+}. The optimal modification temperature of TSBC and TMBC was 600 °C, and the optimal reaction dosage of TSBC-600 and TMBC-600 was 4 g/L and 5 g/L, respectively. The optimal reaction pH was 7. Langmuir model and the pseudo-second-order kinetic model can explain the adsorption behavior of TSBC-600 and TMBC-600 with regard to Cd^{2+}. The adsorption behavior of TSBC-600 and TMBC-600 to Cd^{2+} was mainly chemical adsorption, which can be attributed to the surface functional groups. The maximum adsorption capacity of TSBC-600 and TMBC-600 calculated by the Langmuir model was 19.998 mg/g and 9.631 mg/g, respectively. These results indicated that the thiourea-modified biochar has strong adsorption capacity and good acid resistance, which is promising in the remediation of Cd-polluted water.

References

1. Jin, Z.; Deng, S.; Wen, Y.; Jin, Y.; Pan, L.; Zhang, Y.; Black, T.; Jones, K.C.; Zhang, H.; Zhang, D. Application of Simplicillium chinense for Cd and Pb biosorption and enhancing heavy metal phytoremediation of soils. *Sci. Total Environ.* **2019**, *697*, 134148. [CrossRef] [PubMed]

2. World Health Organization. *Ten Chemicals of Major Public Health Concern*; World Health Organization: Geneva, Switzerland, 2010; pp. 1–4.

3. Asara, Y.; Marchal, J.; Carrasco, E.; Boulaiz, H.; Solinas, G.; Bandiera, P.; Garcia, M.; Farace, C.; Montella, A.; Madeddu, R. Cadmium modifies the cell cycle and apoptotic profiles of human breast cancer cells treated with 5-fluorouracil. *Int. J. Mol. Sci.* **2013**, *14*, 16600–16616. [CrossRef] [PubMed]

4. Shen, Z.; Zhang, J.; Hou, D.; Tsang, D.C.; Ok, Y.S.; Alessi, D.S. Synthesis of MgO-coated corncob biochar and its application in lead stabilization in a soil washing residue. *Environ. Int.* **2019**, *122*, 357–362. [CrossRef] [PubMed]

5. Liu, N.; Huang, X.; Sun, L.; Li, S.; Chen, Y.; Cao, X.; Wang, W.; Dai, J.; Rinnan, R. Screening stably low cadmium and moderately high micronutrients wheat cultivars under three different agricultural environments of China. *Chemosphere* **2020**, *241*, 125065. [CrossRef] [PubMed]

6. Zeng, S.; Ma, J.; Yang, Y.; Zhang, S.; Liu, G.J.; Chen, F. Spatial assessment of farmland soil pollution and its potential human health risks in China. *Sci. Total Environ.* **2019**, *687*, 642–653. [CrossRef] [PubMed]

7. Feizi, M.; Jalali, M.; Antoniadis, V.; Shaheen, S.M.; Ok, Y.S.; Rinklebe, J. Geo-and nano-materials affect the mono-metal and competitive sorption of Cd, Cu, Ni, and Zn in a sewage sludge-treated alkaline soil. *J. Hazard. Mater.* **2019**, *379*, 120567. [CrossRef]

8. Li, H.; Xiong, J.; Zhang, G.; Liang, A.; Long, J.; Xiao, T.; Chen, Y.; Zhang, P.; Liao, D.; Lin, L. Enhanced thallium (I) removal from wastewater using hypochlorite oxidation coupled with magnetite-based biochar adsorption. *Sci. Total Environ.* **2020**, *698*, 134166. [CrossRef]

9. Peng, H.; Gao, P.; Chu, G.; Pan, B.; Peng, J.; Xing, B. Enhanced adsorption of Cu(II) and Cd(II) by phosphoric acid-modified biochars. *Environ. Pollut.* **2017**, *229*, 846–853. [CrossRef]

10. Rajendran, M.; Shi, L.; Wu, C.; Li, W.; An, W.; Liu, Z.; Xue, S. Effect of sulfur and sulfur-iron modified biochar on cadmium availability and transfer in the soil-rice system. *Chemosphere* **2019**, *222*, 314–322. [CrossRef]

11. Li, Y.; Pei, G.; Qiao, X.; Zhu, Y.; Li, H. Remediation of cadmium contaminated water and soil using vinegar residue biochar. *Environ. Sci. Pollut. Res. Int.* **2018**, *25*, 15754–15764. [CrossRef]

12. Yakkala, K.; Yu, M.-R.; Roh, H.; Yang, J.-K.; Chang, Y.-Y. Buffalo weed (Ambrosia trifida L. var. trifida) biochar for cadmium (II) and lead (II) adsorption in single and mixed system. *Desalin. Water Treat.* **2013**, *51*, 7732–7745. [CrossRef]

13. Jing, F.; Chen, C.; Chen, X.; Liu, W.; Wen, X.; Hu, S.; Yang, Z.; Guo, B.; Xu, Y.; Yu, Q. Effects of wheat straw derived biochar on cadmium availability in a paddy soil and its accumulation in rice. *Environ. Pollut.* **2019**, *257*, 113592. [CrossRef] [PubMed]

14. Zhu, L.; Tong, L.; Zhao, N.; Wang, X.; Yang, X.; Lv, Y. Key factors and microscopic mechanisms controlling adsorption of cadmium by surface oxidized and aminated biochars. *J. Hazard. Mater.* **2020**, *382*, 121002. [CrossRef] [PubMed]

15. Gholami, L.; Rahimi, G.; Khademi Jolgeh Nezhad, A. Effect of thiourea-modified biochar on adsorption and fractionation of cadmium and lead in contaminated acidic soil. *Int. J. Phytoremed.* **2019**, *22*, 468–481. [CrossRef]

16. O'Connor, D.; Peng, T.; Li, G.; Wang, S.; Duan, L.; Mulder, J.; Cornelissen, G.; Cheng, Z.; Yang, S.; Hou, D. Sulfur-modified rice husk biochar: A green method for the remediation of mercury contaminated soil. *Sci. Total Environ.* **2018**, *621*, 819–826. [CrossRef]

17. Zhang, Y.; Fan, J.; Fu, M.; Ok, Y.S.; Hou, Y.; Cai, C. Adsorption antagonism and synergy of arsenate(V) and cadmium(II) onto Fe-modified rice straw biochars. *Environ. Geochem. Health* **2019**, *41*, 1755–1766. [CrossRef]

18. Zhang, R.-L.; Xu, J.; Gao, L.; Wang, Z.; Wang, B.; Qin, S.-Y. Performance and Mechanism for Fluoride Removal in Groundwater with Calcium Modified Biochar from Peanut Shell. *Sci. Adv. Mater.* **2020**, *12*, 492–501. [CrossRef]

19. Li, Z.; Sun, Y.; Yang, Y.; Han, Y.; Wang, T.; Chen, J.; Tsang, D.C. Biochar-supported nanoscale zero-valent iron as an efficient catalyst for organic degradation in groundwater. *J. Hazard. Mater.* **2020**, *383*, 121240. [CrossRef]

20. Shi, S.; Yang, J.; Liang, S.; Li, M.; Gan, Q.; Xiao, K.; Hu, J. Enhanced Cr (VI) removal from acidic solutions using biochar modified by Fe3O4@ SiO2-NH2 particles. *Sci. Total Environ.* **2018**, *628*, 499–508. [CrossRef] [PubMed]

21. Ma, Y.; Liu, W.J.; Zhang, N.; Li, Y.S.; Jiang, H.; Sheng, G.P. Polyethylenimine modified biochar adsorbent for hexavalent chromium removal from the aqueous solution. *Bioresour. Technol.* **2014**, *169*, 403–408. [CrossRef] [PubMed]

22. Park, J.H.; Wang, J.J.; Zhou, B.; Mikhael, J.E.R.; DeLaune, R.D. Removing mercury from aqueous solution using sulfurized biochar and associated mechanisms. *Environ. Pollut.* **2019**, *244*, 627–635. [CrossRef] [PubMed]

23. Liu, W.J.; Jiang, H.; Yu, H.Q. Development of Biochar-Based Functional Materials: Toward a Sustainable Platform Carbon Material. *Chem. Rev.* **2015**, *115*, 12251–12285. [CrossRef] [PubMed]

24. Leksungnoen, P.; Wisawapipat, W.; Ketrot, D.; Aramrak, S.; Nookabkaew, S.; Rangkadilok, N.; Satayavivad, J. Biochar and ash derived from silicon-rich rice husk decrease inorganic arsenic species in rice grain. *Sci. Total Environ.* **2019**, *684*, 360–370. [CrossRef] [PubMed]

25. Wei, Y.; Wei, S.; Liu, C.; Chen, T.; Tang, Y.; Ma, J.; Yin, K.; Luo, S. Efficient removal of arsenic from groundwater using iron oxide nanoneedle array-decorated biochar fibers with high Fe utilization and fast adsorption kinetics. *Water Res.* **2019**, *167*, 115107. [CrossRef] [PubMed]

26. Zhao, D.; Yang, X.; Zhang, H.; Chen, C.; Wang, X. Effect of environmental conditions on Pb (II) adsorption on β-MnO2. *Chem. Eng. J.* **2010**, *164*, 49–55. [CrossRef]

27. Gondek, K.; Mierzwa-Hersztek, M.; Kopeć, M.; Mróz, T. The Influence of Biochar Enriched with Magnesium and Sulfur on the Amount of Perennial Ryegrass Biomass and Selected Chemical Properties and Biological of Sandy Soil. *Commun. Soil. Sci. Plan Anal.* **2018**, *49*, 1257–1265. [CrossRef]

28. Liu, Q.; Fang, Z.; Liu, Y.; Liu, Y.; Xu, Y.; Ruan, X.; Zhang, X.; Cao, W. Phosphorus speciation and bioavailability of sewage sludge derived biochar amended with CaO. *Waste Manag.* **2019**, *87*, 71–77. [CrossRef]

29. Gao, Z.; Chen, C.; Chang, J.; Chen, L.; Wang, P.; Wu, D.; Xu, F.; Jiang, K. Porous Co3S4@Ni3S4 heterostructure arrays electrode with vertical electrons and ions channels for efficient hybrid supercapacitor. *Chem. Eng. J.* **2018**, *343*, 572–582. [CrossRef]

30. Wu, C.; Shi, L.; Xue, S.; Li, W.; Jiang, X.; Rajendran, M.; Qian, Z. Effect of sulfur-iron modified biochar on the available cadmium and bacterial community structure in contaminated soils. *Sci. Total Environ.* **2019**, *647*, 1158–1168. [CrossRef]

31. Huang, Y.; Lee, X.; Grattieri, M.; Yuan, M.; Cai, R.; Macazo, F.C.; Minteer, S.D. Modified biochar for phosphate adsorption in environmentally relevant conditions. *Chem. Eng. J.* **2020**, *380*, 122375. [CrossRef]

32. Yang, G.X.; Jiang, H. Amino modification of biochar for enhanced adsorption of copper ions from synthetic wastewater. *Water Res.* **2014**, *48*, 396–405. [CrossRef] [PubMed]

33. Amin, M.T.; Alazba, A.A.; Shafiq, M. Removal of Copper and Lead using Banana Biochar in Batch Adsorption Systems: Isotherms and Kinetic Studies. *Arab. J. Sci. Eng.* **2017**, *43*, 5711–5722. [CrossRef]

34. Tang, N.; Niu, C.G.; Li, X.T.; Liang, C.; Guo, H.; Lin, L.S.; Zheng, C.W.; Zeng, G.M. Efficient removal of Cd(2+) and Pb(2+) from aqueous solution with amino- and thiol-functionalized activated carbon: Isotherm and kinetics modeling. *Sci. Total Environ.* **2018**, *635*, 1331–1344. [CrossRef] [PubMed]

35. Lyu, H.; Tang, J.; Huang, Y.; Gai, L.; Zeng, E.Y.; Liber, K.; Gong, Y. Removal of hexavalent chromium from aqueous solutions by a novel biochar supported nanoscale iron sulfide composite. *Chem. Eng. J.* **2017**, *322*, 516–524. [CrossRef]

36. Wu, H.; Wei, W.; Xu, C.; Meng, Y.; Bai, W.; Yang, W.; Lin, A. Polyethylene glycol-stabilized nano zero-valent iron supported by biochar for highly efficient removal of Cr (VI). *Ecotox. Environ. Saf.* **2020**, *188*, 109902. [CrossRef]

37. Liu, L.; Fan, S. Removal of cadmium in aqueous solution using wheat straw biochar: Effect of minerals and mechanism. *Environ. Sci. Pollut. Res.* **2018**, *25*, 8688–8700. [CrossRef]

38. You, F.; Dalal, R.; Huang, L. Biochar and biomass organic amendments shaped different dominance of lithoautotrophs and organoheterotrophs in microbial communities colonizing neutral copper(Cu)-molybdenum(Mo)-gold(Au) tailings. *Geoderma* **2018**, *309*, 100–110. [CrossRef]

39. Chang, Y.; Zhang, G.; Han, B.; Li, H.; Hu, C.; Pang, Y.; Chang, Z.; Sun, X. Polymer dehalogenation-enabled fast fabrication of N, S-codoped carbon materials for superior supercapacitor and deionization applications. *ACS Appl. Mater. Interfaces* **2017**, *9*, 29753–29759. [CrossRef]

40. Mian, M.M.; Liu, G.; Yousaf, B.; Fu, B.; Ullah, H.; Ali, M.U.; Abbas, Q.; Mujtaba Munir, M.A.; Ruijia, L. Simultaneous functionalization and magnetization of biochar via NH3 ambiance pyrolysis for efficient removal of Cr (VI). *Chemosphere* **2018**, *208*, 712–721. [CrossRef]

41. Song, H.; Liu, Z.; Gai, H.; Wang, Y.; Qiao, L.; Zhong, C.; Yin, X.; Xiao, M. Nitrogen-Dopped Ordered Mesoporous Carbon Anchored Pd Nanoparticles for Solvent Free Selective Oxidation of Benzyl Alcohol to Benzaldehyde by Using O2. *Front. Chem.* **2019**, *7*, 458. [CrossRef]

42. Wu, Z.; Chen, X.; Yuan, B.; Fu, M.-L. A facile foaming-polymerization strategy to prepare 3D MnO2 modified biochar-based porous hydrogels for efficient removal of Cd (II) and Pb (II). *Chemosphere* **2020**, *239*, 124745. [CrossRef] [PubMed]

43. Wei, Y.; Yan, Y.; Zou, Y.; Shi, M.; Deng, Q.; Zhao, N.; Wang, J.; You, C.; Yang, R.; Xu, Y. Sulfonated polyaniline coated bamboo-derived biochar/sulfur cathode for Li-S batteries with excellent dual conductivity and polysulfides affinity. *Electrochim. Acta* **2019**, *310*, 45–57. [CrossRef]

44. Mohan, D.; Pittman Jr, C.U.; Bricka, M.; Smith, F.; Yancey, B.; Mohammad, J.; Steele, P.H.; Alexandre-Franco, M.F.; Gómez-Serrano, V.; Gong, H. Sorption of arsenic, cadmium, and lead by chars produced from fast pyrolysis of wood and bark during bio-oil production. *J. Colloid Interface Sci.* **2007**, *310*, 57–73. [CrossRef] [PubMed]

45. Xia, Y.; Yang, T.; Zhu, N.; Li, D.; Chen, Z.; Lang, Q.; Liu, Z.; Jiao, W. Enhanced adsorption of Pb(II) onto modified hydrochar: Modeling and mechanism analysis. *Bioresour. Technol.* **2019**, *288*, 121593. [CrossRef]

46. Mahdi, Z.; El Hanandeh, A.; Yu, Q. Influence of pyrolysis conditions on surface characteristics and methylene blue adsorption of biochar derived from date seed biomass. *Waste Biomass Valorization* **2017**, *8*, 2061–2073. [CrossRef]

47. Hernandez-Soriano, M.C.; Kerré, B.; Kopittke, P.M.; Horemans, B.; Smolders, E. Biochar affects carbon composition and stability in soil: A combined spectroscopy-microscopy study. *Sci. Rep.* **2016**, *6*, 25127. [CrossRef]

48. Lai, F.; Chang, Y.; Huang, H.; Wu, G.; Xiong, J.; Pan, Z.; Zhou, C. Liquefaction of sewage sludge in ethanol-water mixed solvents for bio-oil and biochar products. *Energy* **2018**, *148*, 629–641. [CrossRef]

49. Zhang, X.; Zhang, P.; Yuan, X.; Li, Y.; Han, L. Effect of pyrolysis temperature and correlation analysis on the yield and physicochemical properties of crop residue biochar. *Bioresour. Technol.* **2020**, *296*, 122318. [CrossRef]

50. Cui, X.; Fang, S.; Yao, Y.; Li, T.; Ni, Q.; Yang, X.; He, Z. Potential mechanisms of cadmium removal from aqueous solution by Canna indica derived biochar. *Sci. Total Environ.* **2016**, *562*, 517–525. [CrossRef]

51. Park, J.H.; Ok, Y.S.; Kim, S.H.; Cho, J.S.; Heo, J.S.; Delaune, R.D.; Seo, D.C. Competitive adsorption of heavy metals onto sesame straw biochar in aqueous solutions. *Chemosphere* **2016**, *142*, 77–83. [CrossRef]

52. Huang, P.; Ge, C.; Feng, D.; Yu, H.; Luo, J.; Li, J.; Strong, P.; Sarmah, A.K.; Bolan, N.S.; Wang, H. Effects of metal ions and pH on ofloxacin sorption to cassava residue-derived biochar. *Sci. Total Environ.* **2018**, *616*, 1384–1391. [CrossRef] [PubMed]

53. Li, D.; Yang, R.; Luo, H.; Liu, S.; Liu, Y.; Peng, O.; Tie, B. Effect of adsorption of cadmium from aqueous solution by hexadecyl trimethyl ammonium bromide modified biochar. *Chin. J. Environ. Eng.* **2019**, *13*, 1809–1821.

54. Enders, A.; Hanley, K.; Whitman, T.; Joseph, S.; Lehmann, J. Characterization of biochars to evaluate recalcitrance and agronomic performance. *Bioresour. Technol.* **2012**, *114*, 644–653. [CrossRef] [PubMed]

55. Lam, Y.Y.; Lau, S.S.; Wong, J.W. Removal of Cd (II) from aqueous solutions using plant-derived biochar: Kinetics, isotherm and characterization. *Bioresour. Technol. Rep.* **2019**, *8*, 100323. [CrossRef]

56. Cui, H.-J.; Wang, M.K.; Fu, M.-L.; Ci, E. Enhancing phosphorus availability in phosphorus-fertilized zones by reducing phosphate adsorbed on ferrihydrite using rice straw-derived biochar. *J. Soil Sediment* **2011**, *11*, 1135. [CrossRef]

57. Jiang, T.-Y.; Jiang, J.; Xu, R.-K.; Li, Z. Adsorption of Pb (II) on variable charge soils amended with rice-straw derived biochar. *Chemosphere* **2012**, *89*, 249–256. [CrossRef]

58. Yin, W.; Zhao, C.; Xu, J. Enhanced adsorption of Cd (II) from aqueous solution by a shrimp bran modified Typha orientalis biochar. *Environ. Sci. Pollut. Res.* **2019**, *26*, 37092–37100. [CrossRef]

59. Wang, S.; Guo, W.; Gao, F.; Yang, R. Characterization and Pb (II) removal potential of corn straw-and municipal sludge-derived biochars. *R. Soc. Open Sci.* **2017**, *4*, 170402. [CrossRef]

60. Caurie, M. The derivation of the GAB adsorption equation from the BDDT adsorption theory. *Int. J. Food Sci. Technol.* **2006**, *41*, 173–179. [CrossRef]

61. Yao, L.; Zhao, Z.; Zhao, L.; Zhang, Z.; Shi, M.; Xu, M.M. Evaluation of Adsorption of Cadmium onto Ferrihydrite-Humic Acid Coprecipitation. *Sci. Adv. Mater.* **2019**, *11*, 1232–1240. [CrossRef]

62. Ao, H.; Cao, W.; Hong, Y.; Wu, J.; Wei, L. Adsorption of Sulfate Ion from Water by Zirconium Oxide-Modified Biochar Derived from Pomelo Peel. *Sci. Total Environ.* **2019**, 135092. [CrossRef] [PubMed]

63. Chen, F.; Luo, Z.; Liu, G.; Yang, Y.; Zhang, S.; Ma, J. Remediation of electronic waste polluted soil using a combination of persulfate oxidation and chemical washing. *J. Environ. Manag.* **2017**, *204*, 170–178. [CrossRef] [PubMed]

Upcycling of Electroplating Sludge to Prepare Erdite-Bearing Nanorods for the Adsorption of Heavy Metals from Electroplating Wastewater Effluent

Yanwen Liu [1], Asghar Khan [1], Zhihua Wang [1], Yu Chen [2], Suiyi Zhu [1,*], Tong Sun [1], Dongxu Liang [1] and Hongbin Yu [1,*]

[1] Science and Technology Innovation Center for Municipal Wastewater Treatment and Water Quality Protection, Northeast Normal University, Changchun 130117, China; liuyw401@nenu.edu.cn (Y.L.); asje962@nenu.edu.cn (A.K.); wangzh807@nenu.edu.cn (Z.W.); sunt281@nenu.edu.cn (T.S.); liangdx891@nenu.edu.cn (D.L.)

[2] Jilin Institute of Forestry Survey and Design, Changchun 130022, China; papermanuscript2@126.com

* Correspondence: zhusy812@nenu.edu.cn (S.Z.); papermanuscript@126.com (H.Y.)

Abstract: Electroplating sludge is a hazardous waste produced in plating and metallurgical processes which is commonly disposed of in safety landfills. In this work, electroplating sludge containing 25.6% Fe and 5.5% Co (named S1) and another containing 36.8% Fe and 7.8% Cr (S2) were recycled for the preparation of erdite-bearing particles via a facile hydrothermal route with only the addition of $Na_2S \cdot 9H_2O$. In the sludges, Fe-containing compounds were weakly crystallized and spontaneously converted to short rod-like erdite particles (SP1) in the presence of Co or long nanorod (SP2) particles with a diameter of 100 nm and length of 0.5–1.5 μm in the presence of Cr. The two products, SP1 and SP2, were applied in electroplating wastewater treatment, in which a small portion of Co in SP1 was released in wastewater, whereas Cr in SP2 was not. Adding 0.3 g/L SP2 resulted in the removal of 99.7% of Zn, 99.4% of Cu, 37.9% of Ni and 53.3% of Co in the electroplating wastewater, with residues at concentrations of 0.007, 0.003, 0.33, 0.09 and 0.002 mg/L, respectively. Thus, the treated electroplating wastewater met the discharge standard for electroplating wastewater in China. These removal efficiencies were higher than those achieved using powdered activated carbon, polyaluminum chloride, polyferric sulfate or pure $Na_2S \cdot 9H_2O$ reagent. With the method, waste electroplating sludge was recycled as nanorod erdite-bearing particles which showed superior efficiency in electroplating wastewater treatment.

Keywords: electroplating sludge; hydrothermal process; heavy metal; electroplating wastewater; upcycling

1. Introduction

Electroplating is a basic process in the machine manufacturing industry and uses various heavy metals to protect plating pieces [1–4]. High volumes of electroplating wastewater are generated, which is an extremely hazardous type of wastewater containing multiple heavy metals [5]. Electroplating wastewater can be categorized into acidic or alkaline wastewater in accordance with the electroplating technology used. Acidic wastewater is easily treated through pH adjustment and coagulation, which transfer heavy metals from wastewater to sludges [2,3]. By contrast, alkaline wastewater comprises complex agents, such as citric acid, ethylene diamine tetra-acetic acid (EDTA) and tartaric acid [6,7], which react with heavy metals to form heavy metal–organic complexes. Thus, heavy metals cannot be hydrolyzed even after adjusting wastewater pH to values above 12. Therefore, heavy metals are difficult to precipitate in alkaline wastewater through pH adjustment and are commonly

treated using time-consuming processes, including pH adjustment, cationic exchange, extraction and/or precipitation with special agents [8–12]. Although the amount of heavy metals detected from the effluents of an electroplating workplace is usually low [10,13], heavy metals should be further removed until the discharge standard for electroplating wastewater is met.

The removal of heavy metals from alkaline electroplating wastewater generally involves two methods [14–21]. One is the decomposition of organic complex reagents by the Fenton reaction and/or wet oxidation [15–17]. For instance, Shin et al. [15] investigated the removal of a citrate–Ni complex in alkaline electroplating wastewater and found that, after the wastewater was adjusted to pH 3, 95% citrate removal was achieved by Fenton oxidation with the addition of 20 mM Fe^{2+} and 1080 mM H_2O_2, and subsequently 99.9% of Ni precipitation occurred when the wastewater was adjusted back to pH 10. Yong et al. also reported that more than 90% of Cu was precipitated after the decomposition of complex gluconic acid in a micro-electrolysis system [17]. Similarly, the derivatives of gluconic acid in the molasses-based distillery wastewater were effectively broken down by wet oxidation at a temperature above 150 °C [16]. Another method is the removal of heavy metals by adding special agents and/or functionalized resin [18–21]. For example, Li et al. [18] found that at a sodium diethyldithiocarbamate/Cu molar ratio of 1, approximately 99.6% of complex Cu (with EDTA as the coordination agent) is trapped by sodium diethyldithiocarbamate and precipitates during coagulation after the addition of polyferric sulfate and polyacrylamide. A few aminopolycarboxylic acids, such as iminodiacetic acid, nitrilotriacetic acid, and diethylenetriaminepentaacetic acid, include the necessary functionalized groups (e.g., carboxyl and amino) to chelate heavy metals [19]. Such organics were also grifted on the resin surface to considerably improve its affinity for heavy metals recycling from electroplating wastewater [20,21]. Although these methods can efficiently remove heavy metals from alkaline wastewater, they require expensive agents and complicated devices. Thus, their applications are limited. By contrast, adsorption is a low-cost process and has a simple operating method. Many adsorbents, such as natural minerals, carbon materials and artificial composites, exhibit a variety of surface groups (such as –OH and –COOH) to adsorb free heavy metals. These surface groups show relatively low affinity to heavy metals compared with complex agents and have low removal efficiencies in alkaline electroplating wastewater treatment [22]. Therefore, a novel adsorbent that can remove complex heavy metals should be urgently developed.

The resource reutilization of electroplating sludge for the preparation of novel adsorbents for electroplating wastewater treatment is a green route involving the "waste to treat wastewater" approach. This type of sludge is composed of heavy metals, precipitant reagent and hydrolyzed flocculant [23–25]. Fe/Al oxyhydroxide from hydrolyzed flocculants are usually used to adsorb free heavy metals in the absence of complex agents [24,25]. However, the reutilization of heavy metal-bearing sludges in alkaline electroplating wastewater has not yet been reported.

The aim of this study is to recycle Co/Cr-bearing sludge for the preparation of a novel erdite material that can be used in the advanced treatment of electroplating wastewater effluent. In contrast to conventional adsorbents, the novel erdite material can be spontaneously hydrolyzed in neutral solutions, thereby generating Fe/S-bearing oxyhydroxide with plenty of –SH groups for heavy-metal coordination. The release of Co and Cr in the prepared erdite materials was investigated during wastewater treatment.

2. Materials and Methods

2.1. Electroplating Sludge Pre-Treatment

The Co-bearing sludge, denoted as S1, was precipitated from the wastewater of a rolling-anode plant (Sanhe company, Changchun, China). The wastewater was first treated with a resin filter (CH-90, Kaiping company, Shanghai, China) to recycle Co, and then coagulated with the addition of polyferric sulfate and polyacrylamide. A yellowish precipitate was generated after coagulation treatment and pumped to a plate and frame filter (XAMY6/450-30U, Runnan company, Shanghai, China)

to perform mechanical dewatering. Thus, the yellowish cake of S1 was generated and stored in the northwestern corner of the waste yard before transport and landfilling. The Cr-bearing sludge, named S2, was generated from the wastewater of the electroplating workshop (Sanhe company, Changchun, China). For Cr recovery, a resin filter (RS10, Kaiping company, Shanghai, China) was also employed to treat the wastewater, and then the effluent was further treated with the coagulation and dewatering process with the abovementioned procedures. The generated Cr-bearing sludge cake was placed at the south side of the waste yard.

The two sludges, S1 and S2, were vacuum-dried at 50 °C overnight and ground to pass through a 1 mm mesh. The powder of each sludge was analyzed by X-ray fluorescence (XRF, S4-Explorer, Bruker, Karlsruhe, Germany); only the diffraction intensity of metallic elements was recorded, except for the nonmetal elements C, H and O. For S1, the percentage of total metallic elements was about 36.31%, whilst the residual in S1 was affiliated with the coordinated groups (e.g., oxide/oxyhydroxide, sulfate and chloride) and the added polymeric flocculant. S2 showed a similar composition to S1, and the major elements are summarized in Table 1. S1 contains 25.6% Fe and 5.5% Co, demonstrating that S1 is a Fe/Co-rich sludge, whereas S2 is a Fe/Cr-rich sludge with 36.8% Fe and 7.8% Cr.

Table 1. Sludge composition.

Element	Relative Weight Percentage (wt.%)	
	S1	S2
Fe	25.6	36.8
Cr	0.06	7.8
Co	5.5	0.04
Ca	0.5	1.3
Si	0.9	1.1
Al	2.05	2.78
Na	1.7	1.4

2.2. Hydrothermal Conversion of Sludge

S1 and S2 were hydrothermally treated in accordance with our previous method [26,27] with the replacement of NaOH by Na_2S. In brief, S1 (1 g), $Na_2S \cdot 9H_2O$ (2.4 g) and deionized water (30 mL) were mixed in a 50 mL Teflon vessel. Then, the vessel was sealed and heated at 180 °C for 10 h in a drying oven (DHG-9037A, Jinghong company, Shanghai, China) and water-cooled to below 25 °C. Finally, the blackish particles at the vessel bottom were collected, freeze-dried at −80 °C in a freeze dryer (FDU-2110, EYELA, Tokyo, Japan) overnight and denoted as SP1. SP2 was hydrothermally treated in accordance with the abovementioned steps, and the obtained product was named SP2.

2.3. Heavy Metal Release

In the Sanhe company, heavy-metal-bearing wastewaters were mixed in a storage tank to generated a comprehensive electroplating wastewater, in which Zn, Cu, Ni, Co and Cr values were 711.5, 36.8, 131.2, 2.7 and 0.9 mg/L. The comprehensive electroplating wastewater was alkaline at pH 13.5, and adjusted to pH 7–7.5 by adding hydrochloric acid (9.8 M, Binghai chemical Group, Jinhua, China), in accordance with the optimal pH range of the resin filter (KP752, Kaiping company, Shanghai, China) operation. The wastewater was then treated with resin (KP752, Kaiping company, Shanghai, China) for the recycling of heavy metals and precipitated with polyferric sulfate. After treatment, the pH of the electroplating wastewater effluent was 7.3, and the concentrations of Zn, Cu, Ni, Co and Cr were 3.03, 0.51, 0.56, 0.19 and 0.003 mg/L, respectively. In the effluent, the concentrations of Zn, Cu and Ni exceeded the emission standard of pollutants for electroplating in China (GB21900-2008). Thus, the effluent needed to be further treated before discharge.

In total, 0.8 g/L of SP1 and SP2 adsorbents were added to 100 mL of electroplating wastewater, and the mixture was magnetically stirred at 90 rpm for 2 h; then, SP1 and SP2 were collected and

freeze-dried after the reaction. The dried SP1 and SP2 were respectively put into 50 mL deionized water until the concentration was 0.3 g/L and stirred magnetically for 24 h. Then, the concentration of heavy metals in the supernatant was determined by an inductively coupled plasma optical emission spectrometer (ICP-OES, AVIO-200, PerkinElmer, Waltham, MA, USA).

2.4. Electroplating Wastewater Treatment

The effluent was treated by placing SP1 in 50 mL of effluent until the SP1 concentration was 0.05 g/L. The mixture was magnetically stirred at 90 rpm for 2 h, and SP1 was separated by centrifuging at 6000 rpm for 5 min. Subsequently, the supernatant was collected, and the residual heavy metals in the supernatant were determined. According to the aforementioned steps, heavy metal removal was optimized by varying the SP1 dosage from 0.05 g/L to 0.8 g/L. Then, the dosage of SP2 on the effluent treatment was also investigated according to the abovementioned steps. Powdered activated carbon is a commercial adsorbent and is used in mass production in the project-scale advanced treatment of electroplating wastewater [28,29]; thus, it was targeted as the control in the experiment. After that, several common chemical reagents and the raw sludge were used to treat the electroplating wastewater, including polyaluminum chloride (PAC) [30], polyferric sulfate (PFS) [31] and $Na_2S \cdot 9H_2O$ [32]. The experimental conditions are similar to the above, but the dose of the chemical reagent was 0.8 g/L, and the mixture was magnetically stirred at 90 rpm for 2 h.

2.5. Kinetic Experiment

A dose of 0.05 g/L SP2 was added to 50 mL electroplating wastewater, and the mixture was magnetically stirred at 90 rpm. The heavy metal concentration in the supernatant was measured at 0.25 h, 0.5 h, 1 h, 1.5 h and 2 h, respectively.

2.6. Adsorbent Regeneration

Adsorbent regeneration was carried out by treating with 15% NaCl of pH 5 for 48 h or calcining at 450 °C for 2 h. The adsorbent after regeneration treatment was put into 50 mL electroplating wastewater with a dose of 0.8 g/L and a reaction time of 2 h. After the reaction, the residual heavy metal concentration in the supernatant was measured.

2.7. Zeta Potential Measurement

In total, 0.5 g/L of SP2 was added to deionized water at pH 5 and magnetic stirring was performed, and the zeta potential of SP2 was measured by a zeta potential analyzer (Zetasizer Nano ZSP, Malvern, UK) at 30 min, 60 min, 180 min and 300 min, respectively.

2.8. Characterisation

The conversion mechanism was explained by characterizing the sludge and products by scanning electron microscopy (SEM, JSM-6400, Jeol, Tokyo, Japan), X-ray diffraction (XRD, Rint2200, Rigaku Corporation, Tokyo, Japan) and X-ray photoelectron spectroscopy (XPS, ADES-400, VG Scientific, Birmingham, Britain).

3. Results and Discussion

3.1. Conversion of the Two Types of Sludge to Erdite-Bearing Particles

The morphology and compositions of the sludges are shown in Figures 1 and 2. S1 was an irregular block (Figure 1a) and did not show the obvious peaks of Fe/Co-bearing compounds (Figure 2, S1). The Fe/Co-bearing compounds in S1 exhibited weakly crystallized forms. S2 showed fine particles (Figure 1b), and its XRD patterns were similar to those of S1 (Figure 2, S2) and corresponded to weakly crystallized Fe/Cr-bearing compounds. After hydrothermal treatment, SP1 synthesized using S1 as raw sludge was characterized by short rod-like particles (Figure 1c), with obvious peaks of erdite and

sulfur (Figure 2, SP1). In comparison with SP1, SP2 from S2 showed long nanorods with diameters of 100 nm and lengths of 0.5–1.5 μm (Figure 1d). These products corresponded to the sharp peaks of erdite in the curve of SP2 (Figure 2, SP2). These findings demonstrated that Fe was involved in the formation of amorphous Fe-bearing compounds in S1 and S2. These Fe-bearing compounds were converted to well-crystallized erdite particles, which were short in SP1 and lengthened in SP2.
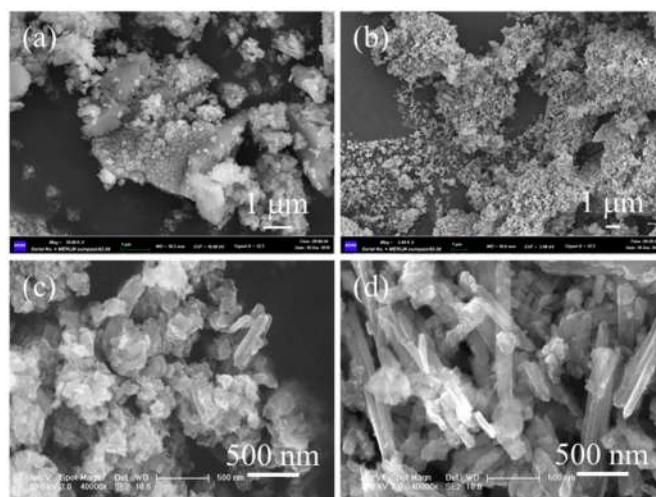

Figure 1. Scanning electron microscope (SEM) images of (**a**) S1, (**b**) S2, (**c**) SP1 and (**d**) SP2.
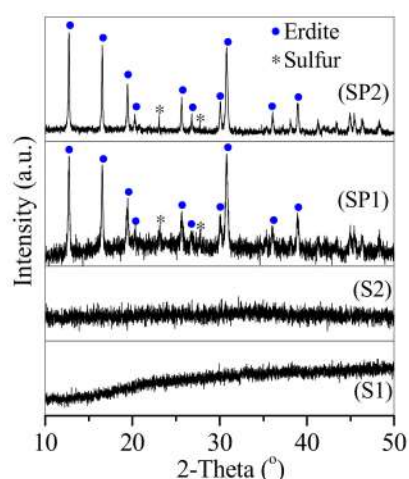
Figure 2. X-ray diffraction (XRD) patterns of S1, S2, SP1 and SP2.

The two types of sludge and the prepared SPs (SP1 and SP2) were further characterized by XPS. The Fe 2p spectra of S1 and S2 showed that the indicative peak at the binding energy of 710.5 eV (Figure 3a, S1 and S2) corresponded to Fe^{3+} in the Fe–O bond and was similar to that in ferrihydrite [33]. After the hydrothermal process, SP1 showed a new peak at the binding energy of 707.8 eV (Figure 3a, SP1). The peak belongs to Fe^{3+} in the Fe–S bond, in accordance with erdite formation. Compared with SP1, SP2 showed an intensified peak of Fe^{3+} in Fe–S bond (Figure 3a, SP2), in agreement with the long rod-sharped erdite. For the S 2p spectra, SP1 and SP2 showed the four major peaks at binding energies of 160.4, 161.3, 163.2 and 167.4 (Figure 3b) corresponding to the S in the Fe–S bond of the $(FeS2)_n^{n-}$ structure, and S^{2-}, sulfur and S in sulfate, respectively. In the Co 2p spectra, a major peak at 782.1 eV with a satellite peak was observed at the curve of S1 (Figure 3c, S1). The peak was related to the Co–O bond [34]. After hydrothermal treatment, new peaks related to Co in the Co–S bond appeared in SP1 at 778.6 eV (Figure 3c, SP1) [34], indicating the involvement of Co in CoS and/or CoS_2 after the addition of Na_2S. In the Cr 2p spectra, S2 exhibited two major peaks at 577.3 and 579.8 eV (Figure 3d,

S2). The peaks were attributed to the Cr(III) and Cr(VI) [35], respectively. However, the peak of Cr(VI) disappeared during the hydrothermal process, and only the peak of Cr(III) remained in SP2 (Figure 3d, SP2), indicating the reduction of Cr(VI) to Cr(III) by $Na_2S \cdot 9H_2O$.
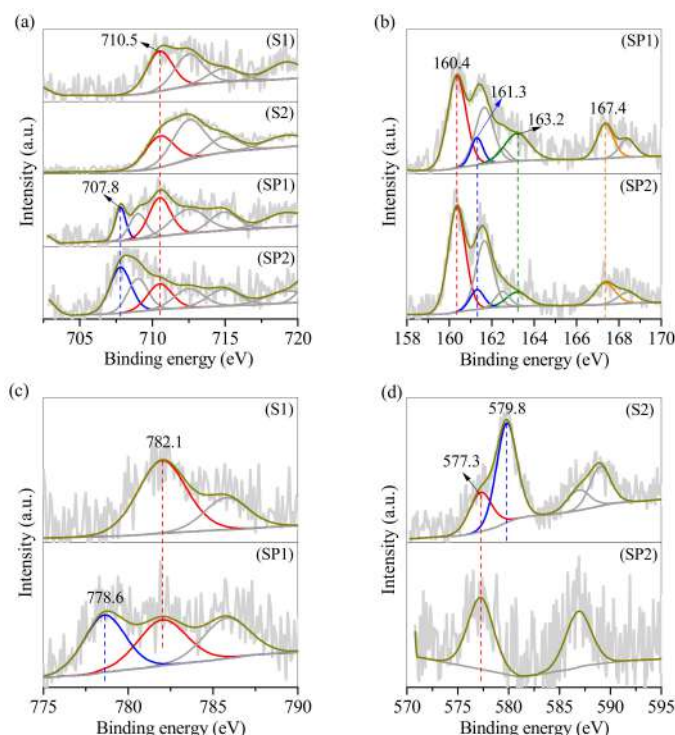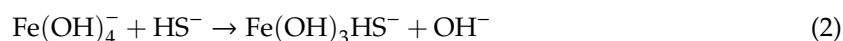

Figure 3. High resolution (**a**) Fe 2p, (**b**) S 2p, (**c**) Co 2p and (**d**) Cr 2p X-ray photoelectron spectroscopy (XPS) curves of S1, S2, SP1 and SP2.

Fe-bearing compounds were rich in S1 and S2 and converted into erdite in four steps. Firstly, the added Na_2S was hydrolyzed to release OH^- and HS^- to the solution, increasing the solution pH to above 13.6. Thus, many OH^- ions in the solution attacked the surface Fe at the Fe-bearing mineral and generated $Fe(OH)_4^-$ (Equation (1)) in the solution [36]. This result indicated the presence of residual Fe (approximately 15 mg/L) in the solution after the hydrothermal process (Figure 4). Secondly, a replacement reaction between free HS^- and the hydroxyl group of $Fe(OH)_4^-$ occurred, thereby generating $Fe(OH)_3HS^-$ (Equation (2)), followed by the conjunction reaction between two adjacent $Fe(OH)_3HS^-$ compounds. Thus, $Fe_2S_2(OH)_4^{2-}$ was generated with the dewatering of two water molecules (Equation (3)) [37]. Finally, the conjunction reaction continued in the presence of sufficient $Fe(OH)_4^-$ to form the final product $(FeS_2)_n^{n-}$. Na^+ neutralized the free charge of $(FeS_2)_n^{n-}$, and free water molecules occupied the free channels in the structure of $(FeS_2)_n^{n-}$, resulting in erdite nanorod formation. Cr(VI) was reduced by free HS^- in SP2, thereby generating Cr(III) with the generation of OH^-. This reaction employed plenty of OH^- during the $Fe(OH)_4^-$ formation, thereby increasing the length of the erdite nanorods in SP2. Conversely, the reaction between Co and HS^- in SP2 also occurred without OH^- generation, the contribution of which in erdite formation was negligible. During the hydrothermal process, Si/Al-bearing compounds were dissolved [38], thereby forming $Si(OH)_4$ and $Al(OH)_4^-$ in accordance with the high concentration of Si/Al in the supernatant (Figure 4). The dissolved Si/Al was not involved in erdite formation.
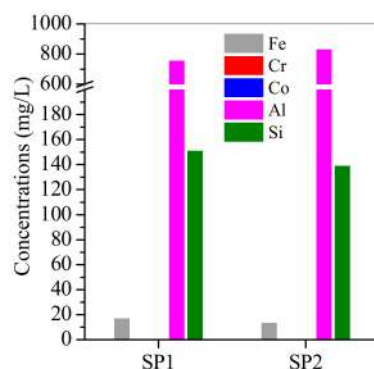
$$Fe(OH)_3 + OH^- \rightarrow Fe(OH)_4^- \tag{1}$$

$$Fe(OH)_4^- + HS^- \rightarrow Fe(OH)_3HS^- + OH^- \tag{2}$$

$$2Fe(OH)_3HS^- \rightarrow 2H_2O + (Fe_2S_2(OH)_4)^{2-} \tag{3}$$

Figure 4. Concentrations of heavy metals in the supernatant after the hydrothermal process.

3.2. Adsorption of Cu, Zn, Ni and Co from Electroplating Wastewater Effluent

In order to study the adsorption stability of SP1 and SP2, the release of heavy metals in used SP1/SP2 after electroplating wastewater treatment was investigated. After stirring at 90 rpm for 24 h, Co was apparently released from used SP1, and its concentration was close to 0.7 mg/L, whist only 0.003 mg/L Co was released from used SP2. Other heavy metals—e.g., Zn, Cu, Ni and Cr—were at a level lower than 0.01 mg/L (Figure 5). This demonstrated that the used SP2 showed a stable adsorption performance in the electroplating wastewater treatment.
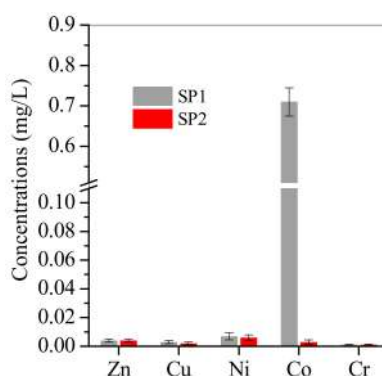

Figure 5. Heavy metals released from SP1/SP2 after electroplating wastewater treatment.

The electroplating wastewater contained 3.03 mg/L Zn, 0.51 mg/L Cu, 0.56 mg/L Ni and 0.19 mg/L Co. The first three heavy metals needed to be treated further because their concentrations exceeded the discharge standard for electroplating wastewater in China (GB21900-2008), and the concentration of Co met the discharge standard. The prepared adsorbents, SP1 and SP2, were employed to remove the first three heavy metals form electroplating wastewater, with powdered activated carbon as reference. At a dose of 0.05 g/L, the removal efficiency of Zn was 77.8% for SP2, 69.1% for SP1 and 29.1% for powdered activated carbon (Figure 6a). SP2 showed a high Zn removal efficiency in comparison with SP1 due to the formation of a well crystallized erdite nanorod in SP2. The mechanism for heavy metals removal by the erdite nanorod will be detailed in the next section. With the dosage increased from 0.05 to 0.3 g/L, the removal efficiency of Zn was elevated to nearly 100% for both SP1 and SP2, but only to 56.5% for powdered activated carbon (Figure 6a). In addition, a comparison experiment between SP2 and other materials were also performed, and their effects on Zn removal were sorted in the following order: SP2 > polyaluminum chloride (PAC) > $Na_2S \cdot 9H_2O$ > Polymeric ferric sulfate (PFS) > S2 > S1. As mentioned in Section 1, Zn was complexed with organic reagents (e.g., citric acid, EDTA and tartaric acid) in the alkaline electroplating process, and thus was not spontaneously precipitated in the generated alkaline wastewater. For the advanced treatment of electroplating wastewater, powdered activated carbon was widely used because it has plenty of surface functional groups; e.g., –COOH, –C=O and –OH, for Zn coordination. However, it showed a low Zn removal

efficiency (<64.7%), even though its dosage was increased to 0.8 g/L, in comparison with SP1 and SP2 (Figure 6a). This demonstrated that these surface groups on powdered activated carbon had a normal affinity to adsorbing Zn in comparison with the complexed organic reagents in wastewater. Ibrado et al. reported that the adsorption capacity of Zn on coconut-derived carbon was nearly 5 mg/g, but this decreased rapidly to 1.7 mg/g in the presence of cyano due to the formation of cyano complexes of Zn [39]. Therefore, the residual Zn was stable in the Zn-complex ligands and did not react with the surface groups of powdered activated carbon [40]. In electroplating wastewater treatment, PAC and PFS were common coagulants, and spontaneously hydrolysed to generate Al/Fe-bearing flocs. The raw sludge, S1 and S2, was rich in weakly crystallized Fe oxyhydroxides. Such Al/Fe-bearing flocs and Fe oxyhydroxides contained abundant of surface hydroxyl groups, similar to powdered activated carbon, for heavy metals adsorption [41]. In addition, $Na_2S \cdot 9H_2O$ was an industrial chemical, and decomposed to HS^- in water, followed by reacting with free Zn to form ZnS precipitate [42], which was in accordance with the removal efficiency of 52.7% for Zn. In summary, the surface functional groups on powdered activated carbon, hydrolysed PAC and PFS, S1 and S2, along with free HS^- from Na_2S, were not particularly efficient in the removal of Zn from electroplating wastewater.

In the electroplating wastewater, Cu was at a low level in comparison with Zn, and was removed at a rate of nearly 100% with the addition of SP1 and SP2 at the dosage of 0.3 g/L. However, only 25.5% Cu removal was achieved by powdered activated carbon in the presence of chelating organics in wastewater (Figure 6b). Chu et al. employed coal-based carbon for Cu-bearing wastewater treatment and found that by adding EDTA at the M_{EDTA}/M_{Cu} ratio of 10, the Cu removal efficiency dropped dramatically from 83.7% to 16.5% [43]. The abovementioned materials—e.g., PAC, PFS, $Na_2S \cdot 9H_2O$, S2 and S1—were also employed for Cu removal, showing similar values to those achieved for Zn removal. The atomic radius of Cu is 1.28 pm, which is close to that of Zn (1.39 pm), and thus Cu showed similar complex performance and removal efficiency to that of Zn in wastewater.

Although Ni was at a low level in wastewater—similar to Cu—its removal efficiency was apparently lower than that of Cu. As shown in Figure 6c, at the maximum dosage of 0.8 g/L, the removal efficiency of Ni was 49.6% for SP2, 44.3% for SP1 and 27.4% for powdered activated carbon. In the comparison experiment, the removal efficiency of Ni was ranked as follows: SP2 > PFS > PAC > $Na_2S \cdot 9H_2O$ > S2 > S1. Compared with Cu and Zn, Ni has a smaller atomic radius (1.24 pm) and easily reacts with chelating organics to form more stable Ni-complexed ligands. For instance, in citric acid, the stability constant of Ni in citric acid is $logK_{NiH_3A}^{Ni}$ 1.75, which is higher than that of Zn (1.25) [44]. In terms of Ni removal efficiency, $Na_2S \cdot 9H_2O$ only achieved 7.5%, which was lower than that of PAC and PFS and close to that of S1 and S2. This is because NiS was metastable in aqueous solution and easily converted to an Ni_2S_3 and Ni-S-bearing mixture to redissolve in wastewater [45]. S1 and S2 showed low removal efficiencies for Ni in comparison with PAC and PFS due to the inadequacy of surface hydrogen groups.

The Co concentration was less than 0.5 mg/L, which met the discharge standard. Approximately 60% of Co was removed by adding SP2, which is higher than the value for powdered activated carbon (nearly 20%) (Figure 6d). However, by adding 0.8 g/L SP1, the Co concentration in the treated wastewater was 0.77 mg/L (Figure 6e), which was apparently higher than that in the raw wastewater (0.19 mg/L), suggesting the release of Co from SP1 to wastewater, probably from the dissolution of CoS and/or CoS_2. Thus, SP1 was not an ideal adsorbent for the effluent treatment. The abovementioned materials were also used for Co removal, as shown in Figure 6f, and showed a similar value as Ni due to the similar radius and chelating performance of Co and Ni [44].
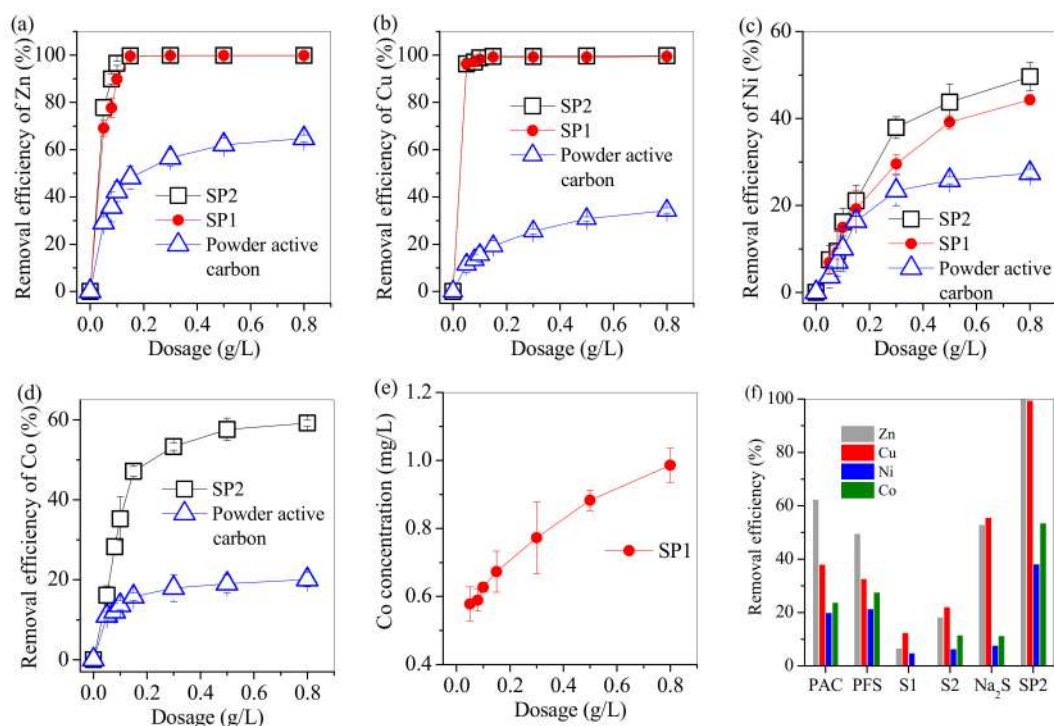
Figure 6. Application of SP1 and SP2 in electroplating wastewater treatment. (**a**–**d**) represent the removal efficiencies of Zn, Cu, Ni and Co, respectively, by SP1 and SP2, whilst (**e**) shows the concentration of Co in the supernatant with the addition of SP1; (**f**) shows the removal of heavy metals by adding SP2 in comparison with polyaluminum chloride (PAC), polyferric sulfate (PFS), the raw sludge S1 and S2 and Na$_2$S·9H$_2$O of chemically pure grade.

In comparison with the abovementioned materials, SP2 exhibited desirable removal efficiencies of Zn, Cu, Ni and Co. By adding 0.3 g/L SP2, the residual concentrations of Zn, Cu, Ni, Co and Cr in the wastewater were 0.007, 0.003, 0.33, 0.09 and 0.002 mg/L, respectively, which met the discharge standard [13]. This demonstrated that SP2 was an efficient reagent in smelting wastewater treatment.

The kinetic experiment of SP2 was investigated as shown in Figure 7, and the adsorption of heavy metal on SP2 was simulated using a pseudo-second-order model (Equation (4)). The kinetic model was expressed as follows:

$$q_t = \frac{kq_e^2 t}{1 + kq_e t} \tag{4}$$

where q_e and q_t are the adsorption capacity (mg/g) of the heavy metal at equilibrium and at any time, t, respectively; and k is the pseudo-second-order adsorption rate constant (g/mg h).
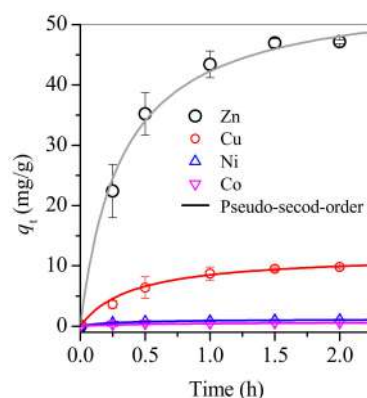

Figure 7. Non-linear plots of the pseudo-second-order model for the adsorption of Zn/Cu on SP2.

The adsorption data of Zn, Cu, Ni and Co on SP2 fitted well with the pseudo-second-order model (Figure 7) with correlation coefficients (R^2) of 0.995, 0.997, 0.991 and 0.989, respectively. This finding indicates the importance of heavy metals chemisorption on SP2. However, the calculated q_e values were in the following order: Zn > Cu > Ni > Co. The value of Zn was 3.03 mg/L in the electroplating wastewater, which was about six times the value of Cu and Ni, and thus showed the highest q_t. In comparison with Cu, Ni and Co have small ionic radii and are easily complexed with organics (e.g., ethylene diamine tetra-acetic acid) to form a stable complex product [6], resulting in a low q_t in comparison with Cu.

The used SP2 was regenerated with 15% NaCl solution at pH 5 for 48 h or calcinated at 450 °C for 2 h. The results showed that SP2 was regenerated easily using NaCl solution as the desorption agent. However, the removal efficiency of Zn, Cu, Ni and Co was dramatically decreased to 33.2%, 27.5%, 11.3% and 18.6% (Figure 8). After being calcinated at 450 °C, the regenerated SP2 also showed a similar low removal efficiency of heavy metals. This indicated that SP2 cannot feasibly be reused.
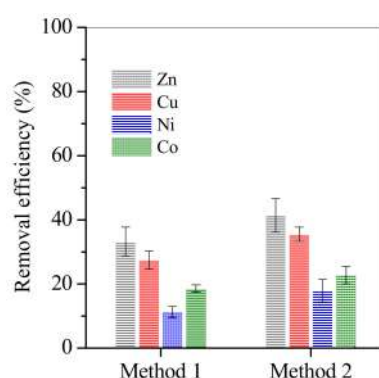

Figure 8. Reuse of the precipitate of hydrolyzed SP2 for electroplating wastewater treatment. In the figure, Methods 1 and 2 represent NaCl solution elution and high-temperature calcination, respectively.

The zeta potential measurement of SP2 showed that SP2 had a negative charge on the surface after hydrolysis (Figure 9), which showed a strong adsorption capacity for positively charged heavy metals. In addition, SP2 can compete with chelates for binding heavy metals and then remove heavy metals from wastewater.
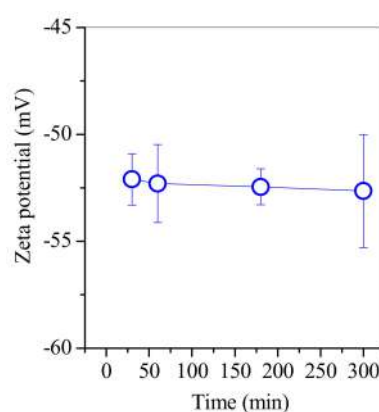

Figure 9. Zeta potential of SP2 in deionized water.

3.3. SP1 and SP2 Characterisation after Electroplating Wastewater Treatment

SP1 and SP2 were collected after wastewater effluent treatment and characterized by SEM, XRD and XPS, and the removal mechanism of heavy metals was investigated. The used SP1 and SP2 were irregular aggregates (Figure 10a,b); the peaks of erdite disappeared, and only peaks of element sulfur remained (Figure 11). Thus, erdite was spontaneously hydrolyzed. SP1 and SP2 spectra showed that

the peaks of Fe^{3+} in the Fe–S bond of erdite were absent; instead, a new peak with a binding energy of 710.2 eV appeared (Figure 12), corresponding to the Fe^{2+} generated from the redox reaction of Fe^{3+}–S [46]. The typical peak of structural S in erdite also disappeared, and the peaks of S^{2-} and S were recorded in the curve of SP1 and SP2, in agreement with erdite hydrolysis (Figure 12). In addition, the peaks of Co and Cr did not change obviously in SP1 and SP2, respectively, indicating that Co/Cr oxidation did not occur (Figure 13).
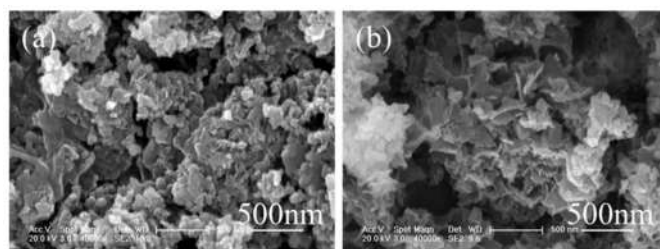

Figure 10. SEM images of (**a**) SP1 and (**b**) SP2 after smelting wastewater treatment.
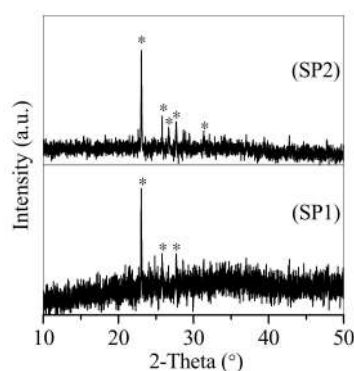

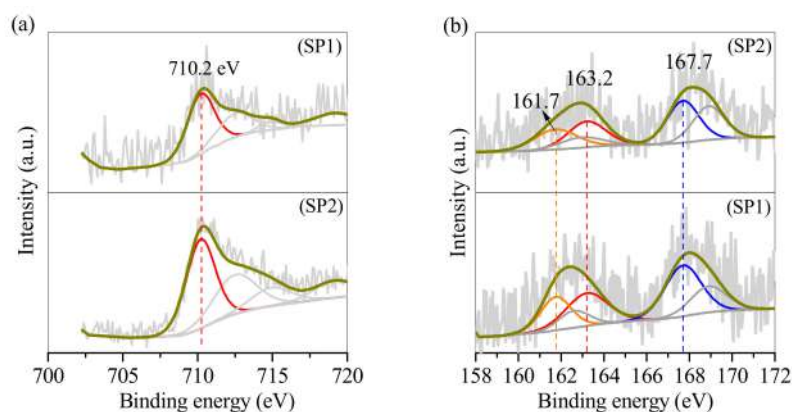**Figure 11.** XRD patterns of SP1 and SP2 after electroplating wastewater treatment.

Figure 12. High resolution (**a**) Fe 2p, (**b**) S 2p XPS spectrum of SP1 and SP2 after smelting wastewater treatment.
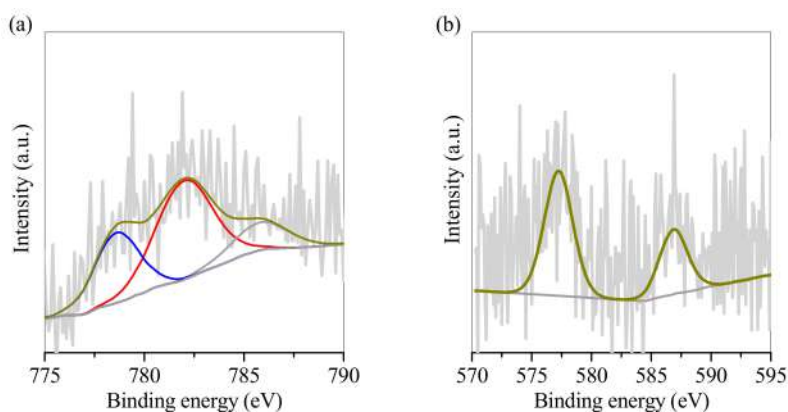
Figure 13. High resolution (**a**) Co 2p, (**b**) Cr 2p XPS spectrum of SP1 and SP2 after smelting wastewater treatment.

In the electroplating wastewater effluent, the residual heavy metals included Zn, Cu, Ni and Co and were chelated with organic matters, such as nitrilotriacetic acid and citric acid [6,7]; as such, they did not precipitate even at an effluent pH of >7.3. When the prepared SPs were introduced to the effluent, erdite was rich in SPs and spontaneously hydrolyzed and generated various Fe/S-bearing complexes and clusters, such as $=Fe(SH)_2$, $=Fe(OH)(SH)$ and $=Fe(SH)^+$ [47]. These products, which are metastable, were further converted to Fe/S-bearing oxyhydroxide (such as $=Fe–SH$ and $=Fe–OH$) through the homolytic cleavage of Fe–S–Fe bonds [48] after the release of OH^- and HS^- to the effluent (Figure 14). This phenomenon corresponds to the increase in the treated effluent pH from 7.3 to 8.6. During erdite hydrolysis, a redox reaction between surface Fe^{3+} and the adjacent free SH^- occurred [47], and thus surface-associated Fe^{2+}, which stabilized the new Fe/S-bearing oxyhydroxide, was generated. Surface functional groups (Fe–SH and Fe–OH) are rich in new Fe/S-bearing oxyhydroxide, and H^+ ions on their sides were dissociated with vacuum surface sites (Fe–S$^-$ and Fe–O$^-$) under alkaline conditions [26]. The adjacent vacuum sites exhibited high affinity to complex Cu and Zn (Figure 14) and competed with chelates, such as EDTA [49], leading to nearly 100% removal of Cu and Zn from the wastewater. However, Ni and Co have small ionic radii and easily react with complex agents to form stable complex products with high stability constants [6]; these products only break with difficulty in the presence of HS^- and hydrolyzed Fe/S-bearing oxyhydroxide, leading to the production of residual Co and Ni in treated effluents. Polyaluminum chloride and polyferric sulfate were hydrolyzed and formed Al/Fe flocs, exhibiting plenty of hydroxyl groups for heavy metal coordination; however, they showed low Zn, Cu, Ni and Co removal efficiencies (Figure 6f) given the absence of an –SH bond on the surface of the hydrolyzed Fe/Al flocs. In addition, the released HS$^-$ from the hydrolyzed erdite can react with heavy metals, such as Zn and Cu, to form S-bearing precipitates; however, they play a minor role in heavy metal removal. For instance, with the addition of Na_2S, approximately 50% of Zn and Cu was removed, whereas lower than 10% of Ni and Co was removed (Figure 6f). Thus, the role of HS^- in the removal of heavy metals is minimal. The Fe/S-bearing oxyhydroxide of hydrolyzed erdite plays a key role in the removal of residual heavy metals.
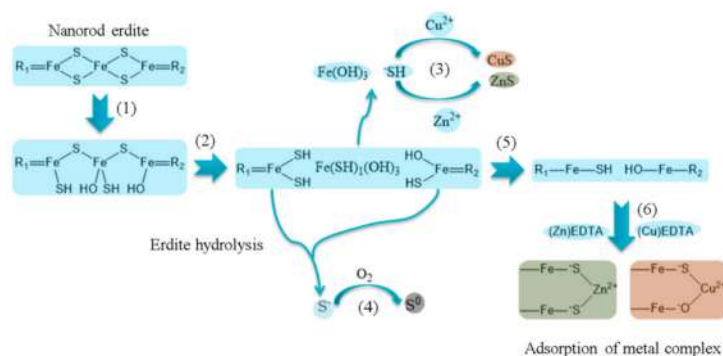
Figure 14. Illustration graph of SP2 for heavy metals removal from electroplating wastewater.

4. Conclusions

Two types of electroplating sludge, namely S1 with 25.6% Fe and 5.5% Co and S2 with 36.8% Fe and 7.8% Cr, were recycled as erdite-bearing particles for the advanced treatment of electroplating wastewater effluent. The weakly crystallized Fe-bearing minerals were rich in sludge and hydrothermally converted to well-crystallized erdite particles through the addition of Na_2S. In S1, Co was involved in CoS and/or CoS_2 formation, and the corresponding product SP1 was characterized by short rod-like particles. However, Cr had two valance states in S2, namely Cr(VI) and Cr(III). Cr(VI) was reduced to Cr(III) by Na_2S, and abundant OH^- was generated, which steadily promoted the conversion of Fe-bearing minerals to erdite. Consequently, the lengths of the erdite nanorods increased, and the corresponding product SP2 was characterized by long nanorods with a diameter of 100 nm and length of 0.5–1.5 μm.

When SP1 was added to the electroplating wastewater effluent, a fraction of Co was released to the effluent, and Zn and Cu were removed efficiently. Compared with SP1, SP2 showed ideal Zn, Cu, Ni and Co removal efficiencies without releasing Co and Cr. When the SP2 dosage was 0.3 g/L, 100% Zn and Cu removal efficiencies were nearly achieved, and 37.9% Ni and 53.3% Co removal efficiencies were observed—higher than those of powdered activated carbon, polyaluminum chloride, polyferric sulfate and Na_2S. After treatment, the concentrations of Zn, Cu, Ni and Co met the emission standard, and the treated effluent was dischargeable. Through the proposed method, the Cr-bearing electroplating sludge was recycled as erdite nanorod particles, and the product was efficient in the advanced treatment of electroplating wastewater.

Author Contributions: Data curation, A.K. and Z.W.; Project administration, Y.C.; Software, T.S.; Supervision, H.Y.; Validation, D.L.; Writing—original Draft, Y.L. and S.Z. All authors have read and agreed to the published version of the manuscript.

Conflicts of Interest: The authors declare no conflict of interest.

References

1. Mizushima, I.; Tang, P.T.; Hansen, H.N.; Somers, M.A. Development of a new electroplating process for Ni–W alloy deposits. *Electrochim. Acta* **2005**, *51*, 888–896. [CrossRef]
2. Wang, G.; Sui, J.; Wang, C.; Cai, G. Treatment of electroplating synthetical wastewater by combined process of oxidation and reduction, coagulation and sedimentation. *China Water Wastewater* **2007**, *23*, 57.
3. Zhang, Z.; Li, L.; Zhu, H.; Wang, F.; Hua, J. Removing chromium from electroplating wastewater by chemical precipitation. *Environ. Sci. Technol.* **2008**, *31*, 96–97.
4. Lin, Y.; Yen, S. Effects of additives and chelating agents on electroless copper plating. *Appl. Surf. Sci.* **2001**, *178*, 116–126. [CrossRef]

5. Celary, P.; Sobik-Szołtysek, J. Vitrification as an alternative to landfilling of tannery sewage sludge. *Waste Manag.* **2014**, *34*, 2520–2527. [CrossRef]

6. Andrus, M.E. A review of metal precipitation chemicals for metal-finishing applications. *Met. Finish.* **2000**, *98*, 20–23. [CrossRef]

7. Guo, X.; Liu, J.; Tian, Q. Elemental behavior of multi-component metal powders from waste printed circuit board during low-temperature alkaline smelting. *Chin. J. Nonferrous Met.* **2013**, *23*, 1757–1763.

8. Sze, Y.K.P.; Xue, L.Z.; Lee, M.Y. Treatment of alloy-electroplating wastewater by an automated solvent extraction technique. *Environ. Technol.* **2001**, *22*, 979–990. [CrossRef]

9. Ajmal, M.; Rao, R.A.K.; Ahmad, R.; Ahmad, J.; Rao, L.A.K. Removal and recovery of heavy metals from electroplating wastewater by using kynaite as an adsorbent. *J. Hazard. Mater.* **2001**, *87*, 127–137. [CrossRef]

10. Zhonghe, M.; Zhumei, W.; Ming, J. Treatment of low concentration complex nickel Chromium(Cr^{6+}) COpper mixed electroplating wastewater. *Mod. Chem. Res.* **2018**, *11*, 26–27.

11. Zhang, H.; Sun, M.; Song, L.; Guo, J.; Zhang, L. Fate of NaClO and membrane foulants during in-situ cleaning of membrane bioreactors: Combined effect on thermodynamic properties of sludge. *Biochem. Eng. J.* **2019**, *147*, 146–152. [CrossRef]

12. Sun, M.; Yan, L.; Zhang, L.; Song, L.; Guo, J.; Zhang, H. New insights into the rapid formation of initial membrane fouling after in-situ cleaning in a membrane bioreactor. *Process Biochem.* **2019**, *78*, 108–113. [CrossRef]

13. Xu, T.; Lei, X.; Sun, B.; Yu, G.; Zeng, Y. Highly efficient and energy-conserved flocculation of copper in wastewater by pulse-alternating current. *Environ. Sci. Pollut. Res. Int.* **2017**, *24*, 20577–20586. [CrossRef] [PubMed]

14. Wang, Z.; Ye, G.; Yang, Y. Low-concentration electroplating wastewater treatment by heavy metal chelator. *J. Zhejiang Univ. (Sci. Ed.)* **2010**, *37*, 665–669. [CrossRef]

15. Shih, Y.; Lin, C.; Huang, Y. Application of Fered-Fenton and chemical precipitation process for the treatment of electroless nickel plating wastewater. *Sep. Purif. Technol.* **2013**, *104*, 100–105. [CrossRef]

16. Tembhekar, P.D.; Padoley, K.V.; Mudliar, S.L.; Mudliar, S.N. Kinetics of wet air oxidation pretreatment and biodegradability enhancement of a complex industrial wastewater. *J. Environ. Chem. Eng.* **2015**, *3*, 339–348. [CrossRef]

17. Yong, L. Progress of electroplating wastewater treatment with micro-electrolysis method. *Guangdong Chem. Ind.* **2008**, *35*, 56.

18. Li, Y.; Zeng, X.; Liu, Y.; Yan, S.; Hu, Z.; Ni, Y. Study on the treatment of copper-electroplating wastewater by chemical trapping and flocculation. *Sep. Purif. Technol.* **2003**, *31*, 91–95. [CrossRef]

19. Repo, E.; Warchoł, J.K.; Bhatnagar, A.; Mudhoo, A.; Sillanpää, M. Aminopolycarboxylic acid functionalized adsorbents for heavy metals removal from water. *Water Res.* **2013**, *47*, 4812–4832. [CrossRef]

20. Fadel, D.; El-Bahy, S.; Abdelaziz, Y. Heavy metals removal using iminodiacetate chelating resin by batch and column techniques. *Desalin. Water Treat.* **2016**, *57*, 25718–25728. [CrossRef]

21. Benouali, D.; Kherici, S.; Belabbassi, M.; Belkandouci, M.; Bennemra, A. Preliminary study of Zinc removal from cyanide-free alkaline electroplating effluent by precipitation using oxalis plants. *Orient. J. Chem.* **2014**, *30*, 515–519. [CrossRef]

22. Šćiban, M.; Radetić, B.; Kevrešan, Ž.; Klašnja, M. Adsorption of heavy metals from electroplating wastewater by wood sawdust. *Bioresour. Technol.* **2007**, *98*, 402–409. [CrossRef] [PubMed]

23. Li, C.; Xie, F.; Ma, Y.; Cai, T.; Li, H.; Huang, Z.; Yuan, G. Multiple heavy metals extraction and recovery from hazardous electroplating sludge waste via ultrasonically enhanced two-stage acid leaching. *J. Hazard. Mater.* **2010**, *178*, 823–833. [CrossRef] [PubMed]

24. Espinosa, D.C.R.; Tenório, J.A.S. Thermal behavior of chromium electroplating sludge. *Waste Manag.* **2001**, *21*, 405–410. [CrossRef]

25. McCafferty, E.; Wightman, J. Determination of the concentration of surface hydroxyl groups on metal oxide films by a quantitative XPS method. *Surf. Interface Anal.* **1998**, *26*, 549–564. [CrossRef]

26. Qu, Z.; Wu, Y.; Zhu, S.; Yu, Y.; Huo, M.; Zhang, L.; Yang, J.; Bian, D.; Wang, Y. Green synthesis of magnetic adsorbent using groundwater treatment sludge for tetracycline adsorption. *Engineering* **2019**, *5*, 880–887. [CrossRef]

27. Zhu, S.; Wu, Y.; Qu, Z.; Zhang, L.; Yu, Y.; Xie, X.; Huo, M.; Yang, J.; Bian, D.; Zhang, H. Green synthesis of magnetic sodalite sphere by using groundwater treatment sludge for tetracycline adsorption. *J. Clean. Prod.* **2020**, *247*, 119140. [CrossRef]

28. Kołodyńska, D.; Krukowska, J.; Thomas, P. Comparison of sorption and desorption studies of heavy metal ions from biochar and commercial active carbon. *Chem. Eng. J.* **2016**, *307*, 353–363. [CrossRef]

29. Luo, Z.; Yang, C.; Zeng, G.; He, H.; Luo, S. Treatment of vanadium smelting wastewater by means of coagulation-sand filtration-activated carbon filter-microfiltration-RO integration technology. *Chin. J. Environ. Eng.* **2014**, *8*, 2257–2261. [CrossRef]

30. Xu, Z. Application and progress of PAC to industrial wastewater treatment. *Shanghai Environ. Sci.* **2003**, *22*, 353–357. [CrossRef]

31. Zhang, L.; Wang, K.; Liu, X.; Liu, P.; Huang, J. Experimental study of advanced treatment of coking wastewater using PFS coagulation-photocatalytic oxidation technology. *Mod. Chem. Ind.* **2015**, *34*, 487–494. [CrossRef]

32. Chen, W.S.; Lin, H.S.; Lin, J.F. Study on treatment technology of waste water with copper in complex system. *Adv. Mater. Res.* **2011**, *317*, 1847–1851. [CrossRef]

33. Glasauer, S.M.; Hug, P.; Weidler, P.G.; Gehring, A.U. Inhibition of sintering by Si during the conversion of Si-rich ferrihydrite to hematite. *Clays Clay. Miner.* **2000**, *48*, 51–56. [CrossRef]

34. Ouyang, C.; Wang, X.; Wang, S. Phosphorus-doped CoS_2 nanosheet arrays as ultra-efficient electrocatalysts for the hydrogen evolution reaction. *Chem. Commun. (Camb.)* **2015**, *51*, 14160–14163. [CrossRef]

35. Ji, M.; Su, X.; Zhao, Y.; Qi, W.; Wang, Y.; Chen, G.; Zhang, Z. Effective adsorption of Cr (VI) on mesoporous Fe-functionalized Akadama clay: Optimization, selectivity, and mechanism. *Appl. Surf. Sci.* **2015**, *344*, 128–136. [CrossRef]

36. Diakonov, I.I.; Schott, J.; Martin, F.; Harrichourry, J.-C.; Escalier, J. Iron (III) solubility and speciation in aqueous solutions. Experimental study and modelling: Part 1. hematite solubility from 60 to 300 °C in NaOH–NaCl solutions and thermodynamic properties of $Fe(OH)_4{}^-$ (aq). *Geochim. Cosmochim. Acta* **1999**, *63*, 2247–2261. [CrossRef]

37. Zhu, S.; Liu, Y.; Huo, Y.; Chen, Y.; Qu, Z.; Yu, Y.; Wang, Z.; Fan, W.; Peng, J.; Wang, Z. Addition of MnO_2 in synthesis of nano-rod erdite promoted tetracycline adsorption. *Sci. Rep.* **2019**, *9*, 1–12. [CrossRef]

38. Zhu, S.; Lin, X.; Dong, G.; Yu, Y.; Yu, H.; Bian, D.; Zhang, L.; Yang, J.; Wang, X.; Huo, M. Valorization of manganese-containing groundwater treatment sludge by preparing magnetic adsorbent for Cu (II) adsorption. *J. Environ. Manag.* **2019**, *236*, 446–454. [CrossRef]

39. Ibrado, A.S.; Fuerstenau, D.W. Adsorption of the cyano complexes of Ag(I), Cu(I), Hg(II), Cd(II) and Zn(II) on activated carbon. *Min. Metall. Explor.* **1989**, *6*, 23–28. [CrossRef]

40. Shi, T.; Tang, B. Adsorption characteristic study of Zn(II) and Zn(II)—EDTA at the activated carbon solution interface. *Ind. Water Treat.* **2000**, *20*, 12–15. [CrossRef]

41. Liu, H.; Yang, Y.; Kang, J.; Fan, M.; Qu, J. Removal of tetracycline from water by Fe-Mn binary oxide. *J. Environ. Sci.* **2012**, *24*, 242–247. [CrossRef]

42. Lewis, A.E. ChemInform abstract: Review of metal sulfide precipitation. *Cheminform* **2012**, *43*, 222–234. [CrossRef]

43. Chu, K.H.; Hashim, M.A. Adsorption of copper (II) and EDTA-chelated copper (II) onto granular activated carbons. *J. Chem. Technol. Biotechnol.* **2000**, *75*, 1054–1060. [CrossRef]

44. Campi, E.; Ostacoli, G.; Meirone, M.; Saini, G. Stability of the complexes of tricarballylic and citric acids with bivalent metal ions in aqueous solution. *J. Inorg. Nucl. Chem.* **1964**, *26*, 553–564. [CrossRef]

45. Legrand, D.L.; Nesbitt, H.W.; Bancroft, G.M. X-ray photoelectron spectroscopic study of a pristine millerite (NiS) surface and the effect of air and water oxidation. *Am. Min.* **1998**, *83*, 1256–1265. [CrossRef]

46. Sun, J.; Zhou, J.; Shang, C.; Kikkert, G.A. Removal of aqueous hydrogen sulfide by granular ferric hydroxide—Kinetics, capacity and reuse. *Chemosphere* **2014**, *117*, 324–329. [CrossRef]

47. Schlosser, C.; Streu, P.; Frank, M.; Lavik, G.; Croot, P.L.; Dengler, M.; Achterberg, E.P. H_2S events in the Peruvian oxygen minimum zone facilitate enhanced dissolved Fe concentrations. *Sci. Rep.* **2018**, *8*, 12642. [CrossRef]

48. Arantes, G.M.; Field, M.J. Ferric–thiolate bond dissociation studied with electronic structure calculations. *J. Phys. Chem. A* **2015**, *119*, 10084–10090. [CrossRef]

49. Yang, X.; Wang, J.-N.; Cheng, C. Preparation of new spongy adsorbent for removal of EDTA–Cu(II) and EDTA–Ni(II) from water. *Chin. Chem. Lett.* **2013**, *24*, 383–385. [CrossRef]

Adsorptive Behavior of an Activated Carbon for Bisphenol A Removal in Single and Binary (Bisphenol A—Heavy Metal) Solutions

M.A. Martín-Lara [1],* , **M. Calero [1],***, **A. Ronda [2], I. Iáñez-Rodríguez [1] and C. Escudero [3]**

[1] Departamento de Ingeniería Química, Universidad de Granada, Avda, Fuentenueva, s/n, 18071 Granada, Spain; ireneir@ugr.es

[2] Departamento de Ingeniería Química y Ambiental, Universidad de Sevilla, Camino de los descubrimientos, s/n, 41092 Sevilla, Spain; aronda@us.es

[3] Departamento de Tecnología de Alimentos, Instituto Nacional de Investigación y Tecnología Agraria y Alimentaria (INIA), Ctra. de A Coruña, km 7.5, 28040 Madrid, Spain; carlos.escudero@inia.es

* Correspondence: marianml@ugr.es (M.A.M.-L.); mcaleroh@ugr.es (M.C.); Tel.: +34-958-240-445 (M.A.M.-L.); +34-958-243-315 (M.C.)

Abstract: Bisphenol A (BPA) is an extensively produced and consumed chemical in the world. Due to its widespread use, contamination by this pollutant has increased in recent years, reaching a critical environmental point. This work investigates the feasibility of bisphenol A adsorption from industrial wastewater solutions, testing the reduction of bisphenol A in synthetic solutions by a commercial activated carbon, AC-40, in batch mode. Besides, mixtures of bisphenol A and different heavy metal cations were also studied. So far, no works have reported a complete study about bisphenol A removal by this activated carbon including the use of this material to remove BPA in the presence of metal cations. First, adsorption experiments were performed in batch changing pH, dose of adsorbent, initial bisphenol A concentration and contact time. Results showed greater retention of bisphenol A by increasing the acidity of the medium. Further, the percentage of bisphenol A adsorbed increased with increasing contact time. The selected conditions for the rest of the experiments were pH 5 and a contact time of 48 h. In addition, an increase in retention of bisphenol A when the dose of adsorbent increased was observed. Then, specific experiments were carried out to define the kinetics and the adsorption isotherm. Equilibrium data were adequately fitted to a Langmuir isotherm and the kinetics data fitted well to the pseudo-second-order model. The maximum adsorption capacity provided by Langmuir model was 94.34 mg/g. Finally, the effect of the presence of other heavy metals in water solution on the adsorption of bisphenol A was analyzed. Binary tests revealed competition between the adsorbates and a significant selectivity toward bisphenol A. Finally, the study of the adsorption performance in three consecutive adsorption–desorption cycles showed efficiencies higher than 90% in all cycles, indicating that the activated carbon has good reusability.

Keywords: activated carbon; adsorption; bisphenol A; equilibrium; heavy metals

1. Introduction

Bisphenol A (BPA) is recognized as a dangerous endocrine disruptor. It causes a number of hazardous effects on living beings such as fertility damage and fetal development problems [1–3]. It has been extensively used as a crude material in the industrial production of epoxy resins and polycarbonate plastics, which accounted for nearly 64% of BPA demand in 2018. These polycarbonate resins are mainly consumed in the electronics, construction and automotive industries. In terms of country distribution, high demand is concentrated in emerging consumers such as China, India,

Southeast Asia and Brazil. China is the largest player in the BPA industry, accounting for half of BPA's global consumption. Western Europe and the United States are the other important players in the BPA market [4].

As a consequence, concentrations of BPA are present both in surface waters as well as industrial wastewaters [5–7]. For all those reasons, novelty alternatives have been proposed for its removal from wastewater during recent years [8]. BPA is present in various types of water at different concentrations. For instance, it has a concentration of 17.2 mg/L in hazardous waste landfill leachate [9,10], 12 μg/L in stream water [11], between 3.5 and 59.8 ng/L in drinking water [7] and around 100 mg/L in effluents from polycarbonate factories [6,12].

Due to its high industrial yield and toxicological effect, the elimination of BPA from water solutions is of great importance and it has been listed as a priority pollutant in water treatment [13]. Several separation techniques such as adsorption, advanced oxidation, membrane separation, phytoremediation and photocatalysis, among others, have been applied to efficiently remove BPA from water effluents [14,15]. Particularly, among wastewater treatment technologies, phytoremediation is arousing attention because it is a promising ecologically friendly alternative to remove BPA from contaminated soil and water systems. For example, Phouthavong-Murphy et al. [9] investigated the potential of two United States native switchgrass varieties for BPA removal and found good BPA removals over approximately three months. Further, advanced oxidation processes are interesting due to their good performance in the degradation of BPA and other micropollutants. Recently, Luo et al. [16] studied the rapid removal of BPA and other organic micropollutants by heterogeneous peroxymonosulfate catalysis and reported that BPA had the highest removal efficiency at pH 9.0, almost 100% removal. Other researchers [17] integrated advanced oxidation processes with membrane filtration to form a catalytic membrane that demonstrated exceptional efficiency for instantaneous degradation of BPA. Moreover, the development of cheap and eco-friendly, effective and rapid remediation technologies for the removal of BPA has increased the investigations based on the use of transition metal-based nanomaterials for photocatalysis. For example, Rani et al. [18] synthesized and examined green zinc and cobalt ferrites nanoparticles for the degradation of BPA from water under direct sunlight. Results showed very good efficiencies, similar to those found with ZnO, Co_3O_4 and Fe_2O_3 nanoparticles.

Even novel technologies are being investigated with very good results: one of the most favorable methods is traditional adsorption onto carbonaceous materials [19]. Particularly, activated carbons have good characteristics to work as an adsorbent: high porosity and surface area (around 3000 m^2/g), high degree of surface reactivity and diverse characteristics of surface chemistry [20,21]. Due to these characteristics, activated carbons have been used for many different applications: as adsorbents, catalysts or catalyst supports. They have been tested as a cleaning material for removing pollutants from gaseous or liquid phases and the purification or recovery of chemicals [22,23]. Adsorption on activated carbon is one of the first water treatments to have been used [24,25] and it is recognized by the United States Environmental Protection Agency (US EPA) as one of the best methods for removing organic and inorganic compounds from water for human consumption. The aqueous-phase adsorption of both organic and inorganic compounds has been a very important application of activated carbons. In fact, around 80% of the world production of activated carbons is used in liquid-phase applications [26,27].

The adsorption mechanism of activated carbons is due to interactions (electrostatic or non-electrostatic) between the carbon surface and the adsorbate. The nature of these interactions, which can be attractive or repulsive, depends on the: (a) charge density of the carbon surface, (b) chemical characteristics of the adsorbate and (c) ionic strength of the solution. Non-electrostatic interactions are always attractive and can include: (a) van der Waals forces, (b) hydrophobic interactions and (c) hydrogen bonding.

Activated carbons can be manufactured by physical or chemical activation processes using a wide range of raw materials. Physical activation uses high temperature for the carbonization of the original

material in absence of oxygen (usually CO_2 or steam atmosphere). During chemical activation, the material is impregnated with a chemical agent prior to its carbonization. One of the most frequent chemical agents extensively used for the production of activated carbons in industry is H_3PO_4 [28,29].

Adsorptive removal of BPA from wastewater solutions by carbon-based materials, such as activated carbon, has been extensively studied [30–35]. For example, Juhola et al. [31] prepared a biomass-based adsorbent with a BPA adsorption capacity of 41.5 mg/g. Pan et al. [33] investigated the BPA adsorption on carbon nanomaterials that showed a very good potential for the removal of BPA of waters. Redding et al. [34] studied the adsorption of BPA on various modified lignite carbons. Specifically, the work demonstrated that these modified carbons prepared using high-temperature steam or methane/steam offered better behavior than conventional activated carbons. However, there are few works available focusing on the BPA removal from water when other types of contaminants are also present in the water [36–39]. BPA is a high-volume industrial chemical used in the production of epoxy resins and polycarbonate plastics. Further, different additives are added in these materials to improve the performance of the plastics. The chemical substances used as additives can be very different depending on the objective. The additives can include metal-containing additives such as heavy metals as cadmium, copper, lead or zinc, among others [40]. Heavy metals are another important type of pollutants that have been found in waters. Some researchers have analyzed the simultaneous adsorption/biosorption of these priority pollutants (heavy metals and organic pollutants) [41–43]. The influence of heavy metals could enhance the removal of BPA or perhaps they could compete with BPA for the available active sites and decrease the removal of BPA when the removal of BPA and heavy metals is carried simultaneously.

Hence, one of the objectives of this investigation is to study the interactions between some of the most common heavy metals in wastewater environments and BPA during adsorption onto activated carbon (AC-40 commercial sample). First, the single adsorption of BPA on AC-40 activated carbon was investigated. The main factors influencing the adsorption process were analyzed. Then, the simultaneous adsorption of BPA and heavy metal cations on AC-40 activated carbon was performed in order to know the type of adsorption (competitive or cooperative) which occurs between BPA and these metal cations. Finally, desorption of BPA in three consecutive cycles was analyzed. Although the study has been performed using a commercial activated carbon, so no novel findings about the material are given, there are not a wide range of research works in the literature about the use of AC-40 for the removal of BPA from wastewaters including (1) the effect of the main parameters, (2) a kinetics study, (3) an isotherms study, (4) simultaneous adsorption of BPA and heavy metals and (5) desorption. The authors consider that specific complete studies about the removal of emergent pollutants with the current technology (adsorption on activated carbons) can be interesting since they increase the knowledge in this field and can be applied in the industrial wastewater sector.

2. Materials and Methods

2.1. Adsorbent

Activated carbon trademark CECA S.L., known as AC-40, was used as an adsorbent in all the experiments. It is an extruded, thermally activated carbon from bituminous coal with a high surface area (1200 m^2/g). The main features of this adsorbent have been determined by Méndez Díaz et al. [44], Abdel Daiem et al. [45] and Velo-Gala et al. [46]. Table 1 shows a summary of the properties.

Table 1. Main physic-chemical characteristics of activated carbon AC-40.

Median particle diameter (MPD) (mm)	3
Density (g/L)	450
Moisture content (%)	4
Specific surface area (m^2/g)	1201
Pore volumes (mean widths of micropores 0.71 nm) (cm^3/g)	0.406
Pore volumes (diameter between 6.6 and 50 nm) (cm^3/g)	0.046
Pore volumes (diameter > 50 nm) (cm^3/g)	0.409
Concentration of acidic groups (μeq/g)	907.7
Concentration of basic groups (μeq/g)	96.0
Point of zero charge (pH$_{pzc}$)	7.5
%C	68.97
%H	1.03
%N	0.45
%S	1.02
%O	20.23
%Ash	8.30

2.2. Reagents

BPA, $C_{15}H_{16}O_{12}$, with 100% purity of Sigma-Aldrich company was used. Solutions of BPA were prepared by dissolving BPA in ultrapure water obtained from Milli-Q® equipment (Millipore). In adsorption tests conducted with mixtures of BPA and metal cations, copper (II) nitrate, $Cu(NO_3)_2 \cdot 3H_2O$, lead (II) nitrate, $Pb(NO_3)_2$, nickel (II) nitrate, $Ni(NO_3)_2 \cdot 6H_2O$, and cadmium (II) nitrate, $Cd(NO_3)_2 \cdot 4H_2O$, were used. All of them had purity higher than 98% and they were supplied by Panreac Quimica S.A. company.

2.3. Methodology

All adsorption experiments were conducted in batch mode in a stirred tank. BPA solutions were prepared in ultrapure water using a mild ultrasonic bath with a temperature of approximately 50 °C (323 K).

In the preparation of mixtures of BPA and metal cations, the proper amount of metal reagent was added to the previously prepared solution of BPA.

Each solution was located in a jacketed reactor with a capacity of 250 mL and maintained at a constant temperature (298 K) with stirring throughout the test by using a magnetic stirrer. When the operation time finished, a liquid sample was taken from the reactor by using an automated pipette. Moreover, a sample of the original solution was taken. The concentrations of initial and final contaminants were determined. Consequently, it was possible to determine the percentage of contaminant removed by the activated carbon.

The effect of main experimental conditions such as adsorbent dose, pH, contact time and initial BPA concentration was studied changing the variables between the following ranges: adsorbent dose (0.1–1.0 g/L), pH (3–10), contact time (0.5–48 h) and initial BPA concentration (1–160 mg/L) at a constant temperature of 25 °C. The desired value of pH was obtained by adding HCl solution (0.1 M) or NaOH solution (0.1 M) to the BPA solution. The real initial concentrations of BPA obtained in a pH range of 3–10 were measured in absence of the adsorbent.

To test the effect of pH on the adsorption process of BPA with activated carbon AC-40, an initial concentration of BPA of 20 mg/L, a contact time of 48 h and an adsorbent concentration of 0.5 g/L were selected. The pH of the medium was changed from 3 to 10. The temperature remained constant at 25 °C. Then, experiments were performed at pH values between 4 and 8 at different contact times in order to analyze the influence of contact time on the BPA removal efficiency.

To determine the minimum amount of activated carbon necessary to achieve maximum removal of BPA, experiments were carried out with a BPA initial concentration of 20 mg/L, three contact times

5.5, 22 and 48 h and a pH of 5, changing the concentration of the adsorbent from 0.1 to 1 g/L. The temperature remained constant during the tests at 25 °C (298 K).

The initial concentration of BPA is one of the most influential parameters in determining the contaminant removal on activated carbon from the aqueous solution. Experiments were carried out to test the effect of the BPA concentration in the adsorption process. A pH value of 5 with an adsorbent concentration of 0.5 g/L, and a contact time of 48 h were selected. The initial concentration of BPA was changed from 1 to 160 mg/L.

To analyze the kinetics of BPA adsorption, experiments were performed with different contact times (until a contact time of 48 h), at pH = 5 and a BPA initial concentration of 20 mg/L, with an adsorbent dose of 0.5 g/L and at a temperature of 298 K.

BPA adsorption isotherms of the activated carbon AC-40 were carried out at pH 5 and a temperature of 298 K. For this purpose, 100 mL of solutions containing different concentrations (1–160 mg/L) of BPA and 0.05 g of activated carbon were introduced into jacketed reactors, which were capped with flexible polyethylene (LDPE) film to avoid evaporation, prevent contamination and protect the solid–liquid system inside the reactor. Adsorption equilibrium was established when the concentration of BPA did not change (for 3 days). The BPA removal efficiency and the amount of BPA adsorbed by gram of activated carbon were calculated by the Equations (1) and (2), respectively:

$$\% \ \mathrm{Removal \ efficiency} = \frac{(C_i - C_f)}{C_i} \times 100 \tag{1}$$

$$q = \frac{(C_i - C_f)}{m} \times V \tag{2}$$

where C_i and C_f are the initial and final concentrations of BPA in solution, respectively, mg/L, q is the amount of BPA adsorbed by gram of adsorbent, mg/g, m is the mass of adsorbent, g, and V is the volume of the solution, L.

The procedure to obtain the data of adsorption of BPA on the activated carbon in the presence of metal cations was similar to methods to obtain adsorption results of single BPA systems. The only difference was the addition of a specific content of some metal cations to each BPA solution. Tests were performed with a concentration of 20 mg/L for both BPA and each metal cation, with an activated carbon dose of 0.5 g/L, during a contact time of 48 h and at pH value of 5. When equilibrium was reached, the BPA and different metal cations concentrations were analyzed.

The determination of the content of BPA was performed by ultraviolet–visible (UV–Vis) spectrophotometry, using the spectrophotometer model Genesys 6. The BPA concentration was determined by absorbance measurements at 277.5 nm. All the samples were collected in triplicate to further ensure precision. Samples used filled three quarters of the 1 cm cell used in the UV–Vis spectrophotometer. This amounted to approximately 1.5 mL of sample. In binary tests, the determination of metal content was performed by atomic absorption spectrophotometry, using the spectrophotometer model Perkin-Elmer AAnalyst 200.

Desorption of the BPA adsorbed onto the AC-40 was studied in a batch system. First, adsorption was performed at pH 5 and an initial BPA concentration of 20 mg/L with a dose of AC-40 of 0.5 g/L. Then, desorption was performed under the following desorption conditions: use of a mixture of methanol/acetic acid of 4:1 (v/v), a dose of AC-40 of 0.5 g/L, operation time of 48 h and temperature of 25 °C, and when the operation time was finished, the supernatant was separated and analyzed by ultraviolet–visible spectrophotometry at 277.5 nm.

3. Results and Discussions

3.1. Influence of pH and Contact Time

The pH is one of the main parameters that control the removal of compounds present in aqueous solutions using solid adsorbents. According to several authors, pH can change the availability and

characteristics of the pollutants in solution and it can modify the chemical state of the functional groups that are responsible for adsorption [47–49].

Some experiments were performed to test the effect of pH on the adsorption process of BPA with activated carbon AC-40. Figure 1 shows the results.
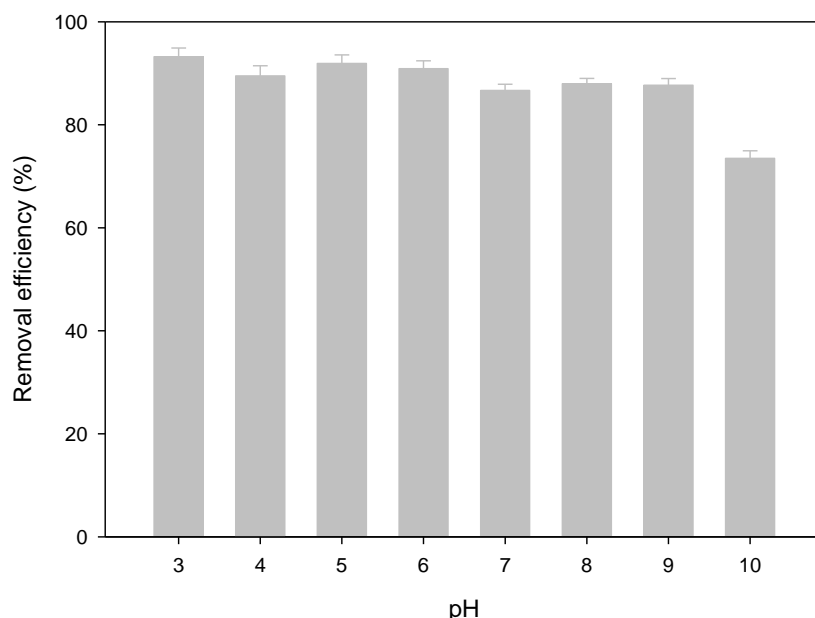

Figure 1. Bisphenol A (BPA) removal efficiency of activated carbon AC-40 according to the pH of the medium.

Data showed that pH did not significantly affect BPA adsorption. However, a slight tendency to obtain greater retention by increasing the acidity of the medium was observed. It could be because the zero point of charge was 7.5. The zero point of charge is the pH at which the surface of the adsorbent is globally neutral. Besides, it is a fundamental parameter of a material surface, governing the adsorbent–adsorbate interactions. Below this point, the surface is positively charged, otherwise it is negatively charged. Therefore, the CA surface was predominantly positive at pH values lower than 7.5. In contrast, negative charges appeared on the surface at pH values higher than 7.5 due to the dissociation of functional groups. In addition, BPA showed different states of equilibrium in an aqueous solution depending on the pH. BPA could be found in its molecular form at a pH less than 8. Deprotonation of the bisphenolate monoanion occurred at a pH of 8 [49], reaching a considerable concentration at pH 9 [50]. Therefore, electrostatic interactions between the negative charge of the surface of the activated carbon and bisphenolate anion could lead to a decrease in the overall adsorption of BPA. However, other interactions could also influence the adsorption rather than electrostatic forces, making the effect of surface charge less intense.

These results were in good agreement with those reported by other researchers. Thus, Wang and Xiao [51] indicated that the adsorption of BPA with four different activated carbons decreased at values of pH higher than 9. Chang et al. [52] found that the pH had an important role in the retention process of BPA with an activated carbon prepared from rice straw. Soni and Padmaja [53] also studied the adsorption of BPA on activated carbon prepared from palm shell. They found that at pH values below 9, the adsorption of BPA was not influenced by the pH of the medium. Bohdziewicz and Liszczyk [54] found a decrease in the adsorption of BPA by commercial activated carbon at pH values higher than or equal to 10. However, at pH values below 10, the adsorption capacity was not affected.

Figure 2 shows the BPA removal efficiency of activated carbon with different contact times. The removal efficiency increased with increasing contact time. At pH 5, the amount adsorbed increased quickly in the first 0.5 h of contact. Then, at 22 h, an adsorption percentage of 80% was reached. If

the process continued until 48 h, the adsorbed percentage would increase approximately up to 91%. Finally, at 72 h of operating time, the removal of BPA reached a value of 92% (a very low change with respect to 48 h). At other pH values, as pH 7 or pH 8, the adsorption was performed in a more progressive way. However, the change between 48 and 72 h was also low.
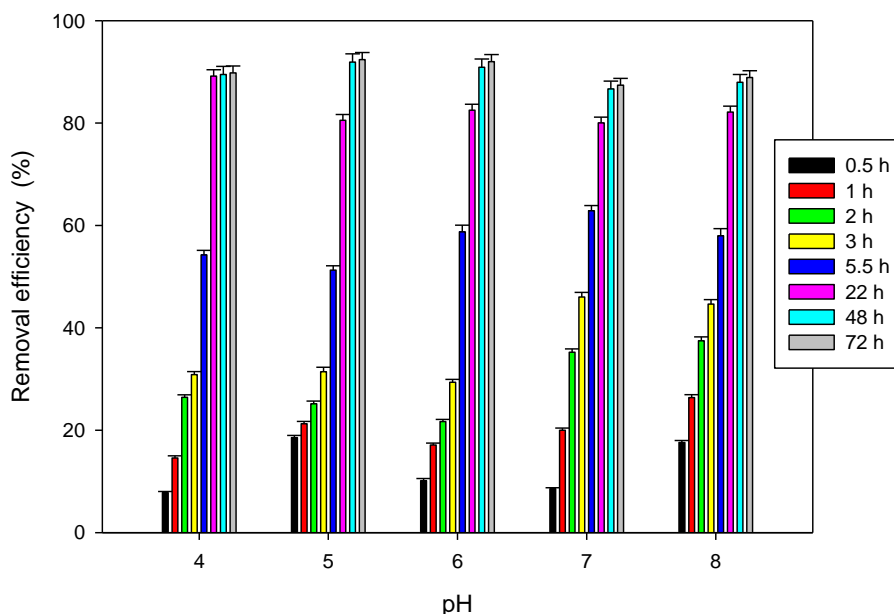

Figure 2. BPA removal efficiency of activated carbon AC-40 depending on pH at different contact times.

Considering the results obtained, from the removal efficiency point of view, a contact time of 48 h and a pH of 5 were selected for the rest of the experiments. There were not important differences in the pH range of 4 and 8. An adjustment by addition of acidic/basic chemicals could represent an important part of the cost of the wastewater treatment process and for that reason, an economic evaluation could indicate other pH values as a better option.
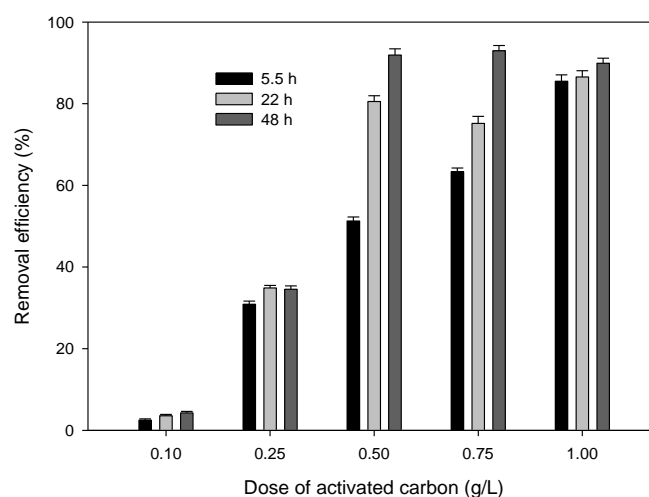
3.2. Influence of Adsorbent Dosage

Figure 3 shows the results of tests performed to determine the minimum dose of activated carbon necessary to achieve maximum removal of BPA.

As the dosage of activated carbon increased, the BPA removal efficiency from solutions increased for all the contact times. However, differences between 0.5, 0.75 and 1 g/L were very slight for long contacts times. For example, BPA removals (%) of 92%, 93% and 90% were achieved with adsorbent dosages of 0.5, 0.75 and 1 g/L, respectively, for a contact time of 48 h. However, great differences were observed at very short times. For example, very high adsorption attained at 5.5 h when using 1 g of adsorbent per L. With regard to the amount of BPA adsorbed by gram of activated carbon, in general, it was higher for a dose of 0.5 g/L. Above this adsorbent dose, a decrease in the uptake of the BPA was observed. In conclusion, if time was not considered, the use of an adsorbent dose of 0.5 g/L was recommended since at 22 h of operating time, very good BPA removals were achieved.

These results agreed with those obtained by numerous authors. Thus, Bautista-Toledo et al. [37] found an increase in the retention of BPA when 0.05 g of activated carbon was used for a period of 24 h in a BPA solution of 175 mg/L. Liu et al. [11] reported an increase in retention of BPA with two carbons activated with nitric acid that were selectively modified. They obtained maximum adsorption of BPA (432 mg/g) when changing the amount of activated carbon used. Tsai et al. [55] detected an increase in retention of BPA when the dose of adsorbent increased. This occurred because the number of adsorption sites increased in parallel with the increase in the dose of the adsorbent, when the

concentration of BPA was small (<20 mg/L). If the concentration was too high, the adsorbent would reach saturation quickly. As a result, it would stop contaminant retention.

According to the results, a concentration of 0.5 g/L of activated carbon was selected, since at this concentration the minimum amount of adsorbent is used with good adsorption removal percentages (if enough contact time is maintained).
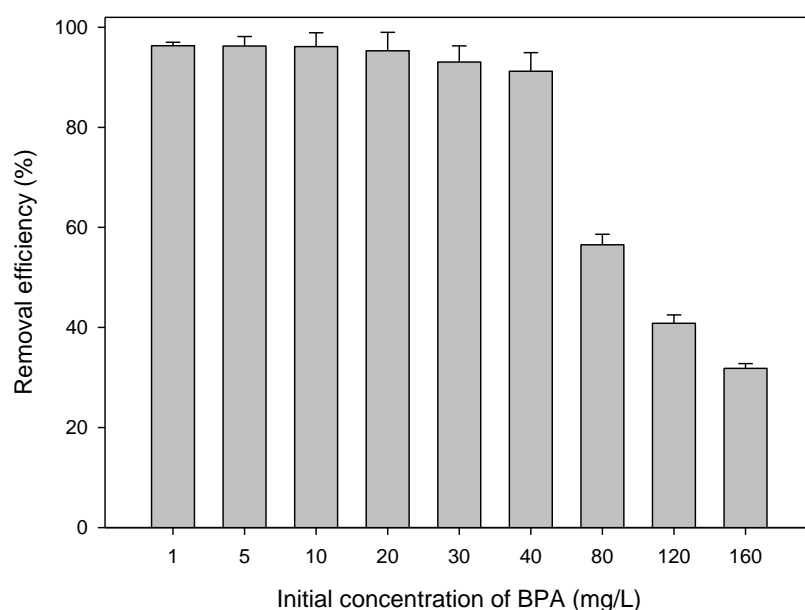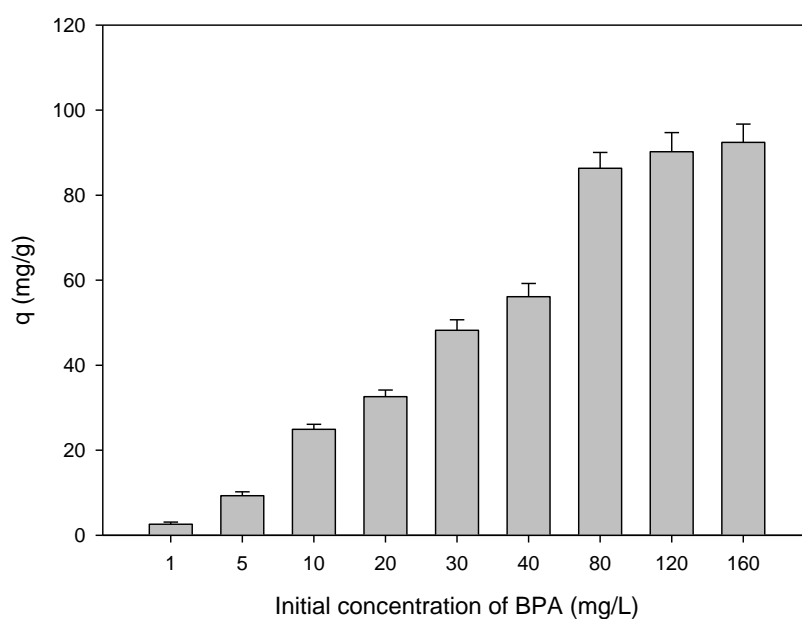

(**a**)
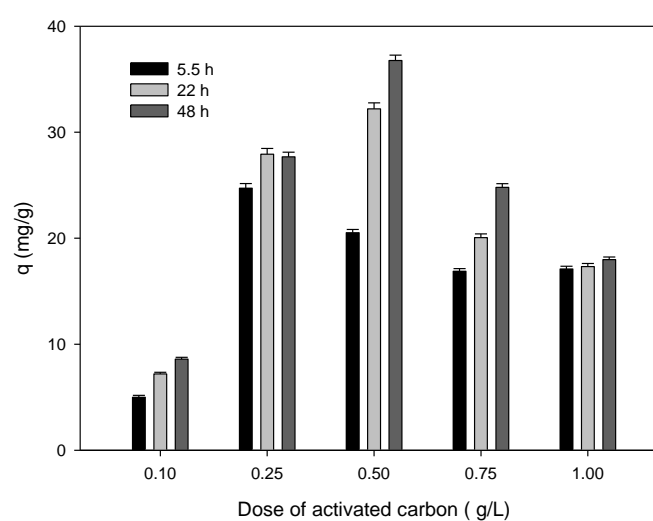
(**b**)

Figure 3. (**a**) BPA removal efficiency and (**b**) amount of BPA adsorbed by gram of activated carbon depending on adsorbent dosage at different contact times.

3.3. Influence of the Initial Concentration of BPA

Figure 4 shows the results of the influence of the initial concentration of BPA on its removal from the aqueous solution by AC-40.

(**a**)

(**b**)

Figure 4. (**a**) BPA removal efficiency and (**b**) amount of BPA adsorbed by gram of activated carbon depending on initial concentration of BPA.

It should be noted that BPA concentration did not influence BPA removal (%) for concentration values below 40 mg/L because the active sites on the adsorbent surface are not saturated. However, when the concentration was higher than 40 mg/L, a significant decrease was observed in the adsorption percentage. In this sense, at concentrations of BPA below 80 mg/L, the retention was higher because the pores of the carbon surface were occupied almost entirely. However, when the concentration of BPA was too high, the carbon surface underwent a supersaturation of its pores. As a consequence, a fraction of BPA was not retained by the adsorbent. These results were in agreement with those obtained by numerous authors. Thus, Bautista-Toledo et al. [37] obtained the same results in several studies with different concentrations of BPA and activated carbon. With regard to the amount of BPA removed expressed in mg/g of adsorbent (Figure 4b), it increased from 2.6 to 92.4 mg/g with an increase in the

initial concentration from 1 to 160 mg/L. The main reason for this important increase is the increase in the mass transfer driving force [56].

Based on the results obtained, an initial concentration of 20 mg/L was selected as the initial concentration of BPA for the rest of the experiments.

3.4. Kinetic Study

A kinetics study in adsorption allows the determination of the BPA removal rate from the aqueous medium. This study provides a basis for understanding the mechanism that controls the process and it is essential to select the optimum operating conditions in the system designed for the effluent treatment with this type of pollutant [57,58].

Experiments were performed with a total contact time of 48 h, pH = 5, a BPA initial concentration of 20 mg/L, an adsorbent concentration of 0.5 g/L and a temperature of 298 K. Figure 5 shows the values of q (mg retained/g sorbent) versus time.
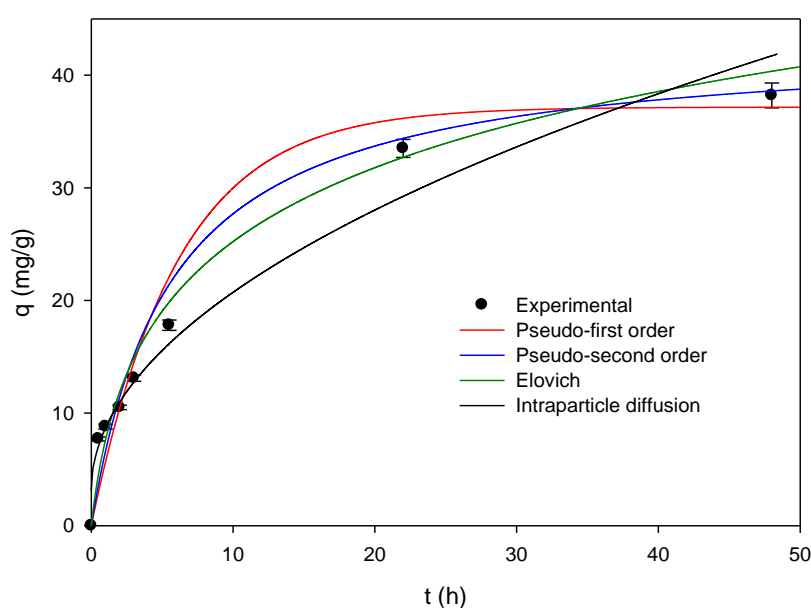

Figure 5. Variation in the adsorption capacity of BPA by activated carbon depending on the contact time and adjustment results of the four kinetic models.

These experimental results were fitted by a nonlinear regression to four kinetic models: pseudo-first-order, pseudo-second-order, Elovich and intraparticle diffusion models. Table 2 shows the representative equations of the models and their parameters. Likewise, Table 3 shows the results obtained when experimental data were fitted to the four selected kinetics models.

The pseudo-first- and pseudo-second-order models reproduced very well the experimental results. However, the intraparticle diffusion model showed a low R^2 value. Specially, the good correlation coefficients (R^2) of the pseudo-second-order model (it presented the highest R^2 value) and the similarity of the experimental and predicted adsorption capacity of this model indicated that the adsorption of BPA by activated carbon could be chemical adsorption, which is consistent with the results of Section 3.1. previously presented. In addition, the retention process was faster at first, but the equilibrium was not reached until 48 h of contact time. This indicates that, although adsorption happened quickly, the process subsequently proceeded more slowly until equilibrium was reached.

Other authors found similar results in their studies about BPA removal by activated carbons. Chang et al. [52] used an activated carbon obtained from rice straw agricultural waste. They found that the pseudo-second-order model fitted the experimental adsorption data better. Wang and Xiao [51] studied the adsorption of BPA by activated carbon reporting that the adsorption process followed the

first-order kinetics. Soni and Padmaja [53] reported that the kinetic data of adsorption of BPA onto palm shell activated carbon could be fitted well by a pseudo-second-order kinetic model. Tang et al. [59] showed that the kinetics of BPA removal onto activated carbon-alginate beads with cetyltrimethyl ammonium bromide fitted good to the pseudo-first-order, pseudo-second-order and Elovich models.

Table 2. Equations and parameters representative of the four selected kinetic models.

Model	Equation	Parameters
Pseudo-first-order	$q = q_e \left(1 - e^{-k_1 \cdot t}\right)$	q_e adsorption capacity, mg/g k_1 kinetic constant of the pseudo-first-order, h^{-1}
Pseudo-second-order	$q = \dfrac{t}{\frac{1}{k_2 \times q_e^2} + \frac{t}{q_e}}$	q_e adsorption capacity, mg/g k_2 kinetic constant of the pseudo-second-order, g/mg·h
Elovich	$q = \frac{1}{b} \ln(a \times b) + \frac{1}{b} \ln(t)$	a velocity of initial adsorption, mg/g·h b area of the occupied surface, g/mg
Intraparticle	$q = k_p \times t^{\frac{1}{2}} + C$	k_p the intraparticle diffusion rate constant (mg/(g·min$^{1/2}$)) C constant of the intraparticle diffusion model (mg/g)

Table 3. Adjustment results of the experimental data to the four selected kinetic models.

Model	Parameters		
Pseudo-first-order	$k_1 = 0.164$	$q_e = 37.17$	$r^2 = 0.995$
Pseudo-second-order	$k_2 = 0.004$	$q_e = 43.06$	$r^2 = 1.000$
Elovich	$a = 11.325$	$B = 0.099$	$r^2 = 0.992$
Intraparticle diffusion	$k_p = 5.577$	$C = 3.082$	$r^2 = 0.964$

3.5. Equilibrium Study

Figure 6 shows the retention capacity of BPA, q_e (mg retained/g of sorbent when equilibrium is reached), versus the equilibrium concentration of BPA in the liquid phase, C_e.
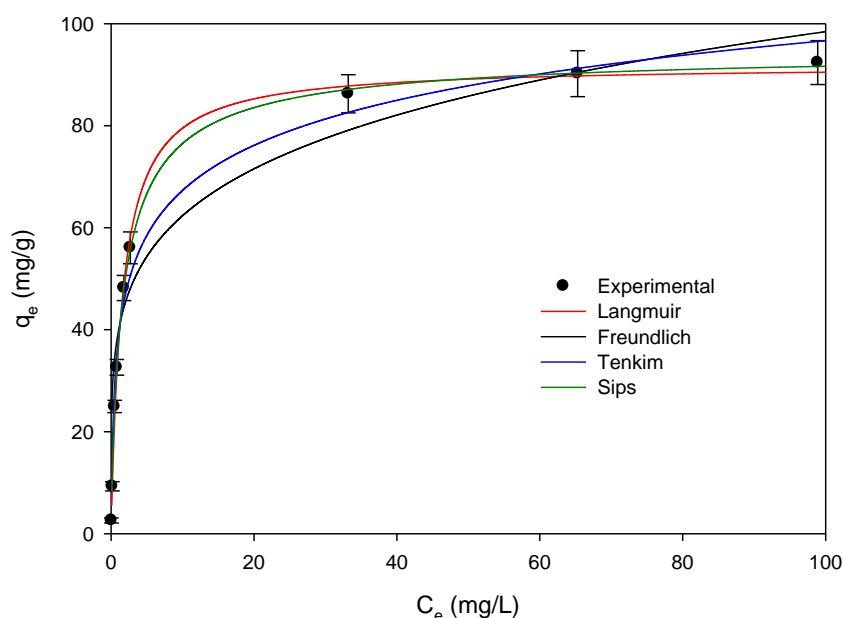

Figure 6. Equilibrium adsorption of BPA with activated carbon. Experimental results and adjustment to the selected models.

Different types of adsorption isotherms were found in the literature [51,60,61]. The isotherm obtained in this work was type I. The type I isotherm is monolayer adsorption easily explained using a Langmuir isotherm. Examples of type I adsorption isotherms are given by microporous solids such

as activated carbon (material used in this study). It is also observed that the maximum adsorption capacity was close to 92 mg/g, and it was reached when the initial concentration of BPA was 160 mg/L.

In order to study the equilibrium of the process, these results have been adjusted to different models which are shown in Table 4. Further, Table 5 shows the fitting results and the parameters of the models obtained. Figure 7 represents the isotherm obtained with the models used.

The Langmuir and Sips models were the best in reproducing the experimental results, as the value of the parameter n of the Sips isotherm was equal to the unit, which indicated that this model tended to be a Langmuir isotherm. This result indicates that adsorption is monolayer on the active sites of the adsorbent that has a homogeneous surface and molecules do not interact with each other. Likewise, the value of the maximum adsorption obtained with the Langmuir and Sips models was very close to the result obtained experimentally. These findings were similar to those obtained by other authors [52–54]. However, maximum capacity values of adsorption of AC-40 activated carbon were higher than those reported in the literature [62–65].

Finally, although adsorption processes performed in batch systems applied to the decontamination of wastewater are more frequent to determine the maximum adsorption capacity as the maximum amount of chemical adsorbed onto the adsorbent by mass of the adsorbent, in this work, the partition coefficients at the studied concentrations were also determined as the ratio of the concentration of BPA in solid phase (AC-40) to the concentration in liquid phase when the two concentrations are at equilibrium. Table 6 shows the partition coefficient as a function of the initial concentration of BPA. Data showed that the degree of partitioning varied with concentration. The linear partition coefficient was about 50–52 L/g (the amount adsorbed versus its solution concentration) at initial BPA concentrations lower or equal than 10 mg/L. This can be observed in Figure 6 since the first experimental points were plotted in a linear trend. However, as the initial concentration of BPA increased, the linear partition coefficient decreased until approximately 1 L/g at 160 mg/L. It also can be observed in the change of the slope of the isotherm (Figure 6) as the BPA concentration was increased. In adsorption studies, when an L-type plot (isotherm) is obtained, the q_m coefficient is a convenient and reliable parameter to be applied for adsorption capacities assessment better than the partition coefficient.

Table 4. Representative equations and parameters of the four selected models for the study of the equilibrium process.

Model	Equation	Parameters
Langmuir	$q_e = \frac{bq_m}{1+b} \frac{C_e}{C_e}$	q_m maximum adsorption capacity, mg/g b constant related to the affinity of the adsorbent for the adsorbate
Freundlich	$q_e = K_F \times C_e^{\frac{1}{n}}$	K_F equilibrium constant, $(mg/g)\cdot(L/mg)^{1/n}$ n constant related to the affinity between the adsorbent and the adsorbate
Sips	$q_e = \frac{q_m b C_e^{1/n}}{1+b C_e^{1/n}}$	q_m maximum adsorption capacity, mg/g b constant related to the affinity of the adsorbent for the adsorbate n parameter characterizing the system's heterogeneity
Temkin	$q_e = \frac{RT}{b} \ln(A_T C_e)$	A_T constant of union of the equilibrium (L/g), b Temkin constant, B constant related to the heat of adsorption (J/mol), $B = \frac{RT}{b}$

Table 5. Adjustment results of the experimental data to the four selected isotherm models.

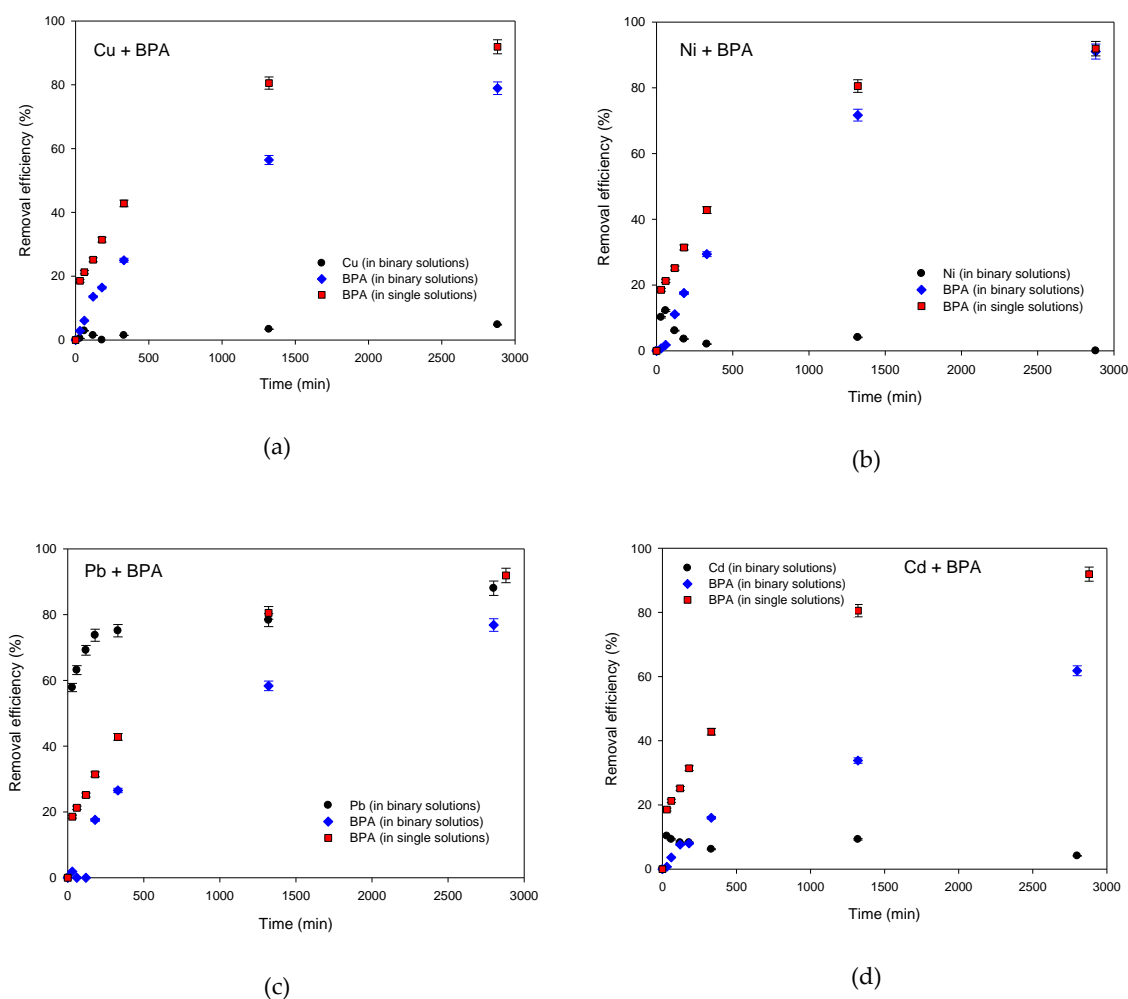| Model	Parameters		
Langmuir	$q_m = 91.90$	$b = 0.64$	$r^2 = 0.996$
Freundlich	$K_F = 39.49$	$n = 5.04$	$r^2 = 0.941$
Sips	$q_m = 95.06$	$b = 0.632$ $\quad$ $n = 1.23$	$r^2 = 1.000$
Temkin	$b = 194.47$	$A_T = 19.65$	$r^2 = 0.981$

Figure 7. BPA removal (%) in single solutions (red marker) and in binary solutions with (**a**) copper, (**b**) nickel, (**c**) lead and (**d**) cadmium (black marker for metal and blue one for BPA) using activated carbon AC-40 as the adsorbent.

Table 6. Partition coefficient in function of concentration.

Initial Concentration of BPA, mg/L	Partition Coefficients, L/g
1	52.00
5	51.40
10	49.80
20	40.75
30	26.78
40	20.78
80	2.60
120	1.38
160	0.93

3.6. Adsorption of BPA-Metals Cations Mixtures

Different contaminants such as BPA and a wide variety of metal ions could be present in wastewater. The presence of these ions in solution can lead to competition between metals and the contaminant for the union with the adsorptive sites but also could enhance the BPA adsorption. For example, Han et al. [39] analyzed the influence of copper (II) and lead (II) ions on the adsorption of BPA onto lignin. These researchers found that the presence of the metal cations modified the surface of lignin,

converting it on a less negatively charged surface. It was an advantage for the adsorption of anion species of BPA. Further, Liu et al. [38] studied the simultaneous adsorption of BPA and cadmium (II) ions on activated montmorillonite and found that the maximum adsorption capacity of BPA changed from 74.55 to 80.77 mg/g when cadmium was presented in the solution. Similarly, Bautista-Toledo et al. [37] reported that the presence of chromium (III) enhanced the adsorption of BPA on different activated carbons. The authors attributed the improvement in BPA adsorption to the in situ formation of complex compounds formed by Cr (III) and BPA (Cr (III)-BPA coordination compounds).

In this section, the interaction of some metal cations present in water with BPA was analyzed. The aim was to observe the possible interactions between the metal and the contaminant and/or metal and adsorbent, especially if they had synergistic properties. In all cases, the experiments of mixtures of metals and BPA have been compared with the initial experiment using only BPA. Cadmium, copper, lead and nickel were selected as the representatives of heavy metals because they are very common in wastewater. Figures 7 and 8 show the results.
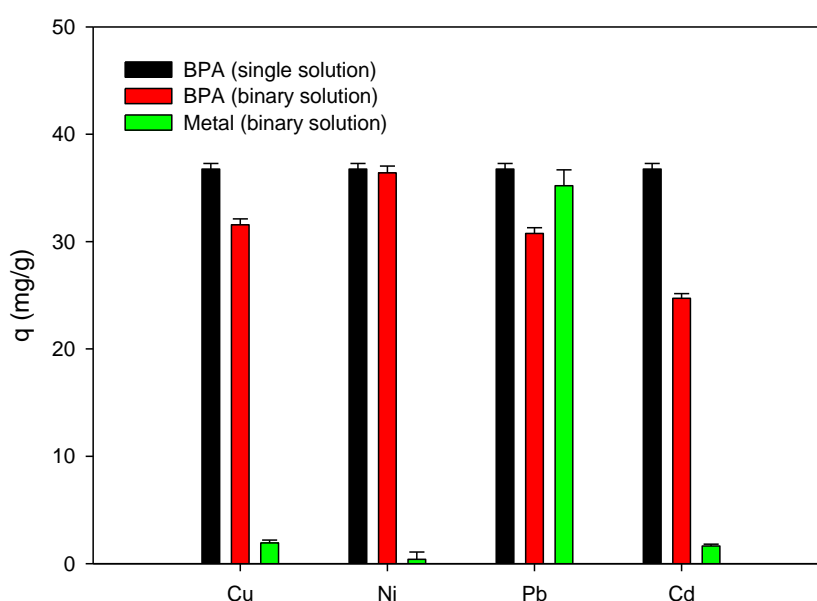

Figure 8. BPA adsorption capacity in single solutions (black color) and in binary solutions with different heavy metals (green marker for metal and red one for BPA) using activated carbon AC-40 as the adsorbent.

Contrary to the referenced studies of Han et al. [39], Lui et al. [38] and Bautista-Toledo et al. [37], the results showed that none of the metal cations improved the efficiency or adsorption capacity of BPA, suggesting a competition with BPA to occupy the porous surface of carbon and consequently decreasing its effectiveness. This is consistent with investigations carried out by Schiewer and Volesky [66], who systematically studied the effect of ionic strength on the adsorption of cations such as Zn^{2+}, Cd^{2+}, Cu^{2+} and Na^+. They reported that an increase in ionic strength led to a decrease in the adsorption achieved due to the increase in the electrostatic charge. Niu and Volesky [67] studied the removal of anionic metal complexes ($Au(CN)^{2-}$, CrO_4^{2-}, SeO_4^{2-} and VO_4^{3-}), concluding that an increase in ionic strength decreases the removal.

In the case of the mixture of Cd (II) and BPA, retention of BPA on activated carbon decreased. The difference in adsorption of BPA in the mixture solution (metal-BPA) and in the BPA solution was significant. BPA adsorption capacity changed from 36.8 (single solution) to 24.7 mg/g (binary solution). However, Cd was not greatly adsorbed (adsorption capacity of 1.6 mg/g). This also occurred in mixtures of Cu (II) and BPA, although to a lesser extent. If the predominant binding force of BPA is electrostatic attraction, a decrease in the positively charged sites on the carbon surface could negatively influence the BPA adsorption. A change in the charge of the carbon surface and pH of the solution

during the process due to the adsorption of metals could explain the decrease in the BPA adsorption. Earlier studies reported that the ionic strength of the solution notably influenced the adsorption of different species [37,67,68]. Further, Meng et al. [69] studied the adsorption of phenol and cadmium onto soil and found that the adsorption of mixed pollutants (Cd^{2+} and phenol) showed an antagonistic effect on adsorption. Chemical adsorption was the main mechanism of adsorption of cadmium ions while physical adsorption was the primary mechanism for phenol adsorption (very influenced by the physic-chemical properties of the carbon surface). This indication was consistent with the pH evolution of the system (Table 7) and the point of zero charge reported in Table 1. The net charge of activated carbon decreases with the increase in pH values. Yang et al. [70] noted that the electrostatic surface charge was smaller with the pH of the adsorption system closer to the pH_{pzc} of the activated carbon. In addition, BPA exists in its molecular form under pH < 8 but begins to deprotonate to a negatively charged form at around pH 8 [13,51,70]. Thus, when pH was increased above 7.5, a repulsive electrostatic interaction may be established between the negatively charged surface of the activated carbon and bisphenolate anion. In the mixture of Ni (II) and BPA, the metal was not adsorbed and BPA removal in the mixture solution was very similar to the BPA removal in the single BPA solution. This means that the presence of Ni (II) did not affect the adsorption of BPA. Finally, in the case of the mixture of Pb (II) and BPA, the results suggested that both Pb (II) and BPA were notably adsorbed by activated carbon, probably because they formed a complex in situ with activated carbon, adsorbing and synergistically removing both contaminants present in the solution, or perhaps they distributed the available active sites of the adsorbent for Pb and BPA adsorption.

Table 7. pH evolution on simultaneous adsorption experiments.

| Time, min	Cd (II) + BPA	Cu (II) + BPA	Ni (II) + BPA	Pb (II) + BPA
0	5	5	5	5
30	6.9	6.3	6.2	6.4
60	7.5	6.7	6.5	6.8
120	7.8	6.8	6.6	7.1
240	8.1	7.2	7.0	7.2
480	8.0	7.5	7.0	7.3
1440	8.0	7.4	7.3	7.3
2880	7.9	7.6	7.5	7.5

In conclusion, the metal ions may affect the sorption of BPA on AC-40 from different aspects: (1) the metal ions can reduce the BPA adsorption due to the decrease in sorption sites on the AC surface; (2) the metal ions can change the ionic strength of the solution and influence the adsorption of the different species; (3) the metal ions can promote the hydrophobic interaction, which may enhance the BPA adsorption on AC; and (4) the metal ions can promote the formation of complex compounds (metal–BPA coordination compounds) which increase the BPA adsorption.

3.7. Cycles of BPA Adsorption/Desorption

The reuse of AC-40 was investigated in three consecutive cycles of adsorption/desorption, without significant loss in the adsorption capacity. The adsorption capacity in the three consecutive adsorption–desorption cycles is reported in the Table 8. Figure 9 shows the desorption percentage of BPA. The removal efficiency was higher than 90% in all cases, indicating that the activated carbon has good reusability. Further, desorption of BPA from the AC-40 was about 86.3% in the first desorption cycle and only decreased slightly after three adsorption–desorption cycles. These results indicated that the interaction of the BPA molecule to the binding sites on the adsorbent surface can be disrupted without any effect on the properties of the adsorbent. Similar results were found by other authors in their studies of the desorption of BPA by mixtures of methanol-acetic acid [71–73].

Table 8. Removal efficiency and adsorption capacity of BPA adsorption in three consecutive cycles.

Cycle	% Removal	q, mg/g
1	92.5	37.00
2	91.4	36.56
3	90.2	36.08
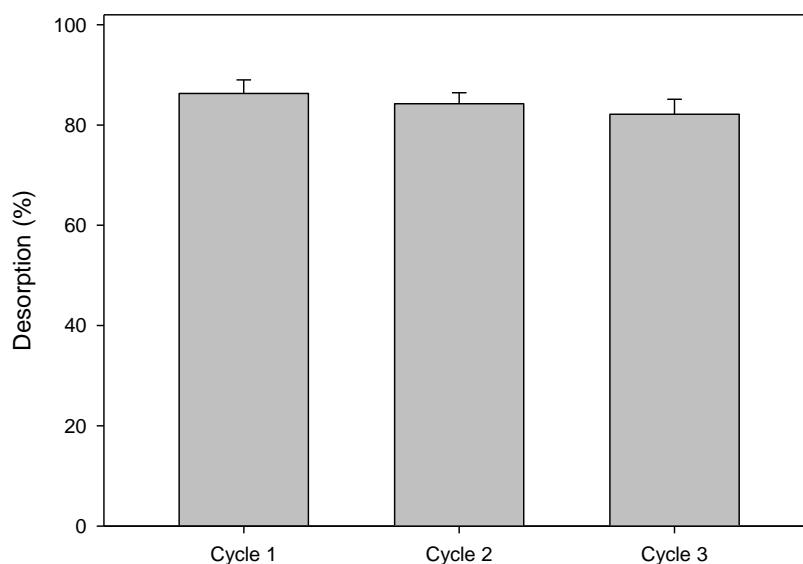
Figure 9. BPA desorption (%) in each adsorption–desorption cycle.

4. Conclusions

The aim of this work was to investigate the application of a commercial activated carbon (AC-40) to remove BPA in single and simultaneous adsorption systems. The results showed that pH did not significantly affect the BPA adsorption at low pH values. However, when the acidity of the medium was increased, a slight improvement in the removal efficiencies was observed. Further, as the dose of activated carbon increased, the BPA removal efficiency increased at all contact times. Additionally, the concentration of BPA did not influence the adsorption, for the values of initial BPA concentration analyzed in this work (similar to those than can be found in some industrial wastewaters).

The isotherm obtained for BPA adsorption onto AC-40 was type I and the maximum adsorption capacity was close to 90 mg/g. The Langmuir and Sips models were the best to reproduce the experimental results.

The experiments with mixtures of metals and BPA showed that none of the metal cations analyzed improved the efficiency of the adsorption process. In the case of the mixtures of Pb (II) and BPA, the results seemed to indicate that both Pb (II) and BPA can be efficiently removed from wastewater using AC-40.

Desorption tests showed good desorption efficiency (higher than 80%) and also BPA adsorption capacities were very similar after three adsorption–desorption cycles, indicating that the activated carbon has good reusability. In conclusion, results of the work showed good adsorptive behavior of AC-40 for BPA removal in batch systems in single- and binary-solute adsorption. However, from a practical point of view and as a potential research line, complete experimental research on packed-bed columns including desorption studies should be carried out.

Author Contributions: Conceptualization, M.C.; formal analysis, M.A.M.-L. and C.E.; investigation, M.A.M.-L. and C.E.; methodology, M.A.M.-L., A.R. and M.C.; software, I.I.-R. and C.E.; supervision, M.A.M.-L.; validation, C.E.; resources, M.C.; writing—original draft, M.A.M.-L., A.R., I.I.-R., and C.E.; writing—review and editing, M.A.M.-L. and M.C. All authors have read and agreed to the published version of the manuscript.

References

1. Gonsioroski, A.; Mourikes, V.E.; Flaws, J.A. Endocrine disruptors in water and their effects on the reproductive system. *Int. J. Mol. Sci.* **2020**, *21*, 1929. [CrossRef] [PubMed]
2. Rubin, B.S. Bisphenol A: An endocrine disruptor with widespread exposure and multiple effects. *J. Steroid Biochem. Mol. Biol.* **2011**, *127*, 27–34. [CrossRef] [PubMed]
3. Orimolade, B.O.; Adekola, F.A.; Adebayo, G.B. Adsorptive removal of bisphenol A using synthesized magnetite nanoparticles. *Appl. Water Sci.* **2018**, *8*, 46. [CrossRef]
4. ISH Markit. *Bisphenol A. Chemical Economics Handbook*; HIS Markit: London, UK, 2018.
5. Inoue, M.; Masuda, Y.; Okada, F.; Sakurai, A.; Takahashi, I.; Sakakibara, M. Degradation of bisphenol A using sonochemical reactions. *Water Res.* **2008**, *42*, 1379–1386. [CrossRef]
6. Ivanov, A.E.; Halthur, T.; Ljunggren, L. Flow permeable composites of lignin and poly(vinyl alcohol): Towards removal of bisphenol A and erythromycin from water. *J. Environ. Chem. Eng.* **2016**, *4*, 1432–1441. [CrossRef]
7. Santhi, V.A.; Sakai, N.; Ahmad, E.D.; Mustafa, A.M. Occurrence of bisphenol A in surface water, drinking water and plasma from Malaysia with exposure assessment from consumption of drinking water. *Sci. Total Environ.* **2012**, *427*, 332–338. [CrossRef]
8. Vandenberg, L.N.; Hauser, R.; Marcus, M.; Olea, N.; Welshons, W.V. Human exposure to bisphenol A (BPA). *Reprod. Toxicol.* **2007**, *24*, 139–177. [CrossRef]
9. Yamamoto, T.; Yasuhara, A.; Shiraishi, H.; Nakasugi, O. Bisphenol A in hazardous waste landfill leachates. *Chemosphere* **2001**, *42*, 415–418. [CrossRef]
10. Phouthavong-Murphy, J.C.; Merrill, A.K.; Zamule, S.; Giacherio, D.; Brown, B.; Roote, C.; Das, P. Phytoremediation potential of switchgrass (*Panicum virgatum*), two United States native varieties, to remove bisphenol-A (BPA) from aqueous media. *Sci. Rep.* **2020**, *10*, 835. [CrossRef]
11. Liu, G.; Ma, J.; Li, X.; Qin, Q. Adsorption of bisphenol A from aqueous solution onto activated carbons with different modification treatments. *J. Hazard. Mater.* **2009**, *164*, 1275–1280. [CrossRef]
12. Yeo, M.K.; Kang, M. Photodecomposition of bisphenol A on nanometer-sized TiO$_2$ thin film and the associated biological toxicity to zebrafish (*Danio rerio*) during and after photocatalysis. *Water Res.* **2006**, *40*, 1906–1914. [CrossRef] [PubMed]
13. Wang, J.; Zhang, M. Adsorption Characteristics and mechanism of bisphenol A by magnetic biochar. *Int. J. Environ. Res. Public Health* **2020**, *17*, 1075. [CrossRef] [PubMed]
14. Ahmed, M.B.; Zhou, J.L.; Ngo, H.H.; Guo, W.S.; Thomaidis, N.S.; Xu, J. Progress in the biological and chemical treatment technologies for emerging contaminant removal from wastewater: A critical review. *J. Hazard. Mater.* **2017**, *323*, 274–298. [CrossRef] [PubMed]
15. Esplugas, S.; Bila, D.M.; Krause, L.G.T.; Dezotti, M. Ozonation and advanced oxidation technologies to remove endocrine disrupting chemicals (EDCs) and pharmaceuticals and personal care products (PPCPs) in water effluents. *J. Hazard. Mater.* **2007**, *149*, 631–642. [CrossRef] [PubMed]
16. Luo, H.; Cheng, Y.; Zeng, Y.; Luo, K.; He, D.; Pan, X. Rapid removal of organic micropollutants by heterogeneous peroxymonosulfate catalysis over a wide pH range: Performance, mechanism and economic analysis. *Sep. Purif. Technol.* **2020**, *248*, 117023. [CrossRef]
17. Lin, H.; Fang, Q.; Wang, W.; Li, G.; Guan, J.; Shen, Y.; Ye, J.; Liu, F. Prussian blue/PVDF catalytic membrane with exceptional and stable Fenton oxidation performance for organic pollutants removal. *Appl. Catal. B Environ.* **2020**, *273*, 119047. [CrossRef]
18. Rani, M.; Rachna; Shanker, U. Efficient photocatalytic degradation of Bisphenol A by metal ferrites nanoparticles under sunlight. *Environ. Technol. Innov.* **2020**, *19*, 100792. [CrossRef]
19. Nakanishi, A.; Tamai, M.; Kawasaki, N.; Nakamura, T.; Tanada, S. Adsorption characteristics of bisphenol A onto carbonaceous materials produced from wood chips as organic waste. *J. Colloid Interface Sci.* **2002**, *252*, 393–396. [CrossRef]
20. Marsh, H.; Heintz, E.A.; Rodriguez-Reinoso, F. *Introduction to Carbon Technologies*; University of Alicante: Alicante, Spain, 1997.
21. Bansal, R.C.; Donnet, J.-B.; Stoeckli, F. *Active Carbon*; Marcel Dekker: New York, NY, USA, 1988.

22. Derbyshire, F.; Jagtoyen, M.; Andrews, R.; Rao, A.; Martin-Gullon, I.; Grulke, E. Carbon materials in environmental applications. *Chem. Phys. Carbon* **2001**, *27*, 1–66.

23. Musmarra, D.; Karatza, D.; Lancia, A.; Prisciandaro, M.; Mazziotti di Celso, G. Adsorption of elemental mercury vapors from synthetic exhaust combustion gas onto HGR carbon. *J. Air Waste Manag. Assoc.* **2016**, *66*, 698–706. [CrossRef]

24. Rivera-Utrilla, J.; Sánchez-Polo, M.; Gómez-Serrano, V. Activated carbon modifications to enhance its water treatment applications. An overview. *J. Hazard. Mater.* **2011**, *187*, 1–23. [CrossRef] [PubMed]

25. Dias, J.M.; Alvim-Ferraz, M.C.M.; Almeida, M.F.; Rivera-Utrilla, J.; Sánchez-Polo, M. Waste materials for activated carbon preparation and its use in aqueous-phase treatment: A review. *J. Environ. Manag.* **2007**, *85*, 833–846. [CrossRef]

26. Moreno-Castillo, C.; Rivera-Utrilla, J. Carbon materials as adsorbents for the removal of pollutants from the aqueous phase. *Mater. Res. Bull.* **2001**, *26*, 890–894. [CrossRef]

27. Radovic, L.R.; Moreno-Castilla, C.; Rivera-Utrilla, J. *Chemistry and Physics of Carbon*; Radovic, L.R., Ed.; Marcel Dekker: New York, NY, USA, 2000; Volume 27, p. 227.

28. Chen, J.; Zhang, L.; Yang, G.; Wang, Q.; Li, R.; Lucia, L.A. Preparation and characterization of activated carbon from hydrochar by phosphoric acid activation and its adsorption performance in prehydrolysis liquor. *BioResources* **2017**, *12*, 5928–5941. [CrossRef]

29. Jagtoyen, M.; Thwaites, M.; Stencel, J.; McEnaney, B.; Derbyshire, F. Adsorbent carbon synthesis from coals by phosphoric acid activation. *Carbon* **1992**, *30*, 1089–1096. [CrossRef]

30. Bhatnagar, A.; Anastopoulos, I. Adsorptive removal of bisphenol A (BPA) from aqueous solution: A review. *Chemosphere* **2017**, *168*, 885–902. [CrossRef] [PubMed]

31. Juhola, R.; Runtti, H.; Kangas, T.; Hu, T.; Romar, H.; Tuomikoski, S. Bisphenol A removal from water by biomass-based carbon: Isotherms, kinetics and thermodynamics studies. *Environ. Technol.* **2020**, *41*, 971–980. [CrossRef]

32. Lu, J.; Zhang, C.; Wu, J.; Luo, Y. Adsorptive removal of bisphenol A using N-doped biochar made of *Ulva prolifera*. *Water Air Soil Pollut.* **2017**, *228*, 327. [CrossRef]

33. Pan, B.; Lin, D.; Mashayekhi, H.; Xing, B. Adsorption and Hysteresis of Bisphenol A and 17-Ethinyl Estradiol on Carbon Nanomaterials. *Environ. Sci. Technol.* **2008**, *42*, 5480–5485. [CrossRef]

34. Redding, A.M.; Cannon, F.S.; Snyder, S.A.; Vanderford, B.J. A QSAR-like analysis of the adsorption of endocrine disrupting compounds, pharmaceuticals, and personal care products on modified activated carbons. *Water Res.* **2009**, *43*, 3849–3861. [CrossRef]

35. Solak, S.; Vakondios, N.; Tzatzimaki, I.; Diamadopoulos, E.; Arda, M.; Kabay, N.; Yüksel, M. A comparative study of removal of endocrine disrupting compounds (EDCs) from treated wastewater using highly crosslinked polymeric adsorbents and activated carbon. *J. Chem. Technol. Biotechnol.* **2014**, *89*, 819–824. [CrossRef]

36. Wu, Z.; Wei, X.; Xue, Y.; He, X.; Yang, X. Removal effect of atrazine in co-solution with bisphenol A or humic acid by different activated carbons. *Materials* **2018**, *11*, 2558. [CrossRef] [PubMed]

37. Bautista-Toledo, M.I.; Rivera-Utrilla, J.; Ocampo-Pérez, R.; Carrasco-Marín, F.; Sánchez-Polo, M. Cooperative adsorption of bisphenol-A and chromium(III) ions from water on activated carbons prepared from olive-mill waste. *Chem. Eng. J.* **2014**, *73*, 338–350. [CrossRef]

38. Liu, C.; Wu, P.; Zhu, Y.; Tran, L. Simultaneous adsorption of Cd^{2+} and BPA on amphoteric surfactant activated montmorillonite. *Chemosphere* **2016**, *144*, 1026–1032. [CrossRef]

39. Han, W.; Luo, L.; Zhang, S. Adsorption of bisphenol A on lignin: Effects of solution chemistry. *Int. J. Environ. Sci. Technol.* **2012**, *9*, 543–548. [CrossRef]

40. Hanladakis, J.N.; Velis, C.A.; Weber, R.; Iacovidou, E.; Purnell, P. An overview of chemical additives present in plastics: Migration, release, fate and environmental impact during their use, disposal and recycling. *J. Hazard. Mater.* **2018**, *344*, 179–199. [CrossRef] [PubMed]

41. Kyzas, G.Z.; Siafaka, P.I.; Pavlidou, E.G.; Chrissafis, K.J.; Bikiaris, D.N. Synthesis and adsorption application of succinyl-grafted chitosan for the simultaneous removal of zinc and cationic dye from binary hazardous mixtures. *Chem. Eng. J.* **2015**, *259*, 438–448. [CrossRef]

42. Stawinski, W.; Wegrzyn, A.; Freitas, O.; Chmielarz, L.; Mordarski, G.; Figueiredo, S. Simultaneous removal of dyes and metal cations using an acid, acid-base and base modified vermiculite as a sustainable and recyclable adsorbent. *Sci. Total Environ.* **2017**, *576*, 398–408. [CrossRef] [PubMed]

43. Morosanu, I.; Teodosiu, C.; Fighir, D.; Paduraru, C. Simultaneous Biosorption of Micropollutants from Aqueous Effluents by Rapeseed Waste. *Process Saf. Environ. Prot.* **2019**, *132*, 231–239. [CrossRef]

44. Méndez-Díaz, J.D.; Abdel Daiem, M.M.; Rivera-Utrilla, J.; Sánchez-Polo, M.; Bautista-Toledo, I. Adsorption/bioadsorption of phthalic acid, an organic micropollutant present in landfill leachates, on activated carbons. *J. Colloid Interface Sci.* **2012**, *369*, 358–365. [CrossRef]

45. Abdel Daiem, M.M.; Rivera-Utrilla, J.; Sánchez-Polo, M.; Ocampo-Pérez, R. Single, competitive and dynamic adsorption on activated carbon of compounds used as plasticizers and herbicides. *Sci. Total Environ.* **2015**, *537*, 335–342. [CrossRef] [PubMed]

46. Velo-Gala, I.; López-Peñalver, J.J.; Sánchez-Polo, M.; Rivera-Utrilla, J. Role of activated carbon on micropollutants degradation by ionizing radiation. *Carbon* **2014**, *67*, 288–299. [CrossRef]

47. Bernal, V.; Erto, A.; Giraldo, L.; Moreno-Pijarán, J.C. Effect of solution pH on the adsorption of paracetamol on chemically modified activated carbons. *Molecules* **2017**, *22*, 1032. [CrossRef] [PubMed]

48. Pereira, R.C.; Anizelli, P.R.; Di Mauro, E.; Valezi, D.F.; da Costa, A.C.S.; Zaia, C.T.B.V.; Zaia, D.A.M. The effect of pH and ionic strength on the adsorption of glyphosate onto ferrihydrite. *Geochem. Trans.* **2019**, *20*, 3. [CrossRef] [PubMed]

49. Bautista-Toledo, M.I.; Ferro-García, M.A.; Rivera-Utrilla, J.; Moreno-Castilla, C.; Vegas, F.J. Bisphenol A removal from water by activated carbon. Effects of carbon characteristics and solution chemistry. *Environ. Sci. Tecnhol.* **2005**, *39*, 6246–6250. [CrossRef]

50. Tursi, A.; Chatzisymeon, E.; Chidichimo, F.; Beneduci, A.; Chidichimo, G. Removal of endocrine disrupting chemicals from water: Adsorption of bisphenol-A by biobased hydrophobic functionalized cellulose. *Int. J. Environ. Res. Public Health* **2018**, *15*, 2419. [CrossRef]

51. Wang, X.; Xiao, Y. Removal of the endocrine disrupting chemical Bisphenol A from water by activated carbon. *Adv. Mater. Res.* **2013**, *671*, 2726–2731. [CrossRef]

52. Chang, K.L.; Hsieh, J.F.; Ou, B.M.; Chang, M.H.; Hseih, W.Y.; Lin, J.F.; Huang, P.J.; Wong, K.F.; Chen, S.T. Adsorption studies on the removal of an endocrine-disrupting compound (Bisphenol A) using activated carbon from rice straw agricultural waste. *Sep. Sci. Technol.* **2012**, *47*, 1514–1521. [CrossRef]

53. Soni, H.; Padmaja, P. Palm shell based activated carbon for removal of bisphenol A: An equilibrium, kinetic and thermodynamic study. *J. Hazard. Mater.* **2014**, *21*, 275–284. [CrossRef]

54. Bohdziewicz, J.; Liszczyk, G. Evaluation of effectiveness of bisphenol a removal on domestic and foreign activated carbons. *Ecol. Chem. Eng. Soc.* **2013**, *20*, 371–379. [CrossRef]

55. Tsai, W.-T.; Lai, C.-W.; Su, T.-Y. Adsorption of bisphenol-A from aqueous solution onto minerals and carbon adsorbents. *J. Hazard. Mater.* **2006**, *134*, 169–175. [CrossRef] [PubMed]

56. Yu, J.; Shen, H.; Liu, B. Adsorption Properties of polyethersulfone-modified attapulgite hybrid microspheres for bisphenol A and sulfamethoxazole. *Int. J. Environ. Res. Public Health* **2020**, *17*, 473. [CrossRef]

57. Ho, Y.S.; Mckay, G. A comparison of chemisorption kinetic models applied to pollutant removal on various sorbents. *Process Saf. Environ. Prot.* **1998**, *76*, 332–340. [CrossRef]

58. King, P.; Srinivas, P.; Prasanna Kumar, Y.; Prasad, V.S.R.K. Sorption of copper(II) ion from aqueous solution by *Tectona grandis* l.f. (teak leaves powder). *J. Hazard. Mater.* **2006**, *136*, 560–566. [CrossRef] [PubMed]

59. Tang, Z.; Peng, S.; Hu, S.; Hong, S. Enhanced removal of bisphenol-AF by activated carbon-alginate beads with cetyltrimethyl ammonium bromide. *J. Colloid Interface Sci.* **2017**, *495*, 191–199. [CrossRef]

60. Rouquerol, F.; Rouquerol, J.; Sing, K.S.W.; Llewellyn, P.; Maurin, G. *Adsorption by Powders and Porous Solids. Principles, Methodology and Applications*, 2nd ed.; Elsevier: New York, NY, USA, 2012. [CrossRef]

61. Brunauer, S.; Deming, L.S.; Deming, W.E.; Teller, E. On a theory of the Van der Waals adsorption of gases. *J. Am. Chem. Soc.* **1940**, *62*, 1723–1732. [CrossRef]

62. Asada, T.; Oikawa, K.; Kawata, K.; Ishihara, S.; Iyobe, T.; Yamada, A. Study of removal effect of bisphenol A and β-estradiol by porous carbon. *J. Health Sci.* **2004**, *50*, 588–593. [CrossRef]

63. Kuo, C.-Y. Comparison with as-grown and microwave modified carbon nanotubes to removal aqueous bisphenol A. *Desalination* **2009**, *249*, 976–982. [CrossRef]

64. Li, S.; Gong, Y.; Yang, Y.; He, C.; Hu, L.; Zhu, L.; Sun, L.; Shu, D. Recyclable CNTs/Fe$_3$O$_4$ magnetic nanocomposites as adsorbents to remove bisphenol A from water and their regeneration. *Chem. Eng. J.* **2015**, *260*, 231–239. [CrossRef]

65. Xu, J.; Zhu, Y.F. Elimination of bisphenol A from water via graphene oxide adsorption. *Acta Phys. Chim. Sinica* **2013**, *29*, 829–836.

66. Schiewer, S.; Volesky, B. Modeling multi-metal ion exchange in biosorption. *Environ. Sci. Technol.* **1996**, *30*, 2921–2927. [CrossRef]

67. Niu, H.; Volesky, B. Biosorption mechanism for anionic metal species with waste crab shells. *Eur. J. Miner. Proc. Environ. Prot.* **2003**, *3*, 75–87.

68. López-Ramón, V.; Moreno-Castilla, C.; Rivera-Utrilla, J.; Radovic, L.R. Ionic strength effects in aqueous phase adsorption of metals ion son activated carbons. *Carbon* **2003**, *41*, 2020. [CrossRef]

69. Meng, Z.-F.; Zhang, Y.-P.; Zhang, Z.-Q. Simultaneous adsorption of phenol and cadmium on amphoteric modified soil. *J. Hazard. Mater.* **2008**, *159*, 492–498. [CrossRef] [PubMed]

70. Yan, L.; Huang, X.; Shi, H.; Zhang, G. Adsorption characteristics of bisfenol A on tailored activated carbon in aqueous solutions. *Water Sci. Technol.* **2016**, *74*, 1744–1751. [CrossRef] [PubMed]

71. Guo, W.; Hu, W.; Pan, J.; Zhou, H.; Guan, W.; Wang, X.; Dai, J.; Xu, L. Selective adsorption and separation of BPA from aqueous solution using novel molecularly imprinted polymers based on kaolinite/Fe$_3$O$_4$ composites. *Chem. Eng. J.* **2011**, *171*, 603–611. [CrossRef]

72. Bayramoglu, G.; Arica, M.Y.; Liman, G.; Celikbicak, O.; Salih, B. Removal of bisphenol A from aqueous medium using molecularly surface imprinted microbeads. *Chemosphere* **2016**, *150*, 275–284. [CrossRef]

73. Yu, C.; Shan, J.; Chen, Y.; Shao, J.; Zhang, F. Preparation and adsorption properties of rosin-based bisphenol A molecularly imprinted microspheres. *Mater. Today Commun.* **2020**, *24*, 101076. [CrossRef]

Article

Removal of Diclofenac in Wastewater Using Biosorption and Advanced Oxidation Techniques: Comparative Results

José M. Angosto, María J. Roca and José A. Fernández-López *

Department of Chemical and Environmental Engineering, Technical University of Cartagena, Paseo Alfonso XIII, 52, 30203 Cartagena, Murcia, Spain; jm.angosto@upct.es (J.M.A.); mjose.roca@upct.es (M.J.R.)
* Correspondence: josea.fernandez@upct.es

Abstract: Wastewater treatment is a topic of primary interest with regard to the environment. Diclofenac is a common analgesic drug often detected in wastewater and surface water. In this paper, three commonly available agrifood waste types (artichoke agrowaste, olive-mill residues, and citrus waste) were reused as sorbents of diclofenac present in aqueous effluents. Citrus-waste biomass for a dose of $2\ \text{g·L}^{-1}$ allowed for removing 99.7% of diclofenac present in the initial sample, with a sorption capacity of 9 mg of adsorbed diclofenac for each gram of used biomass. The respective values obtained for olive-mill residues and artichoke agrowaste were around $4.15\ \text{mg·g}^{-1}$. Advanced oxidation processes with UV/H_2O_2 and $UV/HOCl$ were shown to be effective treatments for the elimination of diclofenac. A significant reduction in chemical oxygen demand (COD; 40–48%) was also achieved with these oxidation treatments. Despite the lesser effectiveness of the sorption process, it should be considered that the reuse and valorization of these lignocellulosic agrifood residues would facilitate the fostering of a circular economy.

1. Introduction

Water is a renewable but limited natural resource, which forces us to manage it, especially in arid and semiarid areas where water resources are limited. The presence of some pollutants can jeopardize water recovery, and the reuse of urban and industrial effluents [1]. In addition to pollution from municipal discharges, water bodies are also contaminated by industry, mining, and pollution from agrochemicals used on irrigated land, which in many cases are discharged directly into lakes and rivers without prior treatment [2].

The reuse of urban and industrial wastewater with some pollutants can contribute to soil contamination, as well as its passage into the tissue of cultivated plants. This can produce adverse effects on the ecosystem [3–6].

While the international scientific community continues to make considerable efforts to minimize or alleviate the problem of what we may call traditional pollutants (heavy metals, organic matter, inorganic nutrients, etc.), other environmental pollutants, called emerging pollutants (ECs), are of growing concern [7] and are leading us to adapt our strategies to respond to their threats [8,9].

Aqueous effluents that arrive at urban wastewater-treatment plants show a complex composition associated with current human and industrial development. Therefore, the presence of certain pollutants can, in many cases, interfere with the proper functioning of biological wastewater-treatment systems. Emerging contaminants are considered among these pollutants [9]. Emerging contaminants

are compounds of different origin and chemical nature of which the presence in the environment has gone largely unnoticed [10].

The lack of international monitoring programs for ECs makes it impossible to fully know their effects, problems, and behavior from an ecotoxicological point of view [2]. They can be a danger to the environment and human health [11,12]. Another particularity of this type of pollutant is that, due to its high production and consumption, and the constant and continuous introduction of these pollutants into the environment, they do not need to be persistent to cause negative effects.

Emerging contaminants can be classified as pharmaceutical and personal-care products, plasticizers, food additives, wood preservatives, contrast media, detergents, surfactants, fire retardants, biocides, hormones, and some disinfection byproducts. Advances in analytical technologies have helped to identify this group of contaminants [13,14].

These compounds have high transformation/disposal rates that can compensate for their continued introduction into the environment. For this reason, it is necessary to raise awareness of their origin and transformation, and the effects that this new generation of pollutants can have in order to propose modifications or improvements in water-treatment mechanisms. Some authors suggested the use of toxicity tests with chemical analysis to evaluate the efficiency of treatment methods [15–18].

The ongoing processing of aqueous effluents in conventional wastewater-treatment systems does not provide an adequate approach for the removal of emerging contaminants. These can arrive in their original form and/or be metabolized, making it difficult to operate biological wastewater treatment, sludge treatment, and the subsequent reuse of wastewater; there is also a lack of knowledge about the possible impact of these pollutants on the environment [19]. In many cases, products resulting from the transformation of the original emerging contaminants produce compounds that turn out to be more toxic than the original ones are [20].

Diclofenac (2-(2,6-dichloroanilino) phenylacetic acid) is one of the best-selling nonsteroidal anti-inflammatory drugs [21]. The high consumption level of this compound means that it is one of the most detected pharmaceuticals in aqueous effluents, and according to reported data, the measured values of diclofenac in municipal wastewater can be up 7.1 $\mu g \cdot L^{-1}$ [22,23]. A distinctive feature of diclofenac is that it undergoes low biodegradability and high persistence in wastewater-treatment plants, leading to its bioaccumulation in surface waters, sediments, and sludges [24,25]. Therefore, it is necessary to implement specific treatments to reduce or eliminate its presence in effluents.

Different sorption studies of diclofenac are reported in the literature. The highest bioremoval efficacies were obtained with carbon nanotubes [26], clays [27], and biochars [28] as sorbents. Raw lignocellulosic biomass was also used as a low-cost biosorbent, but the achieved efficiency was not as high as that with previous sorbents [29,30]. Despite this, biosorption has lately been presented as a very interesting technology, in line with the concept of the circular economy [31,32]. Efficient biowaste management is among the most important challenges in agrifood industries. Suggested uses for these lignocellulosic residues include their utilization as sorbents of pollutants in aqueous effluents [33–35] since they present very interesting physicochemical properties, such as their high surface area and the presence of a variety of functional groups that facilitate the sorption process [36–38]. Bioadsorptive techniques are the best ecofriendly solutions for removing contaminants because they are economical, efficient, highly selective on pollutants, and easily operable.

The most commonly used treatments for the removal of emerging contaminants, such as diclofenac, are advanced oxidation processes [39–43], which utilize free radical reactions to directly degrade chemical contaminants as an alternative to traditional treatments. For these oxidative treatments, it is necessary to carry out research studies that examine what the most appropriate combination of oxidizing reagents is to degrade a specific pollutant.

The main objective of this work was to carry out a comparative study of diclofenac elimination in aqueous effluents through biosorption with agrifood residues and through different advanced oxidation techniques (ultraviolet radiation (UV), sodium hypochlorite, and combinations of ultraviolet radiation with hypochlorite and with hydrogen peroxide).

2. Materials and Methods

2.1. Preparation and Characterization of Agrowaste Biomass

In preliminary studies, different agricultural wastes residues were processed and examined for their ability to remove diclofenac from a test solution. Of these, the three most interesting agrifood waste types that are abundant in the Murcia region (Spain) were chosen to be investigated in this study: artichoke agrowaste, olive-mill residues, and citrus waste from agrifood industries. Biomass samples were washed with distilled water and dried at 70 °C for 24 h before being ground and passed through a sieve with a number 18 mesh (1 mm). The different surface morphologies of each biomass were explored, and a qualitative determination of each was made using a field-emission scanning electron microscope and an energy-dispersive X-ray analyzer (SEM) (Hitachi S-3500N). FTIR measurements of the sorbents were performed in the range of 4000 to 400 cm^{-1} in a Thermo Nicolet 5700 (Karlsruhe, Germany). Moreover, the pH point of zero charge (pH$_{ZPC}$) was determined by the mass-titration method [44].

2.2. Preparation of Diclofenac Solutions

A diclofenac stock solution (1 g·L^{-1}) was prepared using diclofenac sodium (C$_{14}$H$_{10}$Cl$_2$NNaO$_2$, ≥99%; Sigma-Aldrich, Madrid, Spain) in deionized water. The working solution (20 L) was achieved by diluting the stock solution in treated and filtered wastewater from a wastewater-treatment plant. The pH value was adjusted to 6.6 with a 0.1 mol·L^{-1} HCl or 0.1 mol·L^{-1} NaOH solution using a Metrohm 654 pH meter with a pH combination electrode. All chemicals were of analytical grade. The analytical characterization of the working solution was performed by American Public Health Association (APHA) methods [45].

2.3. Batch-Biomass Tests

Batch-biosorption experiments were performed at 25 °C under stirring in a reciprocal contact agitator with 100 mL of the diclofenac working solution at a fixed concentration (C_o = 37.6 mg·L^{-1}) and a known amount of sorbent for 24 h in a conical flask at a constant stirring speed (150 rpm). Lastly, the solutions were filtered and quantified obtaining the final concentration (C_e). The initial (C_o) and final (C_e) concentrations were quantified by high-performance liquid chromatography (HPLC).

The amounts of diclofenac adsorbed at equilibrium (q_e), also called diclofenac removal efficiency and expressed as mg diclofenac/g dry biomass, were determined by mass-balance equation (Equation (1)) on the basis of values of diclofenac concentration in the solution at the beginning (C_o) and end (C_e) of the test:

$$q_e = \frac{(C_o - C_e) \cdot V}{m}, \tag{1}$$

where *V* is the solution volume (L) and m the sorbent dry weight (g).

The percentage of diclofenac elimination in each case was calculated by Equation (2):

$$\% \, Removal = \frac{(C_o - C_e)}{C_o} \times 100, \tag{2}$$

where C_o is the initial concentration (mg·L^{-1}) and C_e is the equilibrium concentration (mg·L^{-1}) of diclofenac.

2.4. Diclofenac Determination

Diclofenac concentration in the water samples was determined by high-performance liquid chromatography (HPLC). A Waters modular liquid chromatography system (Waters, Milford, MA, USA) equipped with two M510 pumps, a 717 plus autosampler, and an M996 photodiode array detector (PDA) was used. HPLC was run by the data system of the Millenium 2010 Chromatography Manager.

An Atlantis C18 5 μm, 25 cm × 4.6 mm i.d. (Waters) column was used. Elution was performed using a gradient between 175 mM phosphoric acid in water and 175 mM acetic acid in acetonitrile as the mobile phase. Flow rate was 0.6 mL/min. Samples, before being analyzed, were filtered using a 0.45 μm pore size cellulose acetate membrane, and the filtrate was analyzed for HPLC. Diclofenac was monitored at 270 nm. The retention time of diclofenac was about 6.4 min.

2.5. Advanced Oxidation Treatments

2.5.1. Sodium Hypochlorite

Treatment with sodium hypochlorite was performed with 1000 mL of filtered diclofenac solution. Four different amounts of available chlorine, namely, 1.0, 2.0, 3.0, and 4.0 mL of a 5% (*w/v*) sodium hypochlorite solution (Panreac, Barcelona, Spain) were added to each sample. Experiments were carried out in sealed glass bottles. They were incubated for 2 h until the moment of their quantification in a dark isothermal chamber at 20 °C, with slow agitation. Lastly, samples were filtered and analyzed by HPLC.

2.5.2. UV Light Treatments

UV radiation was applied using an 8 watt low-pressure UV lamp (UV-C 8 watt Strahler–Messner, Kalletal, Germany), with a flow range of 0.5 to 1.1 L·h^{-1} and a wavelength of 254 nm. The facility was designed to be used with 500 mL of a sample, irradiated for short periods of time of 2, 5, 10, and 15 min. According to these irradiation durations, the provided doses were 15, 37, 73, and 110 mJ·cm^{-2}, respectively. Before each treatment, the lamp was cleaned with deionized water. After irradiation, samples were filtered with a 0.45 μm filter and analyzed by HPLC.

2.5.3. UV Radiation Combined with Sodium Hypochlorite (UV/HOCl) and Hydrogen Peroxide (UV/H$_2$O$_2$)

UV/HOCl and UV/H$_2$O$_2$ assays were conducted as batch experiments using a concentration of 5 mg·L^{-1} sodium hypochlorite and 5 mg·L^{-1} of hydrogen peroxide, respectively, which were added into the initial sample and subjected to different UV exposure times (2, 5, 10, and 15 min) before filtration and analysis of diclofenac concentration was performed by HPLC.

2.6. Chemical Oxygen Demand

Chemical oxygen demand (COD) was determined using the methods described in APHA [45]. For COD measurements, a Spectroquant Nova 30 spectrophotometer (Merck, Darmstadt, Germany) was used.

3. Results and Discussion

3.1. Characterization of Biomass Samples

The surface characteristics of the different biomass samples used in diclofenac bioadsorption studies were investigated using scanning electron microscopy (SEM) and energy-dispersive X-ray spectroscopy (EDS), as shown in Figures 1–3. SEM is considered to be one of the most widely used tools in the scientific field for studying the surface characteristics of biomass used as biosorbent [46]. In the different micrographs that were made in the SEM, important differences in the surface characteristics of the different studied agrifood waste types were observed, presenting a majority composition of carbon and oxygen in all cases.
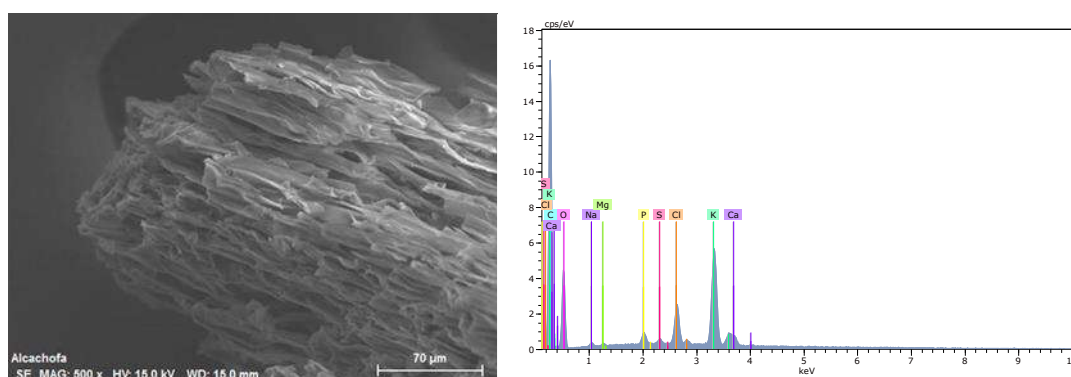
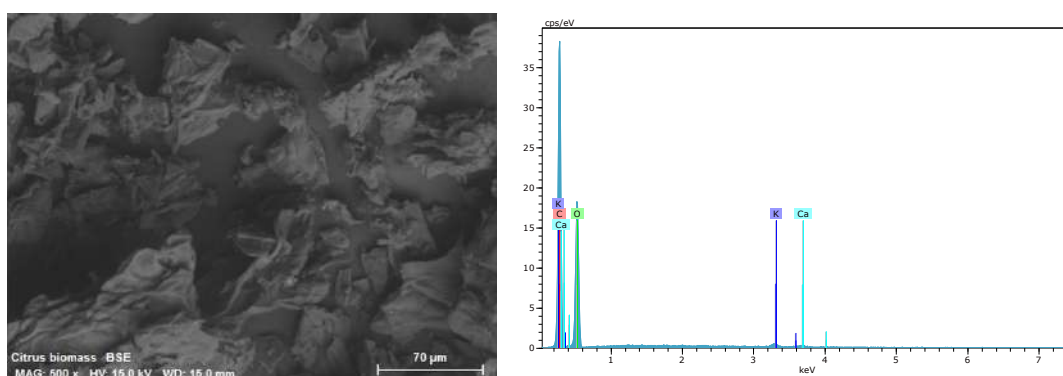**Figure 1.** SEM image and EDS analysis of artichoke-agrowaste biomass.

Figure 2. SEM image and EDS analysis of citrus-waste biomass.
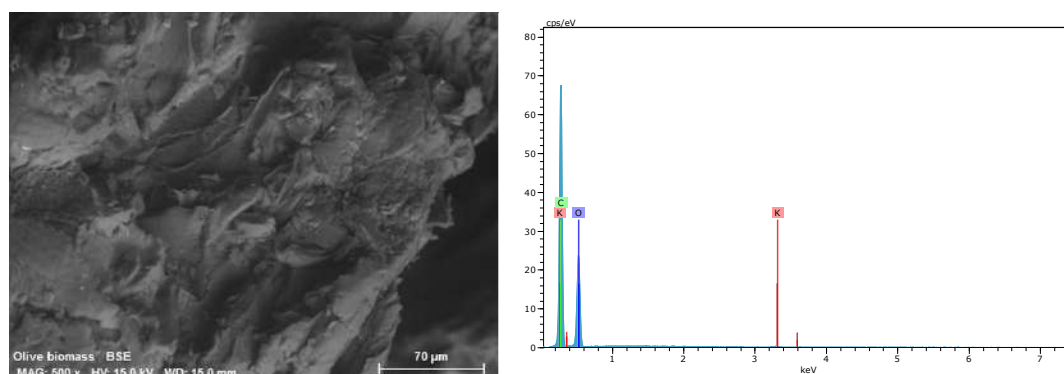

Figure 3. SEM image and EDS analysis of olive-mill residue biomass.

Figure 1 shows that artichoke biomass had filamentous structures made up of fiber cells that were longitudinally aligned. This fibrous structure provides consistency, resistance, and a large surface area [47] that, together with the small channels, allows for the rapid movement of fluids through the fibers, increasing the possibility of retaining diclofenac molecules. SEM analysis also showed that it was a rough surface, with the presence of holes of irregular shape and size [47] that could improve the retention of diclofenac.

Citrus-waste biomass (Figure 2) presented an irregular surface, but with a much more compact appearance and with fewer cavities than in the previous case, although with cracks that provided a large surface for the retention of diclofenac. Olive-mill residues (Figure 3) also presented an irregular surface with a fairly compact appearance, bit with few cavities. In all cases, the presence of cavities of irregular shape and dimensions would enhance the fixation of contaminants to be retained.

FTIR analysis allowed for inferring the structure of the sorbents on the basis of the locations and shapes of the bands in the spectra (Figure 4). The three sorbents showed a broad band at 3600–3100 cm^{-1}

that was assigned to −OH stretching vibrations of hydroxyl and carboxyl groups. A −CH aliphatic stretching vibration band was also observed at 2900–2850 cm^{-1} in all sorbents. Around 1630 cm^{-1}, a band attributed to C=O stretching vibrations and typical skeletal vibrations of aromatic rings was presented. In the region of 1030–1000 cm^{-1}, a broad band, an indication of C−O and C=C vibrational stretching, was revealed. These are, in fact, typical FTIR spectra, corresponding to nonmodified plant biomass samples, where the lignocellulosic constituents are particularly outstanding [32,47–49].
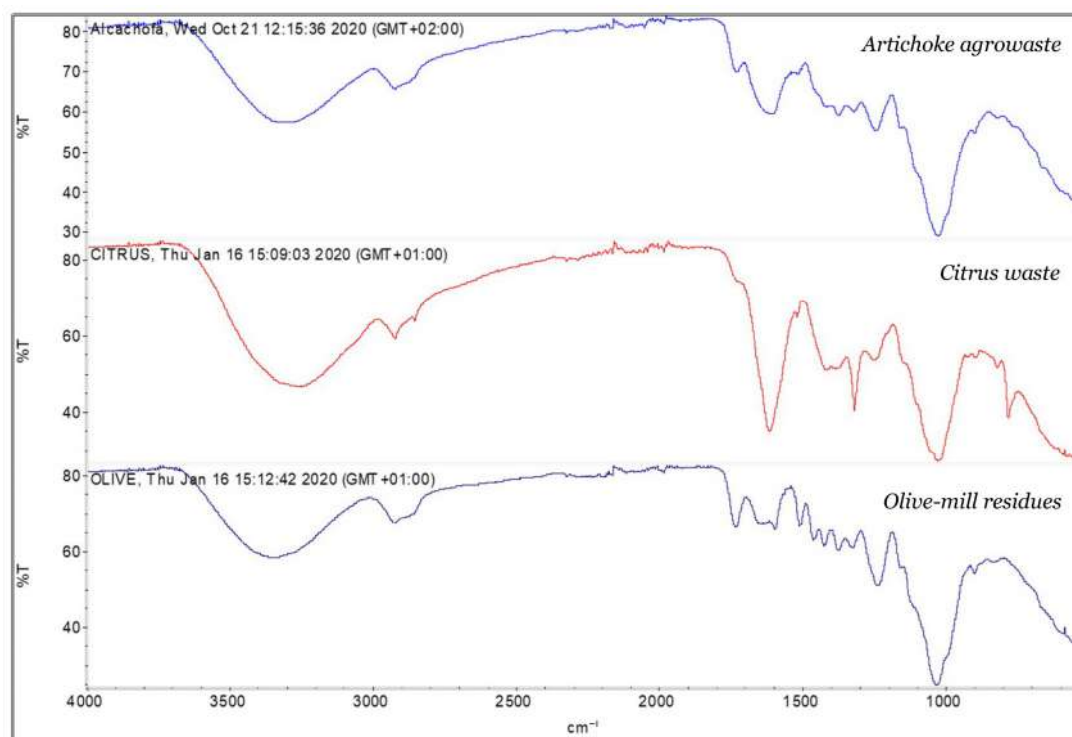

Figure 4. FTIR spectra between 4000 and 400 cm^{-1} for sorbent samples.

3.2. Diclofenac Biosorption

Table 1 shows the characterization of the working water prepared from diclofenac stock solution and filtered effluent from a treatment plant. The initial concentration (C_o) of diclofenac for the different experiments was 37.6 mg·L^{-1} and an initial COD value of 282 mg O$_2$·L^{-1}.

Table 1. Initial composition of working solution. COD, chemical oxygen demand.

Parameter	Value
pH	6.6 ± 0.2 *
Conductivity (μS·cm^{-1})	12.5 ± 2.5
TSS (mg/L)	98.2 ± 8.6
Turbidity (NTU)	4.7 ± 0.3
NO$_3$$^-$ (mg·L^{-1})	16.8 ± 2.7
PO$_4$$^{3-}$ (mg·L^{-1})	5.6 ± 1.1
BOD (mg O$_2$·L^{-1})	113.3 ± 10.2
COD (mg O$_2$·L^{-1})	282.0 ± 15.0
Diclofenac initial (mg·L^{-1})	37.6

* mean ± SD of 3 determinations.

The sorption capacities and percentages of diclofenac removal in the experiments carried out for the different used sorbents and doses (Table 2) revealed that citrus-waste biomass was the most effective. Citrus residues, with a zero point of charge of 4.2, reduced the pH of the solution during the

sorption process to 5.7 by the end of the experiment. These pH reductions were less pronounced in the olive-mill-residue (pH_{ZPC} = 5.4) and in the artichoke-agrowaste (pH_{ZPC} = 4.8) sorption tests, of which the final pH values were 6.4 and 6.1, respectively. In all cases, the modifications in pH were very slight, hardly affecting the solubility of the adsorbate and sorption-capacity values. The biomass of artichoke agrowaste showed the least capacity to retain diclofenac. In the case of citrus waste, for a dose of 2 g/L, all the diclofenac is retained, obtaining a sorption capacity (q_e) of 9 mg·g^{-1}. Olive-mill residues had intermediate and very similar retention values regardless of the dose used in the experiments.

Table 2. Elimination of diclofenac for different biomass samples.

Biomass	Sorbent Dosage (g·L^{-1})	Removal %	q_e (mg·g^{-1})
Artichoke agrowaste	1	18.7 ± 2.4 *	3.9 ± 0.5
	2	19.9 ± 3.1	4.2 ± 0.4
Olive-mill residues	1	46.4 ± 4.4	4.2 ± 0.6
	2	46.3 ± 5.8	4.2 ± 0.8
Citrus-waste	1	87.1 ± 5.7	7.8 ± 1.1
	2	99.7 ± 0.5	9.0 ± 0.3

* mean ± SD of 3 determinations.

The results of this study revealed that the reuse of raw lignocellulosic biomass from agrifood waste for the sorption of diclofenac may be an efficient and common method of wastewater treatment. The sorption capacities of diclofenac obtained in this study were lower than those reported for microalgae biomass (20–28 mg·g^{-1}) [29] and grape bagasse (24 mg·g^{-1}) [49], but comparable for that shown with activated carbon from olive stones (11 mg·g^{-1}) [50]. In the present investigation, the agrifood waste used as sorbent was not previously modified or subjected to any thermal treatment. The obtained results in the present investigation reveal that this is a new line of research that is worth further exploring, and it may be of interest to test some cost-effective activation mechanism that enhances the bioadsorptive capacity of waste to specific contaminants. In this context, future studies will be made in application in real systems, where fixed-bed citrus-waste adsorbers can be implemented for the treatment of wastewater with diclofenac.

3.3. Advanced Oxidation Treatments

As summarized in Table 3, when the working solution (C_o = 37.6 mg·L^{-1}) was exposed to different exposure times of UV radiation ranging from 2 to 15 min, significant reductions in the initial diclofenac concentration were achieved, ranging from 9.78% removal for 2 min of exposure and 88.49% removal for 15 min of exposure, without being able to achieve total removal. A significant reduction in COD values was also achieved, in a similar way to that in other reported investigations [51].

Table 3. Treatment with ultraviolet (UV) radiation.

Contact Time (min)	Diclofenac (mg·L^{-1})	Removed Diclofenac %	COD Reduction %
2	33.9 ± 2.8 *	9.8 ± 2.4	44.3 ± 3.6
5	16.6 ± 2.1	55.9 ± 3.9	62.1 ± 3.5
10	6.1 ± 1.1	83.8 ± 4.6	62.4 ± 4.1
15	4.3 ± 0.9	88.5 ± 3.8	66.3 ± 3.9

* mean ± SD of 3 determinations.

In the treatment with sodium hypochlorite and a contact time of 2 h (Table 4), for a dose of 4 mg·L^{-1}, all diclofenac present in the starting sample was eliminated. As the dose of hypochlorite was increased, greater elimination was achieved. The reduction in COD was also quite significant.

Table 4. Treatment with sodium hypochlorite (contact time 2 h).

Hypochlorite Concentration (mg·L^{-1})	Diclofenac (mg·L^{-1})	Removed Diclofenac %	COD Reduction %
1	14.4 ± 3.3 *	61.7 ± 4.7	24.1 ± 2.3
2	4.4 ± 1.2	88.4 ± 5.1	38.3 ± 2.8
3	3.3 ± 0.9	91.3 ± 4.4	44.0 ± 2.6
4	n.d. [†]	100	44.7 ± 1.8

* mean ± SD of 3 determinations; [†] not detected.

In the treatment that combined UV radiation with the addition of sodium hypochlorite (Table 5), practically all the diclofenac (93.59%) was eliminated for a radiation time of 10 min. When exposure time was increased (15 min), it was possible to eliminate it completely. In addition, the unreacted chlorine in this process provided residual protection for water reuse purposes [52]. Comparable reductions in COD were achieved as those with previous treatments. For the treatment in which UV radiation was combined with hydrogen peroxide (Table 6), the initial diclofenac was eliminated for all treatments. For an exposure time of 2 min of UV radiation, 99.20% of the initial diclofenac was degraded. The achieved elimination of COD was quite comparable in all performed treatments.

Table 5. Ultraviolet radiation treatment combined with sodium hypochlorite (5 mg·L^{-1}).

Contact Time (min)	Diclofenac (mg·L^{-1})	Removed Diclofenac %	COD Reduction %
2	29.1 ± 2.2 *	22.6 ± 2.8	14.2 ± 1.9
5	13.5 ± 1.8	64.2 ± 3.1	22.0 ± 2.4
10	2.4 ± 0.5	93.6 ± 4.8	45.0 ± 3.8
15	n.d. [†]	100	47.9 ± 3.4

* mean ± SD of 3 determinations; [†] not detected.

Table 6. UV radiation treatment combined with H$_2$O$_2$ (5 mg·L^{-1}).

Contact Time (min)	Diclofenac (mg·L^{-1})	Removed Diclofenac %	COD Reduction %
2	0.3 ± 0.1 *	99.2 ± 4.4	23.4 ± 1.7
5	n.d. [†]	100	25.9 ± 2.3
10	n.d.	100	36.5 ± 2.0
15	n.d.	100	40.1 ± 3.1

* mean ± SD of 3 determinations; [†] not detected.

It is scientifically accepted that advanced oxidation processes are highly effective novel methods that accelerate the oxidation and the degradation of a wide range of organic and inorganic pollutants that are resistant to conventional treatment methods [53]. In our experiments, diclofenac was 88% by UV-C degraded irradiation; when the wastewater was treated for a time as short as 15 min, this result verified that this compound absorbs UV irradiation well at 254 nm and can be easily photolyzed [54]. When UV-C irradiation treatment was combined with 5 mg·L^{-1} of sodium hypochlorite, the degradation of diclofenac was increased to 100%. Nevertheless, UV/H$_2$O$_2$ was the most efficient oxidation process, combining the immediate UV effect and the action of the HO$^{·}$ radicals produced from the homolytic disruption of H$_2$O$_2$. The levels of diclofenac degradation under the adopted experimental conditions were higher than the values reported in the literature for oxidation processes, such as ozonation (32%) and UV/H$_2$O$_2$ (39%), after 39 min treatment [55]. The use of hypochlorite to degrade diclofenac in

aqueous effluents was also reported with successful results [56]. Recent research in a Fenton-like system with FeCeOx–H_2O_2 achieved 84% degradation of diclofenac within 40 min [57]. All these results are in accordance with those obtained in our experimental design and confirm the feasibility of the tested methods. A significant reduction in chemical oxygen demand (COD) (40–48%) was also achieved with these oxidation treatments, although there was no direct relationship between the percentage of diclofenac degradation and the decrease in COD.

4. Conclusions

This paper offers a comparative study between the application of biosorption and advanced oxidation techniques to remove diclofenac from wastewater at high concentrations.

Artichoke agrowaste, olive-mill residues, and citrus waste were used as low-cost biosorbents to remove diclofenac from aqueous effluents. Citrus-waste biomass, at a sorbent dosage of 2 g·L^{-1}, showed the highest sorption capacity (9 mg·g^{-1}). This value was achieved with raw biomass without being subjected to any chemical or thermal activation process. The obtained results highlight the sustainable reutilization of agrifood waste for producing cost-effective sorbents, providing additional income for the agroindustrial sector. Waste valorization can efficiently help in reducing environmental stress by decreasing unwarranted pollution and promoting economy circularization.

UV-driven advanced oxidation treatments were effective in the degradation of diclofenac in wastewater. The UV/H_2O_2 (5 mg·L^{-1}) oxidation process was faster than UV/HOCl (5 mg·L^{-1}) to reach the same degradation rate. Chemical oxygen demand (COD) was considerably reduced (40–48%) with these oxidation treatments.

The obtained results in this study confirm biosorption as a low-cost and environmentally sustainable technique, and the high efficiency demonstrated by advanced oxidation techniques, may lead to applying specifically designed techniques that combine biosorption and advanced oxidation to eliminate specific emerging contaminants in aqueous effluents.

References

1. Dalecka, B.; Oskarsson, C.; Juhna, T.; Rajarao, G.K. Isolation of fungal strains from municipal wastewater for the removal of pharmaceutical substances. *Water* **2020**, *12*, 524. [CrossRef]

2. Geisen, V.; Mol, H.; Klumpp, E.; Umlauf, G.; Nadal, M.; Van der Ploeg, M.; van de Zee, S.E.A.T.M.; Ritsema, C.J. Emerging pollutants in the environment: A challenge for water resource management. *Int. Soil Water Conserv. Res.* **2015**, *3*, 57–65. [CrossRef]

3. Sauvé, S.; Desrosiers, M. A review of what is an emerging contaminant. *Chem. Cent. J.* **2014**, *8*, 15. [CrossRef] [PubMed]

4. López-Doval, J.C.; Montagner, C.C.; de Alburquerque, A.F.; Moschini-Carlos, V.; Umbuzeiro, G.; Pompeo, M. Nutrients, emerging pollutants and pesticides in a tropical urban reservoir: Spatial distributions and risk assessment. *Sci. Total Environ.* **2017**, *575*, 1307–1324. [CrossRef] [PubMed]

5. Margenat, A.; Matamoros, V.; Díez, S.; Cañameras, N.; Comas, J.; Bayona, J.M. Ocurrence of chemical contaminants in peri-urban agricultural irrigation waters and assesment of their phytotoxicity and crop productivity. *Sci. Total Environ.* **2017**, *599*, 1140–1148. [CrossRef] [PubMed]

6. Tran, N.; Drogui, P.; Brar, S.K. Sonochemical techniques to degrade pharmaceutical organic pollutants. *Environ. Chem. Lett.* **2015**, *13*, 251–268. [CrossRef]

7. Carmalin, A.; Lima, E. Removal of emerging contaminants from the environment by adsorption. *Ecotoxicol. Environ.* **2018**, *150*, 1–17.

8. Munthe, J.; Brorstrom-Lunden, E.; Rahmberg, M.; Posthuma, L.; Alterburger, R.; Brack, W.; Bunke, D.; Engelen, G.; Gawlik, B.; Gils, J.; et al. An expanded conceptual framework for solution-focused management of chemical pollution in European waters. *Environ. Sci. Eur.* **2017**, *29*, 1072. [CrossRef]

9. Richardson, S.D.; Kimura, S.Y. Emerging environmental contaminants: Challenges facing our next generation and potential engineering solutions. *Environ. Technol. Innov.* **2017**, *8*, 40–56. [CrossRef]

10. Rodriguez-Narvaez, O.M.; Peralta-Hernandez, J.M.; Goonetilleke, A.; Bandala, E.R. Treatment technologies for emerging contaminants in water: A review. *Chem. Eng. J.* **2017**, *323*, 361–380. [CrossRef]

11. Petrovic, M.; Solé, M.; López, M.; Barceló, D. Endocrine disruptors in sewage treatment plants, receiving river waters, and sediments: Integration of chemical analysis and biological effects of feral carp. *Environ. Toxic. Chem.* **2002**, *21*, 2146–2156. [CrossRef]

12. Esplugas, S.; Bila, D.M.; Krause, L.G.T.; Dezotti, M. Ozonation and advanced oxidation technologies to remove endocrine disrupting chemicals (EDCs) and pharmaceuticals and personal care products (PPCPs) in water effluents. *J. Hazard. Mater.* **2007**, *149*, 631–642. [CrossRef] [PubMed]

13. Richardson, S.D. Environmental mass spectrometry: Emerging contaminants and current issues. *Anal. Chem.* **2012**, *84*, 747–778. [CrossRef] [PubMed]

14. Richardson, S.D.; Kimura, S.Y. Water analysis: Emerging contaminants and current issues. *Anal. Chem.* **2016**, *88*, 546–582. [CrossRef]

15. Blanco, M.; Pérez-Albadalejo, E.; Piña, B.; Kuspilic, G.; Milun, V.; Lille-Langoy, R. Assessing the environmental quality of sediments from Split coastal area (Croatia) with a battery of cell-based bioassays. *Sci. Total Environ.* **2018**, *624*, 1640–1648.

16. Boehler, S.; Strecker, R.; Heinrich, P.; Prochazka, E.; Northcott, G.L.; Ataria, J.M. Assessment of urban stream sediment pollutants entering estuaries using chemical analysis and multiple bioassays to characterize biological activities. *Sci. Total Environ.* **2017**, *593*, 498–507. [CrossRef]

17. Abbas, M.; Adil, M.; Ehtisham-ul-Haque, S.; Munir, B.; Yameen, M.; Ghaffar, A.; Abbas Shar, G.; Asif Tahir, M.; Iqbal, M. *Vibrio fischeri* bioluminescence inhibition assay for ecotoxicity assessment: A review. *Sci. Total Environ.* **2018**, *626*, 1295–1309.

18. Schereiber, B.; Fischer, J.; Schiwy, S.; Hollert, H.; Schulz, R. Towards more ecological relevance in sediment toxicity testing with fish: Evaluation of multiple bioassays with embryos of the benthic weatherfish (*Misgurnus fossilis*). *Sci. Total Environ.* **2018**, *619*, 391–400. [CrossRef]

19. Sang, Z.; Jiang, Y.; Tsoi, Y.-K.; Leung, K.S. Evaluating the environmental impact of artificial sweeteners: A study of their distributions, photodegradation ant toxicities. *Water Res.* **2014**, *52*, 260–274. [CrossRef]

20. Funke, J.; Prasse, C.; Eversloh, C.L.; Ternes, T.A. Oxypurinol-A novel marker for wastewater contamination of the aquatic environment. *Water Res.* **2015**, *74*, 257–265.

21. Lonappan, L.; Brar, S.K.; Das, R.K.; Verma, M.; Rao, Y. Diclofenac and its transformation products: Environmental occurrence and toxicity. *Environ. Int.* **2016**, *96*, 127–138. [CrossRef] [PubMed]

22. Grandclément, C.; Piram, A.; Petit, M.E.; Seyssiecq, I.; Laffont-Schwob, I.; Vanot, G.; Tiliacos, N.; Roche, N.; Doumenq, P. Biological removal and fate assessment of diclofenac using *Bacillus subtilis* and *Brevibacillus laterosporus* strains and ecotoxicological effects of diclofenac and 4′-hydroxy-diclofenac. *J. Chem.* **2020**, *2020*, 9789420. [CrossRef]

23. Vieno, N.; Silanpää, M. Fate of diclofenac in municipal wastewater treatment plants—A review. *Environ. Int.* **2014**, *69*, 28–39. [CrossRef] [PubMed]

24. Langford, K.H.; Reid, M.; Thomas, K.V. Multi-residue screening of prioritised human pharmaceuticals, illicit drugs and bactericides in sediments and sludge. *J. Environ. Monit.* **2011**, *13*, 2284–2291. [CrossRef] [PubMed]

25. Kunkel, U.; Radke, M. Fate of pharmaceuticals in rivers: Deriving a benchmark dataset at favorable attenuation conditions. *Water Res.* **2012**, *46*, 5551–5565. [CrossRef]

26. Gil, A.; Santamaría, L.; Korili, S.A. Removal of caffeine and diclofenac from aqueous solution by adsorption on multiwalled carbon nanotubes. *Coll. Interf. Sci. Commun.* **2018**, *22*, 25–28. [CrossRef]

27. Mabrouki, H.; Akretche, D.E. Diclofenac potassium removal from water by adsorption on natural and pillared clay. *Des. Water Treatm.* **2016**, *57*, 6033–6043. [CrossRef]

28. Thi Minh Tam, N.; Liu, Y.; Bashir, H.; Yin, Z.; He, Y.; Zhou, X. Efficient removal of diclofenac from aqueous solution by potassium ferrate-activated porous graphitic biochar: Ambient condition influences and adsorption mechanism. *Int. J. Environ. Res. Public Health* **2020**, *17*, 291. [CrossRef]

29. Coimbra, R.N.; Escapa, C.; Vázquez, N.C.; Noriega-Hevia, G.; Otero, M. Utilization of non-living microalgae biomass from two different strains for the adsorptive removal of diclofenac from water. *Water* **2018**, *10*, 1401. [CrossRef]

30. Li, Y.; Taggart, M.A.; McKenzie, C.; Zhang, Z.; Lu, Y.; Pap, S.; Gibb, S. Utilizing low-cost natural waste for the removal of pharmaceuticals from water: Mechanisms, isotherms and kinetics at low concentrations. *J. Clean. Prod.* **2019**, *227*, 88–97. [CrossRef]

31. Yusuf, M.; Elfghi, F.M.; Zaidi, S.A.; Abdullah, E.C.; Khan, M.A. Applications of graphene and its derivatives as an adsorbent for heavy metal and dye removal: A systematic and comprehensive overview. *RSC Adv.* **2015**, *5*, 50392–50420. [CrossRef]

32. Rosique, M.; Angosto, J.M.; Guibal, E.; Roca, M.J.; Fernández-López, J.A. Factorial design methodological approach for enhanced cadmium ions bioremoval by *Opuntia* biomass. *CLEAN Soil Air Water* **2016**, *44*, 959–966. [CrossRef]

33. Ben-Othman, S.; Jõudu, I.; Bhat, R. Bioactives from agri-food wastes: Present insights and future challenges. *Molecules* **2020**, *25*, 510. [CrossRef] [PubMed]

34. Nowicki, P.; Kazmierczak-Razna, J.; Pietrzak, R. Physico-chemical and adsorption properties of carbonaceous sorbents prepared by activation of tropical fruit skins with potassium carbonate. *Mater. Des.* **2016**, *90*, 579–585. [CrossRef]

35. Castrica, M.; Rebucci, R.; Giromini, C.; Tretola, M.; Cattaneo, D.; Baldi, A. Total phenolic content and antioxidant capacity of agri-food waste and by-products. *Ital. J. Anim. Sci.* **2019**, *18*, 336–341. [CrossRef]

36. Manna, S.; Toy, D.; Adhikari, B.; Thomas, S.; Das, P. Biomass for water defluoridation and current understanding on biosorption mechanisms: A review. *Environ. Prog. Sustain. Energy* **2018**, *37*, 1560–1572. [CrossRef]

37. Ummartyotin, S.; Pechyen, C. Strategies for development and implementation of bio-based materials as effective renewable resources of energy: A comprehensive review on adsorbent technology. *Renew. Sustain. Energy Rev.* **2016**, *62*, 654–664. [CrossRef]

38. Arief, V.O.; Trilestari, K.; Sunarso, J.; Indraswati, N.; Ismadji, S. Recent progress on biosorption of heavy metals from liquids using low cost biosorbents: Characterization, biosorption parameters and mechanism studies. *CLEAN Soil Air Water* **2008**, *36*, 937–962. [CrossRef]

39. Ternes, T.; Stüber, J.; Herrmann, N.; McDowell, D.; Ried, A.; Kampmann, M.; Teiser, B. Ozonation: A tool for removal of pharmaceuticals, contrast media and musk fragrances from wastewater? *Water Res.* **2003**, *37*, 1976–1982. [CrossRef]

40. Cerreta, G.; Roccamante, M.A.; Oller, I.; Malato, S.; Rizzo, L. Contaminants of emerging concern removal from real wastewater by UV/free chlorine process: A comparison with solar/free chlorine and UV/H_2O_2 at pilot scale. *Chemosphere* **2019**, *236*, 124354.

41. Lee, Y.; von Gunten, U. Oxidative transformation of micropollutants during municipal wastewaters treatment: Comparison of kinetic aspects of selective (chlorine, chlorine dioxide, ferrate VI and ozone) and non-selective oxidants (hydroxyl radicals). *Water Res.* **2010**, *39*, 555–566. [CrossRef] [PubMed]

42. Kanakaraju, D.; Glass, B.D.; Oelgemöller, M. Titanium dioxide photocatalysis for pharmaceutical wastewater treatment. *Environ. Chem. Lett.* **2014**, *12*, 27–47. [CrossRef]

43. Jiang, J.; Pang, S.Y.; Ma, J.; Liu, H. Oxidation of phenolic endocrine disrupting chemicals by potassium permanganate in synthetic and real waters. *Environ. Sci. Technol.* **2012**, *46*, 1774–1781. [CrossRef]

44. Fiol, N.; Villaescusa, I. Determination of sorbent point zero charge: Usefulness in sorption studies. *Environ. Chem. Lett.* **2009**, *7*, 79–84. [CrossRef]

45. Eaton, A.D.; American Public Health Association; American Water Works Association; Water Environment Federation. *Standard Methods for the Examination of Water and Wastewater*, 21st ed.; APHA-AWWA-WEF: Washington, DC, USA, 2005.

46. Amiri, H.; Karimi, K. Improvement of acetone, butanol, and ethanol production from woody biomass using organosolv pretreatment. *Bioproc. Biosyst. Eng.* **2015**, *38*, 1959–1972. [CrossRef] [PubMed]

47. Saavedra, M.I.; Doval Miñarro, M.; Angosto, J.M.; Fernández-López, J.A. Reuse potential of residues of artichoke (*Cynara scolymus* L.) from industrial canning processing as sorbent of heavy metals in multimetallic effluents. *Ind. Crops Prod.* **2019**, *141*, 111751. [CrossRef]

48. Mahato, N.; Sharma, K.; Sinha, M.; Baral, E.R.; Koteswararao, R.; Dhyani, A.; Cho, M.H.; Cho, S. Bio-sorbents, industrially important chemicals and novel materials from citrus processing waste as a sustainable and renewable bioresource: A review. *J. Adv. Res.* **2020**, *23*, 61–82. [CrossRef] [PubMed]

49. Antunes, M.; Esteves, V.I.; Guégan, R.; Crespo, J.S.; Fernandes, A.N.; Giovanela, M. Removal of diclofenac sodium from aqueous solution by Isabel grape bagasse. *Chem. Eng. J.* **2012**, *192*, 114–121. [CrossRef]

50. Larous, S.; Meniai, A.-H. Adsorption of diclofenac from aqueous solution using activated carbon prepared from olive stones. *Int. J. Hydrog. Energy* **2016**, *41*, 10380–10390. [CrossRef]

51. Plauta, M.; Tisler, T.; Toman, M.J.; Pintar, A. Efficiency of advanced oxidation processes in lowering bisphenol A toxicity and oestrogenic activity in aqueous samples. *Arch. Ind. Hyg. Toxicol.* **2014**, *65*, 77–87.

52. Zhao, Q.; Shang, C.; Zhang, X.; Ding, G.; Yang, X. Formation of halogenated organic byproducts during medium-pressure UV and chlorine coexposure of model compounds, NOM and bromide. *Water Res.* **2011**, *45*, 6545–6554. [CrossRef] [PubMed]

53. Stasinakis, A. Use of selected advanced oxidation processes (AOPs) for wastewater treatment—A mini review. *Glob. NEST J.* **2008**, *10*, 376–385.

54. De la Cruz, N.; Giménez, J.; Esplugas, S.; Grandjean, D.; de Alencastro, L.F.; Pulgarín, C. Degradation of 32 emergent contaminants by UV and neutral photo-fenton in domestic wastewater effluent previously treated by activated sludge. *Water Res.* **2012**, *46*, 1947–1957. [CrossRef] [PubMed]

55. Vogna, D.; Marotta, R.; Napolitano, A.; Andreozzi, R.; d'Ischia, M. Advanced oxidation of the pharmaceutical drug diclofenac with UV/H_2O_2 and ozone. *Water Res.* **2004**, *38*, 414–422. [CrossRef] [PubMed]

56. Luongo, G.; Guida, M.; Siciliano, A.; Libralato, G.; Saviano, L.; Amoresano, A.; Previtera, L.; Di Fabio, G.; Zarrelli, A. Oxidation of diclofenac in water by sodium hypochlorite: Identification of new degradation by-products and their ecotoxicological evaluation. *J. Pharmac. Biomed. Anal.* **2020**, 113762. [CrossRef] [PubMed]

57. Chong, S.; Zhang, G.; Zhang, N.; Liu, Y.; Huang, T.; Chang, H. Diclofenac degradation in water by $FeCeO_x$ catalyzed H_2O_2: Influencing factors, mechanism and pathways. *J. Hazard. Mat.* **2017**, *334*, 150–159. [CrossRef]

Removal of Phenolic Compounds from Olive Mill Wastewater by a Polydimethylsiloxane/oxMWCNTs Porous Nanocomposite

Antonio Turco [1,2,*] **and Cosimino Malitesta** [1,*]

[1] Department of Biological and Environmental Sciences and Technologies (Di.S.Te.B.A.), University of Salento, Via Monteroni, 73100 Lecce, Italy

[2] CNR-NANOTEC Institute of Nanotechnology, Via Monteroni, 73100 Lecce, Italy

* Correspondence: antonio.turco@nanotec.cnr.it (A.T.); cosimino.malitesta@unisalento.it (C.M.)

Abstract: User-friendly and energy-efficient methods able to work in noncontinuous mode for *in situ* purification of olive mill wastewater (OMW) are necessary. Herein we determined the potential of oxidized multiwalled carbon nanotubes entrapped in a microporous polymeric matrix of polydimethylsiloxane in the removal and recovery of phenolic compounds (PCs) from OMW. The fabrication of the nanocomposite materials was straightforward and evidenced good adsorption capacity. The adsorption process is influenced by the pH of the OMW. Thermodynamic parameters evidenced the good affinity of the entrapped nanomaterial towards phenols. Furthermore, the kinetics and adsorption isotherms are studied in detail. The presence of oil inside the OMW can speed up the uptake process in batch adsorption experiments with respect to standard aqueous solutions, suggesting a possible use of the nanocomposite for fast processing of OMW directly in the tank where they are stored. Moreover, the prepared nanocomposite is safe and can be easily handled and disposed of, thus avoiding the presence of specialized personnel. After the adsorption process the surface of the nanomaterial can be easily regenerated by mild treatments with diluted acetic acid, thus permitting both the recyclability of the nanomaterial and the recovery of phenolic compounds for a possible use as additives in food and nutraceutical industries and the recovery of OMW for fertirrigation.

Keywords: olive mill wastewater; carbon nanotubes; polydimethilsiloxane; waste treatment; phenolic compounds; resources recovery

1. Introduction

Olive mill wastewater (OMW) is an acid waste derived from olive pressing, which has a production range from 10 to 30 million of m^3 per year [1]. OMW is composed of water, oil, and solids and exhibits ecotoxic and phytotoxic properties due to its high content of phenols [2]. For that reason, OMW has been considered as a matter of treatment and minimization [3]. However, it could represent a cheap source of components that can be recovered and used as natural food additives [4,5]. For instance, at low concentrations, phenols of olive have antioxidant properties with potential benefits for the health [6–8]. Moreover, OMW purified from phenols can be a valuable source for fertirrigation [9].

Different methods have been developed to purify OMW from phenols such as electrochemical oxidation [10], physical methods [11], solvent extraction [12], chemical treatments [13–15], filtration [16], and bioremediation [17,18]. However, these techniques could require high energy, the use of chemicals, and could generate secondary pollutants during the remediation process [19]. Moreover, phenolic compounds (PCs) could be degraded during the treatment thus not permitting their recovery. For all these reasons, there is an urgent need to develop alternative methods for the removal and

recovery of PCs from OMW. In this view, adsorption techniques can be an attractive alternative [20–25]. Different adsorbents have been developed, such as granular activated carbon [20], zeolites [26], agricultural wastes [3], and amberlite [27]. One of the major issues is that these materials are in powder form requiring large centrifuges or filtration systems for their management during the treatment. Another approach could be to pack the powder in a column for a continuous flow separation in a plant [21]. However, the seasonally production of OMW and the necessity to collect and transport OMW from the large number of olive mills to the plant can make such systems expensive [19]. Recently we have developed a nanocomposite material in which oxidized carbon nanotubes (oxCNTs) were physically entrapped on the surface of porous polydimethylsiloxane (PDMS) for the removal of phenolic compounds from aqueous solutions with good adsorption capacity. The nanocomposite can be easily handled and disposed of, making easier its recovery after the adsorption process [28]. Although the use of the material to remove phenolic compounds for OMW treatment was suggested a complete characterization of the adsorption process was not performed. In the present work we tested the ability of PDMS/oxidized multiwalled carbon nanotubes (oxMWCNTs)—spongeous materials to remove phenolic compounds from complex matrices such as OMW. The adsorption mechanisms, thermodynamic parameters, and kinetics were studied with different theoretical models. A good and fast adsorption capacity was observed. The system was demonstrated to be effective for the purification of complex OMW matrices in batch samples, suggesting their possible use for *in situ* purification of OMW, being able to work directly in the tank where the waste is stored. It has been demonstrated that the different phenols present in OMW can affect the adsorption process with respect to our previous observations. Moreover, the presence of oil in OMW can speed up the uptake process, probably due to the swelling of the pores inside the adsorbent phase. The reusability of the nanocomposite and the possibility of recovering adsorbed phenols was also demonstrated.

2. Materials and Methods

2.1. Materials

Multiwalled carbon nanotubes with a diameter of 25.4 ± 4 nm were provided by Nanostructured & Amorphous Materials, Inc., Los Alamos, NM, USA. The PDMS polymerization kit (Sylgard 184), comprising monomer and curing agent, were purchased from Dow Corning, Midland, MI, USA. All the other reagents were analytical grade and purchased from VWR International srl, Milano, Italy, and used as received.

2.2. OMW Origin and Composition

OMW was obtained from a three-phase continuous extraction unit in Miggiano, Italy. The pH at 25 °C was equal to 4.8 and the density 1.08 ± 0.02 g/L. Total suspended solids were 2.57 ± 0.05 g/L, the total solids were 25.12 ± 0.8 g/L, the mineral matter was 4.02 ± 0.07 g/L. The phenolic amount equal to 2.089 ± 0.01 g/L was calculated by Folin–Ciocalteau assay [29].

2.3. Preparation of the Spongeous Adsorbent

A sponge of polydimethilsiloxane (PDMS), in which oxidized multiwalled carbon nanotubes (oxMWCNTs) were stably entrapped and homogenously dispersed on pores' surfaces, was prepared following our well-developed procedure [28]. Briefly, microparticles of glucose crystals with an average dimension of 290 ± 170 μm were mixed with a shaker overnight with pristine MWCNTs at 3% *w/w*. The obtained mixture was packed in a centrifuge tube and an appropriate amount of PDMS prepolymer mixed with curing agent in the ratio of 10:1 and diluted with 40% in *wt.%* of hexane was added on the top. The composites were centrifuged at 8000 rpm for 20 min to allow the packing of the mixture and the permeation of the prepolymerization solutions between the sugar particles. The composite was then cured at 60 °C overnight to accomplish the polymerization. Finally, glucose was removed by

firstly soaking the nanocomposite in boiling water under continuous stirring and then by sonication in warm water and ethanol.

MWCNTs entrapped in the nanocomposites were then oxidized. The sponges were placed in water under reduced pressure to allow the permeation of the solution in the pores of the hydrophobic nanocomposite, then nitric acid was added until a concentration of 3 M was reached and left for two hours under continuous stirring. At the end of the process the as-obtained nanocomposites were washed repetitively with water until the pH of the washing solution remained stable. The nanocomposites were dried under vacuum and dipped in H_2O_2 30% *w/w* solution under stirring for 2 h. Finally, the obtained materials (PDMS/oxMWCNTs) were repetitively washed in water and dried at 100 °C overnight.

2.4. Determination of PCs in OMW

The PCs in the OMW were quantified by Folin–Ciocalteu assay [29]. 240 μL of water, 50 μL of OMW, and 250 μL of Folin–Ciocalteau reagent were added in a flask. After 120 s, 2.7 mL of sodium carbonate (20% *w/v*) was added. The mixture was left at 25 °C for 2 h and then centrifuged at 8000 rpm for 5 min. The absorbance of the supernatant was read at 765 nm with a Cary UV 50 spectrophotometer. Gallic acid was used as a standard for the calibration of the method.

2.5. Adsorption Experiments

A proper amount of the PDMS/oxMWCNTs nanocomposite (6 g/100 mL) was immersed in 5 mL of OMW diluted with water (pH = 4.8) with a known concentration of phenols (1.251 g/L) and shacked at 25 °C. Studies at different pH were performed, adjusting the pH with 0.1 M HCl or 0.1 M NaOH. The adsorption rates of phenols were monitored at different times (namely 0, 0.5, 1, 1.5, 2, 2.5, 3, 4, 22, and 24 h) collecting small aliquots from the solution for further spectrophotometric analysis. Removal efficiency (Q%) and equilibrium adsorption capacity (q_e) of the sponges were calculated by Equations (1) and (2) respectively:

$$removal \quad efficiency \quad (\%) \quad = \left[\frac{(C_0 - C_t)}{C_0} \right] \times 100 \tag{1}$$

$$adsorption \quad capacity, \quad q_e\left(\frac{mg}{g}\right) \quad = \left[\frac{(C_0 - C_e)}{W} \right] \times V \tag{2}$$

where C_0 and C_t are respectively the concentration of PCs at the beginning of the experiment and at a given time (hours) in ppm (mg/L), C_e is the PCs concentrations (ppm) at the equilibrium (24 h), W is the weight of the sponge in grams, and V is the volume of the solution in liters.

2.6. Desorption Experiments

The adsorbent was separated from the OMW solution and washed with water. Desorption experiments were conducted by dipping the PDMS/oxMWCNTs sponge in 10% acetic acid, which was vortexed for 2 h.

3. Results and Discussion

3.1. Adsorption of OMW PCs on PDMS/oxMWCNTs Sponges

Our developed fabrication route described in experimental methods can easily allow the synthesis of black porous PDMS/oxMWCNTs sponges (Figure 1a) in which the pores dimensions are comparable to that of the used hard template. The carbon nanotubes are well-dispersed in the polymeric matrices thanks to the mechanical destroying of π-π stacking during the fabrication steps. Moreover, the oxidation of the nanomaterials in the sponges occurred after the synthesis of the 3D nanocomposites thus reducing the need of complex apparatus thanks to the easy handle of the material [28,30]. Although it is known that treatment with strong acid can degrade PDMS matrices [31], it is interesting to note as the oxidation procedure did not significantly affect the mechanical stability of the material.

This is probably due to the low concentration of nitric acid and short time of incubation used for the synthetic procedure. The prepared sponges were dipped in an OMW solution at pH 4.8 and the adsorption of PCs was monitored at different times. As reported in Figure 1c, at the beginning of the process we observed a fast phenols adsorption. After 4 h the adsorption process become slower due to the decrease in the number of easily accessible sites on oxMWCNTs [3,28,32]. Finally, for times higher than 20 h an equilibrium between the adsorbent and adsorbate is achieved. Moreover, we observed that the adsorption of PCs did not occur in 24 h on porous PDMS prepared following the procedure in Section 2.3, but in the absence of MWCNTs, and is very low on a spongeous nanocomposite in which MWCNTs were not oxidized (removal efficiency approximately 2%) (data not shown).
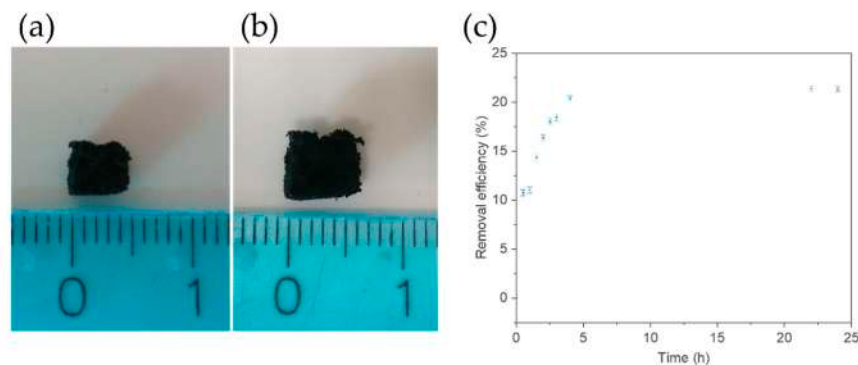
Figure 1. A piece of polydimethylsiloxane/oxidized multiwalled carbon nanotubes (PDMS/oxMWCNTs) sponge (**a**) before and (**b**) after dipping in an olive mill wastewater (OMW) solution. (**c**) Effect of contact time on adsorption of OMW phenolic compounds (PCs) on the PDMS/oxMWCNTs sponge.

Interestingly, most of the uptake process (around 95%) was completed in 4 h, evidencing a faster uptake with respect to what we observed in aqueous solutions [28].

We hypothesized that this can be due to two different reasons: on one hand it could be due to an increased affinity of phenols contained in the OMW with the adsorbent; on the other hand, it could be due to the presence of oil in the OMW, which could cause the swelling of the PDMS/oxMWCNTs sponge [30,33] thus favoring the diffusion of the mixture inside the adsorbent phase. To verify the first hypothesis the PDMS/oxMWCNTs sponge was dipped in two different solutions containing two different PCs, namely 4-nitrophenol and phenol, for which the nanomaterial has evidenced different affinities at the same concentration (i.e., 0.18 mM) [28]. We observed a significant increment in the removal efficiency at equilibrium, but not in the rate of adsorption. In fact, 84% of the process is completed in 4 h in both cases (Figure S1). Therefore, the increment in the adsorption rate was attributed to the evident swelling of the nanocomposite in OMW (Figure 1b).

3.2. Effect of pH and Adsorbent Amount on PCs Adsorption

pH can affect both the adsorption mechanisms and the nature of soluble species' interactions with the adsorbents [34].

We tested the pH effect on the PCs removal from OMW with our porous nanocomposite. As visible in Figure 2, the removal efficiency (%) increases from pH 2 to 4.8, then slightly decreases for pH values up to 6.5 and finally decreases dramatically at higher pH, reaching a removal efficiency (%) close to zero at pH over 10.5.

The increment in removal efficiency observed until pH of around 6.5 is mainly due to π-π interactions. Although this mechanism is still not clear, it is well known that higher pH values can alter the π donation strength of PCs thus causing an increase of their adsorption on the oxMWCNTs' surface [28,35]. However, the removal efficiency decreased very fast at pHs over 6.5 with an apparent different behavior to that observed in adsorption of PCs on oxMWCNTs in aqueous solutions [28]. A similar behavior was also reported for some PCs adsorbed by MWCNTs [35], demonstrating that

the decreased removal efficiency of phenols for pH over their pKa could be due to the increased electrostatic repulsion between the dissociated phenols and negatively charged oxMWCNTs. Moreover, the dissociation of the PCs would increase their hydrophilicity, thus decreasing their adsorption. Consequently, the observed trend can be explained by the fact that most of the PC constituents of OMW are deprotonated at higher pH, due to their pKa lower than 5 (Figure 3) [36]. This suggests also that the adsorption of different type of phenols could be achieved at different pHs.
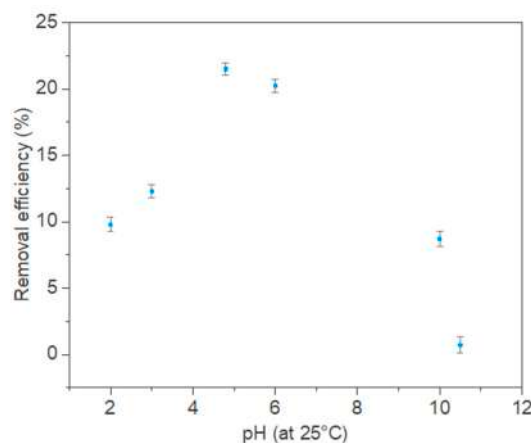
Figure 2. Effect of pH on adsorption of PCs by the PDMS/oxMWCNTs sponge.
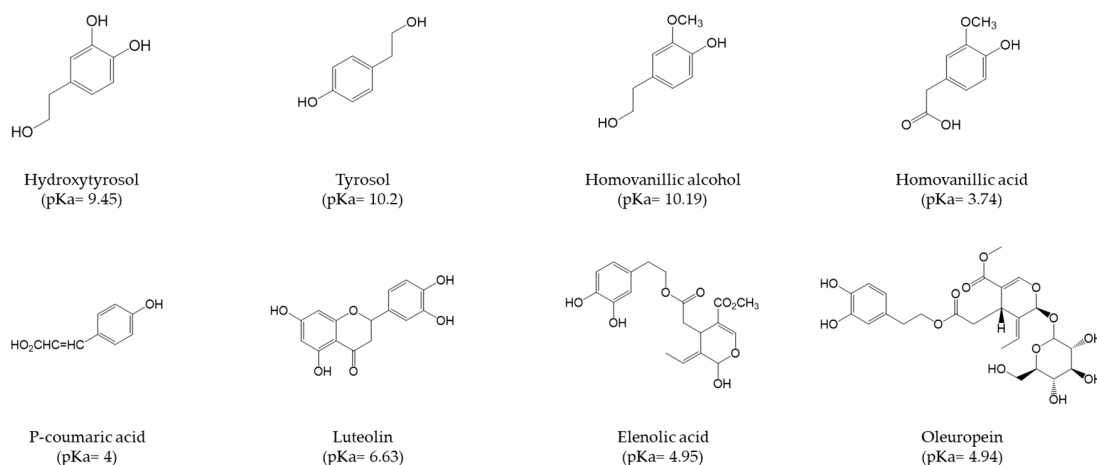
Figure 3. The major constituents of OMW. The common name and the pKa value are reported under each compound.

Figure 4 shows the removal efficiency (%) and adsorption capacity (q_e) of phenols in OMW as a function of the PDMS/oxMWCNTs sponge amount in the given conditions. It is evident that an increase in sponge amount in the mixture results in an obvious increase in the phenol adsorption percent. With the increase in PDMS/oxMWCNTs amount from 4 to 10 g/100 mL, the phenol removal efficiency increased rapidly from 20.2 to 35.5%. This was intuitively due to the increase in the number of adsorption sites with the increase in the sponge amount. The results indicated that it was possible to remove phenols completely from OMW when there was a high enough PDMS/oxMWCNTs sponge amount in the mixture. On the other hand, the q_e was high at low doses and reduced at high doses, thus suggesting that some adsorption sites remain unsaturated during the adsorption process [3,37–40].

The results of this section also indicated that, in order to obtain the optimal adsorbent dosage, higher initial phenol concentrations should be tested in conjunction with appropriate adsorbent dosage depending on the concentration of phenolic compound in OMW [37,38].
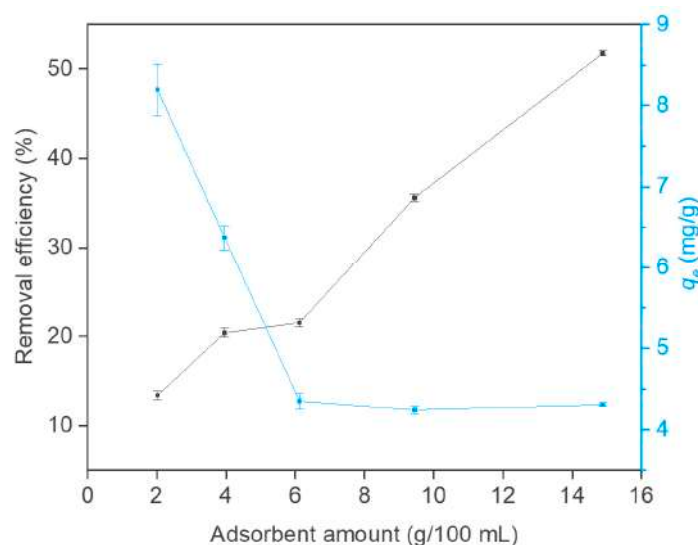
Figure 4. Influence of foam concentration on removal efficiency and adsorption capacity of phenolic compounds in OMW.

3.3. Adsorption Isotherms and Thermodynamic Parameters

Several models have been used to describe adsorption equilibrium, among which the Freundlich and the Langmuir models are the most frequently used.

The Freundlich isotherm [41] describes a reversible process in which the adsorption can occur through homogeneous and/or heterogenous interactions.

The linear form of the equation is:

$$\log q_e = \log K_F + \frac{1}{n} \log C_e \tag{3}$$

where K_F is the Freundlich constant representative of the adsorption capacity of adsorbent and n describes the strength of adsorption. An R^2 of 0.80 was obtained by linear fitting (Figure S2), evidencing that the model did not describe well the experimental data, thus being in contrast with what was observed in aqueous solutions [28]. We ascribe this behavior to the complexity of OMW in which other interferences species can influence the adsorption mechanisms.

Experimental data were also fitted with the Langmuir theory [42], which is valid for monolayer adsorption onto surfaces with homogenous binding sites.

The linearized form of the isotherm is:

$$\frac{C_e}{q_e} = \frac{1}{K_L q_{max}} + \frac{C_e}{q_{max}} \tag{4}$$

where K_L (L/mg) is the Langmuir constant and is representative of the affinity of the sorbate for the sorbent and q_{max} (mg/g) is the maximum adsorption capacity.

The R^2 value higher than 0.99 suggests that the model is more appropriate to describe the adsorption process. From the fitting, a q_{max} of 4.39 mg/g was found. The dimensionless equilibrium parameter (R_L) was calculated as in Equation (5) at different concentrations of PCs.

$$R_L = \frac{1}{1 + K_L C_0} \tag{5}$$

The results summarized in the table of Figure 5 evidenced that the R_L value is always comprised between 0 and 1, confirming the high affinity of PDMS/oxMWCNTs sponge for phenols contained in OMW [3].

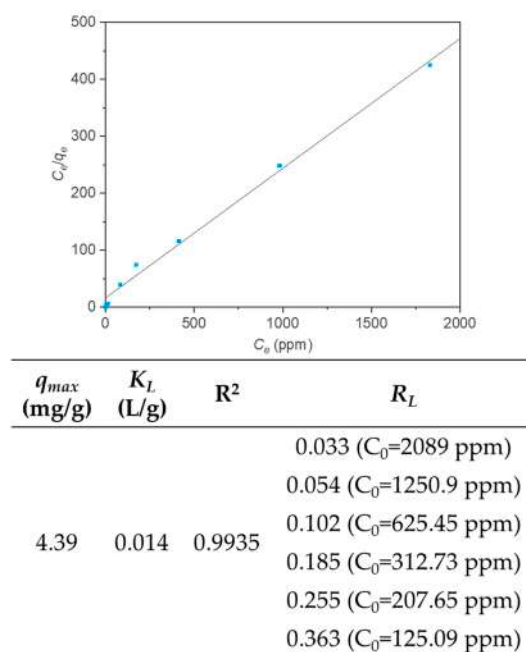| q_{max} (mg/g)	K_L (L/g)	R²	R_L
4.39	0.014	0.9935	0.033 (C_0=2089 ppm)
			0.054 (C_0=1250.9 ppm)
			0.102 (C_0=625.45 ppm)
			0.185 (C_0=312.73 ppm)
			0.255 (C_0=207.65 ppm)
			0.363 (C_0=125.09 ppm)

Figure 5. Fitting of experimental data with the linearized Langmuir isotherm model for phenols in OMW. The table reports calculated values from Equations (6) and (7).

The obtained results were compared with other sorbents used for the same purpose (Table 1). The highest values were reached with wheat bran and banana peel [3,37]. However, it should be pointed out that in this work the adsorption capacities are calculated per gram of sponges and not per gram of oxMWCNTs. This is important since the adsorption of PCs is exclusively due to the oxMWCNTs. Therefore, calculating the q_{max} considering only the grams of oxMWCNTs a value of 454.55 mg/g is obtained, which is comparable with the most efficient materials. Moreover, the PDMS/oxMWCNTs sponge has the advantages of being user-friendly and easy to manipulate during all the steps of the waste treatment.

Table 1. Langmuir constants for PCs adsorption from various absorbents reported in literature.

Adsorbent	q_{max} (mg/g)	K_L (L/g)	References
PDMS/oxMWCNTs	4.39 (454.55)	0.014	This work
Banana peel	688.9	0.24	[3]
Wheat bran	487.3	0.13	[37]
Olive pomace	11.40	0.005	[43]
Activated carbon coated with milk protein	246.45	9.1	[44]
Activated carbon	268.17	0.14	[45]

From the variation of K_L values with temperature we calculate the Gibbs free energy ($\Delta G°$) of adsorption, enthalpy ($\Delta H°$), and entropy ($\Delta S°$) using the following equation:

$$\Delta G° = -RT \ln(K_{LD}) \tag{6}$$

and the van't Hoff equation:

$$\ln(K_{LD}) = \left(\frac{\Delta S°}{R}\right) - \left(\frac{\Delta H°}{RT}\right) \tag{7}$$

in which R is the gas constant (8.314 J/(mol K)), T is the temperature expressed in Kelvin, and K_{LD} is obtained by multiplying K_L by 1000 [46,47].

The van't Hoff plot of $\ln(K_{LD})$ against $1/T$ evidenced a good linearity with an R^2 = 0.96 and both $\Delta H°$ and $\Delta S°$ were calculated (Figure 6). The negative values of $\Delta G°$ suggests that the process occurs

spontaneously. The positive value of $\Delta H°$ represents an endothermic reaction while values of $\Delta S°$ higher than zero evidenced that the randomness increased at the solid liquid interface due to the high affinity of the sorbent for the PCs [46].
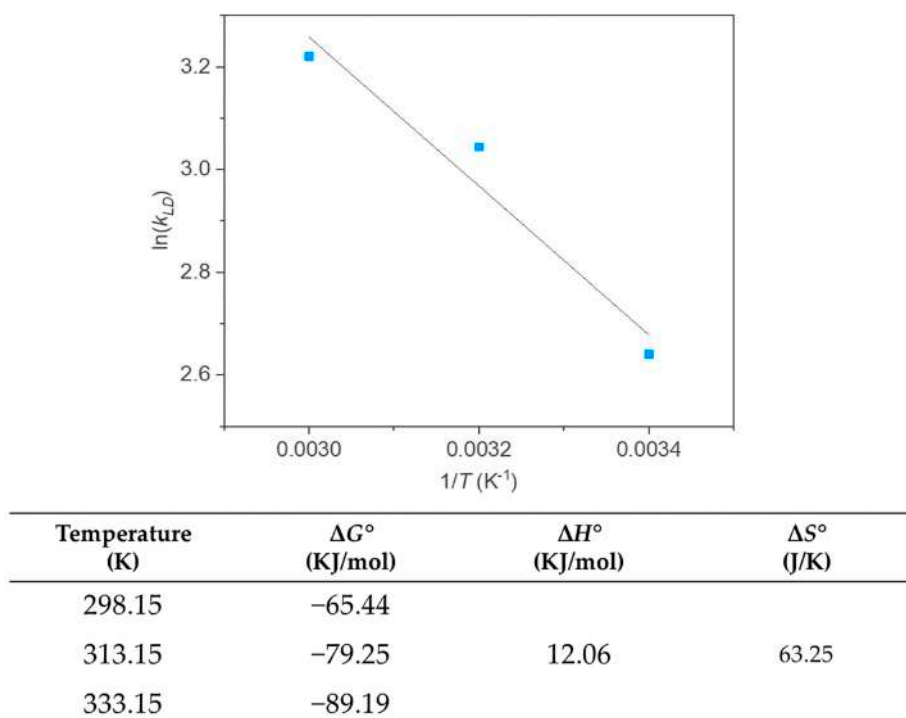

Temperature (K)	$\Delta G°$ (KJ/mol)	$\Delta H°$ (KJ/mol)	$\Delta S°$ (J/K)
298.15	−65.44		
313.15	−79.25	12.06	63.25
333.15	−89.19		

Figure 6. Van't Hoff plot for phenols adsorption from OMW. The calculated values from Equation (7) are reported in the table.

3.4. Kinetic of the Adsorption Process

To elucidate the adsorption mechanisms in OMW, adsorption kinetics have been evaluated. The mechanism of the adsorption strongly depends on the physical and chemical characteristics of the adsorbent as well as on the mass transport process. Pseudo-first-order and pseudo-second-order equations were examined in this study.

The pseudo-first-order equation [48] is represented by the following equation:

$$\ln(q_e - q_t) = \ln q_e - k_1 t \tag{8}$$

in which q_t is relative to the number of PCs adsorbed (mg/g) at any time t (h), and k_1 (h^{-1}) is the equilibrium rate constant of pseudo-first-order sorption. By plotting $\ln(q_e - q_t)$ against t a straight line should be obtained with slope $-K_1$ and intercept $\ln q_e$.

The pseudo-second-order equation [49] is expressed in the form:

$$\frac{t}{q_t} = \frac{1}{k_2 q_e^2} + \frac{t}{q_e} \tag{9}$$

in which k_2 is the rate constant of the pseudo-second-order equation (g/g h). The rate constant (k_2) and the equilibrium adsorption capacity (q_e) can be obtained from the slope and the intercept of the plot of t/q_t versus t. The experimental data fitted with both the models are reported in Figure 7.

It is evident that pseudo-second-order kinetic model better describes the experimental data ($R^2 > 0.99$), thus suggesting that chemical sorption, mainly due to π-π interactions [28], occurs between the PCs and PDMS/oxMWCNTs sponge [3]
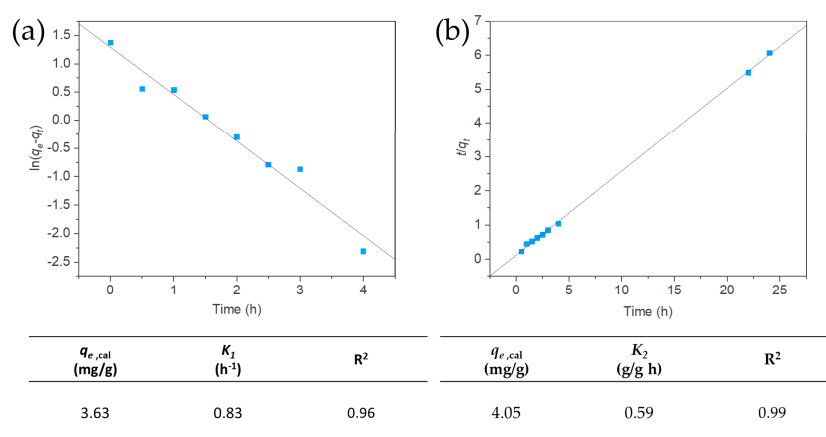
Figure 7. Application of (**a**) pseudo-first-order adsorption model and (**b**) pseudo-second-order adsorption model. The calculated values from Equations (8) and (9) are reported in the tables under graphs (**a**) and (**b**) respectively.

3.5. Intraparticle Diffusion Model

The pseudo-first-order and the pseudo-second-order models can explain the adsorption process, but are not useful to identify the diffusion mechanisms.

$$q_t = k_p t^{1/2} + C \qquad (10)$$

k_p is the rate constant of intraparticle diffusion model and C is a constant for any experiment (mg/g). By plotting q_t versus $t^{1/2}$ (Figure 8) two linear ranges were observed and ascribed to at least two different diffusion mechanisms of adsorption.

The lower value of k_{p2} with respect to k_{p1} (with k_{p1} and k_{p2} representing k_p values for step I and II, respectively) indicated that the free path available for diffusion of PCs inside the sponge became smaller, thus causing the reduction of the diffusion rate [50]. It can be hypothesized that firstly the adsorption occurs on the most accessible sites on the oxMWCNTs surface. Once these sites are saturated, the PCs entered into smaller pores and/or reached the binding sites in the interstitial space between oxMWCNTs, causing a decrease in the diffusion rate [28,32,51].

Interestingly, more than 95% of the total adsorption process occurs at the faster step. Moreover, a higher K_p value in the first step was obtained with respect to that obtained in aqueous solutions [28], thus confirming that the swelling of the sponge in OMW can speed up the entire adsorption process [30,33].
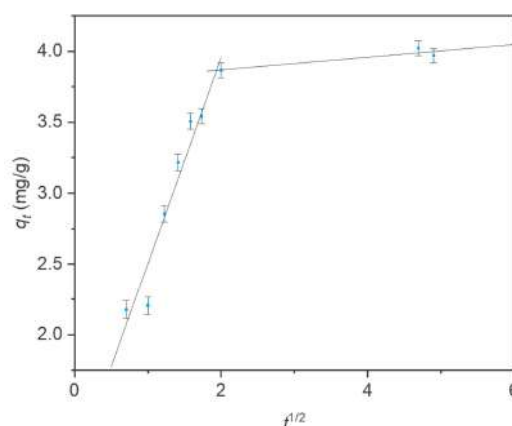

Figure 8. Application of intraparticle diffusion model for the adsorption of phenols in OMW onto PDMS/oxMWCNTs sponges.

3.6. Desorption and Reusability Studies

Since the chemisorption process occurs between phenols and oxMWCNTs, adsorbed compounds can be removed with an acidic treatment [28]. After the first adsorption process, the PDMS/oxMWCNTs sponges were washed in 10% acetic acid at 60 °C to break the π-π interactions. The washing procedure permits the solubilization of most of the adsorbed PCs (~99%) (Figure 9, blue columns), which can thus be used in phenolic-enriched foods after simple further purification steps. Furthermore, the sponge can be reused without losing its adsorption capacity, confirming the high stability of the nanocomposite despite the swelling process. This suggests the possibility to use the nanocomposite for an higher number of adsorption/desorption cycles, thus permitting the decrease of costs for the treatment of OMW with higher phenols concentrations and the complete purification of the waste that can thus be used for fertirrigation [9].
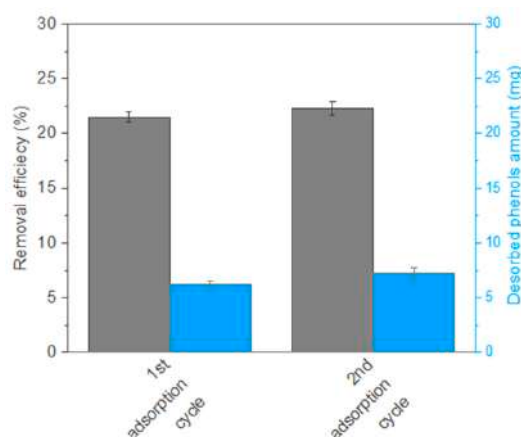
Figure 9. Reusability tests for PDMS/oxMWCNTs sponges reporting removal efficiency % (gray column) and the amount of desorbed phenols (blue column).

4. Conclusions

The present work describes the application of spongeous nanocomposites made of PDMS and oxidized MWCNTs for the adsorption of phenols from olive mill wastewater. The MWCNTs loading was performed with a straightforward method without the use of complex procedures. The oxidation of the nanomaterial was performed directly on the sponge, simplifying the post-treatment and speeding up the whole fabrication process. The entrapped nanomaterials were stable and evidenced good adsorption capacity compared to other systems. The pH of the OMW and pKa of the phenolic compounds can influence the removal efficiency of the nanocomposites. By the evaluation of thermodynamic parameters, we observed that the adsorption process is spontaneous and with a high affinity for the phenolic compounds. The adsorption process in OMW is described by the Langmuir isotherm, suggesting the formation of a monolayer on the nanomaterial surface and evidencing a different behavior of the nanocomposites with respect to what happens in standard aqueous solutions in which the formation of a PCs heterogeneous multilayer on an adsorbent surface was observed. It is also interesting to note that the presence of complex matrices such as OMW can speed up the entire adsorption process (more than 95% of the adsorption is completed in less than 4 h) with respect to standard aqueous solution. We ascribed this behavior to the presence of a small amount of oil inside the OMW that can promote the swelling of the sponge and the diffusion of the mixture inside the polymeric matrices. This is interesting since the oil seasonal production required the fast processing of OMW.

The nanocomposite can thus be easily used to work in batch conditions. This could be useful for a real application of the system. After its production, OMW is stored in a big tank in which the spongeous nanocomposites can be added for the adsorption process. Thus, the nanocomposite can be used directly *in situ*. In this view, the entrapment of oxMWCNTs adsorbent in a porous polymeric matrix represents

a significant advantage; in this way, post-treatment processes, such as filtration and/or centrifugation, are not required to remove the adsorbent phase after the adsorption process, decreasing the time and the costs of the treatment. Moreover, the nanomaterial can be easily handled and disposed in a safe way without the use of specialized personnel. The surface of the nanomaterial can be regenerated with a mild treatment with diluted acetic acid. On one hand this permits us to further decrease the costs of production in wastewater treatment. On the other hand, the adsorbed phenolic compound can be easily desorbed from the sponge and can be used, after small further purification, to produce phenolic-enriched food due to its health benefits ranging from reduced incidence of cardiovascular disease, diabetes, and cancers. Furthermore, the treated OMW can be a useful source for fertirrigation. This could permit us to transform a waste product to a resource, especially for the regions of the Mediterranean area in which is concentrated most of the world's production of olive oil. Moreover, the reusability of the material can be useful for OMW with high concentration of phenols that needs repetitive cycles of purification.

References

1. El-Abbassi, A.; Hafidi, A.; García-Payo, M.C.; Khayet, M. Concentration of olive mill wastewater by membrane distillation for polyphenols recovery. *Desalination* **2009**, *245*, 670–674. [CrossRef]

2. Della Greca, M.; Monaco, P.; Pinto, G.; Pollio, A.; Previtera, L.; Temussi, F. Phytotoxicity of Low-Molecular-Weight Phenols from Olive Mill Waste Waters. *Bull. Environ. Contam. Toxicol.* **2001**, *67*, 352–359. [CrossRef] [PubMed]

3. Achak, M.; Hafidi, A.; Ouazzani, N.; Sayadi, S.; Mandi, L. Low cost biosorbent "banana peel" for the removal of phenolic compounds from olive mill wastewater: Kinetic and equilibrium studies. *J. Hazard. Mater.* **2009**, *166*, 117–125. [CrossRef] [PubMed]

4. Sklavos, S.; Gatidou, G.; Stasinakis, A.S.; Haralambopoulos, D. Use of solar distillation for olive mill wastewater drying and recovery of polyphenolic compounds. *J. Environ. Manag.* **2015**, *162*, 46–52. [CrossRef] [PubMed]

5. Dutournié, P.; Jeguirim, M.; Khiari, B.; Goddard, M.-L.; Jellali, S. Olive Mill Wastewater: From a Pollutant to Green Fuels, Agricultural Water Source, and Bio-Fertilizer. Part 2: Water Recovery. *Water* **2019**, *11*, 768. [CrossRef]

6. Schaffer, S.; Podstawa, M.; Visioli, F.; Bogani, P.; Müller, W.E.; Eckert, G.P. Hydroxytyrosol-Rich Olive Mill Wastewater Extract Protects Brain Cells in Vitro and ex Vivo. *J. Agric. Food Chem.* **2007**, *55*, 5043–5049. [CrossRef]

7. Visioli, F.; Galli, C. The Effect of Minor Constituents of Olive Oil on Cardiovascular Disease: New Findings. *Nutr. Rev.* **2009**, *56*, 142–147. [CrossRef]

8. Bulotta, S.; Celano, M.; Lepore, S.M.; Montalcini, T.; Pujia, A.; Russo, D. Beneficial effects of the olive oil phenolic components oleuropein and hydroxytyrosol: Focus on protection against cardiovascular and metabolic diseases. *J. Transl. Med.* **2014**, *12*, 219. [CrossRef]

9. Colarieti, M.L.; Toscano, G.; Greco, G. Toxicity attenuation of olive mill wastewater in soil slurries. *Environ. Chem. Lett.* **2006**, *4*, 115–118. [CrossRef]

10. Abdelwahab, O.; Nassef, E.M. Treatment of Petrochemical Wastewater Containing Phenolic Compounds by Electrocoagulation Using a Fixed Bed Electrochemical Reactor. *Int. J. Electrochem. Sci.* **2013**, *8*, 1534–1550.

11. Jerman Klen, T.; Mozetič Vodopivec, B. Ultrasonic Extraction of Phenols from Olive Mill Wastewater: Comparison with Conventional Methods. *J. Agric. Food Chem.* **2011**, *59*, 12725–12731. [CrossRef] [PubMed]

12. Pelendridou, K.; Michailides, M.K.; Zagklis, D.P.; Tekerlekopoulou, A.G.; Paraskeva, C.A.; Vayenas, D.V. Treatment of olive mill wastewater using a coagulation–flocculation process either as a single step or as post-treatment after aerobic biological treatment. *J. Chem. Technol. Biotechnol.* **2014**, *89*, 1866–1874. [CrossRef]

13. Hosseini, S.A.; Davodian, M.; Abbasian, A.R. Remediation of phenol and phenolic derivatives by catalytic wet peroxide oxidation over Co-Ni layered double nano hydroxides. *J. Taiwan Inst. Chem. Eng.* **2017**, *75*, 97–104. [CrossRef]

14. Domingues, E.; Assunção, N.; Gomes, J.; Lopes, D.V.; Frade, J.R.; Quina, M.J.; Quinta-Ferreira, R.M.; Martins, R.C. Catalytic Efficiency of Red Mud for the Degradation of Olive Mill Wastewater through Heterogeneous Fenton's Process. *Water* **2019**, *11*, 1183. [CrossRef]

15. Amor, C.; Marchão, L.; Lucas, M.S.; Peres, J.A. Application of advanced oxidation processes for the treatment of recalcitrant agro-industrial wastewater: A review. *Water* **2019**, *11*, 205. [CrossRef]

16. Garcia-Segura, S.; Bellotindos, L.M.; Huang, Y.-H.; Brillas, E.; Lu, M.-C. Fluidized-bed Fenton process as alternative wastewater treatment technology—A review. *J. Taiwan Inst. Chem. Eng.* **2016**, *67*, 211–225. [CrossRef]

17. Ran, N.; Gilron, J.; Sharon-Gojman, R.; Herzberg, M. Powdered Activated Carbon Exacerbates Fouling in MBR Treating Olive Mill Wastewater. *Water* **2019**, *11*, 2498. [CrossRef]

18. Kapellakis, I.; Tzanakakis, V.A.; Angelakis, A.N. Land Application-Based Olive Mill Wastewater Management. *Water* **2015**, *7*, 362–376. [CrossRef]

19. Paraskeva, P.; Diamadopoulos, E. Technologies for olive mill wastewater (OMW) treatment: A review. *J. Chem. Technol. Biotechnol.* **2006**, *81*, 1475–1485. [CrossRef]

20. Bernal, V.; Giraldo, L.; Moreno-Piraján, J.C. Insight into adsorbate–adsorbent interactions between aromatic pharmaceutical compounds and activated carbon: Equilibrium isotherms and thermodynamic analysis. *Adsorption* **2020**, *26*, 153–163. [CrossRef]

21. Takahashi, K.; Yoshida, S.; Urkasame, K.; Iwamura, S.; Ogino, I.; Mukai, S.R. Carbon gel monoliths with introduced straight microchannels for phenol adsorption. *Adsorption* **2019**, *25*, 1241–1249. [CrossRef]

22. Duy Nguyen, H.; Nguyen Tran, H.; Chao, H.-P.; Lin, C.-C. Activated Carbons Derived from Teak Sawdust-Hydrochars for Efficient Removal of Methylene Blue, Copper, and Cadmium from Aqueous Solution. *Water* **2019**, *11*, 2581. [CrossRef]

23. Nikić, J.; Tubić, A.; Watson, M.; Maletić, S.; Šolić, M.; Majkić, T.; Agbaba, J. Arsenic Removal from Water by Green Synthesized Magnetic Nanoparticles. *Water* **2019**, *11*, 2520. [CrossRef]

24. Nabeela Nasreen, S.A.A.; Sundarrajan, S.; Syed Nizar, S.A.; Ramakrishna, S. Nanomaterials: Solutions to water-concomitant challenges. *Membranes* **2019**, *9*, 40. [CrossRef] [PubMed]

25. Nasreen, S.A.A.N.; Sundarrajan, S.; Nizar, S.A.S.; Balamurugan, R.; Ramakrishna, S. Advancement in electrospun nanofibrous membranes modification and their application in water treatment. *Membranes* **2013**, *3*, 266–284. [CrossRef] [PubMed]

26. Aly, A.A.; Hasan, Y.N.Y.; Al-Farraj, A.S. Olive mill wastewater treatment using a simple zeolite-based low-cost method. *J. Environ. Manag.* **2014**, *145*, 341–348. [CrossRef] [PubMed]

27. Frascari, D.; Bacca, A.E.M.; Zama, F.; Bertin, L.; Fava, F.; Pinelli, D. Olive mill wastewater valorisation through phenolic compounds adsorption in a continuous flow column. *Chem. Eng. J.* **2016**, *283*, 293–303. [CrossRef]

28. Turco, A.; Monteduro, A.; Mazzotta, E.; Maruccio, G.; Malitesta, C. An Innovative Porous Nanocomposite Material for the Removal of Phenolic Compounds from Aqueous Solutions. *Nanomaterials* **2018**, *8*, 334. [CrossRef]

29. Singleton, V.L.; Orthofer, R.; Lamuela-Raventós, R.M. Analysis of total phenols and other oxidation substrates and antioxidants by means of folin-ciocalteu reagent. *Methods Enzymol.* **1999**, *299*, 152–178. [CrossRef]

30. Turco, A.; Malitesta, C.; Barillaro, G.; Greco, A.; Maffezzoli, A.; Mazzotta, E. A magnetic and highly reusable macroporous superhydrophobic/superoleophilic PDMS/MWNT nanocomposite for oil sorption from water. *J. Mater. Chem. A* **2015**, *3*, 17685–17696. [CrossRef]

31. Delor-Jestin, F.; Tomer, N.S.; Singh, R.P.; Lacoste, J. Durability of crosslinked polydimethylsyloxanes: The case of composite insulators. *Sci. Technol. Adv. Mater.* **2008**. [CrossRef] [PubMed]

32. Agnihotri, S.; Mota, J.P.B.; Rostam-Abadi, M.; Rood, M.J. Theoretical and experimental investigation of morphology and temperature effects on adsorption of organic vapors in single-walled carbon nanotubes. *J. Phys. Chem. B* **2006**, *110*, 7640–7647. [CrossRef] [PubMed]

33. Turco, A.; Primiceri, E.; Frigione, M.; Maruccio, G.; Malitesta, C. An innovative, fast and facile soft-template approach for the fabrication of porous PDMS for oil–water separation. *J. Mater. Chem. A* **2017**, *5*, 23785–23793. [CrossRef]

34. Turco, A.; Pennetta, A.; Caroli, A.; Mazzotta, E.; Monteduro, A.G.; Primiceri, E.; de Benedetto, G.; Malitesta, C. Easy fabrication of mussel inspired coated foam and its optimization for the facile removal of copper from aqueous solutions. *J. Colloid Interface Sci.* **2019**, *552*, 401–411. [CrossRef] [PubMed]

35. Lin, D.; Xing, B. Adsorption of phenolic compounds by carbon nanotubes: Role of aromaticity and substitution of hydroxyl groups. *Environ. Sci. Technol.* **2008**, *42*, 7254–7259. [CrossRef]

36. Daâssi, D.; Lozano-Sánchez, J.; Borrás-Linares, I.; Belbahri, L.; Woodward, S.; Zouari-Mechichi, H.; Mechichi, T.; Nasri, M.; Segura-Carretero, A. Olive oil mill wastewaters: Phenolic content characterization during degradation by *Coriolopsis gallica*. *Chemosphere* **2014**, *113*, 62–70. [CrossRef] [PubMed]

37. Achak, M.; Hafidi, A.; Mandi, L.; Ouazzani, N. Removal of phenolic compounds from olive mill wastewater by adsorption onto wheat bran. *Desalin. Water Treat.* **2014**, *52*, 2875–2885. [CrossRef]

38. Lin, K.; Pan, J.; Chen, Y.; Cheng, R.; Xu, X. Study the adsorption of phenol from aqueous solution on hydroxyapatite nanopowders. *J. Hazard. Mater.* **2009**, *161*, 231–240. [CrossRef]

39. Han, R.; Zou, W.; Li, H.; Li, Y.; Shi, J. Copper (II) and lead (II) removal from aqueous solution in fixed-bed columns by manganese oxide coated zeolite. *J. Hazard. Mater.* **2006**, *137*, 934–942. [CrossRef]

40. Ho, Y.S.; Chiang, C.C. Sorption studies of acid dye by mixed sorbents. *Adsorption* **2001**, *7*, 139–147. [CrossRef]

41. Freundlich, H.M. Over the adsorption in solution. *J. Physicochem.* **1906**, *57*, 385.

42. Langmuir, I. The constitution and fundamental properties of solids and liquids. Part I. Solids. *J. Am. Chem. Soc.* **1916**, *38*, 2221–2295. [CrossRef]

43. Stasinakis, A.S.; Elia, I.; Petalas, A.V.; Halvadakis, C.P. Removal of total phenols from olive-mill wastewater using an agricultural by-product, olive pomace. *J. Hazard. Mater.* **2008**, *160*, 408–413. [CrossRef] [PubMed]

44. Yangui, A.; Abderrabba, M. Towards a high yield recovery of polyphenols from olive mill wastewater on activated carbon coated with milk proteins: Experimental design and antioxidant activity. *Food Chem.* **2018**, *262*, 102–109. [CrossRef]

45. Senol, A.; Hasdemir, İ.M.; Hasdemir, B.; Kurdaş, İ. Adsorptive removal of biophenols from olive mill wastewaters (OMW) by activated carbon: Mass transfer, equilibrium and kinetic studies. *Asia-Pacific J. Chem. Eng.* **2017**, *12*, 128–146. [CrossRef]

46. Ghosal, P.S.; Gupta, A.K. Determination of thermodynamic parameters from Langmuir isotherm constant-revisited. *J. Mol. Liq.* **2017**, *225*, 137–146. [CrossRef]

47. Milonjić, S.K. A consideration of the correct calculation of thermodynamic parameters of adsorption. *J. Serb. Chem. Soc.* **2007**, *72*, 1363–1367. [CrossRef]

48. Lagergren, S. Zur theorie der sogenannten adsorption geloster stoffe, Kungliga Svenska Vetenskapsakademiens. *Handlingar* **1898**, *24*, 1–39.

49. Blanchard, G.; Maunaye, M.; Martin, G. Removal of heavy metals from waters by means of natural zeolites. *Water Res.* **1984**, *18*, 1501–1507. [CrossRef]

50. Cheng, C.S.; Deng, J.; Lei, B.; He, A.; Zhang, X.; Ma, L.; Li, S.; Zhao, C. Toward 3D graphene oxide gels-based adsorbents for high-efficient water treatment via the promotion of biopolymers. *J. Hazard. Mater.* **2013**, *263*, 467–478. [CrossRef]

51. Pham, X.-H.; Li, C.A.; Han, K.N.; Huynh-Nguyen, B.-C.; Le, T.-H.; Ko, E.; Kim, J.H.; Seong, G.H. Electrochemical detection of nitrite using urchin-like palladium nanostructures on carbon nanotube thin film electrodes. *Sens. Actuators B Chem.* **2014**, *193*, 815–822. [CrossRef]

Publisher's Note: MDPI stays neutral with regard to jurisdictional claims in published maps and institutional affiliations.

Adsorption of Mixed Dye System with Cetyltrimethylammonium Bromide Modified Sepiolite: Characterization, Performance, Kinetics and Thermodynamics

Jian Yu [1], Aiyi Zou [1], Wenting He [1] and Bin Liu [1,2,*]

[1] Department of Water Engineering and Science, College of Civil Engineering, Hunan University, Changsha 410082, China; yujian@hnu.edu.cn (J.Y.); zouaiyi@hhu.edu.cn (A.Z.); lgc@hnu.edu.cn (W.H.)

[2] Department of Chemical Engineering, Process Engineering for Sustainable Systems (ProcESS), KU Leuven, Celestijnenlaan 200F, B-3001 Leuven, Belgium

* Correspondence: ahxclb@163.com

Abstract: In this study, sepiolite was modified by calcination (200 °C) and cetyltrimethylammonium bromide (CTMAB) treatment. Though the specific surface area sharply declined, the adsorption amount of Acid Orange II (AO), Reactive Blue (RB), Acid Fuchsin (AR) and their mixed solution were improved. The morphology of modified sepiolite showed a better dispersibility and looser structure. The adsorption performance was highly impacted by the pH condition and adsorbent dosage. The electrostatic attraction of positively charged adsorption sites on the adsorbent surface and the negatively charged anionic dye could enhance the adsorption amount especially under acid condition. The order of preferentially adsorbed dye was AO > RB > AR. The adsorption process was much correlated to the quasi-second-order reaction kinetics. The adsorption amount and equilibrium amount of single dye system, as well as in the mixed system were in accordance with the Langmuir model and extended Langmuir isotherm.

1. Introduction

Synthetic dyes are common pollutants in industrial wastewater. They are stable, highly soluble and when enter in the water bodies present environmental hazards and potential threats to health [1]. Some of the azo dyes have been found to be carcinogenic, sensitizing and reproductive to humans; some of the triarylmethane dyes are also carcinogenic and have long-term adverse effects in the aquatic environment; some of the anthraquinone dyes are chemically stable and refractory to biodegradable [2–4]. Hence, Acid Orange II (azo dye), Reactive Blue (anthraquinone dye) and Acid Fuchsin (triarylmethane dye) were employed in this study to investigate the various kinds of dye.

The treatment methods for dye-bearing wastewater include physical methods, chemical methods and biological methods [5–11]. Among them, adsorption decolorization is the most effective method [12]. According to the different interaction forces between the adsorbate and the adsorbent, the adsorption can be divided into physical adsorption and chemical adsorption [13]. The physical adsorption is caused by the intermolecular force (Van der Waals force) [14]. Chemical adsorption was caused by the formation of chemical bonds or surface coordination compounds by adsorbate molecules and adsorbents by means of ion exchange, electron transfer and electron pair sharing [15,16].

Sepiolite is a hydrous magnesium silicate with a fibrous cross-section [17,18]. The merits of sepiolite were low thermal conductivity, high salt resistance, non-polluting, environmentally friendly [19]. It has

been widely used in various fields due to the special structural properties and low cost. In China, the sepiolite was presented with two types, hydrothermal type and clay type. The clay type is mainly distributed in Hunan province [17]. The water in sepiolite mainly exists with three forms, adsorbing water, coordinating water and hydroxyl water, in which the adsorption water enters the sepiolite pores, the coordinating water is mainly bound by Mg^{2+} and the hydroxyl water exists as OH group [20]. The structure of sepiolite was greatly impacted by the bound water, especially after heated [21]. The three forms of water are gradually lost and the structure of sepiolite will change differently at various temperatures. Serna et al found that the adsorbed water in the sepiolite pores was mainly lost and the specific surface area of the pores was increased at 25~250 °C, but the structure of the sepiolite is folded when the temperature was higher than 300 °C [22].

The adsorbent generally has the following characteristics, large specific surface area, suitable pore structure and surface structure, high adsorption capacity, no chemically react with the medium, good mechanical strength, etc. [19]. The sepiolite, a fibrous hydrous magnesium silicate, has been widely explored as an adsorbent by two reasons: suitable specific surface area; low price, only 20–30 dollars per ton in China. There are three kinds of adsorption active sites from sepiolite: oxygen atom in silicon tetrahedron, water molecules coordinated with magnesium ions, which can form hydrogen bonds with adsorbate and Si-OH combination, formed after the destruction of Si-O-Si.

In order to further improve the adsorption performance of sepiolite, modifications such as thermal acid treatment, surfactant organic and inorganic modifications have been employed [11]. Mahir Alkan et al found thermally modification at 200, the highest adsorption amount was obtained [23]. A wider temperature range of the sepiolite modification was reported by Jiquan Wang et al [24]. The surfactant modification also attracts researcher's attention. Bulent Armagan et al used an organic modification method of natural sepiolite with cetyltrimethylammonium bromide to investigate its adsorption property for anionic dyes (active black, reactive red, active yellow) [25].

In this study, to improve the adsorption property of sepiolite, a combination of heat and surfactant modification method was applied. To confirm the success of this combined method, unmodified and modified forms of sepiolite were characterized by BET, XRD, XPS, FT-IR and SEM. On the other hand, this study also focused on the adsorption performance and mechanism of mixed dye system with modified sepiolite since the kinetics and thermodynamics of two-component and three-component solution were much more complicated. Hence, the three dyes, Acid Orange II, Reactive Blue and Acid Fuchsin were employed as target adsorbate with single, two-component and three-component solution type.

2. Method and Material

2.1. Materials

In this study, the original sepiolite was obtained from Guangda sepiolite company (Hunan province, China). The three dyes, Acid Orange II (AO), Reactive Blue (RB) and Acid Fuchsin (AR) was purchased from Sigma company and the detail information can be found in previous work [26–28]. The Cetyltrimethylammonium bromide (CTMAB), with the formula of $C_{16}H_{33}(CH_3)_3NBr$, was purchased from Tianjin Bodi Chemical company. The chemical agents were all above analytical grade in this work. To compare the adsorption amount and specific surface area, commercial powder activated carbon (granularity of 180–220 μm) purchased from Xingyuan company (Hunan province, China) was utilized.

2.2. Preparation of Organically Modified Sepiolite

Before the modification process, the sepiolite was first settled and purified, then dried in an oven at 120 °C and sieved with a 100 mesh. The sepiolite was calcined under 200 °C for 2 h in a muffle. Then, the sepiolite was immersed into CTMAB-saturated solution for 8 h. To remove the CTMAB

solution, the modified sepiolite was repeatedly cleaned and settled. Finally, the modified sepiolite was placed into a 60 °C vacuum oven for 24 h.

2.3. Dye Concentration Determination and Adsorption Test

In this study, a multiple linear regression method was used to process the data. When the photometric system satisfied the linear sum of absorbance, the concentration of each component can be obtained by solving linear equations. Suppose dye wastewater contains dyes with *n* different absorbance components without mutual react. The sum of the absorbance of each single-component dye is the total absorbance of the mixed dye. It is measured at different wavelengths according to Beer-Lambert law. The absorbance of the mixed dye can be expressed by Equation (1).

$$
\begin{vmatrix} A_1 \\ A_2 \\ \dots \\ A_n \end{vmatrix} = \begin{vmatrix} k_{11}k_{12}\dots k_{1m} \\ k_{21}k_{22}\dots k_{2m} \\ \dots \\ k_{n1}k_{n2}\dots k_{nm} \end{vmatrix} \begin{vmatrix} C_1 \\ C_2 \\ \dots \\ C_m \end{vmatrix}
\tag{1}
$$

where A_i and a_i presents the absorbance at λ_i, k_{ij} was the absorption coefficient of the *j*th component at wavelength λ_i and C_i is the concentration of the *i*th component in the sample. To determine the concentration of individual dye, the mixed solution was scanned in the wavelength region of 594–474 nm; the results of dye concentration were calculated using MATLAB software.

A lab scale static adsorption experiment was utilized to investigate the adsorption performance of modified sepiolite with the dye system. A beaker with 300 mL target solution was employed in the experiment. The adsorption test was conducted with 2 g/L sepiolite and 200 mg/L dye solution for 240 min under pH value of 1, oscillation rate of 180 r/min and 25 °C. Considering the effect of pH and adsorbent dosage on adsorption performance, pH range from 1 to 9, dosage range from 0.5 to 5 g/L were utilized. For the mixed dye system, for instance, the RB+AO+AR represents mixed dye of 200 mg/L RB, 200 mg/L AO and 200 mg/L AR, the RB+AO represents mixed dye of 200 mg/L RB and 200 mg/L AO. AO (RB + AO + AR) means the concentration of AO in the three-component system.

After the determination of fixed dye, the decolorization percentage and adsorption amount were calculated by Equations (2) and (3).

$$
\eta = \frac{(C_0 - C_e)}{C_0} \times 100\%
\tag{2}
$$

$$
q = \frac{(C_0 - C_e)}{m} V
\tag{3}
$$

where η and q are the percentage of decolorization and adsorption amount of fixed dye, respectively, C_0 and C_e are the initial and final concentration of fixed dye, V is the dye solution volume and *m* is the weight of the sepiolite. In order to ensure the accuracy of the test data, each group of experiment was repeated at least 3 times.

2.4. Adsorption Kinetics and Thermodynamics

The kinetic characteristics of mixed dye removal with sepiolite adsorption were discussed by using the quasi-first-order and quasi-secondary kinetics models. The mathematical expressions of quasi-first-order and quasi-secondary kinetic models were listed in Equations (4) and (5), respectively [29].

quasi-first-order model

$$
\ln(q_e - q_t) = \ln q_e - k_1 t
\tag{4}
$$

quasi-secondary-order model

$$
(\frac{1}{q_t}) = \frac{1}{k_2 q_e^2} + \frac{1}{q_e} t
\tag{5}
$$

where q_e and q_t represent the amount of fixed dye adsorbed by the unit mass adsorbent after equilibrium and at the moment t, k_1 and k_2 represent the adsorption rate constant of the quasi-first-order reaction kinetic equation and the quasi-second-order reaction kinetic equation.

The thermodynamics characteristics of dye solution adsorption were discussed by Langmuir linear fitting model. The mathematical expression of the thermodynamics model was listed in Equation (6).

Langmuir linear fitting model

$$\frac{C_e}{q_e} = \frac{1}{q_{max}K_L} + \frac{C_e}{q_{max}} \tag{6}$$

where q_e is the balanced amount of adsorption, q_{max} is the saturated adsorption capacity of a single layer, c_e is the balanced mass concentration of the dye, K_L is the adsorption equilibrium constant in Langmuir linear fitting model.

In the two-component system, the Langmuir fitting model was transformed to Equations (7) and (8) [30,31]. Where the subscript 1 and 2 present component 1 and component 2 in the mixed system. In this extended Langmuir model, the $\frac{c_{e1}}{q_{e1}}$ shows linear correlation with c_{e1} and $\frac{q_{e2}c_{e1}}{q_{e1}}$.

$$\frac{C_{e1}}{q_{e1}} = \frac{1}{q_{max1}K_{L1}} + \frac{C_{e1}}{q_{max1}} + \frac{q_{e2}C_{e1}}{q_{e1}q_{max2}} \tag{7}$$

$$\frac{C_{e2}}{q_{e2}} = \frac{1}{q_{max2}K_{L2}} + \frac{C_{e2}}{q_{max2}} + \frac{q_{e1}C_{e2}}{q_{e1}q_{max2}} \tag{8}$$

In the three-component system, the Langmuir fitting model was transformed to Equations (9)–(11) [30,31]. Where the subscript 1, 2 and 3 present component 1, component 2 and component 3 in the mixed system. In this extended Langmuir model, the $\frac{C_{e1}}{q_{e1}}$ shows linear correlation with C_{e1}, $\frac{q_{e2}C_{e1}}{q_{e1}}$ and $\frac{q_{e3}C_{e1}}{q_{e1}}$.

$$\frac{C_{e1}}{q_{e1}} = \frac{1}{q_{max1}K_{L1}} + \frac{C_{e1}}{q_{max1}} + \frac{q_{e2}C_{e1}}{q_{e1}q_{max2}} + \frac{q_{e3}C_{e1}}{q_{e1}q_{max3}} \tag{9}$$

$$\frac{C_{e2}}{q_{e2}} = \frac{1}{q_{max2}K_{L2}} + \frac{C_{e2}}{q_{max2}} + \frac{q_{e1}C_{e2}}{q_{e2}q_{max1}} + \frac{q_{e3}C_{e2}}{q_{e2}q_{max3}} \tag{10}$$

$$\frac{C_{e3}}{q_{e3}} = \frac{1}{q_{max3}K_{L3}} + \frac{C_{e3}}{q_{max3}} + \frac{q_{e1}C_{e3}}{q_{e3}q_{max1}} + \frac{q_{e2}C_{e3}}{q_{e3}q_{max2}} \tag{11}$$

2.5. Characterization

A Brunner–Emmet–Teller (BET, QuadraSorb SI, Quantachrome, USA) was utilized for the measurement of specific surface area [32]. An X-ray diffraction spectrometer (D8-Advance, Burke, Germany) was employed for X-ray diffraction spectroscopy (XRD) test [33]. The tube pressure was 20 KV, the scanning range was 5–60° and the scanning speed was 0.02°/0.2 s [34]. A Fourier-transform infrared spectrometer (Spectrum One B, Perkin Elmer, USA) was used to detect the Fourier-transform infrared spectroscopy (FT-IR) [33]. A scanning electron microscopy (Quanta 200, FEI, Hillsboro, OR, USA) was employed to observe the feature of modified sepiolite [35].

3. Result and Discussion

3.1. Characterization of Modified Sepiolite

Figure 1a shows that the adsorption capacity of calcined sepiolite and modified sepiolite were much higher than that of sepiolite ore. The adsorption capacity obviously improved from 45.28 mg/g to 74.82 mg/g and 78.66 mg/g after calcination and CTMAB modification, respectively. The previous study had reported that the calcination process at a suitable temperature range could enhance the adsorption

amount of sepiolite, but the enhancement was undermined at too high temperature. Moreover organic modification could further improve the adsorption capacity.
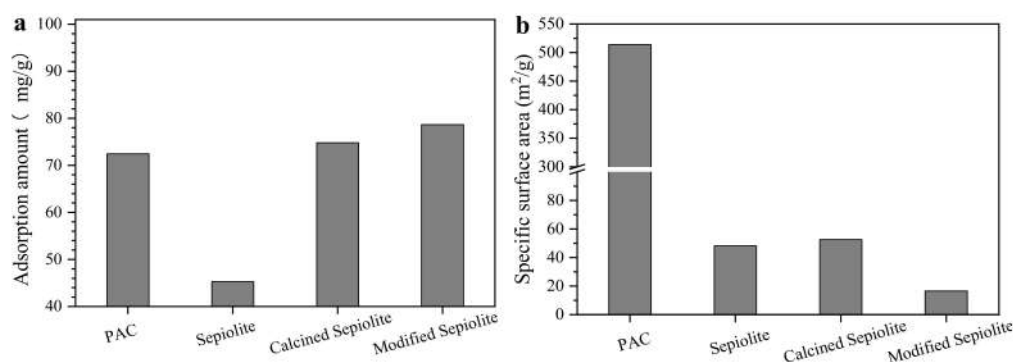

Figure 1. Comparison of Acid Orange II (AO) adsorption amount (**a**) and specific surface area (**b**) of different adsorbents.

Figure 1b shows that the specific surface area of calcined sepiolite was slightly increased, but significantly declined after surfactant modification. Though the specific surface area of CTMAB modified sepiolite highly decreased, the adsorption amount was nearly twice when compared to the sepiolite ore. The decrease of electrostatic repulsion of the adsorption site by CTMAB was the reason for adsorption enhancement. Another interesting point was the adsorption amount of organically modified sepiolite was comparable with the powdered activated carbon (PAC), but the specific surface area of PAC was forty times large than the modified sepiolite [36]. This suggests that the specific surface area was not in line with the adsorption capacity, the property of valid adsorption site was the key factor for adsorption performance.

Figure 2a shows that the characteristic dispersion peak of sepiolite at 2θ value of 9.4/9.44 was significantly strengthened after CTMAB modification and no significant changes occurred at other characteristic peak positions. On the other hand, the diffraction peak of the quartz also enhanced after the surfactant modification, which was different with previous report [34]. The d_{001} value of modified sepiolite was slightly increased to 0.9365 nm, which indicate that the CTMAB intercalated into the sepiolite.

The FT-IR spectrums of original sepiolite, modified sepiolite and modified sepiolite after adsorption saturated are shown in Figure 2b. The 3670 cm^{-1}, 3622 cm^{-1}, 3411 cm^{-1} and 1796 cm^{-1} peaks corresponding to the stretching vibration of O-H bond existed, which reflects the structure of the sepiolite itself. The peak at 3670 cm^{-1} is the stretching vibration of OH (belonging to Mg-OH) which coordinated by the Mg ion octahedron in the sepiolite pore channel. The peak at 3622 cm^{-1} is the crystal water with weak hydrogen bonding and peak at 3411 cm^{-1} is the stretching vibration of the hydroxyl group adsorbing water. The vibration at 1030 cm^{-1} is the stretching vibration of the Si-O group and the absorption band near 796 cm^{-1}, 669 cm^{-1} and 471 cm^{-1} belong to the bending expansion vibration of Si-O and Mg-O in the octahedron. When comparing the spectra of original sepiolite and modified sepiolite, the Si-O and Mg-O stretching vibration peaks of the organically modified sepiolite were enhanced and the peaks at 2920 cm^{-1}, 2856 cm^{-1} and 1420 cm^{-1} appeared [37]. The peaks at 2920 cm^{-1} and 2856 cm^{-1} were corresponding to the stretching vibration of CH_3 and CH_2 from CTMAB, while 1420 cm^{-1} represented the vibration of the C-N. This indicates that cetyltrimethylammonium bromide was electrostatically coated on the surface of sepiolite, which could change the surface of sepiolite from hydrophilic to lipophilic [38]. When comparing the spectra before and after adsorption, the characteristic peak (1500–1600 cm^{-1}) of AO appeared on the sepiolite after adsorption, which indicates the surface adsorption distribution occurs during the adsorption process. The XPS spectrum (Figure 2c) shows that the characteristic peaks of Mg and Si decreased while the characteristic peak of C enhanced after CTMAB modification.
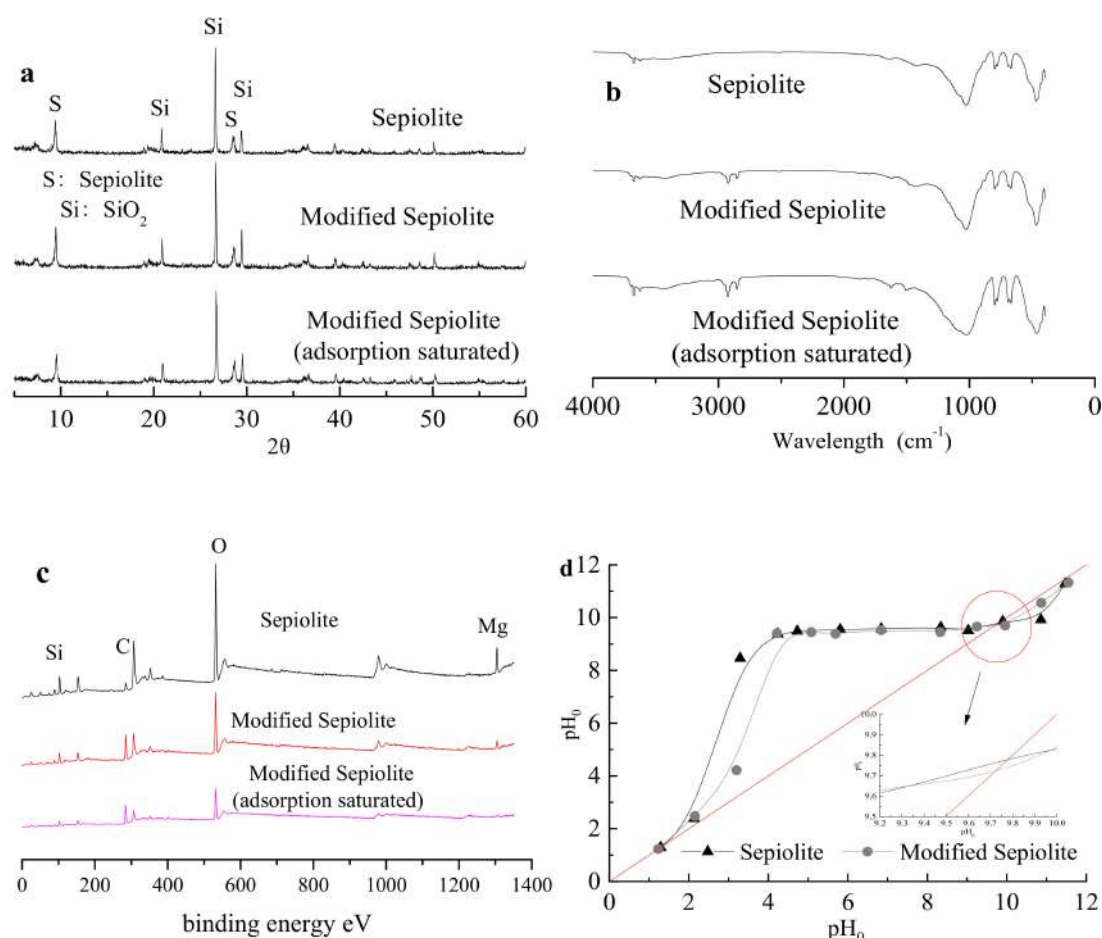
Figure 2. (**a**) X-ray diffraction spectrum of original sepiolite, modified sepiolite and modified sepiolite after adsorption saturated; (**b**) Fourier-transform infrared spectrum of original sepiolite, modified sepiolite and modified sepiolite after adsorption saturated; (**c**) X-ray photoelectron spectrum of original sepiolite, modified sepiolite and modified sepiolite after adsorption saturated; (**d**) Isoelectric point of original sepiolite and modified sepiolite.

The isoelectric point of the sepiolite before and after the modification was shown in Figure 2d. The isoelectric point changed from 9.62 to 9.87 after modification, which indicates that the isoelectric point value of the surface increased and the surface was positive charged. The isoelectric point is important when investigating the effect of pH on the adsorption effect. When the solution pH is lower than the isoelectric point, the surface of the adsorbent was positively charged. At lower pH condition, the surface of the sepiolite was combined with H^+ and the surface was positively charged, while at higher pH condition, the surface of the sepiolite was combined with OH^- and the surface was negatively charged.

$$M - OH + H^+ \rightarrow MOH_2{}^+$$

$$M - OH + OH^- \rightarrow MO^- H_2O$$
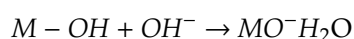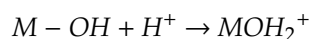
The morphology images confirm that the original crystal structure of the sepiolite was retained after the modification process. Better dispersibility and looser morphology were obtained after modification. The diameter of the fiber increased and the gap between the layered structure was cleaner and smoother (Figure 3a,b).
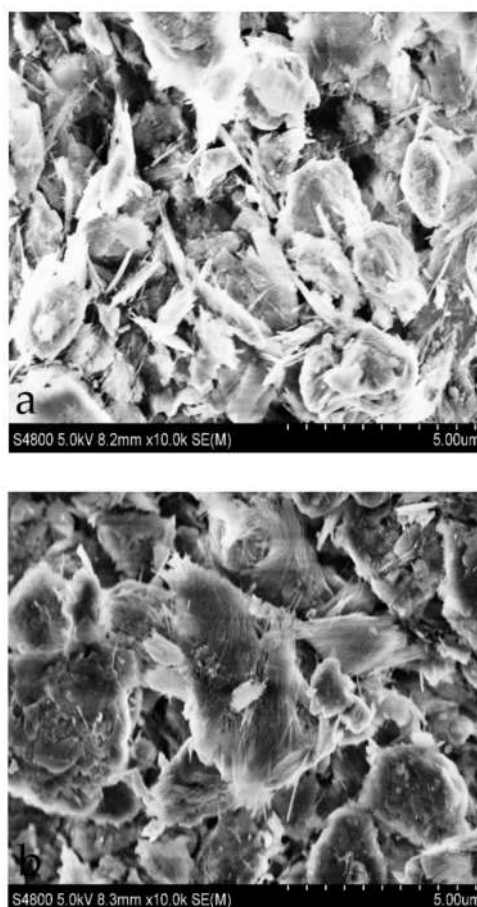
Figure 3. SEM image of original sepiolite (**a**) and modified sepiolite (**b**).

3.2. Effect of the Operation Condition on Adsorption Performance

It can be seen from Figure 4a that the removal efficiency of AO and AR by modified sepiolite declined with the increase of pH, which probably because the anionic dye is more protonated under acidic condition [23]. The negatively charged anionic dye could attracted on the positively charged adsorption sites by electrostatic attraction [39]. When OH⁻ increased, the anionic dye and OH⁻ had competitive adsorption [40]. That is also in accordance with the result from Figure 2. In the two-component and three-component mixed solution, the removal efficiency of each dye was basically as same as that of single dye system. The decolorization efficiency of the single component dye in the multi-component system was lower than that of the single dye system. The reduction degree of removal efficiency was AR > AO > RB. For instance, the removal efficiency of AR in a single dye system was 96.5%, while reduced to less than 30% in the meta-mixing system and the three-component mixed system.

It can be seen from Figure 4c,d that the removal efficiency of each dye was basically the same during the fixed adsorption condition in single dye system. When the dosage was 3 g/L, the removal efficiency of the three dyes were all 100%. In the mixed dye system, the decolorization behavior of the three dyes was distinct compared to the single dye system. When the dosage of adsorbent was 2 g/L, the decolorization efficiency of AO, RB and AR decreased from 97.48%, 94.49% and 93.6% in the single dye system, to 40.09%, 40.62%, and 15.36% in the three-component system. The decolorization efficiency of AR was rapidly decreased compared with the RB and AO. In the three-component system, when the dosage was lower than 2 g/L, the decolorization efficiency of AO and RB was maintained at the same level and much higher than AR. While the removal efficiency of AO and AR increased rapidly when increasing the adsorbent dosage. This indicates that the AO and RB were preferentially adsorbed.

Moreover, the AO was preferentially adsorbed in the two-component system of AO and RB. The above results indicate that AO had the characteristics of preferential adsorption in the two-component system.
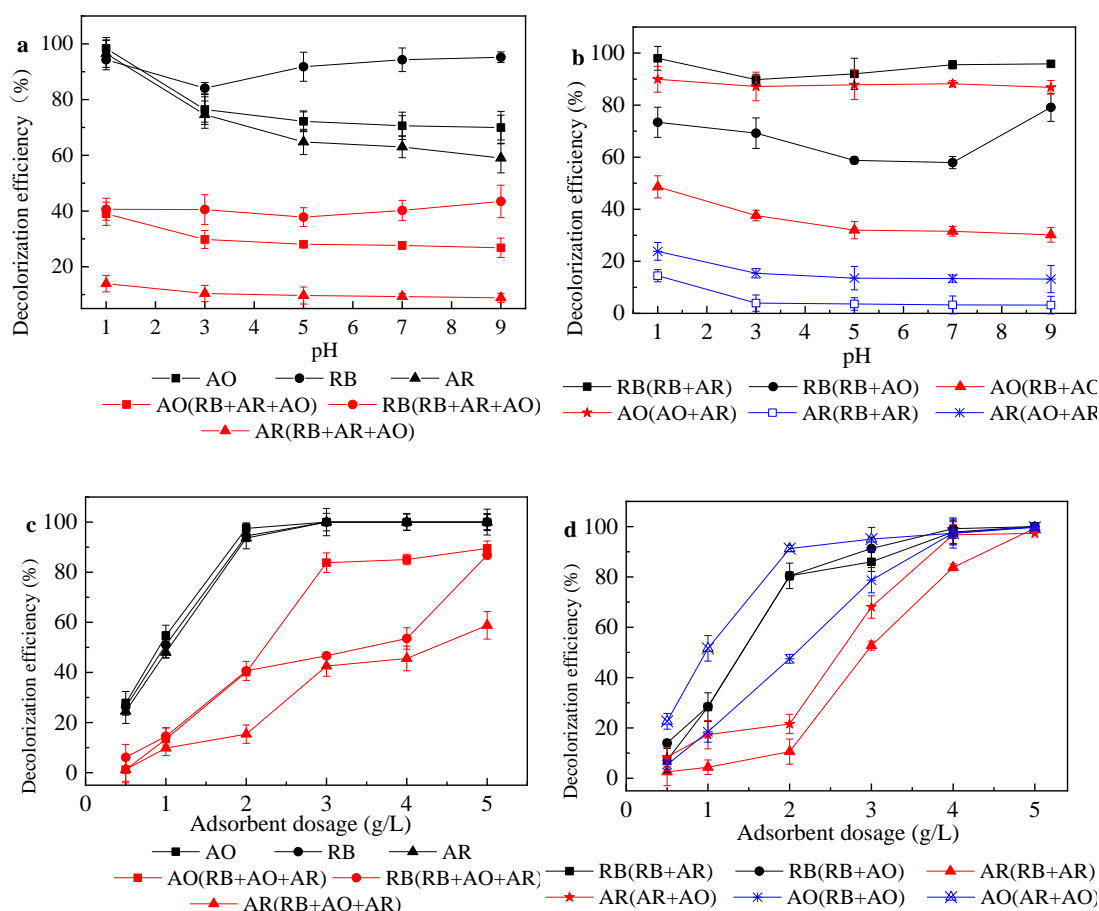

Figure 4. Effect of pH and adsorbent dosage on the Acid Orange II (AO), Reactive Blue (RB) and Acid Red (AR) adsorption performance. In (**a**) and (**b**), the adsorption test was conducted with 2 g/L modified sepiolite; In (**c**) and (**d**), the adsorption test was conducted under initial pH value of 1.

3.3. Adsorption Kinetics and Thermodynamics

Figure 5a is the kinetic process of the one-component and three-component mixed system. In the single dye system, the adsorption of dyes by the organic modified sepiolite reached equilibrium at 120 min; the adsorption amount of the single dye is sorted as: AO > RB > AR. In the three-component system, the adsorption reaction was also quickly balanced. The rapid reaction of dye and adsorbent may be due to the fact that the total concentration of the anionic dye in the three-component system was larger than the one-component system. On the other hand, the adsorption amount of the three anionic dyes in the three-component mixed system was reduced. Figure 5b is the kinetic curve of the two-component mixed system; the adsorption also reached equilibrium in a short time. The AR appears desorption in the mixed system, which may because the decrease of the valid sites of the adsorbent after the adsorption reached saturation, while the RB and AO had a competitive advantage and the "substitution effect" occurred [23]. That is, the RB and AO replaced AR from the adsorption site during competitive adsorption.

Since the adsorption kinetics is very fast, most of the experimental data points belong to the steady state, which may skew the mathematical modelling of the adsorption dynamics. It can be seen from Figure 6 that the correlation of the quasi-second-order reaction kinetics fitting was much better than the first-order reaction kinetics fitting; the data in Table 1 also verified. The coefficient of determination of quasi-second-order fitting was between 0.97–0.99, while the coefficient of determination of the

quasi-first-order reaction kinetics was lower than 0.85. The adsorption amount is also consistent with the rate constant, which indicates that the rate constant may have a certain relationship with the adsorption amount. The adsorption rate of the single dye was sorted as AO > RB > AR.
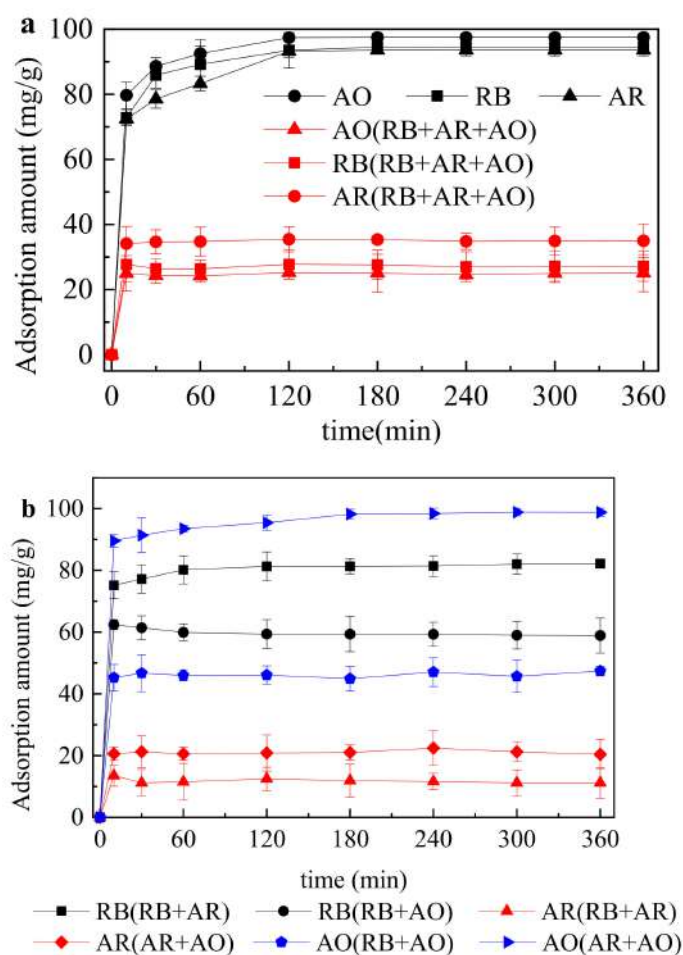

Figure 5. Effect of adsorption duration on the Acid Orange II (AO), Reactive Blue (RB) and Acid Red (AR) adsorption performance. (**a**) one component and three component system; (**b**) two component system.
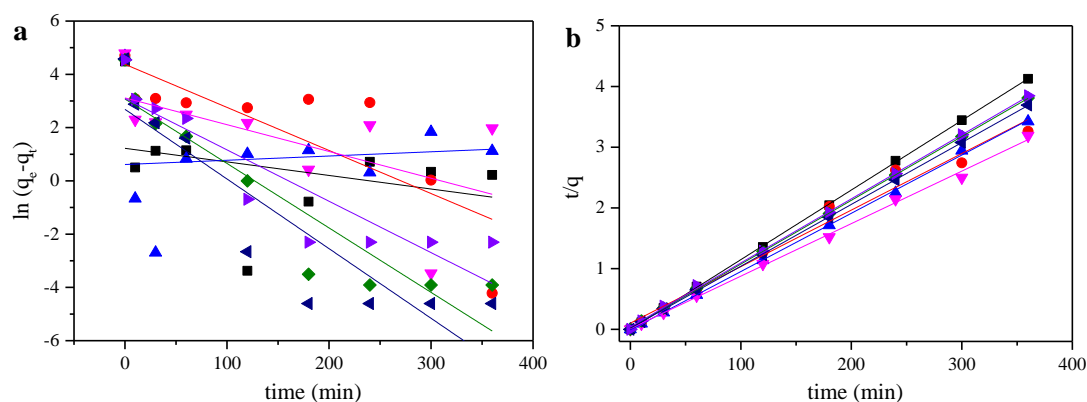

Figure 6. (**a**) fitting of experimental data with quasi-first-order reaction kinetics; (**b**) fitting of experimental data with the quasi-second-order model. The adsorption test was conducted with 2 g/L modified sepiolite and 200 mg/L dye solution for 240 min under oscillation rate of 180 r/min and 25 °C.

Table 1. The adsorption kinetics model with various dyes, the adsorption test was conducted with 200 mg/L Acid Orange II and 2 g/L modified sepiolite under oscillation rate of 180 r/min and initial pH value of 1.

Solution	Quasi-First-Order Reaction Kinetics Model			Quasi-Secondary Reaction Kinetics Model		
	q_{1e} (mg/g)	k_1 (1/min)	R_1^2	$q2_e$ (mg/g)	k_2 (1/min)	R_1^2
RB	21.62	2.42×10^{-2}	0.85	95.24	4.53×10^{-3}	0.99
AO	14.65	2.61×10^{-2}	0.79	98.14	5.36×10^{-3}	0.99
AR	22.01	1.93×10^{-2}	0.80	94.70	2.91×10^{-3}	0.99
RB + AR	79.46	1.61×10^{-2}	0.61	107.30	8.6×10^{-2}	0.97
RB + AO	1.84	1.59×10^{-3}	0.23	104.17	1.10×10^{-2}	0.99
AO + AR	22.53	1.00×10^{-2}	0.28	115.61	7.09×10^{-2}	0.99
RB + AO + AR	3.39	5.09×10^{-3}	0.56	87.18	1.42×10^{-1}	0.99

Figure 7 shows the adsorption isotherms of three anionic dyes in single dye systems, two-component and three-component mixed system. In the single dye system, the amount of adsorption increased rapidly as the initial concentration increased until reached saturation and equilibrates. According to the shape of the adsorption isotherm, it is preliminarily determined that the adsorption of the single dye conforms to the Langmuir model; the adsorption of the dye on the sepiolite is single layer adsorption. In the two-component and three-component system, the adsorption isotherm of each dye is not followed a regular Langmuir model [24]. For example, in the three-component mixed system, the adsorption amount of AR and RB decreased with the increase of initial concentration. This trend mainly because of the competitive effect in the adsorption process.
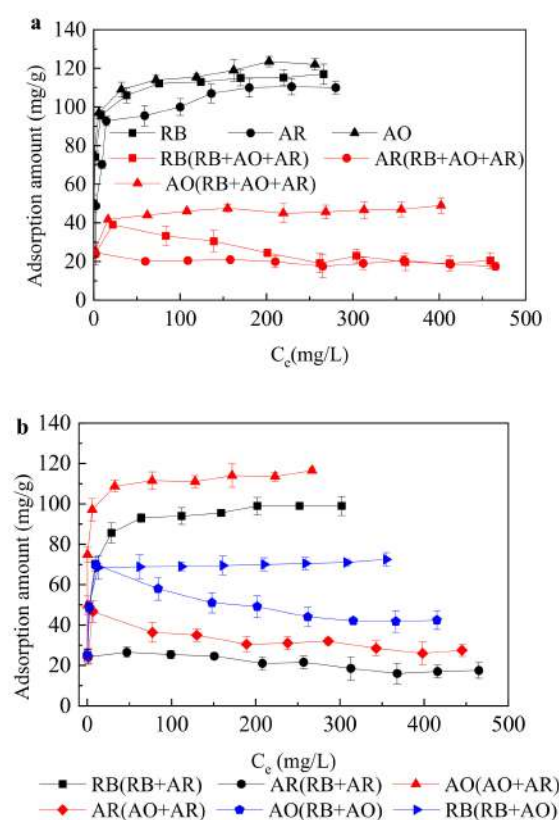

Figure 7. Adsorption isotherm with various dyes. To ensure the adsorbed saturation, the adsorption test was conducted at least 4 h at a certain temperature in a constant temperature oscillating box. (**a**) one component and three component system; (**b**) two component system.

Though Langmuir, Freundlich linear fitting model and intraparticle diffusion are the means to discuss the adsorption isotherm, previous work provided that monolayer adsorption was the main adsorption mechanism during and mixed dye adsorption process [30,31]. Hence, the extended Langmuir model was utilized in this study. As can be seen from Table 2, the saturated adsorption capacities of AO, RB and AR were 119 mg/g, 115 mg/g and 110 mg/g, respectively. The adsorption amount of sepiolite to each dye in the mixed system was lower than that from the single system. For instance, when the AO was mixed with RB or AR, its adsorption capacity decreased by 41.2% and 2.1%, and decreased by 58.8% in the three-component mixed system. In the two-component mixed system, the presence of AR had little effect on the adsorption amount of other dyes, and the amount of adsorption itself was minimized in the competitive adsorption process. The decrease of adsorption capacity in the mixed system may have the following factors: the interaction force between the dye solutions, the change of the surface charge of the adsorbent during the adsorption process, the competition of the dye on the active adsorption sites. The adsorption amount and equilibrium amount of single dye system, as well as in the mixed system, were in accordance with the Langmuir model; the coefficient of determination were all over 0.99.

Table 2. Langmuir model fitting results of modified sepiolite adsorption.

Solution	Langmuir Model		
	q_{max} (mg/g)	K_L (L/mg)	R_1^2
RB	115.0	0.32	0.99
AO	119.0	0.50	0.99
AR	110.0	0.16	0.99
RB + AR	129.9	0.34	0.99
RB in RB + AR	107.5	0.86	0.99
AR in RB + AR	26.5	0.28	0.99
RB + AO	134.9	1.55	0.99
RB in RB + AO	72.5	2.19	0.99
AO in RB + AO	69.9	1.99	0.99
AO + AR	144.9	1.00	0.99
AO in AO + AR	116.5	3.73	0.99
AR in AO + AR	46.7	3.70	0.99
RB + AO + AR	96.2	1.85	0.99
RB in RB + AO + AR	39.0	0.05	0.99
AO in RB + AO + AR	49.0	0.17	0.99
AR in RB + AO + AR	22.7	0.04	0.99

4. Conclusions

In this study, the sepiolite was modified by a two-step method, heat and surfactant modification. The adsorbent was characterized by BET, X-ray diffraction spectroscopy, Fourier-transform infrared spectroscopy and SEM methods. Then the impact of pH and adsorbent dosage on the one-component, two-component and three-component dye system were comprehensively investigated. At last, the kinetics and thermodynamics analysis were studied. The conclusions were listed as follow:

1. The adsorption amounts of Acid Orange II, Reactive Blue and Acid Fuchsin improved after CTMAB modification process, which confirmed the applicability of the modified sepiolite in industrial dye wastewater treatment.
2. The specific surface area of modified sepiolite was obviously decreased, but the adsorption capacity was enhanced. The SEM image shows that the modified sepiolite has a dispersible morphology and the gaps were clean and smooth. The characterization indicate the modification does not deform the sepiolite structure and the CTMAB was successfully loaded.
3. Acid Orange II had the characteristics of preferential adsorption in the two-component system. The electrostatic attraction of positively charged adsorption sites on the adsorbent surface with the negatively charged anionic dye could enhance the adsorption amount under acid condition.

4. The adsorption performance of one-component, two-component and three-component dye system was in accordance with the quasi-second-order reaction kinetics and the adsorption equilibrium time was all around 120 min.

5. The adsorption equilibrium were fitted very well to the Langmuir model and extended Langmuir isotherm.

Conflicts of Interest: The authors declare no conflict of interest.

References

1. Kolmakov, K.; Hebisch, E.; Wolfram, T.; Nordwig, L.A.; Wurm, C.A.; Ta, H.; Westphal, V.; Belov, V.N.; Hell, S.W. Far-Red Emitting Fluorescent Dyes for Optical Nanoscopy: Fluorinated Silicon-Rhodamines (SiRF Dyes) and Phosphorylated Oxazines. *Chem. A Eur. J.* **2015**, *21*, 13344–13356. [CrossRef]

2. Singh, R.L.; Singh, P.K.; Singh, R.P. Enzymatic decolorization and degradation of azo dyes–A review. *Int. Biodeterior. Biodegrad.* **2015**, *104*, 21–31. [CrossRef]

3. Oladipo, A.A.; Gazi, M.; Yilmaz, E. Single and binary adsorption of azo and anthraquinone dyes by chitosan-based hydrogel: Selectivity factor and Box-Behnken process design. *Chem. Eng. Res. Des.* **2015**, *104*, 264–279. [CrossRef]

4. Baptista, M.S.; Indig, G.L. Effect of BSA Binding on Photophysical and Photochemical Properties of Triarylmethane Dyes. *J. Phys. Chem. B* **1998**, *102*, 4678–4688. [CrossRef]

5. Robinson, T.; McMullan, G.; Marchant, R.; Nigam, P.; McMullan, G. Remediation of dyes in textile effluent: A critical review on current treatment technologies with a proposed alternative. *Bioresour. Technol.* **2001**, *77*, 247–255. [CrossRef]

6. Ghoreishi, S.; Haghighi, R. Chemical catalytic reaction and biological oxidation for treatment of non-biodegradable textile effluent. *Chem. Eng. J.* **2003**, *95*, 163–169. [CrossRef]

7. Demirbas, A. Agricultural based activated carbons for the removal of dyes from aqueous solutions: A review. *J. Hazard. Mater.* **2009**, *167*, 1–9. [CrossRef] [PubMed]

8. Shao, S.; Fu, W.; Li, X.; Shi, D.; Jiang, Y.; Li, J.; Gong, T.; Li, X. Membrane fouling by the aggregations formed from oppositely charged organic foulants. *Water Res.* **2019**, *159*, 95–101. [CrossRef] [PubMed]

9. Yu, J.; Zhang, D.; Ren, W.; Liu, B. Transport of Enterococcus faecalis in granular activated carbon column: Potential energy, migration, and release. *Colloids Surf. B Biointerfaces* **2019**, *183*, 110415. [CrossRef] [PubMed]

10. Li, G.; Zhou, S.; Shi, Z.; Meng, X.; Li, L.; Liu, B. Electrochemical degradation of ciprofloxacin on BDD anode using a differential column batch reactor: Mechanisms, kinetics and pathways. *Environ. Sci. Pollut. Res.* **2019**, *26*, 17740–17750. [CrossRef] [PubMed]

11. Li, G.; Liu, B.; Bai, L.; Shi, Z.; Tang, X.; Wang, J.; Liang, H.; Zhang, Y.; Van Der Bruggen, B. Improving the performance of loose nanofiltration membranes by poly-dopamine/zwitterionic polymer coating with hydroxyl radical activation. *Sep. Purif. Technol.* **2020**, *238*, 116412. [CrossRef]

12. Garg, V.; Gupta, R.; Yadav, A.B.; Kumar, R. Dye removal from aqueous solution by adsorption on treated sawdust. *Bioresour. Technol.* **2003**, *89*, 121–124. [CrossRef]

13. Abbas, A.; Al-Amer, A.M.; Laoui, T.; Al-Marri, M.J.; Nasser, M.S.; Khraisheh, M.; Atieh, M. Heavy metal removal from aqueous solution by advanced carbon nanotubes: Critical review of adsorption applications. *Sep. Purif. Technol.* **2016**, *157*, 141–161.

14. Tillotson, M.J.; Brett, P.; Bennett, R.; Grau-Crespo, R. Adsorption of organic molecules at the TiO2(110) surface: The effect of van der Waals interactions. *Surf. Sci.* **2015**, *632*, 142–153. [CrossRef]

15. Song, J.; Xu, T.; Gordin, M.L.; Wang, D. Nitrogen-Doped Mesoporous Carbon Promoted Chemical Adsorption of Sulfur and Fabrication of High-Areal-Capacity Sulfur Cathode with Exceptional Cycling Stability for Lithium-Sulfur Batteries. *Adv. Funct. Mater.* **2014**, *24*, 1243–1250. [CrossRef]

16. Grassi, M.; Rizzo, L.; Farina, A. Endocrine disruptors compounds, pharmaceuticals and personal care products in urban wastewater: Implications for agricultural reuse and their removal by adsorption process. *Environ. Sci. Pollut. Res.* **2013**, *20*, 3616–3628. [CrossRef]

17. Wang, Z.; Liao, L.; Hursthouse, A.S.; Song, N.; Ren, B. Sepiolite-Based Adsorbents for the Removal of Potentially Toxic Elements from Water: A Strategic Review for the Case of Environmental Contamination in Hunan, China. *Int. J. Environ. Res. Public Health* **2018**, *15*, 1653. [CrossRef]

18. Fayazi, M.; Afzali, D.; Ghanei-Motlagh, R.; Iraji, A. Synthesis of novel sepiolite-iron oxide-manganese dioxide nanocomposite and application for lead(II) removal from aqueous solutions. *Environ. Sci. Pollut. Res.* **2019**, *26*, 18893–18903. [CrossRef]

19. Zaini, N.A.M.; Ismail, H.; Rusli, A. Short Review on Sepiolite-Filled Polymer Nanocomposites. *Polym. Plast. Technol. Eng.* **2017**, *56*, 1665–1679. [CrossRef]

20. Kara, M.; Yuzer, H.; Sabah, E.; Çelik, M.S. Adsorption of cobalt from aqueous solutions onto sepiolite. *Water Res.* **2003**, *37*, 224–232. [CrossRef]

21. Chen, Q.; Zhu, R.; Liu, S.; Wu, D.; Fu, H.; Zhu, J.; He, H. Self-templating synthesis of silicon nanorods from natural sepiolite for high-performance lithium-ion battery anodes. *J. Mater. Chem. A* **2018**, *6*, 6356–6362. [CrossRef]

22. Serna, C.; Vanscoyoc, G. Infrared study of sepiolite and palygorskite surfaces. In *Developments in Sedimentology*; Elsevier: Amsterdam, The Netherlands, 1979; pp. 197–206.

23. Alkan, M.; Demirbas, O.; Çelikçapa, S.; Doğan, M. Sorption of acid red 57 from aqueous solution onto sepiolite. *J. Hazard. Mater.* **2004**, *116*, 135–145. [CrossRef] [PubMed]

24. Wang, J.; Wang, D.; Zhang, G.; Guo, Y.; Liu, J. Adsorption of rhodamine B from aqueous solution onto heat-activated sepiolite. *Wuhan Univ. J. Nat. Sci.* **2013**, *18*, 219–225. [CrossRef]

25. Armağan, B.; Ozdemir, O.; Turan, M.; Celik, M.S. Adsorption of Negatively Charged Azo Dyes onto Surfactant-Modified Sepiolite. *J. Environ. Eng.* **2003**, *129*, 709–715. [CrossRef]

26. Yu, J.; He, W.; Liu, B. Adsorption of Acid Orange II with Two Step Modified Sepiolite: Optimization, Adsorption Performance, Kinetics, Thermodynamics and Regeneration. *Int. J. Environ. Res. Public Health* **2020**, *17*, 1732. [CrossRef]

27. Zhang, L.; Zhou, X.; Guo, X.; Song, X.; Liu, X. Investigation on the degradation of acid fuchsin induced oxidation by MgFe2O4 under microwave irradiation. *J. Mol. Catal. A Chem.* **2011**, *335*, 31–37. [CrossRef]

28. Özcan, A.; Ömeroğlu, Ç.; Erdoğan, Y.; Özcan, A.S. Modification of bentonite with a cationic surfactant: An adsorption study of textile dye Reactive Blue 19. *J. Hazard. Mater.* **2007**, *140*, 173–179. [CrossRef]

29. Yang, X.; Yi, H.; Tang, X.; Zhao, S.; Yang, Z.; Ma, Y.; Feng, T.; Cui, X. Behaviors and kinetics of toluene adsorption-desorption on activated carbons with varying pore structure. *J. Environ. Sci.* **2018**, *67*, 104–114. [CrossRef]

30. Kurniawan, A.; Sutiono, H.; Indraswati, N.; Ismadji, S. Removal of basic dyes in binary system by adsorption using rarasaponin–bentonite: Revisited of extended Langmuir model. *Chem. Eng. J.* **2012**, *189–190*, 264–274. [CrossRef]

31. Zhang, Y.-Z.; Li, J.; Zhao, J.; Bian, W.; Li, Y.; Wang, X.-J. Adsorption behavior of modified Iron stick yam skin with Polyethyleneimine as a potential biosorbent for the removal of anionic dyes in single and ternary systems at low temperature. *Bioresour. Technol.* **2016**, *222*, 285–293. [CrossRef]

32. Oliveira, L.C.; Petkowicz, D.I.; Smaniotto, A.; Pergher, S. Magnetic zeolites: A new adsorbent for removal of metallic contaminants from water. *Water Res.* **2004**, *38*, 3699–3704. [CrossRef] [PubMed]

33. Nayak, P.S.; Singh, B.K. Instrumental characterization of clay by XRF, XRD and FTIR. *Bull. Mater. Sci.* **2007**, *30*, 235–238. [CrossRef]

34. Yu, J.; Zhang, L.; Liu, B. Adsorption of Malachite Green with Sodium Dodecylbenzene Sulfonate Modified Sepiolite: Characterization, Adsorption Performance and Regeneration. *Int. J. Environ. Res. Public Health* **2019**, *16*, 3297. [CrossRef] [PubMed]

35. Liu, B.; Qu, F.; Yu, H.; Tian, J.; Chen, W.; Liang, H.; Li, G.; Van Der Bruggen, B. Membrane Fouling and Rejection of Organics during Algae-Laden Water Treatment Using Ultrafiltration: A Comparison between in Situ Pretreatment with Fe(II)/Persulfate and Ozone. *Environ. Sci. Technol.* **2018**, *52*, 765–774. [CrossRef]

36. Shao, S.; Liang, H.; Qu, F.; Li, K.; Chang, H.; Yu, H.; Li, G. Combined influence by humic acid (HA) and powdered activated carbon (PAC) particles on ultrafiltration membrane fouling. *J. Membr. Sci.* **2016**, *500*, 99–105. [CrossRef]

37. Tunç, S.; Duman, O.; Çetinkaya, A. Electrokinetic and rheological properties of sepiolite suspensions in the presence of hexadecyltrimethylammonium bromide. *Colloids Surf. A Physicochem. Eng. Asp.* **2011**, *377*, 123–129. [CrossRef]

38. Yan, L.; Qin, L.-L.; Yu, H.-Q.; Li, S.; Shan, R.-R.; Du, B. Adsorption of acid dyes from aqueous solution by CTMAB modified bentonite: Kinetic and isotherm modeling. *J. Mol. Liq.* **2015**, *211*, 1074–1081. [CrossRef]

39. Habish, A.J.; Lazarević, S.; Janković-Častvan, I.; Jokić, B.; Kovač, J.; Rogan, J.; Janaćković, Đ.; Petrović, R. Nanoscale zerovalent iron (nZVI) supported by natural and acid-activated sepiolites: The effect of the nZVI/support ratio on the composite properties and Cd^{2+} adsorption. *Environ. Sci. Pollut. Res.* **2016**, *24*, 628–643. [CrossRef]

40. Dashamiri, S.; Ghaedi, M.; Asfaram, A.; Zare, F.; Wang, S. Multi-response optimization of ultrasound assisted competitive adsorption of dyes onto Cu (OH)2-nanoparticle loaded activated carbon: Central composite design. *Ultrason. Sonochem.* **2017**, *34*, 343–353. [CrossRef]

Adsorption of Methylene Blue in Water onto Activated Carbon by Surfactant Modification

Yu Kuang [1] **, Xiaoping Zhang** [1,2,3,4,]* **and Shaoqi Zhou** [1]

[1] School of Environment & Energy, Guangzhou Higher Education Mega Centre, South China University of Technology, Guangzhou 510006, China; eskuangyu@mail.scut.edu.cn (Y.K.); fesqzhou@yeah.net (S.Z.)

[2] The Key Laboratory of Pollution Control and Ecosystem Restoration in Industry Clusters of Ministry of Education, Guangzhou 510006, China

[3] Guangdong Environmental Protection Key Laboratory of Solid Waste Treatment and Recycling, Guangzhou 510006, China

[4] Guangdong Provincial Engineering and Technology Research Center for Environmental Risk Prevention and Emergency Disposal, Guangzhou 510006, China

* Correspondence: xpzhang@scut.edu.cn; Tel.: +86-1367-892-0429

Abstract: In this paper, the enhanced adsorption of methylene blue (MB) dye ion on the activated carbon (AC) modified by three surfactants in aqueous solution was researched. Anionic surfactants—sodium lauryl sulfate (SLS) and sodium dodecyl sulfonate (SDS)—and cationic surfactant—hexadecyl trimethyl ammonium bromide (CTAB)—were used for the modification of AC. This work showed that the adsorption performance of cationic dye by activated carbon modified by anionic surfactants (SLS) was significantly improved, whereas the adsorption performance of cationic dye by activated carbon modified by cationic surfactant (CTAB) was reduced. In addition, the effects of initial MB concentration, AC dosage, pH, reaction time, temperature, real water samples, and additive salts on the adsorption were studied. When Na^+, K^+, Ca^{2+}, NH^{4+}, and Mg^{2+} were present in the MB dye solution, the effect of these cations was negligible on the adsorption (<5%). The presence of NO^{2-} improved the adsorption performance significantly, whereas the removal rate of MB was reduced in the presence of competitive cation (Fe^{2+}). It was found that the isotherm data had a good correlation with the Langmuir isotherm through analyzing the experimental data by various models. The dynamics of adsorption were better described by the pseudo-second-order model and the adsorption process was endothermic and spontaneous. The results showed that AC modified by anionic surfactant was effective for the adsorption of MB dye in both modeling water and real water.

Keywords: activated carbon; modification; surfactant; adsorption; methylene blue; ions effect

1. Introduction

As a cationic dye, methylene blue ($C_{16}H_{18}ClN_3S$, MB) is widely used in chemical indicators, dyes and biological dyes. A large amount of organic dye wastewater is produced in the processes of the printing and dyeing industries. The dye wastewater has characteristics such as large discharge, high chromaticity, high organic matter concentration, and poor biodegradability, and greatly affects the water body health and the photosynthesis of microorganisms in the water environment [1,2].

At present, many researchers have used different methods to treat the dye wastewater [3]. Typical treatment methods include physical, chemical, and biological methods, such as flocculation [4], membrane filtration [5,6], advanced oxidation [7], ozonation, photocatalytic degradation [8], and biodegradation. These traditional methods have inherent limitations [9] such as the complex and uneconomical of nature of the technology, and thus it is necessary to seek efficient and simple dye wastewater treatment methods [10].

Compared with other treatment methods, the adsorption method is considered as prevailing over other dye wastewater treatment technology due to its advantages such as high efficiency, low cost, simple operation, and insensitive of toxic substances [11]. Activated carbon is the most commonly used adsorbent, and is widely used to remove the organic and inorganic pollutants in water phase.

Adsorption capacity is an important index to evaluate the adsorption effect of adsorbent. Various low-cost alternative adsorbents from agricultural solid waste, industrial solid waste, agricultural by-products, and biomass are used in wastewater treatment. For example, clay [12], sludge [13], montmorillonite [14], flax fiber [15], zeolite [16,17], and biochar (rice husk [18,19], pinewood [20], wheat [21], sugarcane bagasse [22], switchgrass [23], *Ficus carica* bast [24]) as adsorbents have been used for adsorption treatment of dye wastewater. However, common activated carbon is not widely used to adsorb and remove pollutants due to its low adsorption capacity, which is caused by small specific surface area and poor adsorption selection performance, as well as limitations of the surface functional groups and electrochemical properties.

In many cases, it is required to modify activated carbon surface to enhance its affinity with target pollutants and increase its adsorption capacity and improve the removal effect of pollutants in different types of industrial wastewater. The methods used to modify activated carbon include physical, chemical, and biological methods. As a chemical modification technology of activated carbon, surfactant modification shows great significance. Surfactant modification for activated carbon can improve the hydrophilicity and the dispersion of activated carbon in water due to an increase in the affinity between activated carbon and water and the decrease of the attractive energy between particles. Surfactant has the advantages of low cost [25] and less damage to the structure of activated carbon. Moreover, the surfactant can change the surface charge characteristics of activated carbon and provide more ionic adsorption sites for pollutants, which can not only enhance the adsorption capacity of ionic pollutants on activated carbon [26], but also can promote selective adsorption.

In wastewater treatment, activated carbon modified by surfactant is used as an adsorbent to remove various pollutants, including organic pollutants [26,27], reactive dyes [15,21,28,29], and heavy metals [30,31]. Surfactants are classified into anionic, cationic, non-ionic, and amphoteric ions according to the type and performance of the hydrophilic group [22]. Sodium lauryl sulfate (SLS) is a nontoxic anionic surfactant. Much research into the effect on inorganic metal ions by activated carbon modified by surfactant has been reported, however, the study of organic dyes adsorption by SLS-C has been rarely reported.

Previous research has shown that activated carbon modified by different surfactants have different effects on various water quality dye wastewater. Therefore, it is necessary to determine how the coexistence of other ions would affect the adsorption. Meanwhile, more information is still required in order to better understand of the adsorption behavior of methylene blue cationic dyes on modified-activated carbon.

The feasibility of removing MB from aqueous solution by surfactant-modified activated carbon was investigated. The purposes of the study were to (1) confirm the adsorption rate and capacity through the adsorption models; (2) determine the various parameters that affect sorption, such as initial dye concentration, temperature, pH, adsorbent dose, and additive salts; and (3) obtain the adsorption effect of adsorbent in actual water samples.

2. Materials and Methods

2.1. Materials

Methylene blue (Figure 1, $C_{16}H_{18}ClN_3S$) was used as adsorbent. The molar mass of MB molecule is 319.85 g·mol^{-1}. The surfactants used in this study were sodium lauryl sulfate (SLS, $C_{12}H_{25}SO_4Na$), sodium dodecyl sulfonate (SDS, $C_{12}H_{25}SO_3Na$), and hexadecyl trimethyl ammonium bromide (CTAB). Other chemicals used were calcium chloride ($CaCl_2$), magnesium sulfate heptahydrate ($MgSO_4 \cdot 7H_2O$), sodium sulfate (Na_2SO_4), potassium chloride (KCl), sodium chloride (NaCl), sodium nitrite ($NaNO_2$)

and ferrous sulfate (FeSO$_4$). All chemicals were purchased from Shanghai Aladdin Bio-Chem Technology Co., LTD. The powdered activated carbon (AC) was purchased from Tianjin Fuchen Chemical Reagent Co., Ltd. All the chemicals were used without any further purification.
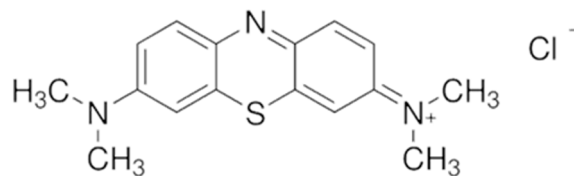

Figure 1. The chemical structure of methylene blue (MB).

2.2. Preparation of Surfactant-modified Activated Carbon

A total of 5 g of AC and 8.60 mM anionic surfactant SLS were added to 100 mL of solution. The mixture was oscillated in a shaker at 301 K for 6 h, and after that, the AC was filtrated and washed with deionized water. The filtrated AC was dried in an air-dry oven at 313 K for 24 h, and then was stored in a sealed and dry environment. Studies have shown that the concentration of surfactant corresponding to critical micelle concentration (CMC) is the best for adsorption [32]. It has been reported that the critical micelle concentration (CMC) of SLS is 8.60 mM at 28°C. The raw AC and surfactant-modified AC were called Virgin-C and SLS-C, respectively. The surfactant sodium dodecyl sulfonate (SDS) and hexadecyl trimethyl ammonium bromide (CTAB) were used to modify AC in the same method at the concentration of 1 CMC, called SDS-C and CTAB-C, respectively.

2.3. Adsorption Experiments

The adsorption capacity of MB on modified AC carried out in the batch adsorption experiment by investigating the effect of experimental variables such as pH (1–12), initial MB concentration (10, 30, 50 mg·L^{-1}), contact time, adsorbent dosage, temperature (298, 308, 318, 328K), and ionic species. The initial pH of the solution was adjusted with 0.1 M hydrochloric acid (HCl) and sodium hydroxide (NaOH) solution and determined with pH meter. A certain amount of modified AC was added to a 250 mL conical flask solution containing 100 mL of solution at certain concentrations of MB. Each mixture was oscillated at 170 r·min^{-1} at 25 °C at the given time interval. After the adsorption process, the samples were filtered and analyzed. The reserve solution of MB (1 g·L^{-1}) was prepared by dissolving the suitable amount MB in distilled water. All the experiments were done in triplicate.

2.4. Analytical Methods

According to the Standard Methods of Water and Wastewater Monitoring and Analysis Method, the absorbance of MB solution was measured by UV-visible spectrophotometer (INESA Scientific Instrument Co., Ltd. Shanghai, China) at 664 nm, which is the maximum absorption peak of MB. The concentration and removal rate of MB was obtained through the curve of relationship between solution concentration and absorbance of MB (Figure S1). The pH was measured using a DZS-706A multi-parameter meter (INESA Scientific Instrument Co., Ltd. Shanghai, China).

By measuring the absorbance of dye solution before and after treatment, the removal of MB on SLS-C adsorbent was studied with the batch equilibrium method. On the basis of Equations (1) and (2), the removal rate of dye in equilibrium state was calculated.

$$Q_e = \frac{(C_0 - C_e)V}{m} \tag{1}$$

$$Removel\ percentage = \frac{(C_0 - C_e)}{C_0} \times 100, \tag{2}$$

where Q_e represents the quantity of dye per unit mass of adsorbent (mg·g^{-1}); C_0 and C_e are the initial and equilibrium concentrations, respectively; V is the volume of MB dye solution in liters; and m is the weight of SLS-C adsorbent in grams.

3. Results

3.1. Effect of Different Surfactants

Figure 2 showed the extent of adsorption of MB on AC modified with different surfactants in aqueous solution at the initial MB concentration of 50 mg·L^{-1}. The results showed that SLS-C represents the highest MB adsorption capacity, followed by Virgin-C, SDS-C, and CTAB-C.

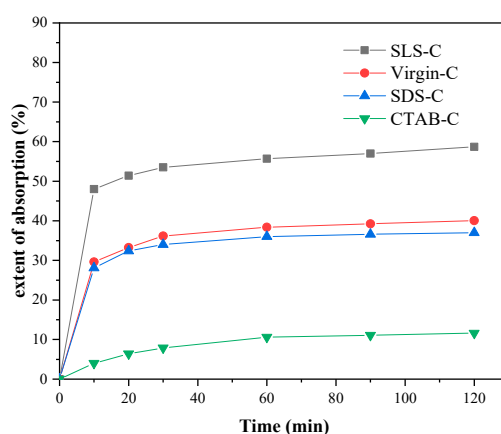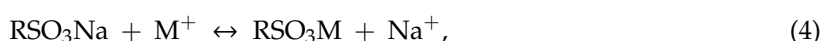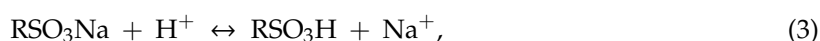**Figure 2.** MB removal by using different activated carbons (ACs) (initial MB concentration = 50 mg·L^{-1}, S/L = 0.15 g·L^{-1}, T = 298 K, pH = 5.0).

Compared with SLS-C and SDS-C, CTAB-C showed the weakest adsorption for MB dye. As a cationic surfactant, CTAB had a repulsive force with dye cations and occupied the adsorption sites on activated carbon, resulting in a low adsorption capacity of cationic MB dye.

Compared with the unmodified AC, surfactants loaded on activated carbon may clog the pores of AC, which reduces its ability to adsorb MB. On the other hand, the ionic functional groups of loaded surfactants can provide ion exchange sites with a higher affinity for MB than the unmodified AC surface. The higher MB adsorption on SLS-C compared with Virgin-C indicated that the positive effect of the functional group of SLS-C exceeded the negative effect of the pore blocking, whereas the lower MB removal by SDS-C compared with Virgin-C indicated that the negative effect of the pore blocking exceeded the positive effect of the functional group of SDS-C.

AC modified by anionic surfactants showed a strong adsorption capacity for MB dye due to the strong binding between the anionic surfactant and the cationic MB dye. The chemical properties of the functional groups of surfactant play an important role in adsorption. The cations attached to the strong acid conjugate base of SLS, such as sodium ions (e.g., R-SO$_3^-$ Na$^+$) and protons (e.g., R-SO$_3^-$ H$^+$), can be easily dissociated in aqueous solution and exchanged with an MB ion [27]. Therefore the SLS-C showed high MB removal effect. The affinity between the functional group on SDS and MB dye was weaker than that of SLS due to it being without strong acid conjugate base, which made the adsorption effect on MB lower than SLS-C.

The possible chemical adsorption processes of MB on SLS-C are shown in Figure 3. The reactions between MB dye cation (M$^+$) with RSO$_3$Na on SLS-C occurred regarding Equations (3)–(5). RSO$_3$Na is the active hydrophilic group of SLS and ROH represents the carboxyl, phenolic hydroxyl on AC.
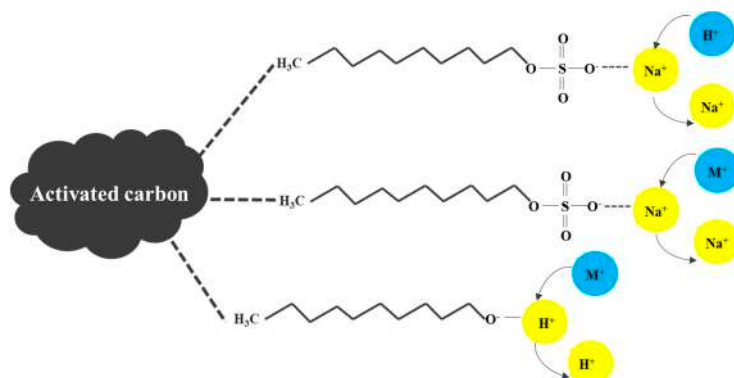
$$RSO_3Na + H^+ \leftrightarrow RSO_3H + Na^+, \tag{3}$$

$$RSO_3Na + M^+ \leftrightarrow RSO_3M + Na^+, \tag{4}$$

$$ROH + M^+ \leftrightarrow ROM + H^+, \tag{5}$$

Figure 3. The chemical adsorption between MB dye and the surface functional groups on sodium lauryl sulfate (SLS)-C.

3.2. Characterization of SLS-C

FE-SEM (Field Emission Scanning Electron Microscope) was used to observe the surface of the adsorbent. Figure 4 shows the detailed surface characteristics of the adsorbent. Figure 4a shows the surface of Virgin-C with a small amount of carbon debris and micropore of different sizes. Figure 4b shows the surface of SLS-C with a great quantity of pores and a large number of material debris occupying the pores compared with untreated AC. This was due to the electrostatic interaction and adhesion of SLS molecules. A large number of material debris occupied the pores, which could lead to a reduction in surface area, but could provide adsorption and ion exchange sites for MB.
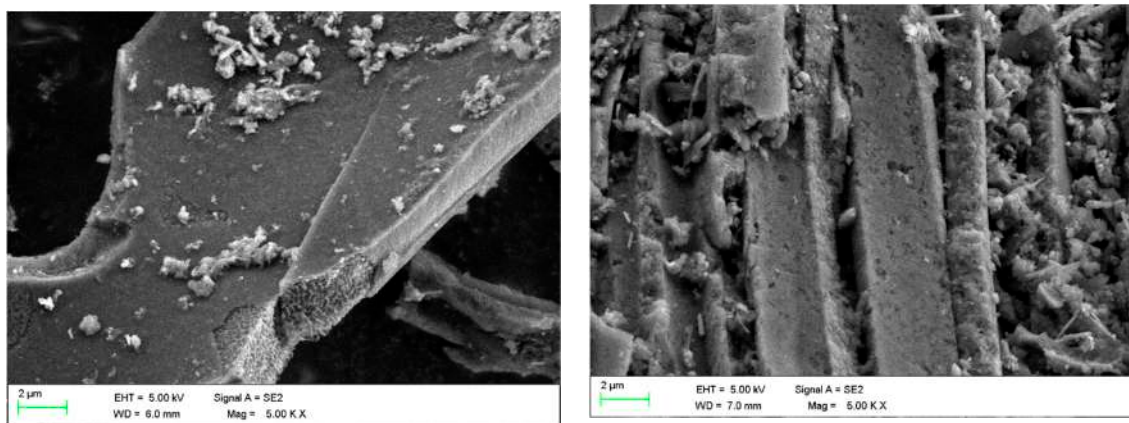
(**a**) FE-SEM-image of Virgin-C   (**b**) FE-SEM-image of SLS-C

Figure 4. FE-SEM pictures of (**a**) Virgin-C and (**b**) SLS-C.

3.3. Effects of Initial Solution pH

Figure 5 shows the variation of removal rate and adsorption capacities of MB on SLS-C at various pH values. As can be seen from Figure 5a, the alkaline condition was favorable for the adsorption of MB on SLS-C. According to Figure 5b, when the initial concentration of MB was 10, 30, and 50 mg·L^{-1}, the adsorption capacities of MB were 62.67, 168.39, and 193.33 mg·g^{-1}, respectively, at a natural pH value of 4.8, and the adsorption capacities of MB were 62.90, 179.78, and 220.49 mg·g^{-1} at a pH of 12.00. Thus, both the MB adsorption removal rate and adsorption capacities were increased with the increase of pH value.
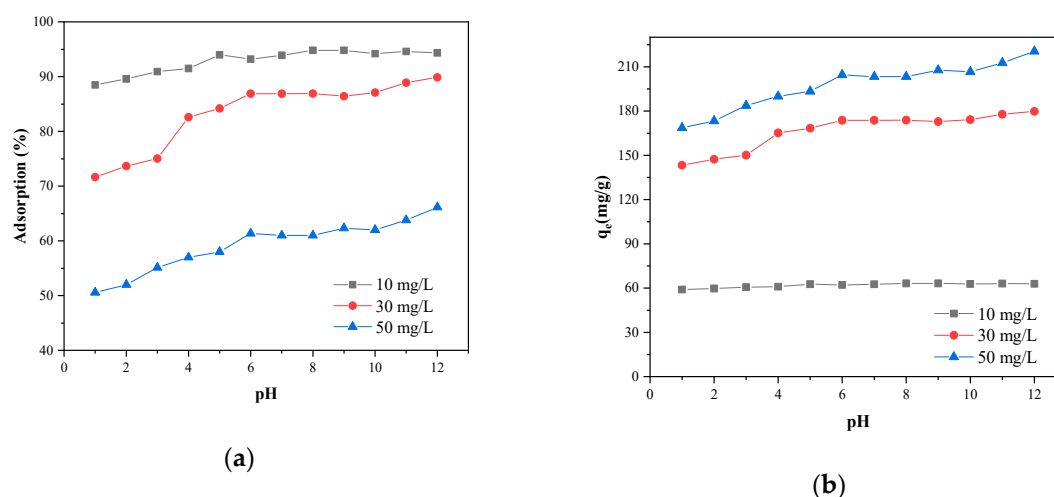
Figure 5. The adsorption rate (**a**) and the adsorption capacity (q_e) (**b**) of MB adsorption on the SLS-C sample at various pH values (S/L = 0.15 g·L^{-1}, contact time = 120 min, 25 °C).

The pH values of dye solution control the extent of ionization of the acidic and basic compounds and affect the surface charge of SLS-C [7,33]. At lower pH, the dissociation of hydrogen ions (H$^+$) by oxygen-containing functional groups on SLS-C would be inhibited, and the electronegativity of SLS-C and electrostatic attraction force between dye cation and SLS-C were relatively weak. Moreover, the fact that the free hydrogen ions inhibited the adsorption reaction of dye cation onto AC site by competing adsorption could lead to a reduction in MB removal rate. The increase in the concentration of hydroxide ions in the solution made the dissociation degree of MB small, and thus the removal rate of MB was improved as the pH value increased [34]. In addition, the dissociation degree of H$^+$ by the oxygen-containing functional groups on the surface of the SLS-C increased with the increase of pH, which increased the electronegativity of SLS-C and the electrostatic attractive force between the dye cation and SLS-C [25]. Furthermore, hydroxyl groups (O-H) and carbonyl groups (C=O) on the surface of the adsorbent can also attract the cationic dye molecules under the condition of high pH value [35]. Therefore, SLS-C has a good adsorption capacity of MB in an alkaline environment.

The results have resemblance to previous studies by Karaca [11]. The study by Yagub et al. [36] showed that the adsorption rate of cationic dye MB by raw pine leaf biochar at high pH values was better than that at low pH values. The adsorption rate had a noticeable increase at pH from 2 to 7, and slightly increased at the range of pH 7–9. The effect of pH on MB adsorption by various ACs was studied by Kannan N et al. [37], showing that the adsorption capacity of dye increased with the increase of initial pH.

Figure 6 shows the zeta potential variation of AC with pH before and after modification. The pH$_{PZC}$ of SLS-C and Virgin-C were 3.37 and 4.10. The result demonstrated that SLS-C has a higher surface electronegativity than that of Virgin-C, which was attribute to the hydrophobic alkyl end of surfactant attached to the nonpolar surface of activated carbon by van der Waals force. The AC surface oxygen-containing functional groups such as carboxyl and phenolic hydroxyl were covered with SLS to lead the amount of dissociated H$^+$ to decrease. The enhanced electronegativity of SLS-C made it have a better electrostatic attraction and adsorption capacity to MB than Virgin-C. When pH was around 4 to 8, the adsorption rate of MB on SLS-C was relatively stable in this experiment. Therefore, a pH value of 5 was chosen for the adsorption research.
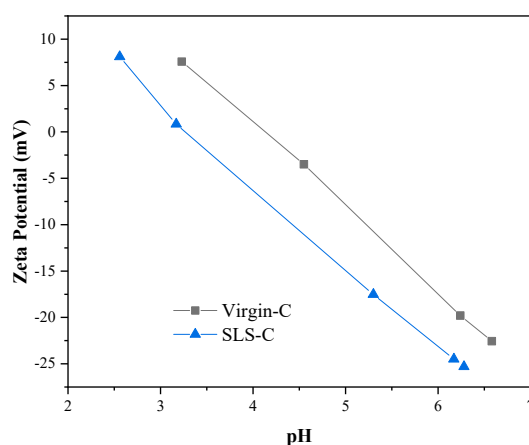
Figure 6. The zeta potential of Virgin-C and SLS-C.

3.4. Effect of Adsorbent Dose

Adsorbent dose is an important factor that affects the adsorption performance. The influence of adsorbent dose in adsorption of MB was studied to obtain a most appropriate amount of adsorbent at various MB concentrations [38]. The effect of adsorbent dose was studied by 100 mL of three different MB concentrations (10, 30, and 50 mg·L^{-1}) under different adsorbent doses (5, 7.5, 10, 15, 20, 30, 40, 50, 75, and 100 mg), as shown in the diagram below (Figure 7). A similar trend in adsorption behavior of MB on SLS-C under various MB concentrations was observed.
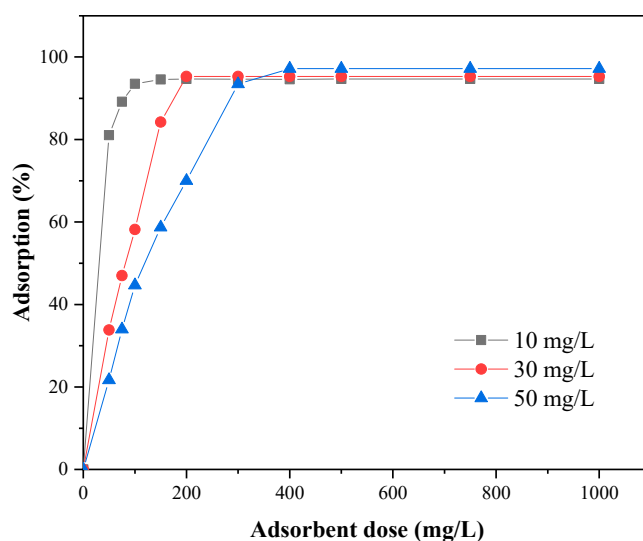

Figure 7. Effect of adsorbent dose on MB adsorption on SLS-C sample (contact time = 120 min).

As the mass of adsorbents increased, the removal rate of MB gradually increased due to the increases of the number of adsorbent pores and adsorption sites. The adsorption would tend to an equilibrium when the mass of adsorbent reached a certain value. The removal rate of MB reached the saturated value at adsorbent mass of 15, 20, and 30 mg corresponding to the initial MB concentration of 10, 30, and 50 mg·L^{-1}, respectively. At high adsorbent dosages, the available number of MB dye molecules in solution was not enough to completely combine with all effective adsorption sites on the adsorbent, resulting in a surface equilibrium state and a reduction in the adsorption capacity per unit mass of adsorbent.

3.5. Effects of Contact Time

Figure 8 showed the relationship between the adsorption rate and the adsorption capacity of MB on SLS-C and time at three initial MB concentrations (10, 30, and 50 mg·L^{-1}).
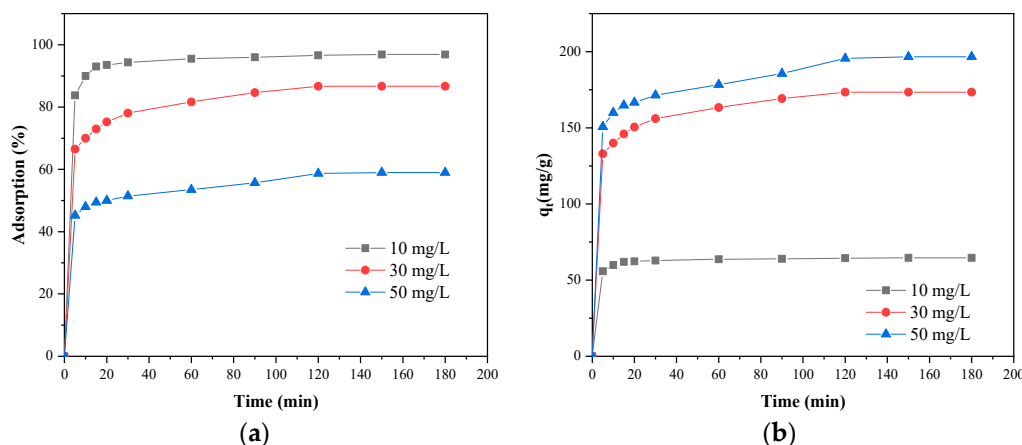

Figure 8. Effect of contact time on adsorption of MB on SLS-C at pH = 5.0, S/L = 0.15 g·L^{-1}. (**a**) The adsorption rate; (**b**) the adsorption capacity.

It can be seen in Figure 8 that the removal efficiency and adsorption capacity of MB by SLS-C was increased with an increase in contact time and then reached a maximum value. The process was divided into two phases. The first step took 5–30 min to reach the relative adsorption equilibrium state called fast adsorption. This performance was due to the binding process between MB dye and the adsorption active sites, and functional groups on the SLS-C adsorbent were fully and efficiently completed. The absorption rate of the dye was controlled by the rate of the dye transported from the solution to the surface of the adsorbent particles. The second step was called slow adsorption process. After 30 min of contact time, the relative increase in the removal extent of MB was not significant, and with the increase of time, the adsorption rate decreased and gradually stabilized. This performance was due to the binding process between MB dye and the adsorption active sites, and functional groups on the SLS-C adsorbent were gradually saturated. The absorption rate of the dye was controlled by the rate of the dye transported from the exterior to the interior pore sites of the adsorbent particles [39].

Moreover, the lower the dye initial concentration, the shorter the time to achieve the adsorption equilibrium state. The results were basically consistent with previous studies on the removal rate of dyes [29]. Considering the relationship between the contact time and the MB removal, the contact time for subsequent experiments was selected as 120 min.

3.6. Effects of Initial MB Concentration

The influence of different initial dye concentrations (10, 20, 30, 40, 50 mg·L^{-1}) on the decolorization efficiency of MB dye was studied using the same mass of SLS-C and adjusting the dye solution pH to 5. A 15 mg adsorbent sample was added to 100 mL dye solution and adsorbed for 120 min at 298K. The experimental data are given in Table 1.

According to the listed data (Table 1), the decolorization rate (%) of MB by 15 mg of the SLS-C adsorbent decreased from 96.6% to 58.7% when the initial dye concentration increased from 10 to 50 mg·L^{-1}. However, as the initial dye concentration increased from 10 to 50 mg·L^{-1}, the adsorption capacity at equilibrium (Q_e) increased from 64.4 to 195.8 mg·g^{-1}. Moreover, the maximum adsorption capacity at equilibrium (Q_e) was calculated up to value of 195.8 mg·g^{-1} when the dye concentration was 40 mg·L^{-1}. It was found that when the MB concentration was greater than 40 mg·L^{-1}, the adsorption sites on the adsorbent were completely adsorbed, and thus the adsorption amount of activated carbon at a MB concentration of 40 mg·L^{-1} was similar to that at MB concentration of 50 mg·L^{-1}.

Table 1. Effect of initial MB concentration on the percentage extraction of dye.

MB Concentration (mg·L^{-1})	SLS-C		Virgin-C	
	Percent Adsorption (%)	Adsorption Capacity (mg·g^{-1})	Percent Adsorption (%)	Adsorption Capacity (mg·g^{-1})
10	96.6	64.4	80.9	53.9
20	90.6	120.8	72.7	96.0
30	86.7	173.4	66.3	132.6
40	73.4	195.8	51.9	138.4
50	58.7	195.7	41.3	137.6

The removal extent of dyes was decreased with an increase in the initial MB concentration due to the lack of available active sites under high concentration condition of MB [40], whereas the adsorption capacity of MB on SLS-C increased with the increase of initial MB concentration. The sulfate functional group of SLS provided ion exchange sites conducive to the MB ion adsorption. Compared with untreated AC, activated carbon modified by anionic surfactant has more positively charged adsorption sites and high adsorptive capacity for removing cationic dye [12,27].

3.7. Adsorption Kinetics and Isotherm

3.7.1. Adsorption Kinetics

Adsorption kinetics mainly studies the reaction rate between adsorbents and adsorbates and the factors affecting the reaction rate. The adsorption data were fitted by kinetic models and the adsorption mechanism was discussed according to the fitting results. The adsorption kinetics of MB on SLS-C were studied by using four kinetic equation models to confirm the most effective equation. The consistency between the experimental results and the theoretical values of the model was assessed on the basis of the coefficient of determination (R^2 value was close to or equal to 1).

The principle of the pseudo-first-order kinetic model is that the reaction rate is proportional to the number of ions remaining in the solution, assuming that adsorption is controlled by diffusion steps [41]. It is assumed that the adsorption rate is proportional to the difference between the saturated concentration and the adsorption amount of SLS-C with time. The integral equation is shown below in Equation (6).

$$\ln(Q_e - Q_t) = \ln Q_e - k_1 t \tag{6}$$

where k_1 is the rate constant of adsorption (min^{-1}), Q_e is the quantity of dye adsorbed at equilibrium (mg·g^{-1}), and Q_t is the equilibrium concentration at various times t (in mg·L^{-1}). The rate constant in this model was determined by the slope of the plot of $\ln(Q_e - Q_t)$ over time (t). The results of R^2 calculated were in the range of 0.644–0.974. In addition, the large differences between the value of $Q_{e,exp}$ and $Q_{e,cal}$ indicated that the pseudo-first order model was not an effective model to explain the adsorption process.

The pseudo-second-order kinetic model, which can be expressed as the reaction rate being proportional to the concentrations of the two reactants, assuming the adsorption is controlled by chemical adsorption steps, can be expressed by Equation (7) [42].

$$\frac{t}{Q_t} = \frac{1}{k_2 Q_e^2} + \frac{t}{Q_e} \tag{7}$$

where k_2 is the second-order-rate constant (g·mg^{-1}·min^{-1}) that can be determined for different MB concentrations according to the linear plots of t/Q_t versus t, as shown in Figure 9. The calculated correlation coefficients (R^2) were found to be greater than 0.999, and the experimental Q_e differing from the calculated ones are listed in Table 2. Obviously, from the values calculated by pseudo-second-order

kinetic model, $Q_{e,cal}$ had good agreement with the experimental $Q_{e,exp}$. This behavior indicated that the pseudo-second order model was the best model to explain the adsorption process of MB on SLS-C.
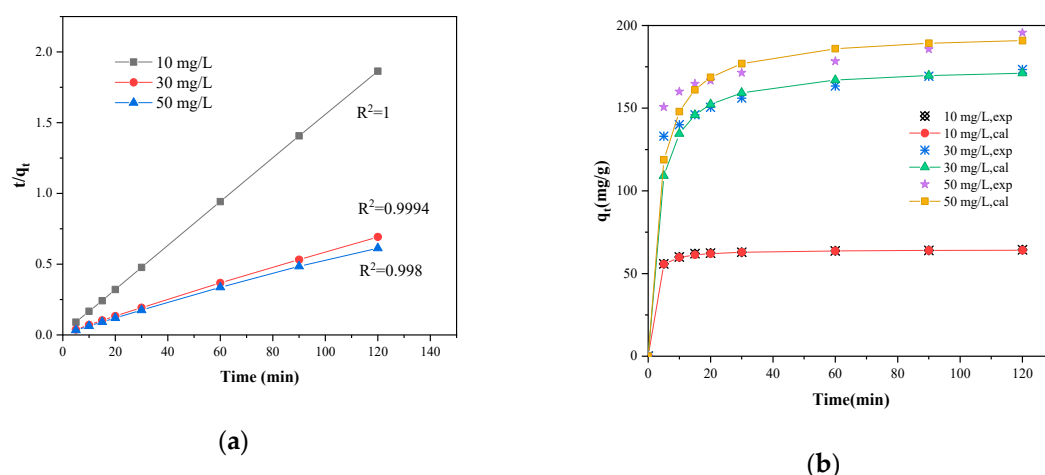

Figure 9. (**a**) Pseudo-second order plots and (**b**) the adsorption capacity (q_e) for the adsorption of MB on SLS-C at various initial concentrations, pH = 5.0, S/L = 0.15 g·L^{-1}, T = 25 °C.

Table 2. Pseudo-First-Order model and Pseudo-Second-Order model form removal of MB by SLS-C.

C_0 (mg.L^{-1})	$Q_{e,cal}$ (mg.g^{-1})	Pseudo-First-Order Model			Pseudo-Second-Order Model		
		k_1 (min^{-1})	Q_e (mg.g^{-1}) (exp.)	R^2	k_2 (g.mg^{-1}. min^{-1})	Q_e (mg.g^{-1}) (exp.)	R^2
10	64.4	0.0090	4.4	0.644	0.00195	64.1	1
30	173.4	0.0107	40.9	0.966	0.00188	171.1	0.999
50	195.7	0.0069	42.1	0.974	0.00157	190.9	0.998

The intra-particle diffusion model divides the adsorption process into two main steps including the migration of solute molecules from aqueous solution to the surface of adsorbent particles and the diffusion of adsorbate molecules into the interior pores of the adsorbent [43].

The adsorption process was studied Weber–Morris intra-particle diffusion model which is expressed as Equation (8).

$$Q_t = k_{ip}t^{\frac{1}{2}} + C_i \tag{8}$$

where k_{ip} (mg·g^{-1}·min$^{-1/2}$) is the rate constant of the intra-particle diffusion model, and C_i is the constants related to boundary layer thickness expressed in milligrams per gram (mg·g^{-1}), which can be calculated according to slope and intercept of the plot of Q_t versus the square root of time $t^{1/2}$.

The straight line fitted by the intra-particle model (as shown in Figure S2) without passing through the origin indicated that the adsorption process was controlled not only by the intra-particle diffusion but also by other adsorption processes. The constant C_i (57.64, 127.73, 144.74) was found to increase with the increase of MB dye concentration, which may have been due to the increase of the boundary layer thickness (as shown in Table 3). The high values of C_i indicated that the external diffusion of MB molecule on SLS-C was very important in the initial adsorption period. The values of R^2 were close to 1 and show a good application of the intra-particle model in the sorption process.

Table 3. Intra-particle diffusion model and Elovich model from removal of MB by SLS-C.

C_0 (mg·L^{-1})	Intra-Particle Diffusion Model			Elovich Model		
	k_{ip} (mg·g^{-1}·min$^{-1/2}$)	C_i	R^2	α (mg·g^{-1}·min^{-1})	β (mg·g^{-1})	R^2
10	$K_{ip1} = 3.800$ $K_{ip2} = 0.303$	57.64	0.985 0.974	2.395	0.436	0.816
30	4.426	127.73	0.957	14.373	0.078	0.997
50	4.542	144.74	0.974	14.197	0.078	0.970

The Elovich model of adsorption process was expressed as Equation (9), which describes adsorption in a non-ideal state. The adsorption process is divided into the fast adsorption and slow adsorption process.

$$Q_t \ = \ \frac{1}{\beta} \ln \alpha \, \beta + \frac{1}{\beta} \ln t \tag{9}$$

where α represents the initial adsorption rate (mg·g^{-1}·min^{-1}) and β is the desorption coefficient (mg·g^{-1}). The graph of Q_t versus $\ln t$ is a line with a slope of $1/\beta$ and an intercept of $1/\beta \ \ln(\alpha \, \beta)$. The correlation coefficient (R^2) at MB concentrations of 10, 30, and 50 mg·L^{-1} were identified as being 0.816, 0.997, and 0.970, respectively. The fitting data calculated from Elovich kinetic model showed that when the initial concentration of MB was 10 mg·L^{-1}, the models described the observations not well. Nevertheless, that the experimental results could be well described by the Elovich model at the initial concentration of MB higher than 10 mg·L^{-1} indicated that the rate-limiting step was the intraparticle diffusion process but not the only process [22,44].

The results showed that the pseudo-second-order kinetic model can be used to describe the adsorption of MB on SLS-C and proved that chemical adsorption dominated the adsorption process. The adsorption process not only included the processes of the liquid film diffusion and the internal diffusion of micropores, but also the chemical adsorption process with electrons shared and gained or loss of electrons between cationic dyes and functional groups on the SLS-C surface [30].

3.7.2. Adsorption Isotherm

The adsorption process is divided into two parts, adsorbent adsorption pollutants and pollutants desorption from the adsorbent. When the rate of the two processes is the same, the adsorption will enter a dynamic equilibrium state. Adsorption isotherms are used to study the relationship between the equilibrium adsorption capacity and the equilibrium concentration of pollutants under certain conditions (temperature and pH remain unchanged). The adsorption isotherms were studied to provide a basis for revealing adsorption behavior, indicating possible adsorption mechanism, and estimating adsorption capacity. Three models, the Langmuir model, Freundlich model, and Temkin model, were used to describe adsorption isothermal behavior.

The Langmuir model assumes that adsorption is localized on a monolayer, and all adsorption sites on the adsorbent are homogeneous and have the same adsorption capacity [45]. The Langmuir isotherm equation is Equation (10):

$$\frac{C_e}{Q_e} \ = \ \frac{1}{Q_{max} \, K_L} + \frac{C_e}{Q_{max}} \tag{10}$$

where C_e is the equilibrium concentration (mg·L^{-1}), Q_e is the amount of adsorbed dye at equilibrium (mg·g^{-1}), Q_{max} (mg·g^{-1}) is the Langmuir constants that are related to the adsorption capacity, and K_L (L·mg^{-1}) is the adsorption rate. The value of R^2 obtained from the linear graph of C_e/Q_e versus C_e was 0.993, which demonstrated that the adsorption process meets the Langmuir isotherm model, as exhibited in the diagram (Figure 10). The value of Q_{max} and K_L are shown in Table 4.
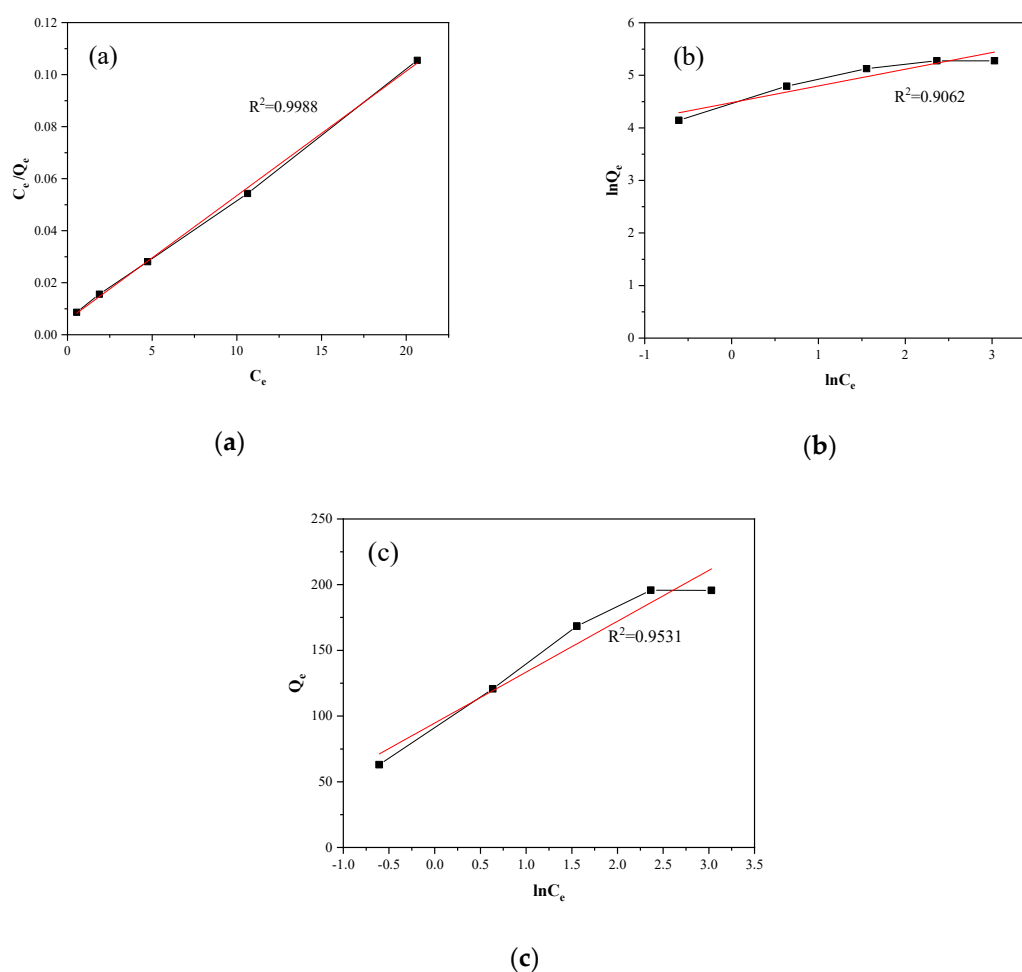
(**a**)

(**b**)

(**c**)

Figure 10. (**a**) Langmuir, (**b**) Freundlich, and (**c**) Temkin isotherm plots for adsorption of MB on SLS-C.

Table 4. Isotherm parameters of the Langmuir, Freundlich, and Temkin models.

Adsorption Model	Isotherm Parameters	R^2
Langmuir	Q_{max} = 232.5 mg·g^{-1} K_L = 0.842 L·m^{-1}·g^{-1} R_L = 0.106	0.999
Freundlich	K_f = 88.235 mg·g^{-1} $1/n$ = 0.318	0.906
Temkin	B = 38.73 J·mol^{-1} A = 11.53 L·g^{-1} b = 63.98 L·g^{-1}	0.953

The feasibility of adsorbent adsorption was evaluated by R_L. It can be defined by Equation (11) [46]:

$$R_L = \frac{1}{1 + K_L C_0} \tag{11}$$

where C_0 (mg·L^{-1}) is initial dye concentration. The value of R_L indicates the type of the isotherm: irreversible (R_L = 0), favorable (0 < R_L < 1), linear (R_L = 1), or unfavorable (R_L > 1). The R_L value of MB adsorption on SLS-C was in the range of 0.661–0.842. It can be testified that the adsorption process was favorable.

The Freundlich isotherm model is based on the assumption that multi-layer adsorption processes occur on heterogeneous surfaces. The Freundlich isotherm linear equation is shown in Equation (12):

$$\ln Q_e = \ln K_f + \frac{1}{n} \ln C_e \tag{12}$$

where K_f (mg·g^{-1}) is a constant related to the adsorption energy. The value of R^2 obtained from the linear graph of $\ln Q_e$ versus $\ln C_e$ was 0.906. Compared the values of R^2 of two isotherms models, the Langmuir model was more suitable for the experimental equilibrium adsorption data than the Freundlich model, as shown in Figure 10. The values of $1/n$ and K_f were calculated and listed in Table 4. The slope ($1/n$) values reflected adsorption intensity or surface heterogeneity. It is generally considered as a sign of a good adsorption process when the value of $1/n$ is in the range of 0.1 to 1.0. In this experiment, the index value was within the range, indicating that the adsorption process was favorable. This was in line with the conclusion of the Langmuir model.

The Temkin model considers the interaction between adsorbent and contaminant as a chemical adsorption process. The Temkin isotherm equation are shown in Equations (13) and (14):

$$Q_e = \frac{RT}{b} \ln A + \frac{RT}{b} \ln C_e \tag{13}$$

$$B = \frac{RT}{b} \tag{14}$$

where b (mg·L^{-1}) is the Temkin isotherm constant, A (L·g^{-1}) is the Temkin isotherm equilibrium binding constant, and B is the constant related to the heat of adsorption (J·mol^{-1}). The calculated values of A, B, and b are shown in Table 4.

The isotherm data were linearized using the Langmuir equation, as shown in Figure 10. The parameters of Langmuir isotherm are shown in Table 4. The high value of R^2 indicated that there was a good agreement between the model parameters. The theoretical maximum adsorption capacity of MB on SLS-C, obtained by the Langmuir adsorption isothermal equation fitting, was up to 232.5 mg·g^{-1}, whereas the theoretical maximum adsorption capacity of Virgin-C was 153.8 mg·g^{-1}. The Freundlich equation and Temkin equation were also used to fit the same data, as shown in Figure 10. The relevant coefficients can be calculated from three isotherms, such as K_L, Q_{max}, R_L, K_f, n, A, B, and b. The values are listed in Table 4.

The adsorption isotherm analysis results were in good agreement with the Langmuir, Freundlich, and Temkin models, but the Langmuir model had better consistency. These results indicated that the MB adsorption sites of the adsorbent were homogeneous, which was consistent with the assumption of the Langmuir model. For SLS-C, the surfactant molecules covered the AC surface uniformly, resulting in the homogeneous adsorption sites. Therefore, it can be inferred that the adsorption mechanism of MB adsorption by SLS-C was the physical and chemical monolayer adsorption.

3.8. Temperature Effect and Thermodynamic Parameters

The influence of temperature was studied by three MB concentrations (10, 30, and 50 mg.L^{-1}) at different temperature values (25, 35, 45, and 55°C) and the results are graphed in Figure 11. The higher the temperature, the higher the adsorption ability of MB on SLS-C at all concentrations. This indicated that the adsorption was a spontaneous endothermic process.

The thermal motion, the solubility, and the chemical potential of dye molecules increased with the increase of temperature [47]. Moreover, the pore structure of AC was closely related to temperature. The pore structure and number of active adsorption sites of AC increased with the increase of temperature due to thermal expansion. These reasons led to the increase of adsorption capacity of MB on SLS-C with the increase of temperature.
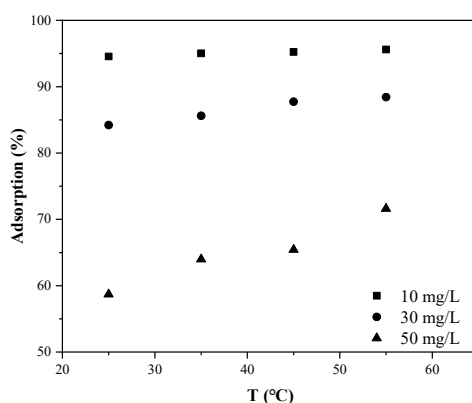
Figure 11. Influence of temperature on MB removal efficiency by SLS-C (adsorbent dosage S/L = 0.15 g·L^{-1}, pH = 5.0, contact time = 120 min).

The temperature effect and sorption mechanism were further discussed in the study of adsorption thermodynamics. The thermodynamics of adsorption of SLS-C were analyzed from the view of energy. Studying on the driving force of adsorption by the adsorption thermodynamics method determined whether the adsorption process was spontaneous or not. The values of thermodynamic parameters, such as free energy change (ΔG), enthalpy change (ΔH), and entropy change (ΔS), are usually calculated on the basis of the thermodynamic formulas shown in Equations (15)–(18) [48]:

$$\Delta G = -RT \ln K_C, \tag{15}$$

$$K_c = \frac{Q_e}{C_e}, \tag{16}$$

$$\ln K_C = \frac{\Delta S}{R} - \frac{\Delta H}{RT} \tag{17}$$

$$\Delta G = \Delta H - T\Delta S \tag{18}$$

where K_C is the thermodynamic constant, R is the universal gas constant (8.314 J·mol^{-1}·K^{-1}), and T is the absolute temperature (K). The ΔG is the Gibbs free energy change (kJ·mol^{-1}), ΔS is the entropy change (kJ·mol^{-1}·K^{-1}), and ΔH is the enthalpy change (kJ·mol^{-1}). The slope and intercept of the linear graph about ln K_C versus 1/T, as shown in Figure 12, can be respectively obtained from the values of ΔH and ΔS, as listed in Table 5.
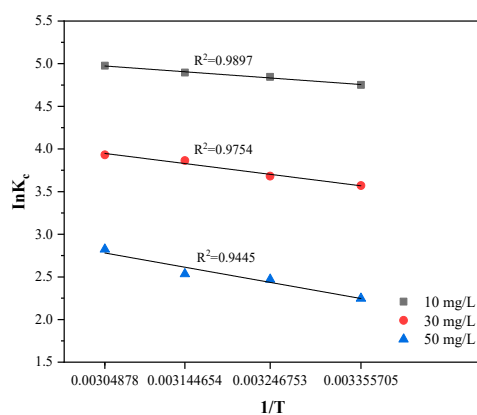

Figure 12. Thermodynamics parameters on the adsorption of MB by SLS-C.

Table 5. Thermodynamic parameters for removal efficiency of MB on SLS-C.

		Thermodynamics		
$c/mg \cdot L^{-1}$	T/K	$\Delta G/kJ \cdot mol^{-1}$	$\Delta S/kJ \cdot mol^{-1} \cdot K^{-1}$	$\Delta H/kJ \cdot mol^{-1}$
10	298	−11.78	0.059	5.90
	308	−12.38		
	318	−12.97		
	328	−13.56		
30	298	−8.84	0.064	10.28
	308	−9.48		
	318	−10.12		
	328	−10.77		
50	298	−5.57	0.067	14.46
	308	−6.24		
	318	−6.91		
	328	−7.58		

The negative ΔG values, which can be seen from Table 5, demonstrated the discolored process of MB on SLS-C in terms of feasibility and spontaneity [49]. The positive ΔH values of 5.90, 10.28, and 14.46 KJ·mol^{-1} at different temperatures prove that the adsorption was an endothermic process at initial dye concentrations of 10 mg·L^{-1}, 30 mg·L^{-1}, 50 mg·L^{-1}, respectively [50]. In the adsorption of different MB dye concentrations on SLS-C, ΔS values were 0.059, 0.064, and 0.067 kJ·mol^{-1}·K^{-1}, respectively. The positive values of ΔS indicated that the randomness of the solid/solution interface increased during the adsorption process [13].

3.9. Effect of Additive Salts

The effects of different salts such as NaCl, KCl, CaCl$_2$, NH$_4$Cl, MgSO$_4$.7H$_2$O, NaNO$_2$, and FeSO$_4$ on adsorption were studied in 100.0 mL MB solution under the different concentration conditions of 10, 30, and 50 mg·L^{-1}. A total of 200.0 mg of additive salt was added into the dye solution, adjusting the pH value to 5.0 and oscillating for 30 min. The effect of salt species on the adsorption of MB on SLS-C are listed in Table 6.

Table 6. Effect of salt species on the removal efficiency (%) of MB at 25°C, t = 30 min.

MB Concentration $(mg \cdot L^{-1})$	Removal Efficiency (%) in Presence of Salt Species							
	None	NaCl	KCl	CaCl$_2$	NH$_4$Cl	MgSO$_4$	NaNO$_2$	FeSO$_4$
10	94.3	94.6	94.6	94.6	94.6	94.6	94.6	90.4
30	78.1	79.7	77.0	78.3	78.3	73.7	85.3	60.5
50	53.2	55.5	52.7	53.9	53.9	52.0	56.9	44.2

The presence of coexisting ions (Na$^+$, K$^+$, Ca^{2+}, NH^{4+}, Mg^{2+}) had little effect on the adsorption of MB on SLS-C. When the concentration of MB was 30 mg·L^{-1}, the removal rates of MB in the presence of coexisting ions were 73.7%-79.7%, which was similar to the removal rates of 78.1% in the absence of ions. When the dye concentration was 50 mg·L^{-1}, the removal rate of MB in the presence of coexisting ions (52.0%-55.5%) was similar to that in the absence of ions (53.2%). This result is similar to the study on effect of the cations (Na$^+$, K$^+$, Ca^{2+}) on adsorption of ammonium on SLS-C by Wooram Lee [27]. It indicated that the adsorption process was as insensitive to ionic as Na$^+$, K$^+$, Ca^{2+}, NH^{4+}, and Mg^{2+} [51].

The adsorption capacity of MB on SLS-C increased slightly when NaCl, CaCl$_2$, or NH$_4$Cl were present in the solution system. It may have been due to the increase of dimerization reaction of MB in solution in the presence of forces such as ion dipole, dipole–dipole interaction, and van-der-Waals force among dye molecules. The result agreed well with the article of Mohamed E. Mahmoud that additive salts (NaCl, NaAc, KCl, MgSO$_4$, NH$_4$Cl, and CaCl$_2$) improve the removal rate of dye

by surfactant-modified AC [22]. When the ion (NO^{2-}) was present, it had a greater impact on the adsorption of MB by SLS-C. When MB concentration was 30 mg·L^{-1}, the removal rate of MB (85.3%) in the presence of coexisting ions (NO^{2-}) was higher than that in the absence of ions (78.1%). The reason may be that NO^{2-} has strong oxidation capacity in dilute solutions. Nitrite such as sodium nitrite and potassium nitrate are widely used in dye production. At a MB concentration of 50 mg·L^{-1}, the removal rate of MB (44.2%) by SLS-C in the presence of competitive cation (Fe^{2+}) was lower than that in the absence of ions (53.2%). The rate of adsorption was reduced because the strong reducibility ferrous ions occupied the adsorption site of MB on SLS-C.

3.10. Decolorization of MB in Real Water Samples by SLS-C

The adsorption rate of MB by SLS-C in three different real water samples of tap water, raw water, and waste samples are listed in Table 7. The tap water sample was collected from laboratory faucets, raw water sample was collected from the back of the Pearl River, and waste water sample was collected from a nameless river in the campus. The parameters of the water samples are shown in Table S1. A certain amount of MB was added into 100.0 mL water samples and prepared at concentrations of 10.0, 30.0, and 50.0 mg·L^{-1}, respectively. All the samples were adjusted to pH of 5.0 and shaken for 30min in a shaker. Distilled water samples were treated as blank water samples for comparison. The experimental results expressed that the adsorption rate of MB by SLS-C in real water samples was slightly improved relative to modeling dye wastewater.

Table 7. Adsorptive removal of MB dye from real water samples' SLS-C adsorbent.

Water Sample	MB Concentration (mg·L^{-1})	Removal (%)
Distilled water	10	94.3
	30	78.1
	50	53.4
Tap water	10	94.3
	30	80.1
	50	54.1
Raw water	10	94.3
	30	81.0
	50	55.3
waste water	10	94.3
	30	81.1
	50	55.9

4. Conclusions

This study showed that AC modified by anionic surfactants could significantly improve the adsorption properties of MB on AC. The solution initial pH, adsorbent dosage, contact time, initial MB concentration, temperature, and additive salts had a great impact on adsorption properties. The high adsorption capacity of SLS-C can be attributed to the hydrophobic group of the surfactant, which is expected to bind to the hydrophobic surface of AC. A specific binding site with the anionic functional group on SLS-C provided an efficient sorption field for the MB target dye cations. The SLS-C has advantages such as a strong affinity of acid conjugate base, a number of functional groups per unit mass adsorbent, and good dispersibility. The study of adsorption of dyes in aqueous solutions at pH values in the range of 1.0–12.0 confirmed that the adsorption rate increased with the increase of pH. The adsorption rate of MB by SLS-C increased with increased temperature. The adsorption kinetics conformed to the pseudo-second-order reaction model and the adsorption isotherm conformed to the Langmuir adsorption isotherm. The negative ΔG values and positive ΔH values proved that the adsorption process was an endothermic and spontaneous process. The theoretical maximum adsorption capacity of MB on SLS-C was 232.5 mg·g^{-1}, whereas the theoretical maximum adsorption

capacity of Virgin-C was 153.8 mg·g^{-1}. The adsorption equilibrium time was about 120 min. The presence of cations such as Na$^+$, K$^+$, Ca^{2+}, NH^{4+}, and Mg^{2+} had negligible impact on the adsorption of MB on SLS-C (< 5%). The adsorption capacity was significantly improved in the presence of NO^{2-} and decreased in the presence of cation Fe^{2+}. The application of SLS-C in the decolorization of MB in tap water, raw water, and waste water proved that the existence of ions has little influence in the MB adsorption in real water samples.

Supplementary Materials: The following are available online at http://www.mdpi.com/2073-4441/12/2/587/s1, Figure S1: title, Table S1: title, Video S1: title. Figure S1: MB standard curve (at pH of 5). Figure S2: The intraparticle diffusion model plots for the adsorption of MB on SLS-C (a) at MB concentration of 10 mg/L, and (b) at MB concentrations of 10, 30, and 50 mg/L. Table S1: The water quality parameters of different water samples.

Author Contributions: Y.K. conceived the study. She also conducted the experiment, data collection, and analysis of data, and prepared the first edition of the manuscript. X.Z. participated in the design of the study and helped to draft and edit the manuscript. S.Z. helped to edit the manuscript. All authors read and approved the final manuscript.

Conflicts of Interest: The authors declare no conflict of interest.

References

1. Wong, Y.C.; Szeto, Y.S.; Cheung, W.H.; McKay, G. Adsorption of acid dyes on chitosan—equilibrium isotherm analyses. *Process. Biochem.* **2004**, *39*, 695–704. [CrossRef]
2. Tan, I.A.W.; Ahmad, A.L.; Hameed, B.H. Adsorption of basic dye on high-surface area activated carbon prepared from coconut husk: Equilibrium, kinetic and thermodynamic studies. *J. Hazard. Mater.* **2008**, *154*, 337–346. [CrossRef]
3. Pavithra, K.G.; Kumar, P.S.; Jaikumar, V.; Rajan, P.S. Removal of colorants from wastewater: A review on sources and treatment strategies. *J. Ind. Eng. Chem.* **2019**, *75*, 1–19. [CrossRef]
4. Verma, A.K.; Dash, R.R.; Bhunia, P. A review on chemical coagulation/flocculation technologies for removal of colour from textile wastewaters. *J. Environ. Manag.* **2012**, *93*, 154–168. [CrossRef] [PubMed]
5. Yu, S.; Liu, M.; Ma, M.; Qi, M.; Lü, Z.; Gao, C. Impacts of membrane properties on reactive dye removal from dye/salt mixtures by asymmetric cellulose acetate and composite polyamide nanofiltration membranes. *J. Membr. Sci.* **2010**, *350*, 83–91. [CrossRef]
6. Alventosa-deLara, E.; Barredo-Damas, S.; Alcaina-Miranda, M.I.; Iborra-Clar, M.I. Ultrafiltration technology with a ceramic membrane for reactive dye removal: Optimization of membrane performance. *J. Hazard. Mater.* **2012**, *209–210*, 492–500. [CrossRef] [PubMed]
7. Asghar, A.; Abdul Raman, A.A.; Wan Daud, W.M.A. Advanced oxidation processes for in-situ production of hydrogen peroxide/hydroxyl radical for textile wastewater treatment: A review. *J. Clean. Prod.* **2015**, *87*, 826–838. [CrossRef]
8. Kordouli, E.; Bourikas, K.; Lycourghiotis, A.; Kordulis, C. The mechanism of azo-dyes adsorption on the titanium dioxide surface and their photocatalytic degradation over samples with various anatase/rutile ratios. *Catal. Today* **2015**, *252*, 128–135. [CrossRef]
9. Yagub, M.T.; Sen, T.K.; Afroze, S.; Ang, H.M. Dye and its removal from aqueous solution by adsorption: A review. *Adv. Colloid Interface Sci.* **2014**, *209*, 172–184. [CrossRef]
10. Sun, D.; Zhang, X.; Wu, Y.; Liu, X. Adsorption of anionic dyes from aqueous solution on fly ash. *J. Hazard. Mater.* **2010**, *181*, 335–342. [CrossRef]
11. Karaca, S.; Gürses, A.; Açıkyıldız, M.; Ejder, M.K. Adsorption of cationic dye from aqueous solutions by activated carbon. *Microporous Mesoporous Mater.* **2008**, *115*, 376–382. [CrossRef]
12. Xiang, Y.; Gao, M.; Shen, T.; Cao, G.; Zhao, B.; Guo, S. Comparative study of three novel organo-clays modified with imidazolium-based gemini surfactant on adsorption for bromophenol blue. *J. Mol. liquids* **2019**, *286*. [CrossRef]
13. Fan, S.; Wang, Y.; Wang, Z.; Tang, J.; Li, X. Removal of methylene blue from aqueous solution by sewage sludge-derived biochar: Adsorption kinetics, equilibrium, thermodynamics and mechanism. *J. Environ. Chem. Eng.* **2017**, *5*, 601–611. [CrossRef]

14. Wang, G.; Wang, S.; Sun, Z.; Zheng, S.; Xi, Y. Structures of nonionic surfactant modified montmorillonites and their enhanced adsorption capacities towards a cationic organic dye. *Appl. Clay Sci.* **2017**, *148*, 1–10. [CrossRef]

15. Wang, W.; Huang, G.; An, C.; Zhao, S.; Chen, X.; Zhang, P. Adsorption of anionic azo dyes from aqueous solution on cationic gemini surfactant-modified flax shives: Synchrotron infrared, optimization and modeling studies. *J. Clean. Prod.* **2018**, *172*, 1986–1997. [CrossRef]

16. Hailu, S.L.; Nair, B.U.; Mesfin, R.A.; Diaz, I.; Tessema, M. Preparation and characterization of cationic surfactant modified zeolite adsorbent material for adsorption of organic and inorganic industrial pollutants. *J. Environ. Chem. Eng.* **2017**, *5*, 3319–3329. [CrossRef]

17. Jiménez-Castañeda, M.; Medina, D. Use of Surfactant-Modified Zeolites and Clays for the Removal of Heavy Metals from Water. *Water* **2017**, *9*, 235. [CrossRef]

18. Leng, L.; Yuan, X.; Zeng, G.; Shao, J.; Chen, X.; Wu, Z.; Wang, H.; Peng, X. Surface characterization of rice husk bio-char produced by liquefaction and application for cationic dye (Malachite green) adsorption. *Fuel* **2015**, *155*, 77–85. [CrossRef]

19. Mohamed, M.M. Acid dye removal: Comparison of surfactant-modified mesoporous FSM-16 with activated carbon derived from rice husk. *J. Colloid Interface Sci.* **2004**, *272*, 28–34. [CrossRef]

20. Abdel-Fattah, T.M.; Mohamed, T.M.; Mahmoud, E.; Somia, B.; Matthew, A.; Huff, D.; James, W.L.; Sandeep, K. Biochar from woody biomass for removing metal contaminants and carbon sequestration. *J. Ind. Eng. Chem.* **2015**, *22*, 103–109. [CrossRef]

21. Mubarik, S.; Saeeda, A.; Athar, M.M.; Iqbal, M. Characterization and mechanism of the adsorptive removal of 2,4,6-trichlorophenol by biochar prepared from sugarcane baggase. *J. Ind. Eng. Chem.* **2016**, *33*, 115–121. [CrossRef]

22. Mahmoud, M.E.; Nabil, G.M.; El-Mallah, N.M.; Bassiouny, H.I.; Kumar, S.; Abdel-Fattah, T.M. Kinetics, isotherm and thermodynamic studies of the adsorption of reactive red 195 A dye from water by modified Switchgrass Biochar adsorbent. *J. Ind. Eng. Chem.* **2016**, *37*, 156–167. [CrossRef]

23. Pathania, D.; Sharma, S.; Singh, P. Removal of methylene blue by adsorption onto activated carbon developed from Ficus carica bast. *Arab. J. Chem.* **2017**, *10*, S1445–S1451. [CrossRef]

24. Rafatullah, M.; Sulaiman, O.; Hashim, R.; Ahmad, A. Adsorption of methylene blue on low-cost adsorbents: A review. *J. Hazard. Mater.* **2010**, *177*, 70–80. [CrossRef] [PubMed]

25. Zhang, R. Adsorption of Dye by Modified Activated Carbon and Heavy and Heavy Metals by Rice Husk-Based Activated Carbon. Master's Thesis, Nanjing Agricultural University, Nanjing, China, 2011. (In Chinese).

26. Choi, H.D.; Jung, W.S.; Cho, J.M.; Ryu, B.G.; Yang, J.S.; Baek, K. Adsorption of Cr(VI) onto cationic surfactant-modified activated carbon. *J. Hazard. Mater.* **2009**, *166*, 642–646. [CrossRef]

27. Lee, W.; Yoon, S.; Choe, J.K.; Lee, M.; Choi, Y. Anionic surfactant modification of activated carbon for enhancing adsorption of ammonium ion from aqueous solution. *Sci. Total Environ.* **2018**, *639*, 1432–1439. [CrossRef]

28. Lin, S.Y.; Chen, W.f.; Cheng, M.T.; Li, Q. Investigation of factors that affect cationic surfactant loading on activated carbon and perchlorate adsorption. *Colloids Surf. A Physicochem. Eng. Asp.* **2013**, *434*, 236–242. [CrossRef]

29. Choi, H.D.; Shin, M.C.; Kim, D.H.; Jeon, C.S.; Baek, K. Removal characteristics of reactive black 5 using surfactant-modified activated carbon. *Desalination* **2008**, *223*, 290–298. [CrossRef]

30. Namasivayam, C.; Suresh Kumar, M.V. Removal of chromium (VI) from water and wastewater using surfactant modified coconut coir pith as a biosorbent. *Bioresour. Technol.* **2008**, *99*, 2218–2225. [CrossRef]

31. Zhou, Y.; Wang, Z.; Andrew, H.; Ren, B. Gemini Surfactant-Modified Activated Carbon for Remediation of Hexavalent Chromium from Water. *Water* **2018**, *10*, 91. [CrossRef]

32. Akhter, M.S. Effect of acetamide on the critical micelle concentration of aqueous solutions of some surfactants. *Colloids Surf. A Physicochem. Eng. Asp.* **1997**, *121*, 103–109. [CrossRef]

33. Fu, J.; Chen, Z.; Wang, M.; Liu, S.; Zhang, J.; Zhang, J.; Han, R.; Xu, Q. Adsorption of methylene blue by a high-efficiency adsorbent (polydopamine microspheres): Kinetics, isotherm, thermodynamics and mechanism analysis. *Chem. Eng. J.* **2015**, *259*, 53–61. [CrossRef]

34. Wu, S.H.; Pendleton, P. Adsorption of anionic surfactant by activated carbon: Effect of surface chemistry, ionic strength, and hydrophobicity. *J. Colloid Interface Sci.* **2001**, *243*, 306–315. [CrossRef]

35. Wang, C. Fabrication of Polyacrylonitrile-Based Activated Carbon Fibers Functionalized Sodium Dodecyl Sulfate for the Adsorptive Removal of Organic Dye from Aqueous Solution. Master's Thesis, Hunan University, Changsha, China, 2017. (In Chinese).

36. Yagub, M.T.; Sen, T.K.; Ang, H.M. Equilibrium, Kinetics, and Thermodynamics of Methylene Blue Adsorption by Pine Tree Leaves. *Water Air Soil Pollut.* **2012**, *223*, 5267–5282. [CrossRef]

37. Kannan, N.; Sundaram, M.M. Kinetics and mechanism of removal of methylene blue by adsorption on various carbons—a comparative study. *Dye Pigment* **2001**, *51*, 25–40. [CrossRef]

38. Salleh, M.A.M.; Mahmoud, D.K.; Karim, W.A.; Idris, A. Cationic and anionic dye adsorption by agricultural solid wastes: A comprehensive review. *Desalination* **2011**, *280*, 1–13. [CrossRef]

39. Amin, N.K. Removal of reactive dye from aqueous solutions by adsorption onto activated carbons prepared from sugarcane bagasse pith. *Desalination* **2008**, *223*, 152–161. [CrossRef]

40. Eren, Z.; Acar, F.N. Adsorption of Reactive Black 5 from an aqueous solution: Equilibrium and kinetic studies. *Desalination* **2006**, *194*, 1–10. [CrossRef]

41. Plazinski, W.; Rudzinski, W.; Plazinska, A. Theoretical models of sorption kinetics including a surface reaction mechanism: A review. *Adv. Colloid Interface Sci.* **2009**, *152*, 2–13. [CrossRef]

42. Ho, Y.S.; Mckay, G. Pseudo-second order model for sorption processes. *Process Biochem.* **1999**, *34*, 451–465. [CrossRef]

43. Feng, M.; You, W.; Wu, Z.; Chen, Q.; Zhan, H. Mildly alkaline preparation and methylene blue adsorption capacity of hierarchical flower-like sodium titanate. *ACS Appl. Mater. Interfaces* **2013**, *5*, 12654–12662. [CrossRef] [PubMed]

44. Huang, X.; Bu, H.; Jiang, G.; Zeng, M. Cross-linked succinyl chitosan as an adsorbent for the removal of Methylene Blue from aqueous solution. *Int. J. Biol. Macromol.* **2011**, *49*, 643–651. [CrossRef] [PubMed]

45. Mall, I.D.; Srivastava, V.C.; Agarwal, N.K. Removal of Orange-G and Methyl Violet dyes by adsorption onto bagasse fly ash—kinetic study and equilibrium isotherm analyses. *Dyes Pigment* **2006**, *69*, 210–223. [CrossRef]

46. Yao, Y.; Xu, F.; Chen, M.; Xu, Z.; Zhu, Z. Adsorption behavior of methylene blue on carbon nanotubes. *Bioresour. Technol.* **2010**, *101*, 3040–3046. [CrossRef]

47. Mouni, L.; Belkhiri, L.; Bollinger, J.C.; Bouzaza, A.; Assadi, A.; Tirri, A.; Dahmoune, F.; Madani, K.; Reminie, H. Removal of Methylene Blue from aqueous solutions by adsorption on Kaolin: Kinetic and equilibrium studies. *Appl. Clay Sci.* **2018**, *153*, 38–45. [CrossRef]

48. Gobi, K.; Mashitah, M.D.; Vadivelu, V.M. Adsorptive removal of methylene blue using novel adsorbent from palm oil mill effluent waste activated sludge: Equilibrium, thermodynamics and kinetic studies. *Chem. Eng. J.* **2011**, *171*, 1246–1252. [CrossRef]

49. Auta, M.B.H. Hameed, Chitosan–clay composite as highly effective and low cost adsorbent for batch and fixed-bed adsorption of methylene blue. *Chem. Eng. J.* **2014**, *237*, 350–361. [CrossRef]

50. Bulut, Y.; Aydın, H. A kinetics and thermodynamics study of methylene blue adsorption on wheat shells. *Desalination* **2006**, *194*, 259–267. [CrossRef]

51. Que, W.; Jiang, L.H.; Wang, C.; Liu, Y.G.; Zeng, Z.W.; Wang, X.H.; Ning, Q.M.; Liu, S.H.; Zhang, P.; Liu, S.B. Influence of sodium dodecyl sulfate coating on adsorption of methylene blue by biochar from aqueous solution. *J. Environ. Sci.* **2018**, *70*, 166–174. [CrossRef]